DISS. ETH No. 22549

Towards next generation fundamental precision measurements with muons

A thesis submitted to attain the degree of

DOCTOR OF SCIENCE of ETH ZURICH

(Dr. sc. ETH Zurich)

presented by

Kim Siang Khaw

MSc, Physics, The University of Tokyo

born on 04.02.1984

citizen of
Malaysia

accepted on the recommendation of

Prof. Dr. Klaus Kirch, examiner
Prof. Dr. Christoph Grab, co-examiner

2015

_____

_____   _____
Prof. Dr. Klaus Kirch, examiner   Date

Abstract

Several previous fundamental precision measurements with muons (μ^+), such as that of the muonium (Mu) 1S-2S transition frequency and ground-state hyperfine splitting, were limited by the statistics and the beam quality, in terms of vacuum yield, low energy and long term stability. A Mu source with a larger flux can be achieved either by improving the $\mu^+ \rightarrow$ Mu conversion rate or by improving the μ^+ beam (smaller phase space, low energy, high intensity). This thesis reports the ongoing efforts at ETH Zurich (ETHZ) and PSI towards a high yield cryogenic Mu source and a new, low energy, high brilliance positive μ^+ beam. The former is based on mesoporous silica materials while the latter is making use of a phase space compression of μ^+ stopping and drifting in a helium gas density gradient within suitable electric and magnetic fields.

The first observation of cryogenic Mu emission into vacuum following muon implantation in mesoporous thin silica films is reported. Based on a simple Geant4 Monte Carlo simulation, a yield of Mu into vacuum of $F_{\mathrm{Mu}}^v = 0.38(4)$ at 250 K and $F_{\mathrm{Mu}}^v = 0.20(4)$ at 100 K for 5 keV μ^+ implantation energy is extracted from the measurements. Based on the implantation energy dependence of the vacuum yield deduced from a quantum tunneling model, a second experiment was performed for implantation energies below 5 keV where higher Mu vacuum yields are expected. Due to an upgrade in the LE-μSR apparatus at PSI, new full muon transport simulations had to be performed in order to understand the propagation of μ^+ beam at very low energy. Mu physics and energy losses in the carbon foil are implemented and validated using time-of-flight (TOF) measurements. The feasibility of Mu confinement is also demonstrated by using a SiN membrane as the μ^+ entrance window. These two achievements, high vacuum yield and confinement, represent important steps towards next generation Mu spectroscopy.

Research and development (R&D) of the new μ^+ beam compression scheme which is ongoing at ETHZ and PSI are very encouraging. The feasibility of the longitudinal compression stage was successfully demonstrated in 2011. This demonstration relies on the agreement between the experimental results and the simulation based on Geant4, after implementing μ^+ physics processes at low energy such as elastic collisions and charge exchange. A neutron radiography experiment has demonstrated the feasibility to sustain the necessary density gradient for the transverse compression stage. A gas density gradient concept was implemented into Geant4 simulations. With this, the simulated time spectra and the experimental data can be compared when data will available. An engineering run towards the test of transverse compression has been done in Dec 2014. The realization of this beam line will enable one to produce a micro-beam of muons and it will have many applications, especially to the μSR and precision physics community.

Zusammenfassung

Mehrere bisherige fundamentale Präzisionsexperimente mit Myonen (μ^+), wie die Messungen der Myonium (Mu) 1S-2S Übergangsfrequenz und die Hyperfeinstrukturaufspaltung, waren limitiert durch Statistik und Strahlqualität bezüglich Vakuumausbeute, Langzeitstabilität und niedrigen Energien. Eine Mu-Quelle mit höherer Intensität kann entweder durch Verbesserung der $\mu^+ \rightarrow$ Mu Umwandlungsrate, oder durch Verbesserung des μ^+ Strahls (kleinerer Phasenraum, niedrige Energie, hohe Intensität) erreicht werden. In dieser Arbeit wird von den fortlaufenden Bemühungen der ETH Zürich (ETHZ) und des PSI berichtet, welche auf eine kryogene Mu-Quelle mit hohem Ertrag und einen neuen, niederenergetischen μ^+ Strahl mit hoher Brillanz abzielen. Ersteres wird mittels mesoporösen Silica Materialen erreicht, und letzteres mittels einer Phasenraumkompression der μ^+, welche in einem Helium Gas mit einem Dichtegradienten gestoppt werden und durch entsprechende elektrische und magnetische Felder driften.

Es wird von der erstmaligen Beobachtung kryogenischer Myonium-Emission ins Vakuum berichtet, der Myon-Implantation in mesoporöse, dünne Silica-Schichten vorangeht. Anhand einer einfachen GEANT4-Monte-Carlo-Simulation erhält man eine Ausbeute von Myonium ins Vakuum von $F_{Mu}^v = 0.38(4)$ bei 250 K und $F_{Mu}^v = 0.20(4)$ bei 100 K für 5 keV Implantationsenergie. Basierend auf der Abhängigkeit der Vakuumausbeute von der Implantationsenergie wurde ein zweites Experiment mit Implantationsenergien kleiner als 5 keV durchgeführt, bei welchen eine höhere Vakuumausbeute erwartet wird. Aufgrund einer Verbesserung in der LE-μSR Apparatur am PSI musste eine neue, komplette Transportsimulation durchgeführt werden, um die Propagation des μ^+ Strahls bei niedrigen Energien zu verstehen. Die Physik und Energieverluste von Mu in Kohlenstofffolien wurden implementiert und mittels Time-of-Flight (TOF) Messungen validiert. Die Machbarkeit von Mu-Confinement wurde ebenfalls gezeigt indem eine SiN-Membran als μ^+ Eintrittsfenster benutzt wurde. Diese zwei Errungenschaften, hoher Vakuumertrag und Confinement, sind wichtige Schritte auf dem Weg zu Mu-Spektroskopie der nächsten Generation.

Die Forschung und Entwicklung (R&D) für das neue μ^+ Strahlkompressions-Projekt, welches an der ETHZ und am PSI stattfinden, ist vielversprechend. Die Machbarkeit der longitudinalen Kompressionsstrecke wurde erfolgreich in 2011 demonstriert. Diese Demonstration stützt sich auf die Übereinstimmung zwischen den experimentellen Resultaten und Simulationen basierend auf GEANT4, nachdem die physikalischen Prozesse bei niedrigen Energien für μ^+, wie elastische Stösse und Charge Exchange, implementiert wurden. Durch ein Radiographie-Experiment mit Neutronen konnte die Umsetzbarkeit, den für die transversale Kompression erforderlichen Dichtegradienten aufrecht zu erhalten, gezeigt werden. Ein Konzept für den Dichtegradienten im Gas wurde in

GEANT4-Simulationen eingebaut. Mit diesem können simulierte Spektren und experimentelle Daten verglichen werden. Ein "Engineering-Run" in Richtung transversale Kompression wurde im Dezember 2014 durchgeführt. Die Umsetzung dieser Strahllinie wird ein μ^+ Micro-Beam ermöglichen, welcher viele Anwendungen haben wird, speziell in der μSR und Teilchen- und Atomphysik.

Acknowledgments

I would like take this opportunity to express my gratitude to many people who have been extremely helpful throughout my stay at the ETHZ, Switzerland for my daily life, teaching duties and my doctoral research work.

First and foremost, my utmost gratitude to my thesis supervisor **Klaus Kirch** for giving me the chance to work on very interesting projects regarding muon and muonium which are now compiled into my PhD thesis. He has been very supportive to my research work, my participation in conferences and summer schools. I have received from him many valuable advice regarding future career path.

Aldo Antognini is another mentor that I owed a lot to, for his patience and support of my entire research life at ETHZ. His involvement and experience in many experiments at PSI and ETHZ makes him my walking dictionary whenever I am in trouble understanding difficult research works. He always goes the extra mile in proofreading my presentation and written materials and I am extremely grateful for that.

A big fan of Malaysian cuisines, **Florian Piegsa** is another senior in the group who has given me many useful advice in my research work, especially in the data analysis. I have learned a lot from him regarding neutron physics, especially from his lecture.

Jochen Krempel, even though spending most of the time at PSI, is an expert in electronics and I am glad to learn some from him. We are both badminton enthusiasts and are playing in the Swiss Badminton League for different teams, but have never played against each other before. Perhaps this will change after finishing this thesis.

Paolo Crivelli who is mainly involved in positronium researches has been very supportive to my doctoral work, especially about the Monte Carlo simulation and the data analysis of the muonium production. He has also given me many valuable advice for my presentation, article, and postdoc job hunting. Working together with him has broaden my research interest horizon especially in the positronium and antihydrogen physics.

Working with **Thomas Prokscha** from the Low Energy Muon (LEM) group of PSI is very inspiring, for his full support during the beam time at the LEM beam line, and also for his willingness to exchange thousands of emails with me who seems to have endless questions about anything related to the hardware and software of the LEM. Barefoot tennis-playing in Würenlingen together with Aldo, Paolo and him after our first beam time is a truly amazing experience that I will not forget.

For the phase space compression of a muon beam, **Yu Bao** and **Angela Papa** were very collaborative and we had great time working together. With Yu, it was perhaps for the first time I have used Chinese as the medium language to discuss daily research works. I must also mention that it has been a great experience to work together with **David Taqqu**. Even though he has retired, he is still providing us with dozens of ideas

to solve the technical problems in phase space compression. I have received countless of constructive suggestions from him for my research works.

I would like to thank **Laszlo Liskay** from CEA Saclay for the preparation of the mesoporous silica thin films, which were used for the muonium production in this thesis. During my trip to CEA, I have benefited a lot from him.

My PhD life would be very different without the companion of PhD mates; **Karsten Schuhmann** for his thousands of interesting life stories and cutting edge news in laser physics, **Andreas Eggenberger** for his advice and information regarding running sports and the technical details on the helium gas leak testing and helium gas target construction for the muon beam compression experiment, **Gunther Wichmann** for his assistance and the technical details on the cryogenic system and gas density gradient, and **Ivana Belošević** for her wonderful work on the leak test and the readout of scintillator using wavelength shifting fiber and G-APD.

Secretaries from the Institute for Particle Physics and PSI have been extremely helpful for all the administrative works. A big thank to **Johanna Amberg** especially for her assistance in getting me an air ticket to come here and helping me to settle down in Zurich. **Rosa Bächli**, **Yvonne Engelberger**, **Gabriela Amstutz** and **Bettina Lareida** have provided me with excellent supports, from business travel arrangement to PhD thesis printing, which enables me to concentrate on my research works.

I owe it to the help of **Katarina Manthey**, and **Christoph Kittel** for providing a good start to my life in Zurich when I had zero knowledge of Swiss German or even German. Thanks to Katarina for picking me up during my arrival at the Zurich airport prior to the start of my PhD and also as a wonderful PhD mate for a year in the same office. Thanks to Christoph, I managed to find some places where I can stay during the first few months.

Many thanks to my mostly-Malaysian-buddies **Jia En Low**, **Zuo Yen Lee**, **Alessio Bolognesi**, **Kong Ooi Tan**, **Yi Cheng Ng**, **Zhi Yang Tam**, **Cheng Choon Ang** and **Woon Yew Siau** for providing all the mental and physical supports and making me feeling at home in this faraway land. I am very glad that you guys are always around no matter whether it is sunny or rainy.

Working as a volunteer in the **Telejob** has prepared me better for my future career and has broadened my view about what is going on inside and outside of academia. Moreover, working together with fellow PhD students from other fields has helped me to understand a lot regarding cultural differences among research fields.

Finally I would like to thank **Chow Lih Yew** for her love, understanding and support throughout my PhD life. Things would be different without her company in Switzerland. My sister, parents and grandparents receive my deepest gratitude for their mental supports and encouragement.

Contents

List of Figures

List of Tables

Acronyms

QM   quantum mechanics

QED   quantum electrodynamics

NMR   nuclear magnetic resonance

SM   Standard Model

HIPA   High Intensity Proton Accelerator

μSR   Muon Spin Rotation

MuSR   Muonium Spin Rotation

PSI   Paul Scherrer Institute

J-PARC   Japan Proton Accelerator Research Complex

LEM   Low Energy Muon

LE-μSR   Low Energy Muon Spin Rotation

PST   Positron Shielding Technique

RIKEN-RAL   RIKEN-Rutherford Appleton Laboratory

MCP   micro channel plate

APD   Avalanche Photo Diodes

GUI   Graphical User Interface

HFS   hyperfine structure

Chapter 1

Introduction

The hydrogen atom (H) [2–4] is the simplest atom in the universe. Because of its simplicity, it represents an ideal platform to compare predictions from fundamental theories like quantum field theory (see for example [5]) with measurements. H was an essential player in the development of quantum mechanics (QM), representing the most crucial test for the Dirac equation and triggering the development of quantum electrodynamics (QED) [6]. In addition, studies on H have led to better understanding of the nature of the nuclear force and to many techniques which are the base of all modern technology such as atomic clock [7], nuclear magnetic resonance (NMR) [8] and frequency combs [9, 10]. Precision spectroscopy measurements on H (see for example [11]) have also led to precise determinations of the fundamental constants such as the Rydberg constant R_∞, the proton radius r_p as well as the mass and electric charge ratio between the electron and the proton, m_e/m_p, q_e/q_p, respectively.

However, comparisons of the H energy spectra as predicted by bound-state QED with experiments are limited by the complexity of the proton structure. Fortunately, nature has provided us with some exotic "atoms" whose "nuclei" have no structure such as positronium (Ps, bound state of e^+ and e^-) [12] and muonium (Mu, bound state of μ^+ and e^-) [13]. Since high energy scattering experiments and measurements of the g-2 have shown that leptons such as electrons and muons have no internal structure down to dimensions of 10^{-18} m [14], both systems are free of nuclear effects and are thus clean systems to test bound-state QED. Moreover, recent results from the precision muon g-2 measurement at BNL [16] and the precision spectroscopy of muonic hydrogen at PSI [17, 18] where discrepancies between experiment and theory of about 3σ and 7σ, respectively have been observed, have renewed the interest in these H-like systems. Even though new experiments such as muon g-2 experiments at FNAL [19] and Japan Proton Accelerator Research Complex (J-PARC) [20], muonium hyperfine structure (HFS) at J-PARC [21], Lamb shift in muonic helium at PSI [22] and transition frequency

1
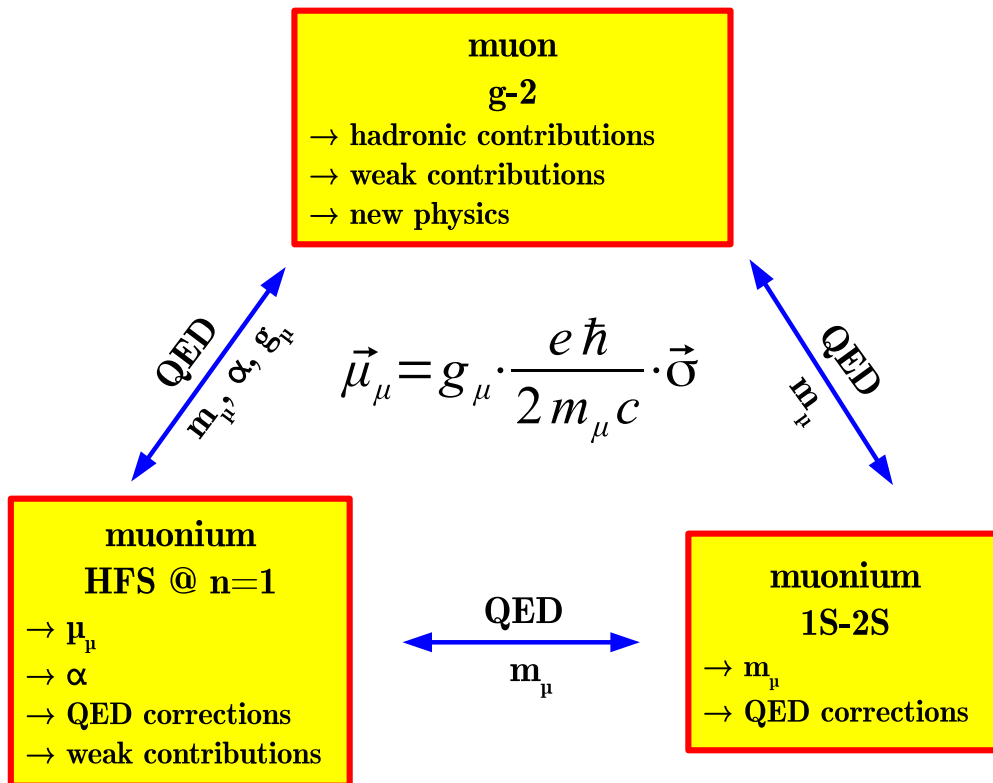
Figure 1.1: *The precise measurement of the muon g-2 factor is closely related to the muonium ground-state hyperfine splitting and the muonium 1S-2S transition frequency. The measurements are best tests of the internal consistency of the theory of electroweak interaction and can be used to extract fundamental constants. Adapted from [15].*

measurements in H and helium at MPQ [23, 24], Amsterdam [25, 26], Paris [27] and Toronto [28] are running to shed some light on these discrepancies, the same is also attempted by studying Mu, as some of the measurements are closely connected to each other as shown in Figure 1.1. It should be noted that a more precise value of the muon g-2 can only be obtained experimentally with an improvement in the knowledge of the fundamental constants such as the muon to proton magnetic moment μ_μ/μ_p. Muonium spectroscopy is the best way of extracting it [29–31].

In the following sections, a brief introduction about muon and muonium physics which is relevant to this thesis will be given. For a thorough review about muons, see [32, 33] and for muonium, see [34–38].

1.1 Properties and production of muons

The muon was discovered as a constituent of cosmic-ray particle showers in 1936 by the physicists Carl D. Anderson and Seth Neddermeyer [39, 40] and its properties are still being studied. Within the framework of the elementary particle physics in the Standard Model (SM), it is a second generation charged lepton. It has two charge types (positive μ^+ and negative μ^-), and has an interesting mass value intermediate between the proton mass and the electron mass. Its properties are summarized in Table 1.1.

Table 1.1: *Fundamental properties of the muon taken from [41].*

Mass, m_μ	105.6583715(35) MeV/c^2
Lifetime, τ_μ	2.1969811(22) μs
Charge, q_μ	$\pm$e
Spin, s	$\hbar/2$
Magnetic moment, μ_μ	4.49044786(16)$\times 10^{-26}$ J/T
Spin g-factor, g_μ	2.0023318414(12)
Gyromagnetic ratio, $\gamma_\mu = g_\mu \mu_\mu / h$	2$\pi \times$135.69682(5) MHz/T

Besides the ones which are produced in the upper atmosphere as a result of primary cosmic rays interactions and pion decays, muons are normally produced in medium-energy proton accelerators such as at PSI where protons with energies of about 600 MeV are directed at a production target consisting of a light element such as beryllium or carbon. The most abundant particles arising from the proton-nucleus reaction are charged pions $(\pi^\pm)$, produced via the following channels:

$$p + p \rightarrow \pi^+ + n + p \tag{1.1}$$

$$p + n \rightarrow \pi^- + p + p \; . \tag{1.2}$$

Most of the produced $\pi^\pm$ escape the production target while some of them are thermalized and stopped in the target itself. With a lifetime of $\tau_\pi = 26$ ns, the pion decays through the weak interaction into a muon and a neutrino:

$$\pi^+ \rightarrow \mu^+ + \nu_\mu \; . \tag{1.3}$$

Muons originated from the pions which decay at rest on the surface of the target are called **surface muons** [42]. Surface muons are approximately mono-energetic (4.1 MeV energy corresponding to a momentum of 29.8 MeV/c). This is a consequence of the two-body decay of the π (Figure 1.2) and the fact that μ^+ produced at the surface of the target cross only a thin layer of material before being emitted out of the production
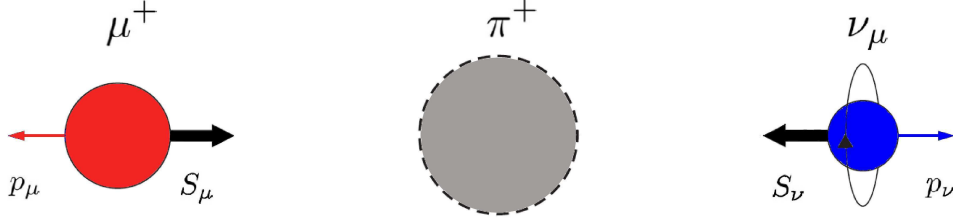
Figure 1.2: *Due to the parity violation of the weak interaction, only left-handed neutrino ν_μ is produced in a pion decay. This implies that the μ^+ spin $\boldsymbol{S}_\mu$ is anti-parallel to its momentum since the neutrino momentum $\boldsymbol{p}_\nu$ and its spin $\boldsymbol{S}_\nu$ must be anti-parallel. Adapted from [43].*

target. Furthermore, due to the parity violation of the weak interaction, the μ^+ spin is aligned anti-parallel to its momentum as shown in Figure 1.2 since only the left-handed neutrino is involved in the weak interaction. Therefore, a μ^+ beam with nearly 100% polarization can be extracted from the production target and transported through secondary beam lines to the experiments.

The μ^+ also decays through the weak interaction with a lifetime of $\tau_\mu = 2.2 \ \mu$s into a positron and two neutrinos

$$\mu^+ \rightarrow e^+ + \nu_e + \bar{\nu}_\mu \ . \tag{1.4}$$

Since this is a three-body decay, the positrons are not mono-energetic but have a distribution (Michel spectrum) with an end-point energy of about $E_e^{max} \approx 52.8$ MeV. Again due to the parity violation of the weak decay, the direction of the decay positron is distributed asymmetrically with respect to the spin of the muon $\boldsymbol{S}_\mu$. The positrons are emitted with an angular distribution and asymmetry parameter given by:

$$N_e(\theta, E_e) \ \propto \ 1 - A(E_e) \cos\theta \tag{1.5}$$
$$A(E_e) \ = \ (E_e^{max} - 2E_e)/(3E_e^{max} - 2E_e) \ . \tag{1.6}$$

where θ is the angle between $\boldsymbol{S}_\mu$ and the positron momentum $\boldsymbol{p}_e$, E_e the positron energy, $E_e^{max} = m_\mu c^2/2 = 52.8$ MeV and A is defined as the muon decay asymmetry. The angular distributions of the emitted positrons for different energies are plotted in Figure 1.3. At the end-point energy where $E_e = E_e^{max}$, the decay asymmetry has the maximum absolute value and is equal to -1. This case is shown in Figure 1.4. The integration of $A(E_e)$ over the whole positron energy spectrum yields a mean value of

$$\overline{A(E_e)} = \int_0^{E_e^{max}} A(E_e) dE_e = \frac{1}{3} \ . \tag{1.7}$$

4
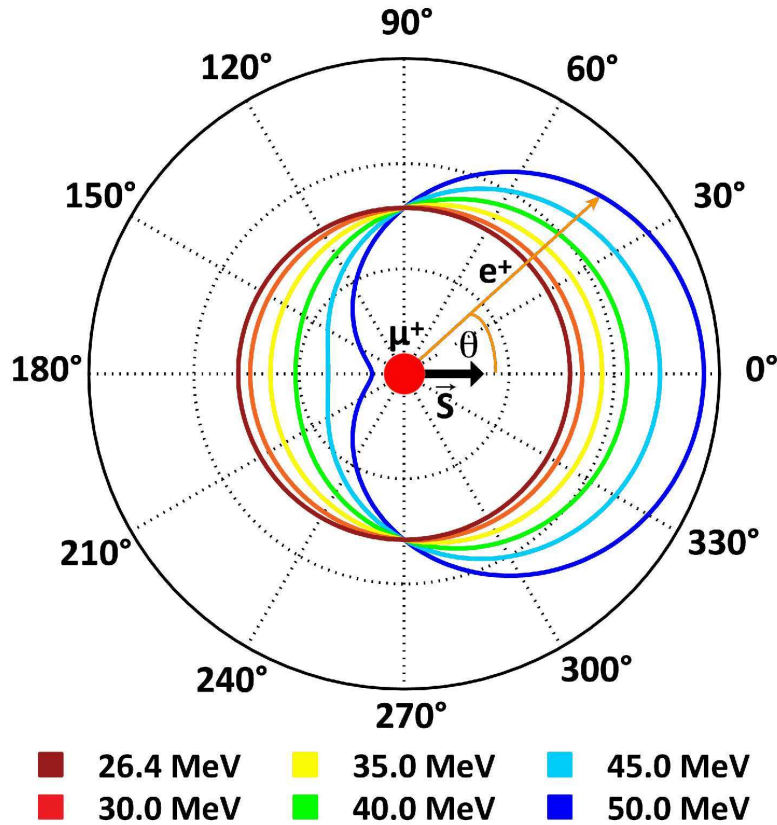
Figure 1.3: *Spatial distribution of the emitted positron for different positron energies. At the end-point energy, the decay asymmetry reaches the maximum. Adapted from [44].*

As a result, the positrons are emitted preferentially in the direction of the muon spin at the moment of its decay. The μSR technique utilizes this property to monitor the precession of the muon spin inside a material. It was exactly this technique that led to the discovery of Mu. Further detail about the μSR technique will be given in Chapter 3.

1.2 Properties of muonium

The discovery of the muonium atom can be traced back to the 1950's when the physicists at Chicago and Columbia were studying muon depolarization in various materials after the discovery of the parity violation in the weak decay [45]. They discovered that the muon polarization could range from 0 to 100% depending on the target material. While μ^- could form muonic atoms with successive decay or capture by the nucleus, μ^+ decay into a positron and two neutrinos. As mentioned previously, the resultant decay
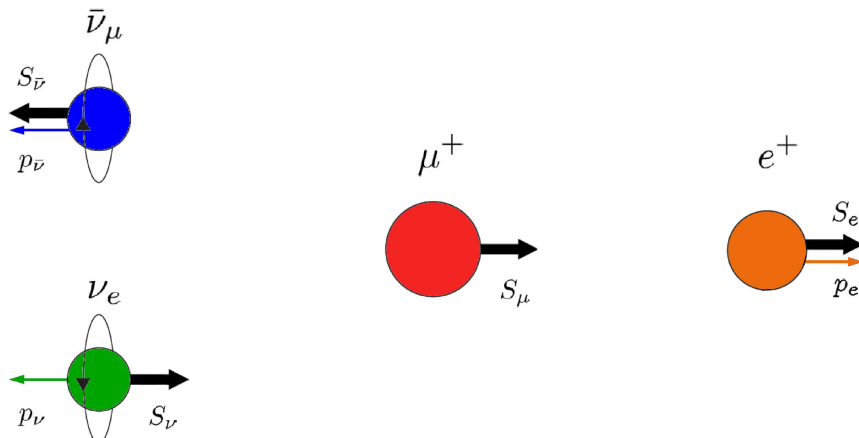
Figure 1.4: *The positive muon decays into a positron and two neutrinos. The highest positron end-point energy $E_e^{max} \approx 52.8$ MeV scenario is shown to demonstrate the anisotropy of the muon decay, where the e^+ is emitted to the direction of the μ^+ spin. Adapted from [43].*

asymmetry with respect to the muon spin direction can be used to determine the muon polarization at the decay time. The Chicago group which was then led by Val Telegdi noted in one of their 1957 papers [46] that "The formation of a μ^+e^- atom (**muonium**) can be a possible cause for the reduced asymmetry of μ-e decay in certain materials".

Table 1.2: *Fundamental properties of the muonium in the ground-state.*

Mass, m_{Mu}	106.169369 MeV/c^2
Lifetime, τ_{Mu}	2.1969811(22) μs
Charge, q_{Mu}	0
Spin, s	singlet or triplet
Gyromagnetic ratio, γ_{Mu}	2$\pi\times$13.94 GHz/T=102.88γ_μ

Since then, a lot of experiments were performed to search for the muonium atom and to understand its properties (see Table 1.2) and its interactions with various materials, for example, see [47]. Throughout this thesis, the muonium atom will be denoted by Mu according to the definition given by [48], even though it was abbreviated by the late V. Telegdi with the symbol M, and also being used by V. W. Hughes and collaborators throughout their experiments.

Nowadays, Mu is understood as a hydrogen-like exotic atom and is one of the simplest bound states governed by QED. Free from the hadronic uncertainties related with
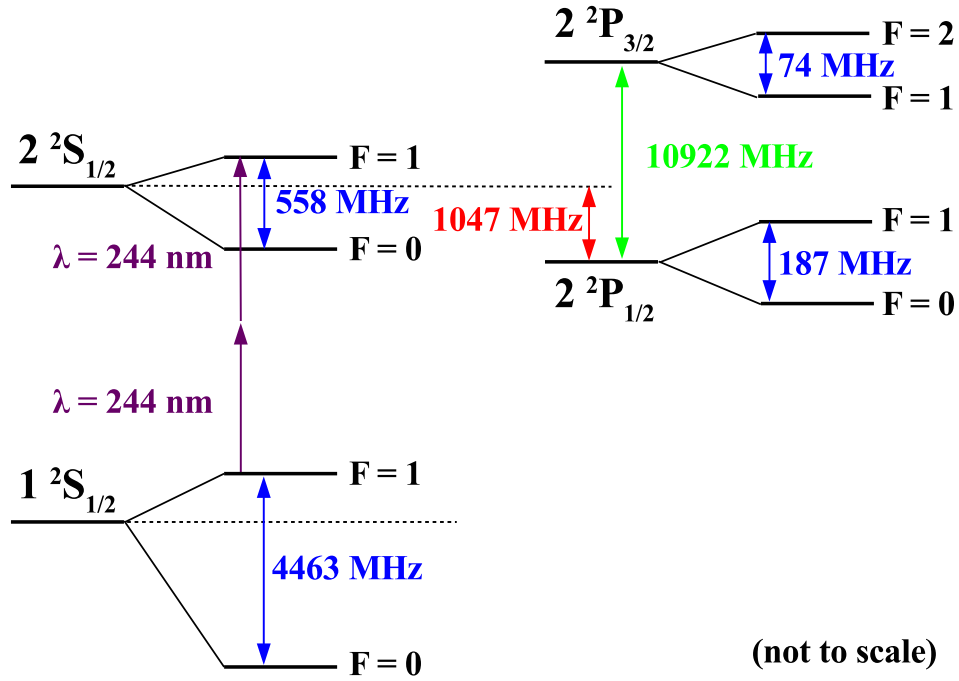
Figure 1.5: *Energy levels of the muonium atom and the related transition frequencies: the 1S-2S transition which can be excited with two photons at 244 nm wavelength, the ground-state hyperfine splitting at 4463 MHz, and the 2S-2P Lamb shift at 1097 MHz.*

the nuclear structure [4, 34], basic properties of the μ-e interaction can be examined and fundamental constants related to it can be extracted by means of high-precision spectroscopy. Some of its transition frequencies are calculated and measured to very high precision as shown in Figure 1.5. Particularly, the ground-state hyperfine splitting [29] and the $1S$-$2S$ transition frequency [30, 31] provide the best determination of the muon mass, of the muon magnetic moment, and of the charge ratio between muon and electron. The latter best verifies the charge equivalence between the first two lepton generations (implicit input in the SM). Mu can also be used to probe for new physics such as lepton flavor violation via searches of muonium-antimuonium oscillations [49]. Recently, a test of antimatter gravity by means of Mu atom interferometry technique [50–52] and a search of Lorentz and CPT symmetry violation using Mu atom [53] were proposed.

1. Gas stop
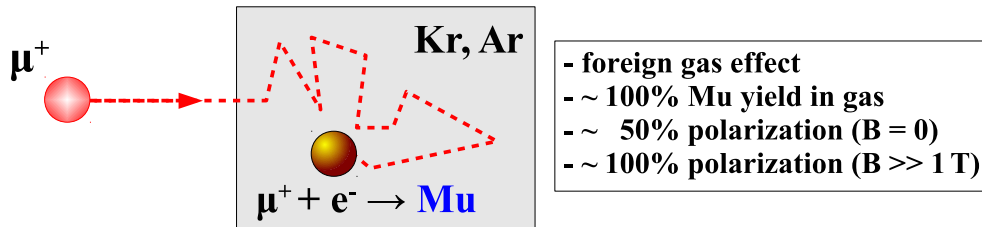
2. Beam foil
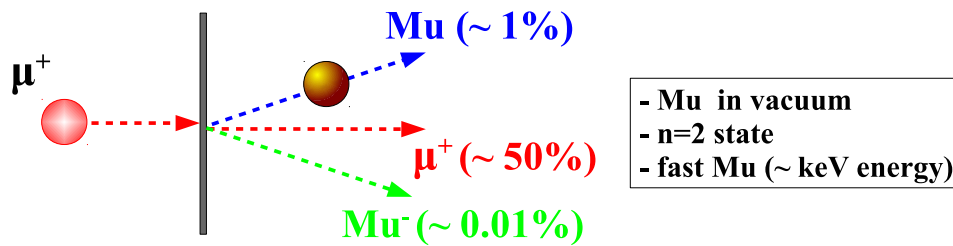
3. Silica power/aerogel
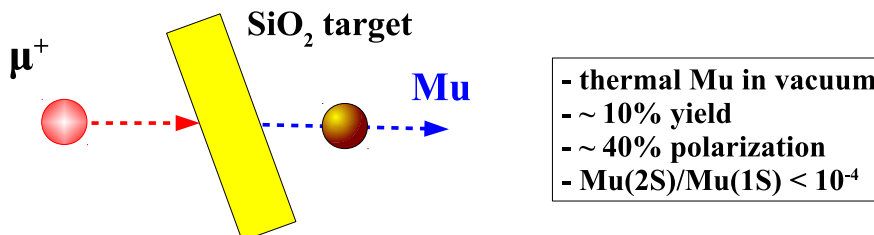
Figure 1.6: *Muonium atoms for precision measurements have been produced by three different methods. 1) Stopping muons in a noble gas target (Kr, Ar) produces Mu atoms at thermal energies with almost 100% yield. However, Mu atoms produced with this method are subjected to collisional effects. Mu in vacuum is produced typically by two techniques, 2) beam foil techniques which produce also Mu in vacuum in the $n = 2$ state with keV energies, and 3) stopping a low energy μ^+ beam in a solid target such as silica powders and silica aerogels. The stopped μ^+ catches an electron near to the end of its ionization path and forms a Mu atom mostly in the ground state. Mu atoms diffuse with thermal energies to the surface of the solid where emission into vacuum occurs. Adapted from [54].*

1.3 Formation and detection of muonium atoms

In the early years, most of the experiments related to Mu atoms were done in a material environment. An example of this is the measurement of the ground-state hyperfine splitting of the Mu [55]. In the 1980s, several techniques were developed to produce the Mu atoms in vacuum and this has expanded significantly the spectrum of possible precision measurements, e.g. the measurement of the Mu 1S-2S transition frequency.

Since then, Mu in vacuum is typically produced by stopping an intermediate energy or surface μ^+ beam in a solid target such as tungsten foils [56], silica powders [57, 58] or silica aerogels [59, 60] as shown in Figure 1.6. The stopped μ^+ catches an electron near to the end of its ionization path and forms a Mu atom. Mu then diffuses to the surface of the solid where emission into vacuum occurs. Mu which diffuses to the surface is emitted into vacuum. Prior to this thesis work, the highest measured vacuum yield was $(18\pm2)\%$ per stopped μ^+ obtained in SiO_2 powders at 300 K [57, 58, 61].

Mu yield in vacuum is measured typically using a series of positron telescopes as shown in Figure 1.7. The positron track is reconstructed back to the region in front of the silica sample (muon target). From the time difference between the start detector and the telescopes, the velocity distribution of the Mu can be determined.

1.4 Towards better muon and muonium sources

One of the main limitations in the experiments with low energy μ^+ and Mu atoms is the quality of the μ^+ and Mu sources [34]. A Mu source with a larger flux can be achieved either by improving the $\mu^+ \rightarrow$ Mu conversion rate or by improving the μ^+ beam (smaller phase space, low energy, high intensity) as proposed in [62, 63]. Hence, this thesis has been devoted to the optimization of the μ^+ to Mu conversion using mesoporous SiO_2 thin films (see for example [64]) and to the development of a novel high brilliance low energy μ^+ source as proposed in [63].

Optimization of μ^+ to Mu conversion

The choice of the mesoporous SiO_2 as the conversion target was motivated by the fact that Ps and Mu share similar formation mechanisms in the powder silica [57]. Recently, a yield of Ps into vacuum as high as 40% from these porous samples has been measured down to cryogenic temperatures [64]. In contrast to SiO_2 powders, these samples can be produced under well-controlled conditions with uniform pore sizes and distributions. The long term stability was measured with Ps for which the vacuum yield was constant in a time scale of months.
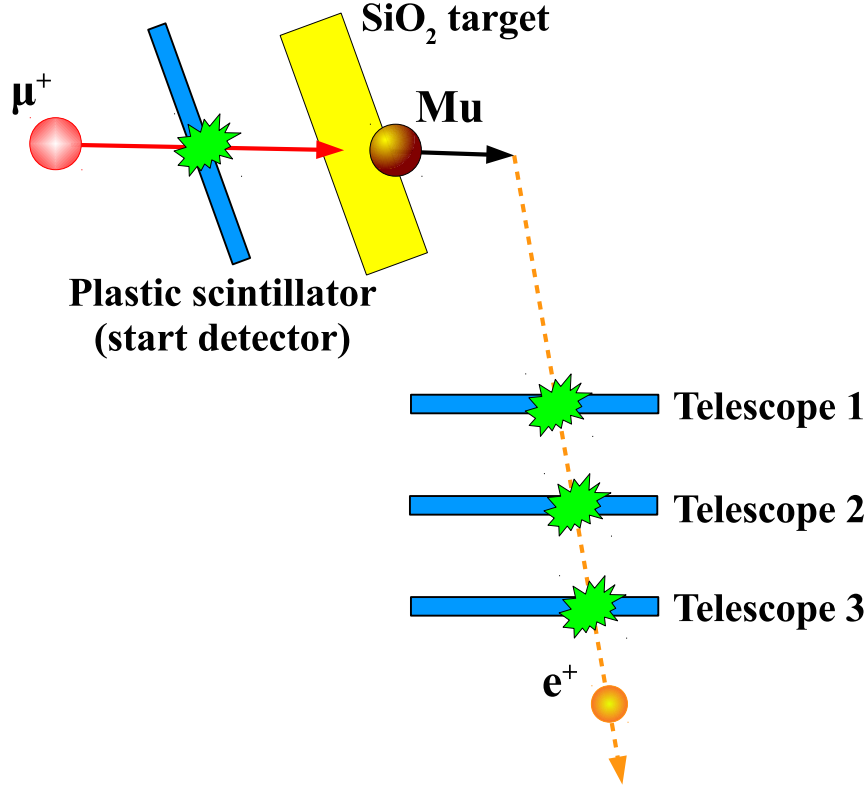
Figure 1.7: *A typical setup for detecting muonium in vacuum. The positron from μ^+ decay of the Mu atom is used to reconstruct the decay position of the Mu.*

There is also a recent effort by Beer *et al.* to improve the emission of Mu atoms into vacuum by using a laser-processed aerogel [65]. Hole-like regions with diameter of about 270 μm in a triangular pattern with hole separation in the range of 300-500 μm were created using laser ablation. The achieved Mu yield in vacuum is 3% and it is 8 times higher than the previous best measurement with aerogel samples before treated with laser ablation [60]. Another order of magnitude improvement is needed to reach the requirement for the proposed muon g-2 measurement at J-PARC [66].

In this thesis, in contrast to the typical detection technique where the Mu atom is extracted downstream of the muon beam, a new type of arrangement is used where the Mu atom is re-emitted into the opposite direction of the initial muon momentum as shown in Figure 1.8. This technique is only possible by using keV energy muons. Mesoporous silica is used for the Mu production in vacuum and several techniques are used to extract the information regarding Mu formation.

typical configuration   **new configuration**
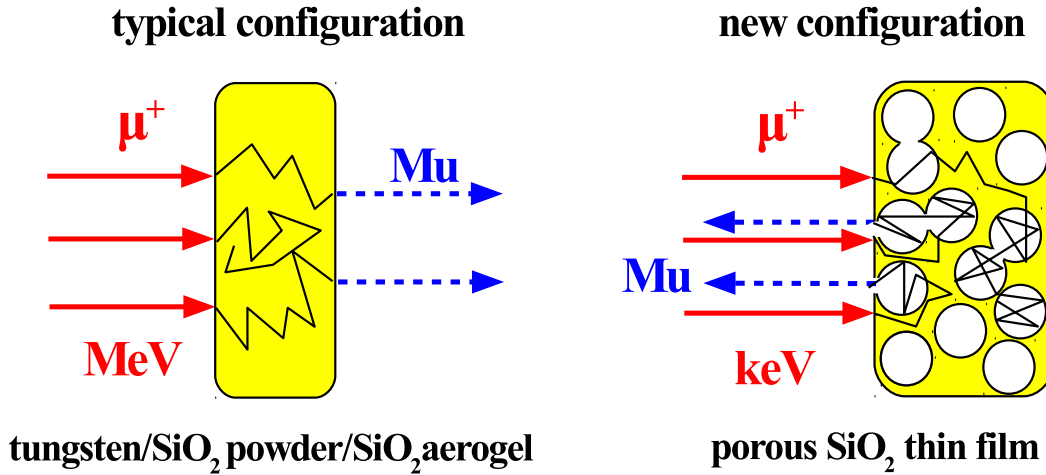
Figure 1.8: *(left) For the typical techniques using hot tungsten foil or silica powder, the Mu atom is extracted downstream of the muon beam. (right) In this thesis, the muon beam is implanted into the mesoporous silica thin film with a mean depth of 50 - 300 nm. The muons will form Mu atoms and thermalize inside the bulk material before diffusing out to the vacuum region.*

A novel high brilliance low energy muon beam line

This new beam line of low energy μ^+ [63] leads to a reduction of phase space of up to a factor of 10^{10} compared to a conventional muon beam line, with an overall efficiency of 10^{-3}. It is based on a position-dependent muon drift velocity in a helium gas cell with gas density gradient, electric and magnetic fields. The final average kinetic energy of the muon beam is 1 eV and with a beam size below 1×1 mm^2. Such a tertiary beam may serve as an add-on to an existing or a future high intensity muon beam. It can, in principle, be applied and used on several beam lines and also potentially at other future facilities. It can also be used for next generation μSR applications (for small sample sizes below 1×1 mm^2), precision experiments such as muon g-2 [16] and searches for muon electric dipole moment (μEDM) [67]. Additionally, a novel high brilliance low energy μ^+ source that is currently being developed at PSI can be implanted into a superfluid helium target to produce a quasi-mono-energetic Mu beam [50, 52, 63]. Even though the formation of Mu inside the superfluid helium has been measured [68, 69], the predicted quasi-mono-energetic emission of the Mu atom from the superfluid surface [70] has not been verified. Such a verification is planned at PSI in the coming years. In this thesis, research and development going on at ETH and PSI for this novel beam line will be

elaborated.

The subsequent parts of the thesis are organized as follows:

Chapter 2 is essentially about the main features of the PSI proton accelerator, Low Energy Muon (LEM) beam line and its spectrometer for μSR and PST measurements. The preparation of the mesoporous silica thin film is also discussed in this chapter.

Chapter 3 and Chapter 4 are devoted to the principle of the experiment to optimize the μ^+ to Mu conversion rate. Two different techniques are used to obtain the information regarding the muonium formation in the mesoporous silica material. In Chapter 3, the μSR technique that is used to extract the muonium formation probability is described. The later part of the chapter will be concentrated on the data analysis of the μSR. In Chapter 4 the PST that is used to extract the muonium yield in vacuum will be elaborated. It is then followed by the data analysis. A quantum mechanical diffusion model is used to explain the observations. Possible improvements are also discussed at the end of the chapter.

Based on the results from Chapter 4, Chapter 5 focuses on the second attempt of optimization to go further down in the muon implantation energy. An upgraded LEM beam line will be discussed where a spin rotator is installed and the positions of several elements have been optimized. Several physics models have been added to the simulation in order to reproduce the measured time spectra. Then the data analysis methods from the Chapter 3 and Chapter 4 are again applied to the data taken with the upgraded beam line and several problems are discussed.

Chapter 6 focuses on the confinement of the Mu atom in a small volume. It is an important step for the muonium spectroscopy especially for the 1S-2S transition frequency measurement. The resulting longer interaction time between the Mu atom and the laser will increase the number of excited Mu atoms and hence the event rate of the measurement. A preliminary result of the analysis will be presented.

Chapter 7 is devoted to the research and development of a novel high brilliance slow μ^+ beam line. The principle of the beam line is first explained and is followed by the simulations and the experimental results.

Chapter 8 is the conclusion of this thesis.

Chapter 2

Experimental setup

This chapter first describes the source of μ^+ used for the optimization of the $\mu^+ \to$ Mu conversion, which is the LEM beam line at PSI. Next the LE-μSR apparatus, installed at the end of this beam line and dedicated to μSR measurements, is presented. This is followed by an introduction to mesoporous materials and finally the preparation of the mesoporous silica thin films which are studied in this thesis for $\mu^+ \to$ Mu conversion.

2.1 The high intensity proton accelerator at PSI

The measurements described in this thesis were done at PSI using the LE-μSR apparatus at the μE4 [71] beam line as shown in Figure 2.1. The High Intensity Proton Accelerator (HIPA) delivers a proton beam of 590 MeV energy at a current up to 2.2 mA (1.3 MW). The proton beam is pre-accelerated in a Cockcroft-Walton electrostatic column to an energy of 870 keV and this is increased to 72 MeV in the 4-sector Injector 2 cyclotron. Final acceleration of the main beam to 590 MeV occurs in the large 8-sector Ring Cyclotron, followed by transportation of the beam to the 4-cm long graphite production target E. Pions are produced from the nuclear interaction of the proton with the graphite. The μE4 beam line which starts with two normal conducting solenoids is optimized to collect muons coming from the decay of the pions stopped close to the surface of the target ("surface muons"). The muon beam is then transported to the LE-μ^+ apparatus using optical elements such as bending magnets and quadrupoles.

2.2 The low energy muon spin rotation apparatus

The PSI low-energy muon beam line with μSR spectrometer (LE-μ^+) [73] is an instrument dedicated for muon spin spectroscopy in thin films and multi-layers to study
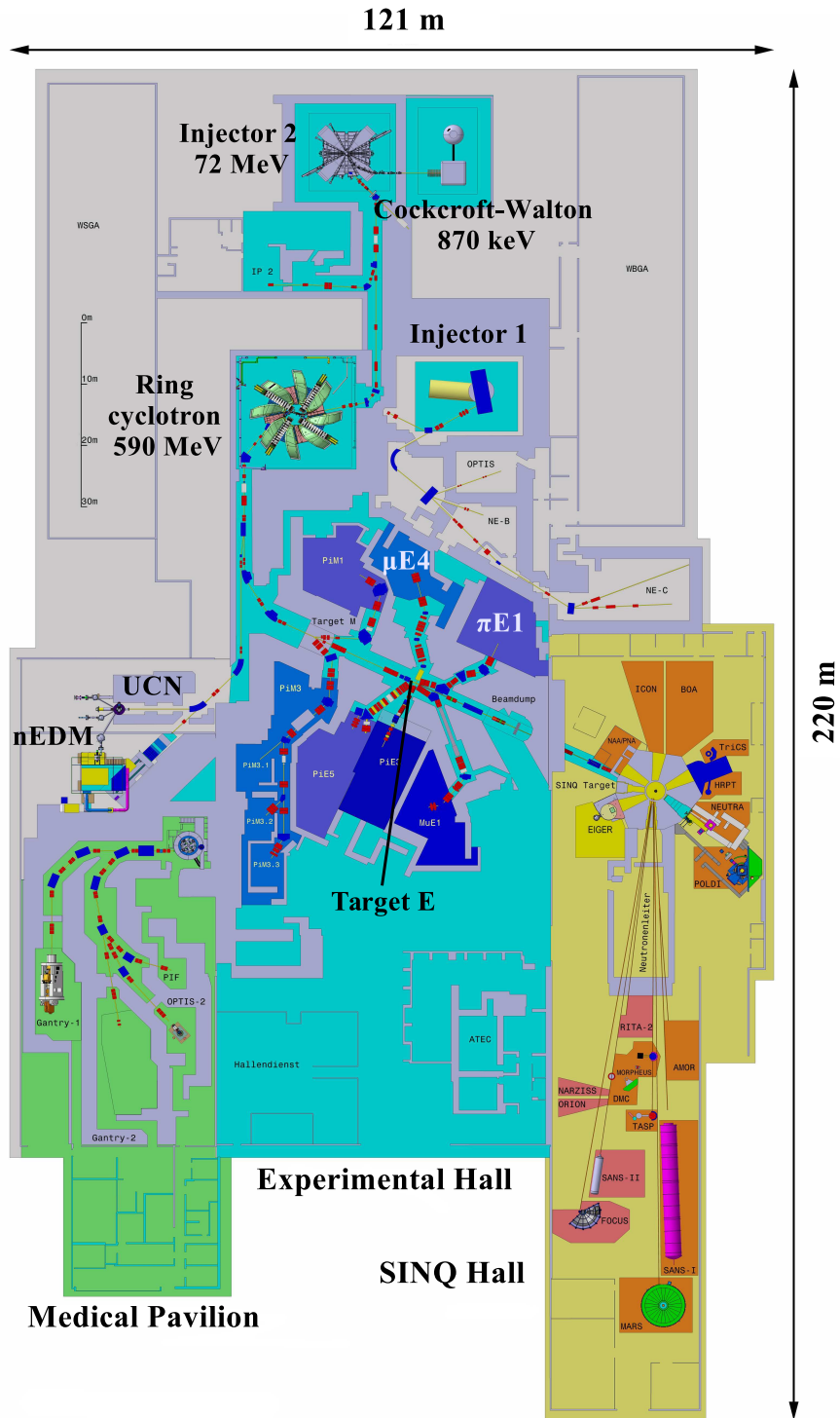
Figure 2.1: *The PSI experimental hall and High Intensity Proton Accelerator (HIPA). Adapted from [72]. See text for descriptions.*

magnetism, superconductivity [74], the behavior of hydrogen-like muonium impurities in semiconductors (see for example, [75]), organic materials (see for example [76]) and many more. The high intensity ($> 10^8$ μ^+/s) beam of 4.1 MeV surface muons from the μE4 channel at PSI [71], as shown in Figure 2.2, is focused onto a moderator consisting of a patterned 125 μm thick Ag substrate at 10 K followed by a 200-300 nm thick solid Ar film with a 10 nm solid N_2 capping layer. The moderator (detailed later) is set to HV. The N_2 capping layer improves high voltage stability [77].

A small fraction (10^{-5} - 10^{-4}) of incoming μ^+ escapes from the solid moderator with a mean energy of 15 eV and a width of similar order [79, 80]. The moderation efficiency η depends on the gas deposited and its thickness [81]. These moderated μ^+ are then transported to the sample region that has low background contamination. The majority of the μ^+ will either go through the moderator with higher energies (several 100 keV) or be stopped by the moderator [82]. Since the moderation process is very fast compared to the depolarization mechanisms, μ^+ retain almost all their polarization [83].

The Ag substrate is set to a positive voltage V_{mod} which can be varied from 2.5 kV to 20 kV. Thus the μ^+ of eV kinetic energy leaving the moderator have an electrostatic potential energy of $E_{mod} = e \cdot V_{mod}$. These μ^+ are thus accelerated while leaving the moderator, focused by a LN_2 cooled einzel lens (L1) and deflected by 90° in an electrostatic mirror as shown in Figure 2.2. The potential applied to the mirror is equal to that of the V_{mod} to separate the low energy μ^+ (LE-μ^+) from the "high energy" μ^+ crossing the moderator. Since the deflection is purely electrostatic, only the momentum of the LE-μ^+ is changed while the spin direction remains unaltered. After the deflection, the spin of the LE-μ^+ and its momentum are perpendicular to each other. To be more precise, the initial muon spin is not exactly perpendicular to its momentum due to the separator (the muon spin is rotated 10° clockwise) as is shown in Figure 2.2, before the moderator in the μE4 beam line.

After traversing the mirror, the LE-μ^+ is focused by another einzel lens (L2) onto the trigger detector (TD), which gives the start signal for the LE-μSR measurements. This TD was developed to register the LE-μ^+ in order to perform the time differential LE-μ^+SR measurements [84]. It consists of a very thin carbon foil (thickness of 2.2 μg/cm^2) combined with a micro channel plate (MCP) located perpendicularly to the foil. It is based on the detection of electrons which are ejected by the LE-μ^+ traversing the foil. These electrons are directed by a small grid system to the MCP3 where they are detected (see Figure 2.3). In the carbon foil, the LE-μ^+ loses an energy of $E_{loss} \cong 0.8$ keV with an energy straggling (RMS) of $\Delta E_{loss} \cong 500$ eV.

Finally the LE-μ^+ is transported to the sample chamber by an einzel lens (L3) and a conically shaped electrostatic lens (RA). A position sensitive MCP2 can be mounted at the sample position to optimize the transport system settings, as shown in Figure 2.2.
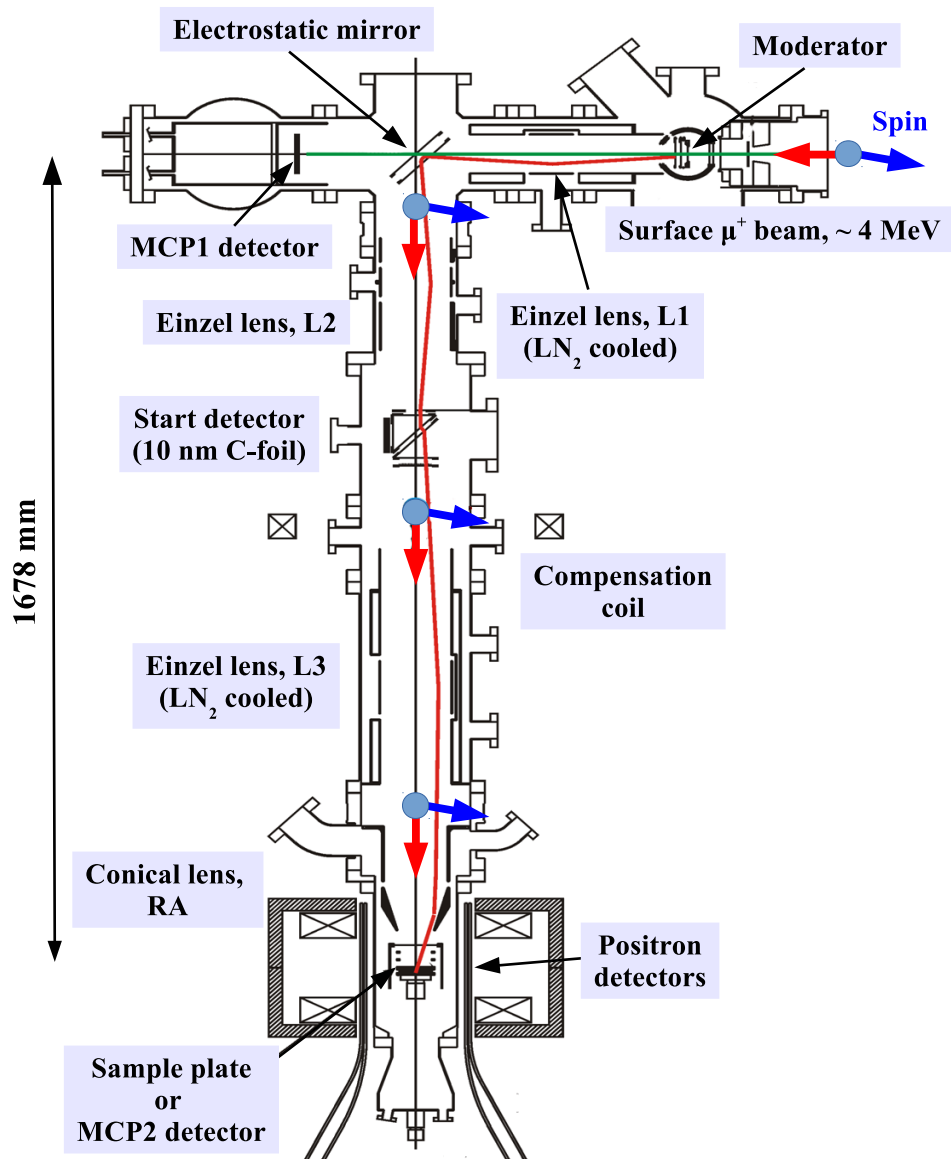
Figure 2.2: *An overview of the LE-μ^+ apparatus at PSI. Surface muons coming from the $\mu E4$ beam line are moderated down to 15 eV and re-accelerated towards the 45° electrostatic mirror. The momentum of the LE-μ^+ are flipped from anti-parallel to the spin to perpendicular in this step and the LE-μ^+ are guided towards the sample by electrostatic lenses. A start detector marks the starting signal for the μSR measurement. Shortly before they reach the sample plate, their kinetic energy are adjusted by applying high voltage on the sample plate. The positron generated in the decay process of the LE-μ^+ hits one of the detectors around the sample and ends the event [78].*
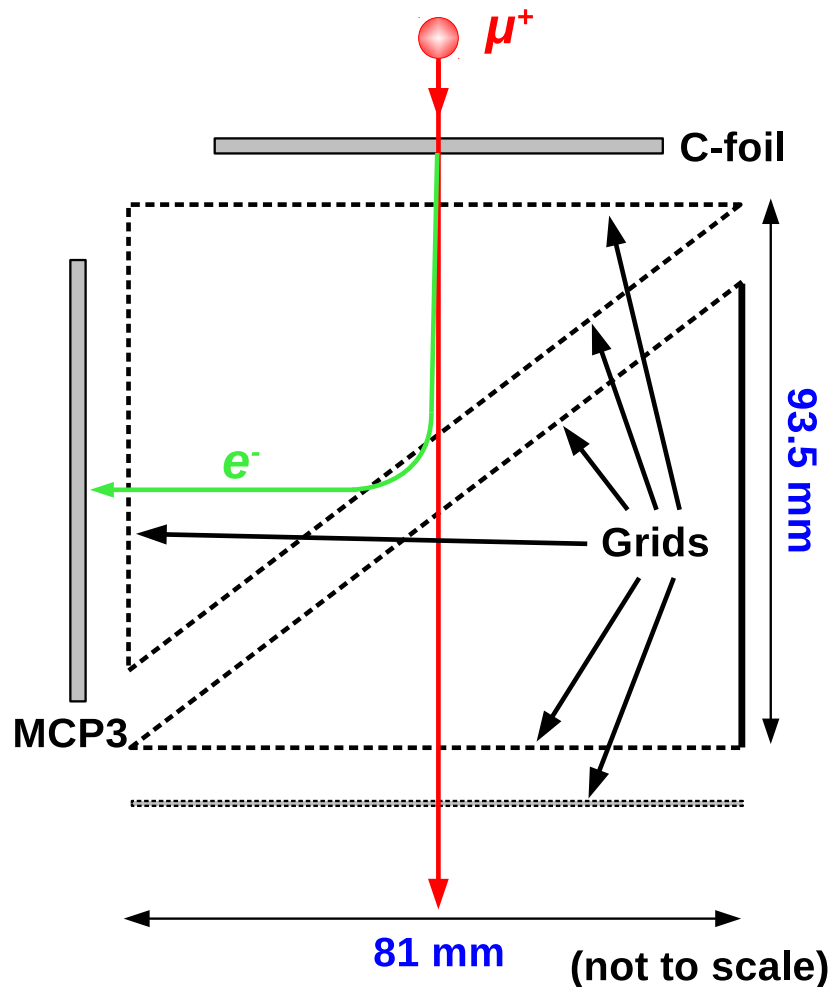
Figure 2.3: *A schematic of the start detector for LE-μ^+. Secondary electrons are emitted after LE-μ^+ traversing the thin carbon foil. These electrons are directed by a small grid system to the MCP3 where they are detected. Adapted from [84].*

The optimized HV settings of the various beam line elements (leading to a high beam transmission and a minimal beam size at the sample position) are summarized in Table 2.1 for two different moderator energies E_{mod}.

Table 2.1: *Optimized LE-μ^+ beam line high voltage settings during the beam time 2011 for the moderator voltages $V_{mod} = 12, 15$ kV [43].*

Element	High voltage settings (kV)	
	12 kV	15 kV
Moderator	12	15
L1	7.2	8.5
Mirror	12	15
L2	11.2	14
L3	6.67	9
RA	8.1	10.75

Figure 2.4 shows the schematic diagram of the LE-μSR sample chamber and its spectrometer [78]. The sample plate is surrounded by a radiation shield to reach cryogenic temperatures down to 2.5 K. In the transverse field μSR configuration, a magnetic field (WEW magnet) of up to 3400 G can be applied along the beam direction. A typical value of the magnetic field is 100 G for a LE-μSR measurement and it is 6 G for a LE-Muonium Spin Rotation (MuSR) measurement.

The sample is electrically-insulated mounted on the cryostat in order to apply an acceleration or deceleration high voltage V_{sample}. The final kinetic energy of the LE-μ^+ implanted into the sample E_{in} is given by

$$E_{\mathrm{in}} = E_{\mathrm{mod}} - E_{\mathrm{loss}} - e \cdot V_{\mathrm{sample}} \ , \qquad (2.1)$$

where E_{mod} is the electrostatic potential energy of the μ^+ leaving the moderator, E_{loss} the energy loss of LE-μ^+ in the carbon foil and V_{sample} the HV applied on the sample plate. It is possible to tune the E_{in} of the LE-μ^+ from 0.5 keV to 31 keV by adjusting V_{sample} (± 12 kV). The implantation depth can be chosen by varying the kinetic energy of the μ^+, between 0-500 nm. This technique is now called LE-μSR [78]. Examples of implantation depth versus implantation energy are given in Figure 2.5 and Figure 2.6.

The μ^+ stopping distribution in the mesoporous SiO_2 thin film at the different implantation energies was calculated using TrimSP [85, 86] and plotted in Figure 2.5. From the stopping distribution, the mean implantation depth is calculated and plotted in Figure 2.6. The mean implantation depth is about 80 nm for an implantation energy of 5 keV. This is in contrast to the implantation depth of a surface muon beam where
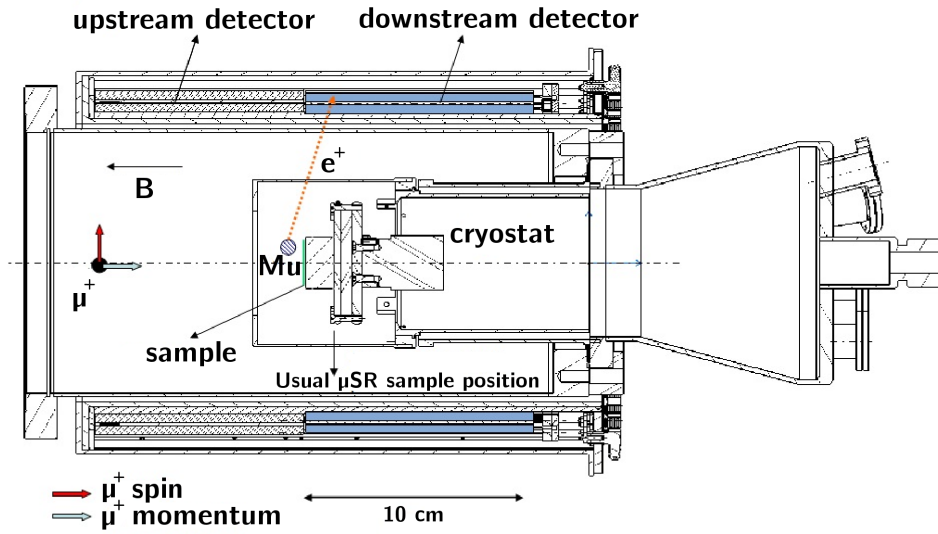
Figure 2.4: *Schematic of the LE-μSR sample chamber. The sample is glued on a silver coated copper mount contacted to a cryostat. The sample is surrounded by a thermal shield. Scintillators for the positron detection are grouped in upstream and downstream counters. Each of them is additionally segmented into top, bottom, left and right.*

the stopping depths in solids are of the order of several 100 μm. Due to the scattering processes involved in thermalization, the straggling range is about 50-100 μm.

For PST measurements that will be described in Chapter 4, an additional Ag-coated copper plate (nose sample plate) is mounted upstream of the usual sample plate holder to increase the contrast in the detection efficiency. The positrons from μ^+ decays are detected by 64 BC-400 scintillator (5 mm thick, 120 mm in length) segments surrounding the vacuum tube in a cylinder-like shape. They are grouped in upstream and downstream counters, and each of them is additionally segmented into top, bottom, left and right. Readout of the scintillators is achieved by Avalanche Photo Diodes (APD). This detector provides the stop signal of an μSR event. The time difference between the start detector and the APD is then registered as an event by TDC.

2.3   Facilities for low energy muon spin rotation

Due to their relatively high momentum, surface muons are usually implanted deep into the sample (0.1-1.0 mm). Such muons can be used to the study of properties of bulk materials. Recent developments of low-energy μ^+ beams with tunable kinetic energies
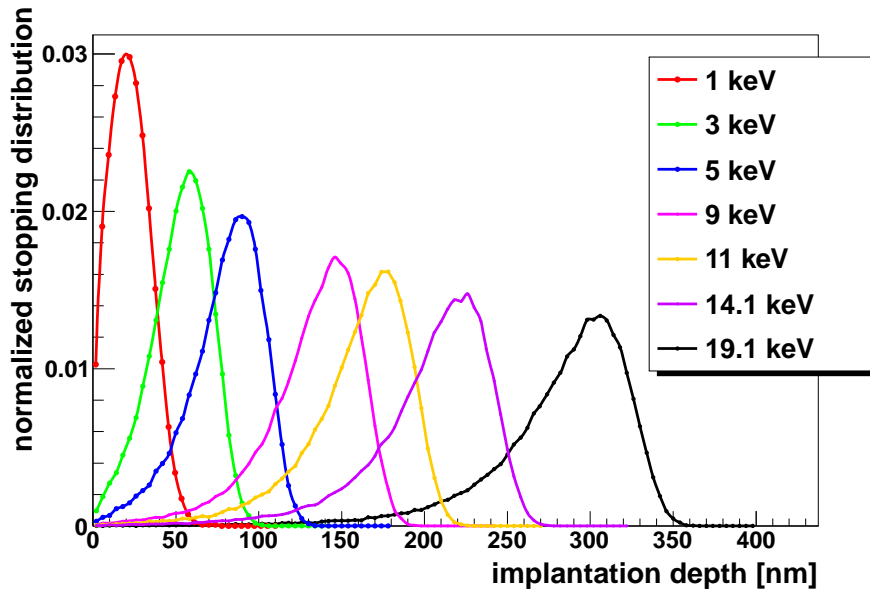
Figure 2.5: *Normalized muon stopping distribution in the mesoporous SiO_2 thin film (F-sample, $\rho = 1.1$ g/cm^3) at various implantation energies, calculated using TrimSP [85, 86].*
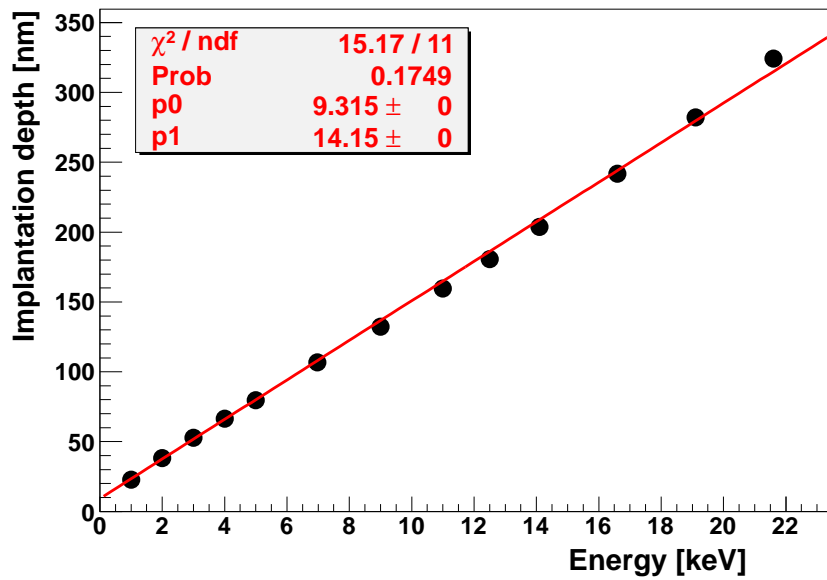
Figure 2.6: *Mean implantation depth versus implantation energy in mesoporous SiO_2 thin film (F-sample, $\rho = 1.1$ g/cm^3).*

between 0.5-30 keV allow the use of the μSR technique with thin films. The implantation depth can be chosen by varying the kinetic energy of the μ^+, between 0-500 nm. This technique is now called LE-μSR [78]. Several methods were proposed to generate low

Table 2.2: *Parameters of the currently available LEM beam line.*

	PSI (continuous)	RIKEN-RAL (pulsed)
Surface muon beam intensity	$4.2{\times}10^8$ μ^+/s	$1.2{\times}10^6$ μ^+/s
Repetition rate	continuous	25 Hz
Time resolution	5 ns	7 ns
Energy resolution	500 eV	14 eV
Spin polarization	99%	50%
Beam spot	10 mm	4 mm
LEM intensity	5000 μ^+/s	15 μ^+/s
Moderation efficiency	$10^{-5} - 10^{-4}$	3×10^{-5}

energy muon beams but currently only two of them are realized as summarized in Table 2.2.

- Continuous LEM beam at PSI [74]: Surface μ^+ are moderated by a thin layer (a few 100 nm) of a van der Waals bound rare gas solid or solid nitrogen deposited on the downstream side of a 125 μm Ag substrate.

- Pulsed (25 Hz) LEM beam at RIKEN-RAL muon facility at ISIS (UK): Surface μ^+ are moderated and stopped in a 2500 K hot tungsten foil. Mu atoms are re-emitted from the hot surface into vacuum. Laser ionization of the emitted Mu produces μ^+ with thermal energy [87].

However, only the PSI LEM beam line has a reasonable rate (5000 μ^+/s) to perform routine experiments. All data presented in this thesis were taken between 2011 and 2014 with this apparatus installed at the secondary μE4 beam line at PSI [71]. The situation would change with the installation of the pulsed LEM beam line at J-PARC [88] in the coming years based on the same principle as the one of the RIKEN-Rutherford Appleton Laboratory (RIKEN-RAL) muon facility.

Recently, another effort to produce an ultra slow muon beam line at PSI was proposed [63]. The proposal is based on a position-dependent muon drift velocity in a helium gas cell with gas density gradient, electric and magnetic fields. The final average kinetic energy of the muon beam will be 1 eV with beam size below 1×1 mm^2. Research and development are on-going at PSI (see Chapter 7).

2.4 Mesoporous silica thin film for the muonium production

2.4.1 Definition of mesoporous materials

Porous materials are classified according to their pore sizes into microporous (<2 nm), mesoporous (2-50 nm) and macroporous (>50 nm) [89]. Mesoporous materials were first discovered by the Kuroda group [90] and Mobil Company [91] in the early 1990s. These materials has since then attracted the attention of many researchers as their pore size is beyond the limit of the conventional zeolites and thus can be used in a broader field, for example, as a catalyst where large molecules are involved.

Mesoporous silica thin films used in this thesis were synthesized via a sol-gel method as sketched in Figure 2.7. The sol-gel process uses a pure aqueous evaporation-induced self-assembly (AEISA) method [92]. In this method, the inorganic species (e.g. tetraethyl orthosilicate, TEOS) is first hydrolyzed and condensed into an oligomeric silica gel, followed by a sol-gel transition due to further condensation, accompanied by the self-assembly of surfactants and inorganic species to form mesostructures. Acid or base is used as the catalyst for the hydrolysis and condensation of silica precursors, and therefore commonly the reaction is conducted in either acidic or basic conditions.

The formation of mesoporous materials has been considered to be highly dependent on the interaction between organic (surfactant) and inorganic (silica oligomers) species. Different synthesis strategies are needed for different types of surfactants so that they can maintain these interactions.

Surfactants are classified into the following types according to their charging properties: (a) anionic (S^-), with negatively charged head groups, for example alkyl carboxylate, (b) cationic (S^+), with positively charged head groups, for example hexadecyltrumethylammonium chloride (CTACl), and (c) non-ionic (S^0), with neutral head groups, for example pluronic F-127 triblock copolymer ($EO_{106}PO_{70}EO_{106}$).

2.4.2 Sample preparation

TEOS was used as the silica source, cationic surfactants like Cetyl trimethyl ammonium chloride (CTACl) and hexadecyltrumethylammonium bromide (CTAB) and non-ionic pluronic F-127 triblock copolymer ($EO_{106}PO_{70}EO_{106}$) were used as structuring agents, respectively as shown in Figure 2.8. The thin films were prepared on polished silicon wafers (semiconductor quality silicon by SILTRONIX, P-Bore type) by spin-coating at 3000 rpm using precursor sols of TEOS, surfactant, anhydrous ethanol (EtOH), distilled water and hydrochloric acid (HCl) or nitrite acid (HNO_3). The sol-gel was constantly

structuring agent

CH$_3$

N$^+$

CH$_3$ CH$_3$

Cl$^-$

(CTACl)

CH$_3$

O CH$_2$CH$_3$

CH$_3$CH$_2$ O – Si – O CH$_2$CH$_3$

(TEOS)

O CH$_2$CH$_3$

inorganic precursor

Mesoporous silica

solvent
evaporation

solvent
evaporation

Calcination
450° C

initial solution

wet gel

structured gel
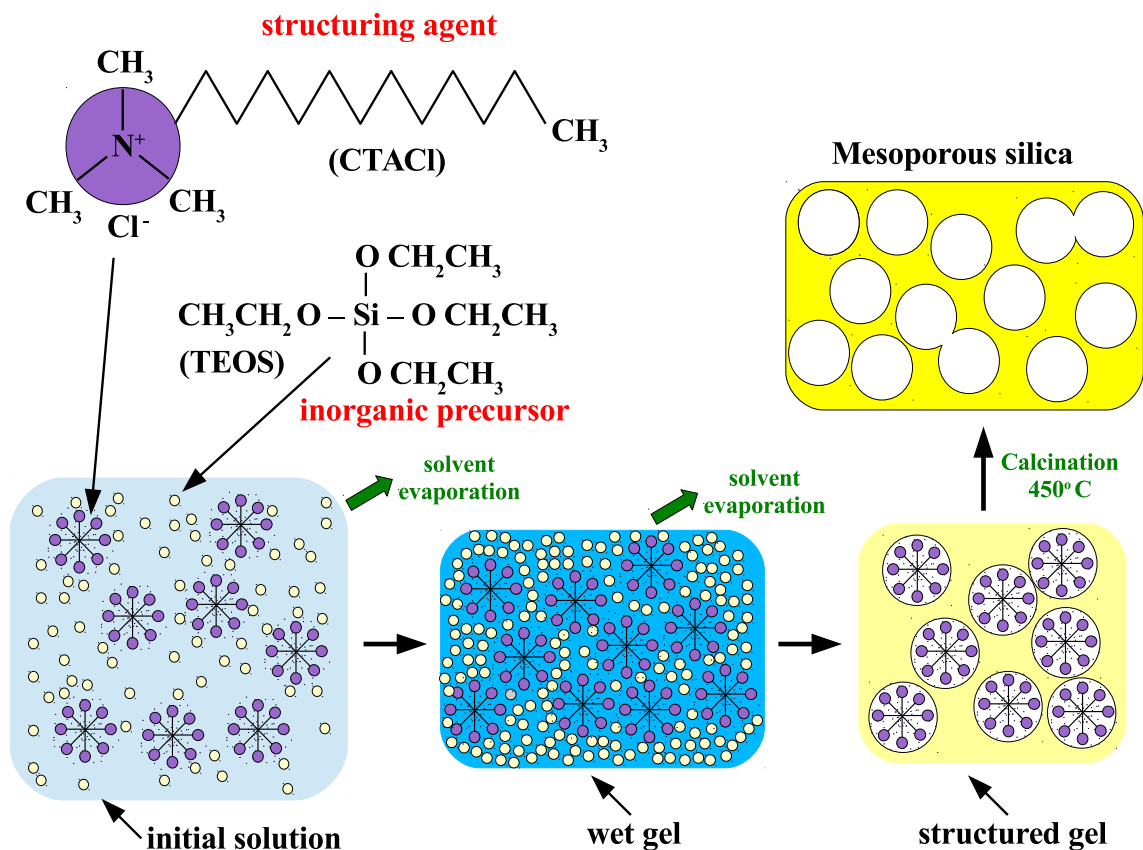
Figure 2.7: *The process of mesoporous silica formation. The initial solution contains cetyltrimethylammonium chloride (CTACl) as structuring agent, tetraethoxysilane (TEOS) as silica precursor. The inorganic condensation is achieved via the sol-gel process. In the first step, the structuring agents form liquid micelles crystalline in the solution. With the evaporation process, a silica network will form around the micelles. Structuring agent can be removed by calcinating the gel up to 450° and this will yield a mesoporous silica material. It is denoted by **C-sample** throughout this thesis. Likewise, mesoporous silica made from F-127 structuring agent is denoted by **F-sample**.*
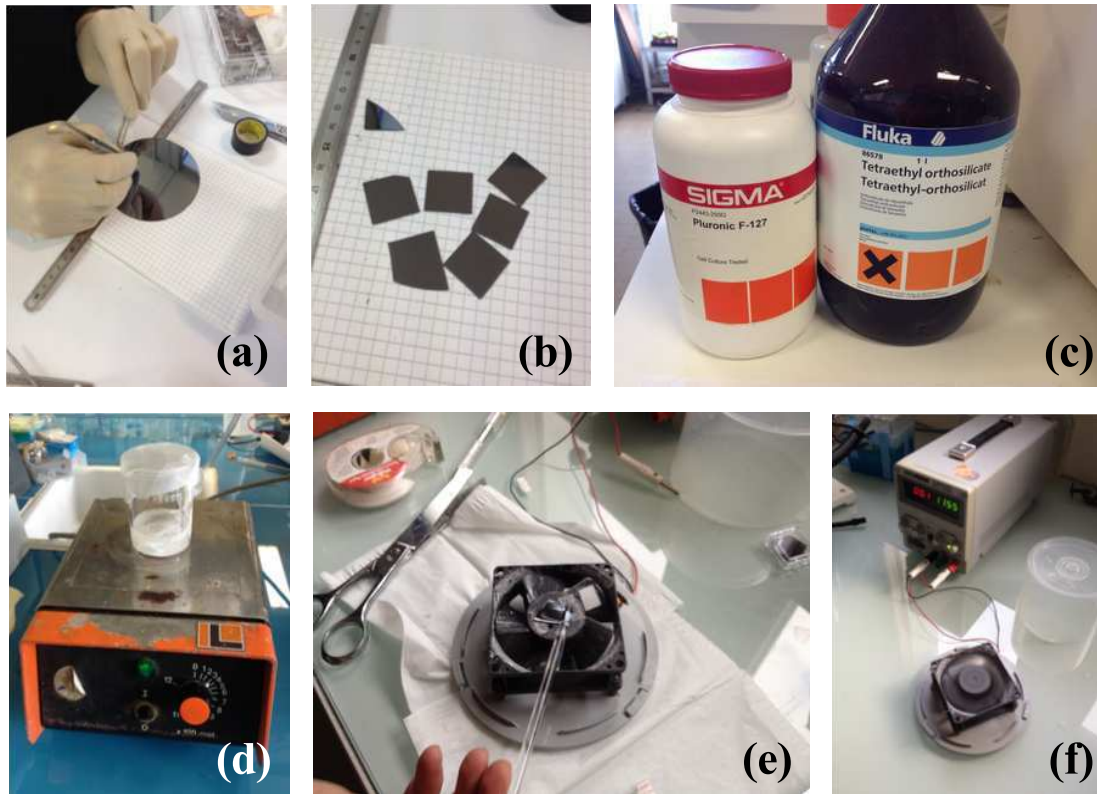
Figure 2.8: *An overview of the mesoporous silica thin film preparation done at CEA Saclay. (a) A 500 µm thick semiconductor quality silicon wafer (SIL-TRONIX) is used as the deposition substrate for the mesoporous silica thin film. (b) The silicon wafer is cut into square pieces of 20×20 mm^2. (c) Non-ionic pluronic F-127 triblock copolymer ($EO_{106}PO_{70}EO_{106}$ and Tetraethoxysilane (TEOS) used in the sample preparation. (d) Precursor sols of TEOS, surfactant, anhydrous ethanol (EtOH), distilled water and nitric acid (HNO$_3$) are stirred at 300 rpm for 3-6 hours. (e) The sol-gel is deposited on a 20×20 mm^2 silicon substrate. (f) The spin-coating device used in the preparation. The angular frequency, which is measured by a tachometer, is tuned to 3000 rpm by varying the applied voltage.*

stirred at 200 rpm for several hours. The density of the C-sample (F-sample) is approximately 1.2(1.1) g/cm^3 and the thickness is about 1 μm. There was a thin layer of non-porous SiO_2 (several nm) on the silicon wafer. The thin films were calcined at 250° in air soon after the spin-coating process for several hours in order to remove the organic species.

Various samples were preselected with the ETHZ slow positron beam [64] and were heated at 450° for 15 mins in air immediately before it is glued with a conductive silver (G302 from Plano GMBH) to the sample plate (see Figure 2.9). The procedure mentioned above is the same as in [64] and is summarized in Appendix D.
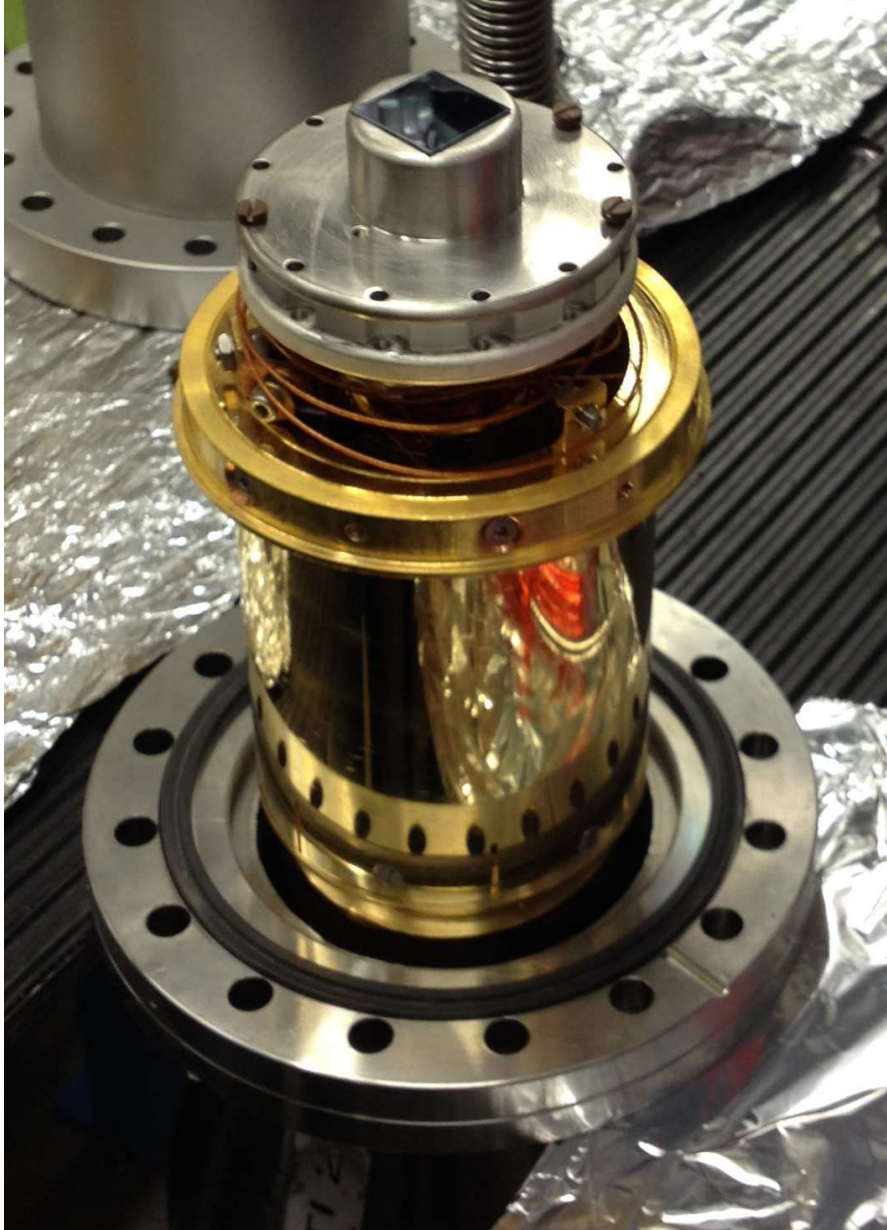
Figure 2.9: *Porous silica which is sitting on top of a 0.5 mm thick* $20 \times 20\ mm^2$ *silicon plate is glued to the nose sample plate with a conductive silver glue (G302 from Plano GMBH) which is attached to the cold finger of the LE-μSR apparatus.*

Chapter 3

Optimization of muon to muonium conversion: muonium formation probability

In this chapter, the measurement of the Mu formation probability in mesoporous silica materials is reported. The Mu formation probability, defined as the fraction of Mu produced per μ^+ implanted into the sample, can be measured by the μSR technique. This technique, as explained in this chapter, provides information on the Mu formation probability but not on the fraction of Mu that is emitted into vacuum. The Mu yield in vacuum is studied with another technique that will be explained in Chapter 4.

3.1 Principle of the time-differential muon spin rotation technique

The acronym μSR stands for muon spin rotation, or relaxation, or resonance, depending respectively on whether the μ^+ spin motion is predominantly a rotation (more precisely a precession around a magnetic field), or a relaxation of the μ^+ ensemble polarization, or a more complex dynamics induced by additional radio frequency pulses to induce spin-flips. It is a powerful tool capable of providing valuable information regarding various chemical and solid-state physics phenomena especially for superconductivity and magnetism investigation. Studying materials using μSR technique requires implantation of polarized μ^+ of several keV to MeV initial kinetic energy into the sample. The time evolution of the μ^+ spin is then monitored on the time scale of the μ^+ lifetime by means of the correlation between μ^+ spin and positron emission as explained in Section 1.1. A detailed description of the μSR technique can be found in [33, 93].
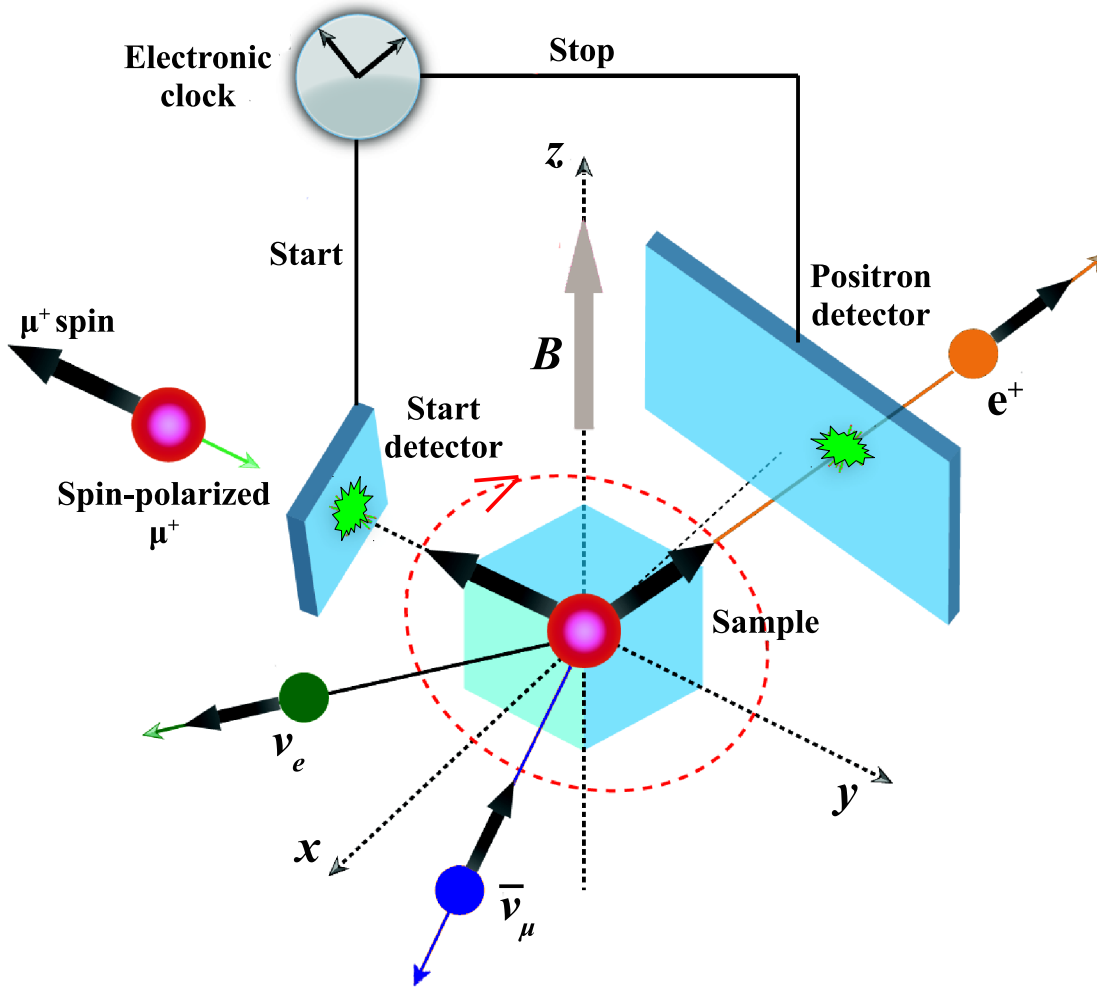
Figure 3.1: *A schematic view of a time-differential μSR technique. After registering a signal in the start detector, the spin-polarized μ⁺ is implanted into the sample and undergoes Larmor precession due to the magnetic field $\vec{B}$. The positron is emitted preferentially along the direction of the μ⁺ spin at the time of the μ⁺ decay. Hence the time evolution of the μ⁺ spin can be monitored with a positron detector. Adapted from [94].*
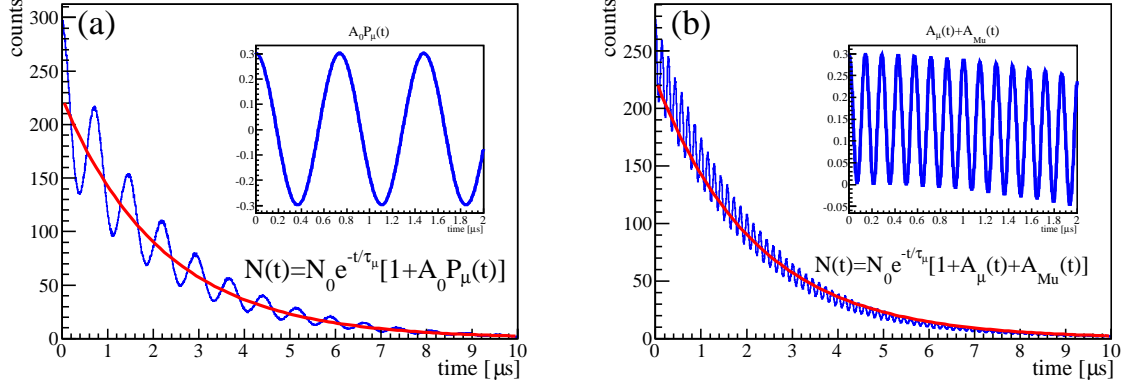
Figure 3.2: *Typical µSR time histograms. Each histogram consists of an exponential decaying function which describes the μ^+ decay modulated at a frequency given by the (a) μ^+ spin precession in a 100 G magnetic field and (b) μ^+ and Mu spin precessions in a 5 G magnetic field. The red lines are the exponential parts of the fits.*

Most of the µSR experiments are time-differential measurements, as their purpose is to monitor the μ^+ polarization as a function of time. A schematic view of a typical experimental setup is shown in Figure 3.1. A beam of μ^+ with nearly 100% spin polarization first passes through a μ^+ entrance detector, which is commonly referred to as the **start detector**, starting the clock for the time differential measurement. In the material, where the μ^+ stops, there is a magnetic field (external and internal) which causes the μ^+ spin to precess. With a lifetime of 2.2 µs, the μ^+ decays by emitting a positron preferentially in the direction of the μ^+ spin. The clock is stopped when the positron detector, usually a plastic scintillator partially surrounding the sample, has detected the decay positron. All the time entries are then recorded in a histogram resulting in a time distribution of the form

$$N(t) = N_0 e^{-t/\tau_\mu}[1 + A_0 P_\mu(t)] \;, \tag{3.1}$$

where t is the time difference between the start and the stop signals, and A_0 the μ^+ decay asymmetry mentioned in Section 1.1 which depends on the initial polarization of the μ^+ beam, the solid angle of the positron detector and the energy of the positron detected. $P_\mu(t)$ is the projection of the spin polarization of the μ^+ ensemble in the direction of the positron detector $\boldsymbol{n}$, normalized to the initial spin polarization:

$$P_\mu(t) = \boldsymbol{P}_\mu(t) \cdot \boldsymbol{n}/P_\mu(0) \;. \tag{3.2}$$

An example of the time histogram for a µSR measurement is shown in Figure 3.2(a).

29

3.2   Transverse-field muon spin rotation

Once the μ^+ is thermalized in the sample, the μ^+ spin interacts magnetically with its surroundings. The μ^+ polarization $\boldsymbol{P}_\mu(t)$ is precessing with time if it is subjected to a local magnetic field $\boldsymbol{B}$. The local field is consisting of an internal field $\boldsymbol{B}_{int}$ and in case of the transverse field μSR, an external field $\boldsymbol{B}_{ext}$ applied perpendicular to the initial spin polarization:

$$\boldsymbol{B} = \boldsymbol{B}_{int} + \boldsymbol{B}_{ext} . \tag{3.3}$$

The internal fields can be originating from the surrounding atoms and nuclei and from the interaction with the electrons of the sample. The time evolution of the μ^+ spin polarization is given by the classical Bloch equation

$$d\boldsymbol{P}_\mu(t)/dt = \gamma_\mu \boldsymbol{P}_\mu(t) \times \boldsymbol{B} , \tag{3.4}$$

which describes the Larmor precession of $\boldsymbol{P}_\mu$ around $\boldsymbol{B}$. If $\boldsymbol{B}_{ext}$ is the dominating field ($\boldsymbol{B}_{ext} \gg \boldsymbol{B}_{int}$), $\boldsymbol{B}_{ext}$ and the local field $\boldsymbol{B}$ lie approximately in the same direction. In this scenario, the time-dependent decay asymmetry can be written simply as:

$$A_\mu(t) = A_0 P_\mu(t) = A_\mu \cos(\omega_\mu t + \phi_\mu) , \tag{3.5}$$

where ϕ_μ is the angle between $\boldsymbol{P}_\mu(0)$ and the direction of the positron detector, and $A_\mu = A_0 P_\mu(0)$ the decay asymmetry at $t = 0$. The precession frequency $\omega_\mu = \gamma_\mu B$ is correlated the local magnetic field experienced by the μ^+. Moreover, a damping term is introduced to account for inhomogeneities of the magnetic field and depolarization effects:

$$A_\mu(t) = A_\mu e^{-\lambda_\mu t} \cos(\omega_\mu t + \phi_\mu) . \tag{3.6}$$

A similar description can also be applied to the Mu atom. The implanted μ^+ may capture an e^- from the surrounding and form Mu. Because of the hyperfine interaction with the bound electron, the magnetic interaction of the μ^+ in the Mu atom is enhanced by about a factor of 100, more precisely $\gamma_{Mu} = 102.88 \gamma_\mu$ (see Appendix A for more details). The corresponding time-dependent decay asymmetry can thus be written as

$$A_{Mu}(t) = A_{Mu} e^{-\lambda_{Mu} t} \cos(\omega_{Mu} t + \phi_{Mu}) , \tag{3.7}$$

where A_{Mu} is the Mu decay asymmetry, λ_{Mu} the Mu spin depolarization rate, $\omega_{Mu} = \gamma_{Mu} B$ the Mu precession frequency, and ϕ_{Mu} the angle between $\boldsymbol{P}_{Mu}(0)$ and the direction of the positron detector.

When a μ^+ is implanted into a sample, a fraction of it remain in the diamagnetic state as a μ^+ and another fraction is forming Mu. Therefore combining Equation 3.1, Equation 3.6 and Equation 3.7, the time-dependent positron count can be written as:

$$N(t) = N_0 e^{-t/\tau_\mu} [1 + A_\mu(t) + A_{Mu}(t)] + N_{bg} . \tag{3.8}$$

This is the most commonly used fit function for a μSR measurement involving both μ^+ and Mu precessions. Possible uncorrelated background is accounted for by the fit parameter N_{bg}. The decay asymmetries A_μ and A_{Mu} are proportional to the fraction of μ^+ which remain as a free μ^+ and form Mu, respectively. Figure 3.2(b) is showing a time histogram where the fractions of μ^+ and Mu are equal ($A_\mu = 0.15$ and $A_{\mathrm{Mu}} = 0.15$). This is clearly visible from Figure 3.2(b) a fast oscillating $A_{\mathrm{Mu}}(t)$ term and slowly oscillating $A_\mu(t)$ term.

3.3 Muon spin rotation measurements

Muon spin rotation (μSR) measurements were done with mesoporous silica F- and C-samples and a fused quartz sample during the beam time in 2011. The mesoporous silica samples were pre-selected with the ETHZ slow positron beam [95] and the fused quartz was used as a reference measurement to compare the Mu formation probability. Data from μSR measurements were stored in the ROOT [96] file format and were analyzed using ROOT-based musrfit [97] framework developed at PSI for μSR data analysis. Most of the data was taken for 8 million events. Datasets used for the data analysis are summarized in Appendix E.

As the positron detection system (both upstream and downstream) of the LE-μSR spectrometer is segmented into left (L), bottom (B), right (R) and top (T) (see Figure 3.3), the time-dependent decay asymmetry $A(t)$ of each individual detector can be written as:

$$A_L(t) = A_\mu e^{-\lambda_\mu t}\cos(\omega_\mu t + \phi_\mu) + A_{\mathrm{Mu}} e^{-\lambda_{\mathrm{Mu}} t}\cos(\omega_{\mathrm{Mu}} t + \phi_{\mathrm{Mu}}) \tag{3.9}$$

$$A_B(t) = A_\mu e^{-\lambda_\mu t}\cos(\omega_\mu t + \phi_\mu + \frac{\pi}{2}) + A_{\mathrm{Mu}} e^{-\lambda_{\mathrm{Mu}} t}\cos(\omega_{\mathrm{Mu}} t + \phi_{\mathrm{Mu}} - \frac{\pi}{2}) \tag{3.10}$$

$$A_R(t) = A_\mu e^{-\lambda_\mu t}\cos(\omega_\mu t + \phi_\mu + \pi) + A_{\mathrm{Mu}} e^{-\lambda_{\mathrm{Mu}} t}\cos(\omega_{\mathrm{Mu}} t - \phi_{\mathrm{Mu}} + \pi) \tag{3.11}$$

$$A_T(t) = A_\mu e^{-\lambda_\mu t}\cos(\omega_\mu t + \phi_\mu + \frac{3\pi}{2}) + A_{\mathrm{Mu}} e^{-\lambda_{\mathrm{Mu}} t}\cos(\omega_{\mathrm{Mu}} t + \phi_{\mathrm{Mu}} - \frac{3\pi}{2}) \tag{3.12}$$

as each of them are phase shifted relative to each other due to their relative geometrical positioning. $A_{\mu,\mathrm{Mu}}$, $\lambda_{\mu,\mathrm{Mu}}$, $\omega_{\mu,\mathrm{Mu}}$ and $\phi_{\mu,\mathrm{Mu}}$ are the decay asymmetry, the spin relaxation rate, the Larmor precession frequency and the initial spin phase of the μ^+ and Mu, respectively. The opposite sign of the initial phase between μ^+ and Mu terms is due to the fact that μ^+ is precessing in the clockwise direction whereas Mu is precessing in the anti-clockwise direction as they have magnetic moments of opposite sign [98]. Equations 3.9 to 3.12 are used as fit functions for low-field measurements where the Mu precession can be resolved within the time resolution of the apparatus. For higher magnetic field (> 50 G), the Mu precession is so fast that it is not resolvable by the
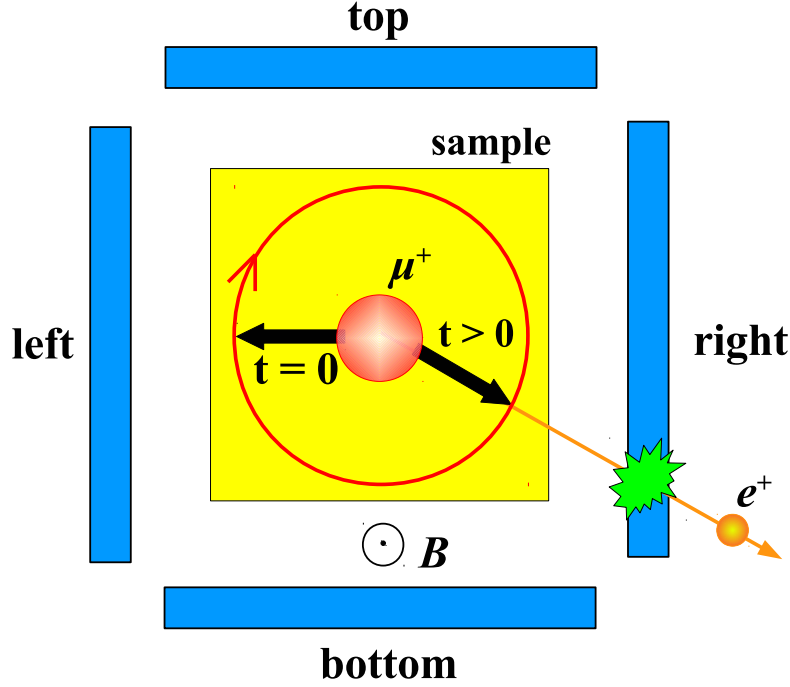
Figure 3.3: *The LE-µSR spectrometer is segmented into left (L), bottom (B), right (R) and top (T) positron detectors. At $t = 0$, the μ^+ spin is pointing towards the left detector. The μ^+ spin is precessing in the clockwise direction. The direction angle of the μ^+ spin will evolve accordingly to $\theta = \omega_\mu t$. The decay positron emitted preferentially along the μ^+ spin direction hitting a positron detector delivers the stop signal for the event.*

μSR spectrometer and the fit functions simplify to:

$$
\begin{aligned}
A_L(t) &= A_\mu e^{-\lambda_\mu t}\cos(\omega_\mu t + \phi_\mu) \,, & (3.13) \\
A_B(t) &= A_\mu e^{-\lambda_\mu t}\cos(\omega_\mu t + \phi_\mu + \frac{\pi}{2}) \,, & (3.14) \\
A_R(t) &= A_\mu e^{-\lambda_\mu t}\cos(\omega_\mu t + \phi_\mu + \pi) \,, & (3.15) \\
A_T(t) &= A_\mu e^{-\lambda_\mu t}\cos(\omega_\mu t + \phi_\mu + \frac{3\pi}{2}) \,. & (3.16)
\end{aligned}
$$

These functions are used to fit the μSR time histograms of the four detectors (L, B, R, T) simultaneously with common parameters A_μ, λ_μ, ω_μ and ϕ_μ as shown in Figure 3.5. The typical fit region of the time spectra is from $t = 0.05$ μs to $t = 8$ μs and the histogram binning is about 10 ns/bin. Typical fit results using the Graphical User Interface (GUI) of musrfit are shown in Figure 3.4 for a 6 G measurement and in Figure 3.5 for a 100 G
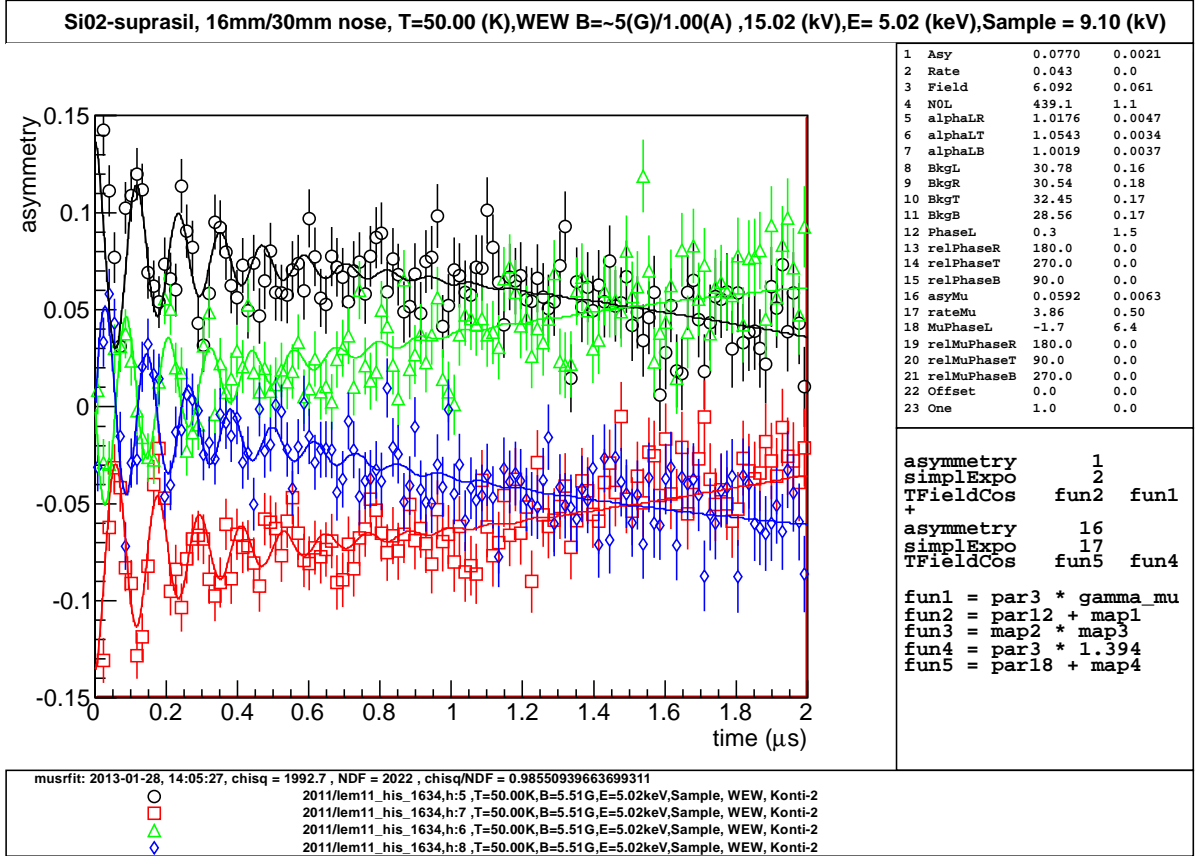
Figure 3.4: *A typical fit from musrfit toolkit using Equations 3.9 to 3.12 for a 6 G magnetic field and a fused quartz sample. Only data of upstream detectors are considered. Fast spin precession of Mu can be seen on top of the slow μ^+ spin precession.*

measurement, on a fused quartz sample. The asymmetry plots $(A_\mu(t))$ of Figure 3.4 and Figure 3.5 were extracted from the L, B, R and T segments of the upstream detectors only. A distortion of the asymmetry occurs for the downstream detector as shown in Figure 3.6 due to Mu emission into vacuum as explained in Chapter 4. This effect is however negligible for the upstream detector and hence Equations 3.9 to 3.16 can be used to fit the data of the upstream detector.

Figure 3.5: *A typical fit from musrfit toolkit using Equations 3.13 to Equation 3.16 for a 100 G magnetic field and a fused quartz sample. Only data of upstream detectors are considered. μ^+ spin precession is clearly visible.*

3.4 Fraction of muon and muonium in the samples

In this section, the method to determine the fraction of μ^+ which remain as free μ^+ or form Mu after implantation is described. These fractions are defined as

$$F_\mu = \frac{\text{number of } \mu^+ \text{ after implantation}}{\text{number of implantated } \mu^+} \tag{3.17}$$

$$F_{\text{Mu}} = \frac{\text{number of Mu after implantation}}{\text{number of implantated } \mu^+} \,. \tag{3.18}$$

For a weak magnetic field (≈ 6 G), the fraction of free μ^+ and Mu in the samples after μ^+ implantation of can be determined from the experimentally fitted values of decay asymmetries A_μ and A_{Mu}. This is because A_μ and A_{Mu} are proportional to the fraction of μ^+ and Mu at the moment of the μ^+ decay [86]. In order to calculate F_μ and F_{Mu}
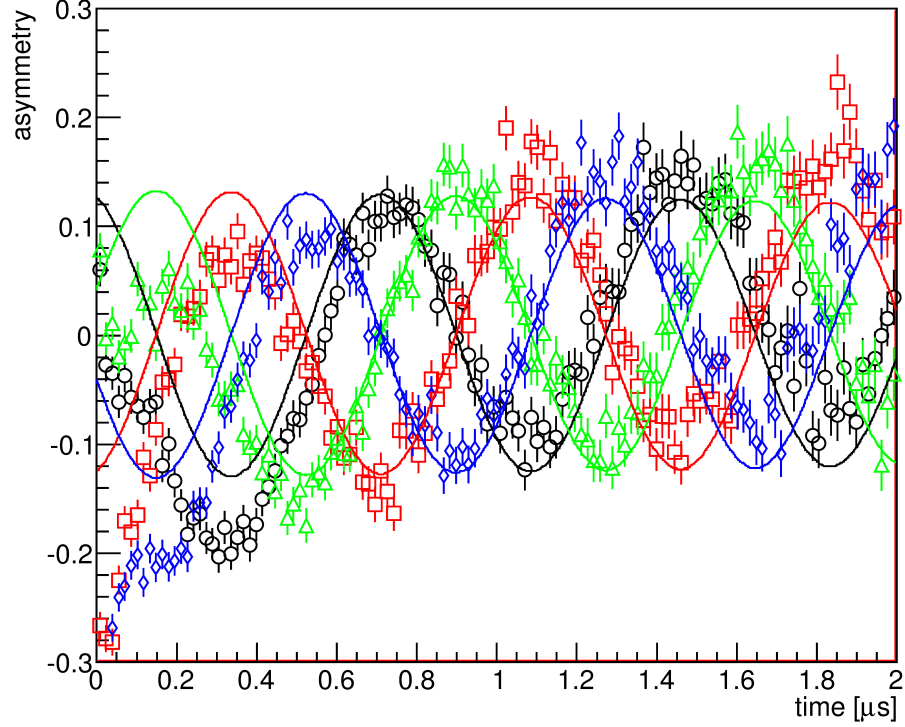
Figure 3.6: *Measured μ^+ decay asymmetry $A_\mu(t)$ of a mesoporous silica sample for the downstream detectors (L,B,R,T). $A_\mu(t)$ do not follow a simple $cos(\omega t - \phi)$ time evolution as described by Equation 3.13 to Equation 3.16 because of Mu emission into vacuum. As a comparison, fitted $A_\mu(t)$ for the upstream detectors (L,B,R,T) are shown.*

which are given by

$$F_\mu = \frac{A_\mu}{A_{\text{tot}}} \tag{3.19}$$

$$F_{\text{Mu}} = \frac{2A_{\text{Mu}}}{A_{\text{tot}}} \ , \tag{3.20}$$

the normalization factor which is called "total observable decay asymmetry" A_{tot} of the apparatus has to be known. It is important to note that this "total observable decay asymmetry" is always smaller than the theoretical value $\overline{A(E_e)} = 1/3$ that was described in Section 1.1. This is mainly due to the fact that positron detectors are not infinitely small. As a consequence, the measured decay asymmetry is an integrated value over certain angle and hence is reduced. For simplicity, the "total observable decay asymmetry" will be denoted as "total decay asymmetry" in the later part of the thesis. The factor of 2 in front of A_{Mu} is due to the fact that only 50% of the μ^+ precession in

Mu can be resolved experimentally (see Appendix A for more details).

Determination of the total decay asymmetry

A_{tot} of the apparatus can be determined by using a fused quartz sample, which is known to have negligible so called "missing fraction" of μ^+ precession signal [99]. The missing fraction is the fraction of implanted μ^+ which do not contribute to the observable asymmetries due to fast depolarization effects. Taking this into account, the total decay asymmetry A_{tot} can be written as

$$A_{\text{tot}} = A_\mu + 2A_{\text{Mu}} + A_{\text{miss}} \ , \tag{3.21}$$

where now A_{miss} accounts for fast depolarization ($t < 5$ ns). This missing fraction is mainly caused by μ^+ in Mu which lose its polarization rapidly due to the spin exchange with the electrons of the surrounding [100, 101]. The existence of a missing fraction, if not accounted for, will lead to an overestimation of F_μ and F_{Mu}. For a sample with negligibly missing fraction (quartz sample), the total observable asymmetry of the μ^+ decay is given by

$$A_{\text{tot}} = A_\mu + 2A_{\text{Mu}} \ . \tag{3.22}$$

Another complication is represented by the limited time resolution of the LE-μSR spectrometer which is about 5 ns. Due to the fast Mu precession even at low magnetic fields and the limited time resolution, the fitted value of A_{Mu} from the time spectrum is smaller than the real A_{Mu}. The real A_{Mu} can be determined by applying a correction $C_t(\nu)$ to the fitted A_{Mu}

$$A_{\text{Mu}} \rightarrow C_t(\nu)A_{\text{Mu}} \ , \tag{3.23}$$

where $C_t(\nu)$ describes the reduction of observable asymmetry due to the finite time resolution. This correction $C_t(\nu)$ depends on the precession frequency ν and thus on the applied magnetic field. $C_t(\nu)$ is evaluated from a calibration measurement using a Ag sample [102] as follows:

$$C_t(\nu) = \frac{A_\mu(\nu = 0)}{A_\mu(\nu)} \ , \tag{3.24}$$

where $A_\mu(\nu = 0)$ is the fitted μ^+ decay asymmetry at zero precession frequency (zero magnetic field) and $A_\mu(\nu)$ the fitted μ^+ decay asymmetry in a magnetic field with precession frequency ν. (A similar correction applies to the Mu precession as well but it is very challenging to perform such a calibration.) The main idea of this calibration method is that the physical A_μ generally does not depend on the precession frequency. Hence, a reduction in the fitted A_μ can be attributed to the limited time resolution of the apparatus. At $B = 6$ G where the Mu precession frequency is $\nu_{\text{Mu}} = 8.38$ MHz,

$C_t \approx 1.3$. Such a correction is not needed for A_μ at $B = 6$ G as the precession frequency $\nu_\mu = 0.081$ MHz is sufficiently small.

For fused quartz at 250 K, the A_{tot} at 5, 14 and 19 keV μ^+ implantation energies and $B = 6$ G are given by:

$$A_{\text{tot}}(E_{\text{in}}, \text{sample}) = A_\mu + 2C_t A_{\text{Mu}} \tag{3.25}$$

$$A_{\text{tot}}(5 \text{ keV}, \text{quartz}) = 0.084(2) + 2 \cdot 1.3 \cdot 0.052(2) = 0.218(6) \tag{3.26}$$

$$A_{\text{tot}}(14 \text{ keV}, \text{quartz}) = 0.052(2) + 2 \cdot 1.3 \cdot 0.069(2) = 0.230(6) \tag{3.27}$$

$$A_{\text{tot}}(19 \text{ keV}, \text{quartz}) = 0.041(2) + 2 \cdot 1.3 \cdot 0.075(2) = 0.235(7) \ . \tag{3.28}$$

The smaller value of $A_{\text{tot}}(5 \text{ keV})$ compared to the others is due to the backscattering effects at low implantation energies. The backscattered μ^+ has a high probability to capture an electron and form Mu [87] which moves rapidly from the sample plate towards the surrounding materials. Due to the magnetic field inhomogeneity which increases when moving away from the sample plate, the Mu precession suffers a strong dephasing effect and hence a fraction of the μ^+ polarization is lost. Since A_{tot} does not depend on temperature as visible in Figure 3.7(a), average values for each implantation energy are used in analysis:

$$A_{\text{tot}}(5 \text{ keV}, \text{quartz}) = 0.233(5) \tag{3.29}$$

$$A_{\text{tot}}(14 \text{ keV}, \text{quartz}) = 0.238(4) \tag{3.30}$$

$$A_{\text{tot}}(19 \text{ keV}, \text{quartz}) = 0.240(4) \ . \tag{3.31}$$

For the mesoporous silica F-sample shown in Figure 3.7(b), the A_{tot} are much smaller compared to those of fused quartz. This is caused by the fast depolarization of the Mu just after its formation ($t < 5$ ns) in the mesoporous material. This is the "missing fraction" [103, 104] mentioned at the beginning of this section. For example, for F-sample at 250 K:

$$A_{\text{tot}}(5 \text{ keV}, \text{F}) = 2 \cdot 1.3 \cdot 0.020(2) + 0.123(2) = 0.175(6) \tag{3.32}$$

$$A_{\text{miss}}(5 \text{ keV}, \text{F}) = A_{\text{tot}}(5 \text{ keV}, \text{quartz}) - A_{\text{tot}}(5 \text{ keV}, \text{F}) \tag{3.33}$$

$$= 0.233(5) - 0.175(6) = 0.058(8) \tag{3.34}$$

$$F_{\text{miss}} = \frac{0.058(8)}{0.233(5)} = 0.25(3) \ . \tag{3.35}$$

This means that about 25(3)% of Mu formed in the F-sample undergoes fast depolarization after its formation. The fraction of implanted μ^+ which remains as free μ^+ in the sample is given by

$$F_\mu = \frac{A_\mu(5 \text{ keV}, \text{F})}{A_{\text{tot}}(5 \text{ keV}, \text{quartz})} = \frac{0.123(2)}{0.233(5)} = 0.53(1) \ , \tag{3.36}$$
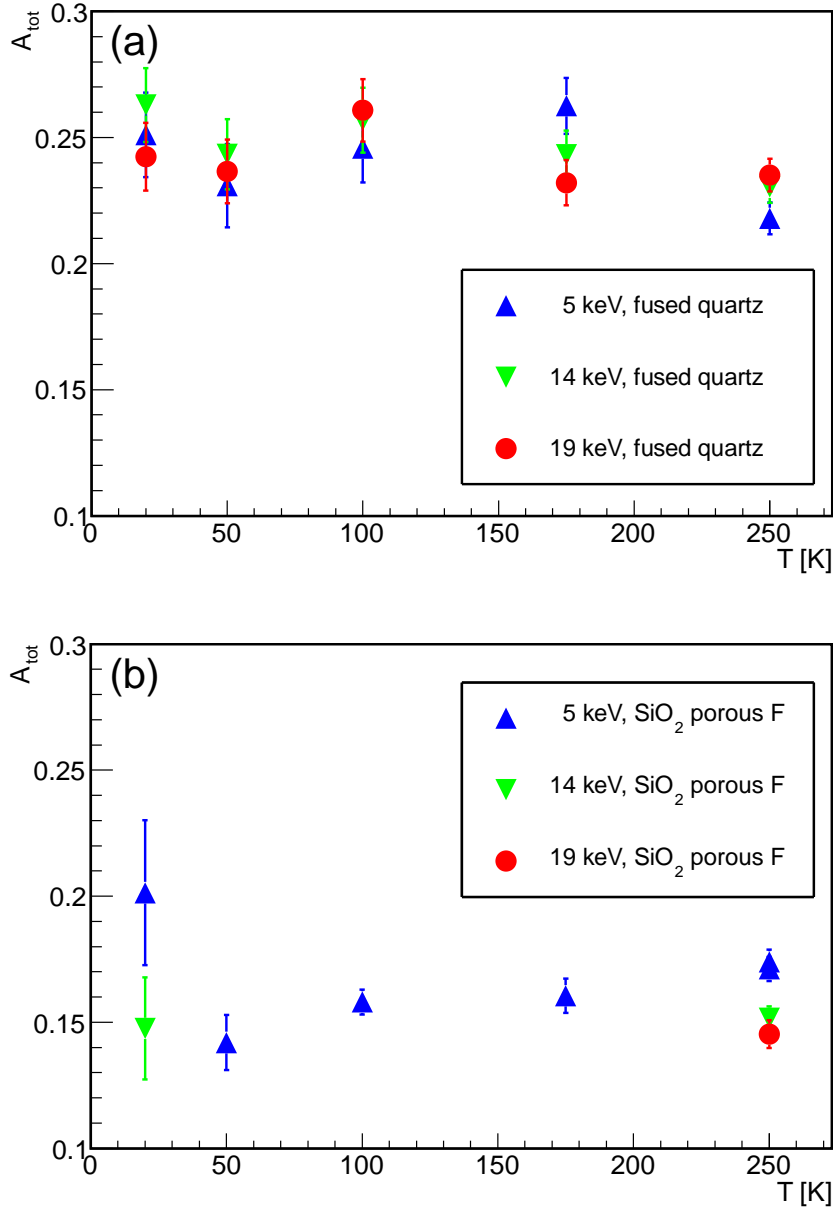
Figure 3.7: *Total decay asymmetry $A_{\rm tot}$ versus temperature for (a) fused quartz and (b) mesoporous F-sample, at various implantation energies. No strong temperature dependence is observed. For the F-sample, the values are smaller than those of fused quartz due to the fast depolarization of the Mu soon after its formation. This fast depolarization gives rise to the "missing fraction" of the total decay asymmetry $A_{\rm tot}$. The error bars are the fit errors only.*

whereas the fraction of implanted μ^+ that has formed Mu and kept their polarization until before decaying is given by

$$F_{\mathrm{Mu}} = \frac{2C_t A_{\mathrm{Mu}}(5\ \mathrm{keV}, \mathrm{F})}{A_{\mathrm{tot}}(5\ \mathrm{keV}, \mathrm{quartz})} = \frac{2 \cdot 1.3 \cdot 0.020(2)}{0.233(5)} = 0.22(2) \ . \tag{3.37}$$

From Equations 3.35 to 3.37, it results that for mesoporous silica F-sample, 53(1)% of the implanted μ^+ remains as free μ^+ whereas 22(2)% forms Mu keeping their polarization until decay, and 25(3)% forms Mu depolarizing within the first 5 ns. About 50% of the Mu formed in the mesoporous materials undergoes fast depolarization probably due to the spin-exchange collisions in the pores.

Similar calculations can be repeated for the fused quartz sample using the asymmetries from Equation 3.26, and the corresponding fractions are $F_\mu = 0.62(3)$, $F_{\mathrm{Mu}} = 0.39(1)$ and $F_{\mathrm{miss}} = 0$ since it was assumed at the beginning that there is no missing fraction in a fused quartz sample.

It should be noted such a determination of F_{Mu} from A_{Mu} is possible only at low magnetic fields (≈ 6 G). At medium or high magnetic fields, Mu precession is too fast to be resolved experimentally and A_{Mu} is washed out.

3.5   Mu formation probability

There are two ways to determine the Mu formation probability F_{Mu}^0 per implanted μ^+:

(I) Directly: using the fitted value of A_{Mu} and A_{tot}, through equation $\dfrac{2C_t A_{\mathrm{Mu}}}{A_{\mathrm{tot}}}$ as explained in previous section

(II) Indirectly: using the fitted value of A_μ and A_{tot}, through equation $1 - \dfrac{A_\mu}{A_{\mathrm{tot}}}$.

Direct method

As explained in Section 3.4, this measurement is only possible at low magnetic fields. However in a magnetic field of 6 G, μ^+ precesses only about $180°$ in the 10 μs measurement time window (e.g., Figure 3.4). This strongly limits the accuracy of the fitted asymmetry A_μ. From Table 3.1 and Table 3.2, it can be seen that the fitted values of A_μ are larger for 6 G measurements than that for 100 G measurements. This could be due to a systematic fit problem when fitting a small fraction of a modulation: there is a strong correlation between A_μ and $e^{-\lambda_\mu t}$ in the fit function of e.g. Equation 3.9. An underestimated damping factor λ_μ could give rise to an overestimation of A_μ. Moremore, A_{Mu} is only sensitive to the Mu fraction, which does not undergo fast depolarization.

Because of these two problems, an "indirect method" is used to extract a more precise value of the Mu formation probability.

Indirect method

To get a more precise F_{Mu}^0 value, measurements at 100 G were used. F_{Mu}^0 is determined indirectly from the fraction of disappearing μ^+ via

$$F_{\mathrm{Mu}}^0 = 1 - F_\mu \ . \tag{3.38}$$

The correctness of this indirect approach relies on the fact that A_μ is not expected to depolarize in silica [105]. Summarizing, this indirect method is more precise because several oscillations (e.g. Figure 3.5) of the μ^+ can be measured and it is insensitive to the Mu depolarization effect.

Not all the μ^+ from the LEM beam are implanted into the sample. Part of the μ^+ are hitting the sample and the rest are hitting the Ag coating of the Cu nose sample plate. Since no Mu is formed in the Ag, the F_μ determined from the fit is an overestimation of the actual value. The fraction x of μ^+ which is hitting the sample (normalized to the total μ^+ in the beam) can be determined as explained in Appendix C. Accounting for this fraction x, the corrected Mu formation probability is then given by

$$F_{\mathrm{Mu}}^{0,\mathrm{cor}} = \frac{1 - F_\mu}{x} \ . \tag{3.39}$$

For mesoporous silica F-sample at 250 K and 5 keV $x = 0.75$. Thus, the corrected Mu formation probability is

$$F_{\mathrm{Mu}}^{0,\mathrm{cor}}(5 \text{ keV}, \text{F}) = \frac{1 - \frac{0.117(1)}{0.233(5)}}{0.75(4)} = \frac{0.50(1)}{0.75(4)} = 0.66(4) \ . \tag{3.40}$$

The Mu formation probability for F-sample resulting from an average at various temperatures and implantation energies as shown in Figure 3.8 is 0.64(2). The corresponding value for C-sample is 0.60(2). These values are comparable with the results obtained in silica powders [57]. Table 3.1 and Table 3.2 summarizes the values obtained using mesoporous silica C-sample and F-sample for the beam time in 2011.

Mu formation probability in mesoporous silica

The Mu formation probability for the fused quartz sample calculated using Equation 3.39 is $F_{\mathrm{Mu}}^{0,\mathrm{cor}} = 0.87(4)$, in good agreement with [106]. The difference in $F_{\mathrm{Mu}}^{0,\mathrm{cor}}$ between the mesoporous SiO_2 and quartz samples is probably caused by the absence of "delayed Mu
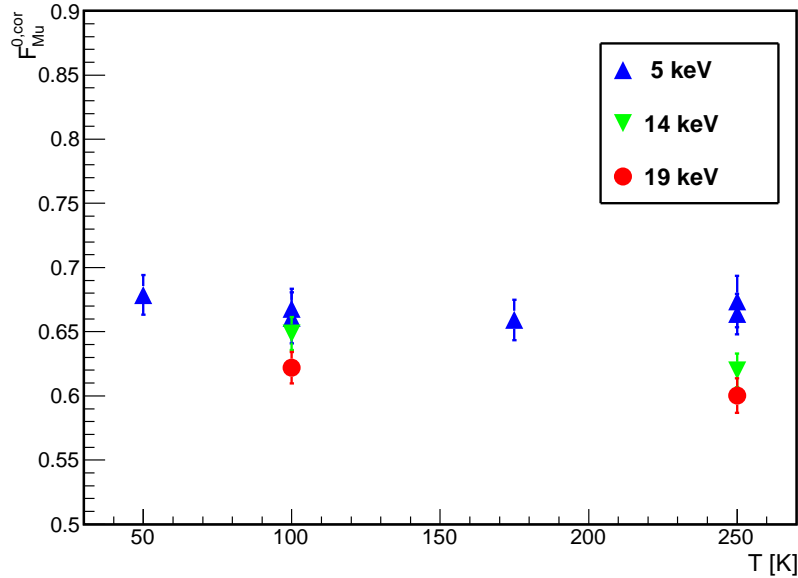
Figure 3.8: *Initial fraction of Mu formed in the sample for a mesoporous silica F sample.*

formation" in the porous samples. Here "delayed Mu formation" refers to the capture of an electron by a thermalized μ^+, where the electron originates from the μ^+ own ionization track. This process is in contrast to the "prompt" Mu formation in charge-exchange collisions during the μ^+ slowing down, which occurs at about hundred eV to keV energies, followed by thermalization as Mu and not as μ^+. At low implantation energies, when the number of generated track electrons is less than 1000 or in the presence of defects, "delayed Mu formation" is suppressed and only the "prompt" process accounts for Mu formation [106]. In the mesoporous SiO_2 samples, Mu formation is expected to be dominated by the "prompt" process because track electrons will be hindered to recombine with thermalized μ^+ by scattering and capturing at pore boundaries. This is why $F_{Mu}^{0,cor}$ does not depend on implantation energy for the mesoporous silica samples.

Summarizing, for mesoporous silica C-sample, 60(2)% of the implanted μ^+ form Mu whereas 40(2)% remain as free μ^+. The corresponding values of $F_{Mu}^{0,cor}$ for F-sample and fused quartz are 64(2)% and 87(4)%, respectively. About 50% of the formed Mu in the mesoporous material depolarizes very fast (< 5 ns) whereas this depolarization is absent in fused quartz.

Table 3.1: *Mu formation probability obtained using µSR technique for meso-porous silica C sample in beam time 2011. T is the sample temperature, B the magnetic field, E the μ^+ implantation energy, A_μ the μ^+ decay asymmetry, A_{Mu} the Mu decay asymmetry, A_{tot} the total decay asymmetry, F_{Mu}^0 the Mu formation probability and $F_{\mathrm{Mu}}^{0,\mathrm{cor}}$ the corrected Mu formation probability.*

T (K)	B (G)	E (keV)	A_μ	A_{Mu}	A_{tot}	F_{Mu}^0	$F_{\mathrm{Mu}}^{0,\mathrm{cor}}$
250	6	3	0.140(1)	0.006(1)	0.155(3)	0.38(10)	0.56(15)
250	6	5	0.139(1)	0.003(1)	0.147(3)	0.40(1)	0.53(3)
250	6	10	0.134(2)	0.004(2)	0.144(5)	0.45(10)	0.52(11)
250	6	14	0.126(2)	0.002(1)	0.131(2)	0.47(1)	0.51(2)
250	100	3	0.133(2)	-	-	0.41(9)	0.60(14)
250	100	5	0.127(2)	-	-	0.45(1)	0.61(3)
250	100	10	0.116(2)	-	-	0.52(9)	0.60(10)
250	100	14	0.111(2)	-	-	0.53(1)	0.58(3)
175	6	3	0.142(2)	0.003(2)	0.150(5)	0.37(10)	0.54(15)
175	6	5	0.150(3)	0.004(3)	0.160(9)	0.36(2)	0.48(4)
100	6	3	0.141(2)	0.011(2)	0.169(6)	0.37(10)	0.54(15)
100	6	5	0.134(2)	0.007(3)	0.152(8)	0.42(2)	0.56(4)
50	6	3	0.146(2)	0.001(1)	0.150(3)	0.35(10)	0.51(15)
50	6	5	0.144(5)	0.005(5)	0.157(13)	0.38(3)	0.51(5)

Table 3.2: *Mu formation probability obtained using μSR technique for meso-porous silica F sample in beam time 2011. T is the sample temperature, B the magnetic field, E the μ^+ implantation energy, A_μ the μ^+ decay asymmetry, A_{Mu} the Mu decay asymmetry, A_{tot} the total decay asymmetry, F_{Mu}^0 the Mu formation probability and $F_{\mathrm{Mu}}^{0,\mathrm{cor}}$ the corrected Mu formation probability.*

T (K)	B (G)	E (keV)	A_μ	A_{Mu}	A_{tot}	F_{Mu}^0	$F_{\mathrm{Mu}}^{0,\mathrm{cor}}$
250	6	5	0.123(2)	0.020(2)	0.174(5)	0.47(1)	0.63(4)
250	6	14	0.115(2)	0.014(2)	0.152(5)	0.52(1)	0.57(3)
250	6	19	0.108(2)	0.009(2)	0.130(5)	0.55(1)	0.57(3)
250	100	5	0.117(1)	-	-	0.50(1)	0.66(4)
250	100	14	0.102(2)	-	-	0.57(1)	0.62(3)
250	100	19	0.102(3)	-	-	0.57(1)	0.59(3)
175	6	5	0.133(2)	0.011(3)	0.161(7)	0.43(1)	0.57(3)
175	100	5	0.118(1)	-	-	0.49(1)	0.65(4)
100	6	5	0.135(2)	0.009(2)	0.158(5)	0.42(2)	0.56(4)
100	100	5	0.116(2)	-	-	0.50(1)	0.66(4)
100	100	14	0.096(2)	-	-	0.60(1)	0.65(3)
100	100	19	0.097(2)	-	-	0.60(1)	0.63(3)
75	6	5	0.133(2)	0.024(9)	0.194(23)	0.43(1)	0.57(3)
50	6	5	0.134(1)	0.005(2)	0.174(4)	0.42(1)	0.56(3)
50	100	5	0.114(1)	-	-	0.51(1)	0.68(4)
20	6	5	0.123(3)	0.030(11)	0.201(29)	0.47(2)	0.63(4)
20	6	14	0.117(3)	0.012(8)	0.148(20)	0.51(2)	0.55(3)
20	6	19	0.111(5)	0.16(24)	0.130(5)	0.54(2)	0.56(3)

Chapter 4

Optimization of muon to muonium conversion: muonium yield in vacuum

As explained in Chapter 3, the μSR measurements provide information regarding the Mu formation probability per implanted μ^+, but do not provide information regarding the Mu yield in vacuum. It only gives a value of the total formed Mu, but can not distinguish between a Mu in vacuum and a Mu in the sample at the time of decay. To extract this information, the LEM apparatus at PSI was modified and a new technique, here called positron shielding technique (PST), was developed. The principle of this technique along with the determined Mu yield in vacuum for mesoporous silica materials will be discussed in this chapter.

4.1 Positron shielding technique

The principle of this technique is based on the idea that positrons from Mu decaying in the sample and emitted in the direction of the downstream detector are stopped by the sample itself, by the sample plate and by the cold finger of the cryostat. This is illustrated in Figure 4.1(a). Due to this shielding effect, the positron detection efficiency ϵ_{det} of the downstream detector is a function of μ^+-decay-position as shown in Figure 4.1(c).

As expected, for no Mu emission into vacuum where the Mu staying inside the sample, an exponential decay time spectrum from μ^+ decay is observed (see Figure 4.1(d)). This is due to the fact that the detection efficiency do not change over time since Mu (μ^+) is not moving. However, if Mu is emitted into the vacuum region in front of the sample, the detection probability increases with time, as the decay positron is less shielded from the
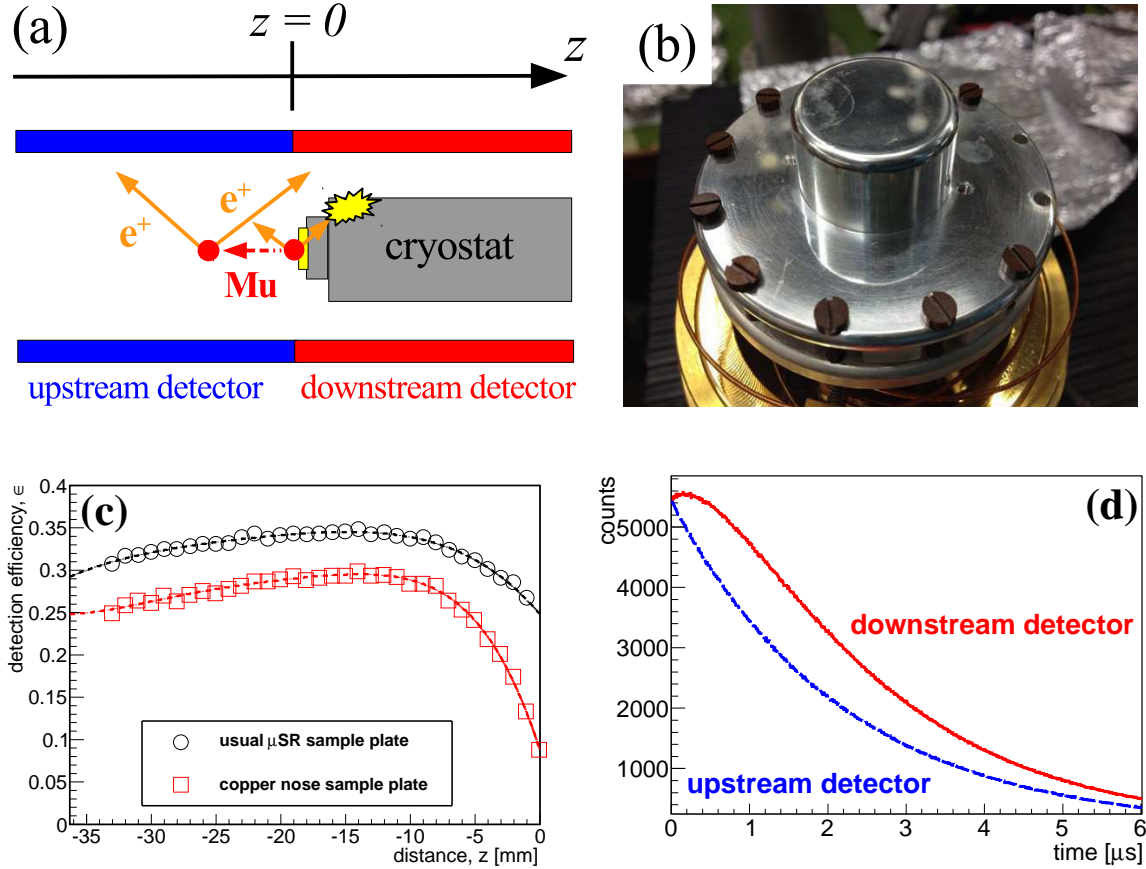
Figure 4.1: *(a) Principle of the positron shielding technique (PST). For Mu emitted into vacuum, the detection probability in the downstream detector increases due to reduced shielding effects of the cryostat materials. (b) "Nose sample plates" used in the PST measurements to increase the z-dependence of the positron detection efficiency. (c) Positron detection efficiency of the downstream detector as a function of μ^+-decay-position z. The newly designed copper nose sample plate gives a higher contrast compared to the usual μSR sample plate made of aluminum. (d) Positron time spectra for downstream (red) and upstream (blue) detectors assuming that Mu atoms are emitted in upstream direction from the sample plate. Due to Mu emission in vacuum, the time spectrum of the downstream detector shows a strong deviation from a simple exponential decay expected from μ^+ decay. The downstream time spectra can be used to determine the Mu vacuum yield.*

downstream detector. Thus the time spectrum of the downstream detector deviates from an exponential decay as shown in Figure 4.1(d). The time spectrum of the upstream detector however remains almost unaltered because no shielding effect occurs there.

Due to the z-position (on the μ^+ beam axis) dependence of the positron detection efficiency, the time spectrum of the upstream detector bears information on the fraction and the velocity distribution of Mu emitted into vacuum. Note that for the PST data analysis, the sum of the time spectra of left, right, top and bottom segments of the downstream detector are used. This is to remove the modulation related to the μ^+ spin precession. A comparison between measured and simulated time spectra thus can be used to extract the the Mu yield in vacuum as described in Section 4.3.

A new sample plate was designed to replace the sample plate usually used in the μSR measurements to provide a positron-detection efficiency with a stronger z-position dependence. The z-dependent efficiencies for standard and new sample plates are compared in Figure 4.1(c). The usual μSR sample plate made of aluminum has low positron stopping power and do not provide a strong position dependence: on the axis at $z = 0$ mm $\epsilon_{det} = 0.26$ whereas at $z = -10$ mm $\epsilon_{det} = 0.33$. The new sample plate which is shown in Figure 4.1(b) (denoted as "nose sample plate" throughout this thesis) is made of copper and provide a stronger position-dependent positron detection efficiency: at $z = 0$ mm $\epsilon_{det} = 0.10$ and at $z = -10$ mm $\epsilon_{det} = 0.27$. The thickness was optimized as a trade-off between contrast (z-dependence) and count rate (statistical accuracy).

The positron detection efficiency strongly depends not only on z but also on the transverse coordinates x and y. Therefore the downstream time spectra strongly depends on the initial space distribution of the Mu atoms which corresponds to the beam size of the implanted μ^+. Qualitatively, a large beam size results in a small contrast between the time spectra with and without emission, because at large distances from the beam axis the shielding effects decrease due to smaller amount of material the positron need to cross to reach the surrounding scintillators. The μ^+ beam size is μ^+-implantation-energy dependent as the implantation energy can be decreased by applying a positive high voltage (HV) on the sample plate which give rise to defocusing field lines. Therefore the beam size increases with decreasing implantation energy. Knowledge of the μ^+ beam size for all energies is essential for a precise simulation of the downstream time spectra and successive comparison with measured data. Hence, a calibration method has been developed to extract the correct beam size at different implantation energies.

4.2   Calibration of the beam size

This calibration method relies on the correlation between the μ^+ beam size and a parameter here defined as upstream-downstream asymmetry

$$A_{ud} = \frac{N_{\mathrm{u}} - N_{\mathrm{d}}}{N_{\mathrm{u}} + N_{\mathrm{d}}} \; , \tag{4.1}$$

where N_u and N_d are the total number of positron counts in the upstream and downstream detectors, respectively. The correlation curve, A_{ud} vs beam size, as shown in Figure 4.2(a) has been determined using Geant4 simulations. For this purpose, the space distribution of the muons on the sample has been approximated by a Gaussian distribution and simulation for various x- and y-variances $\sigma_{x,y}$ have been computed. As expected, A_{ud} decreases with increasing μ^+ beam size because the shielding effect of the sample plate and cryostat materials decreases.

The measured A_{ud} asymmetries are shown in Figure 4.2(b). The fitted values are then reported also on Figure 4.2(a). A decrease of the asymmetry for decreasing μ^+ implantation energy is observed. As already mentioned this has to be associated with the increasing of beam size due to the defocusing effect caused by the required positive HV applied to the sample plate to have lower implantation energy.
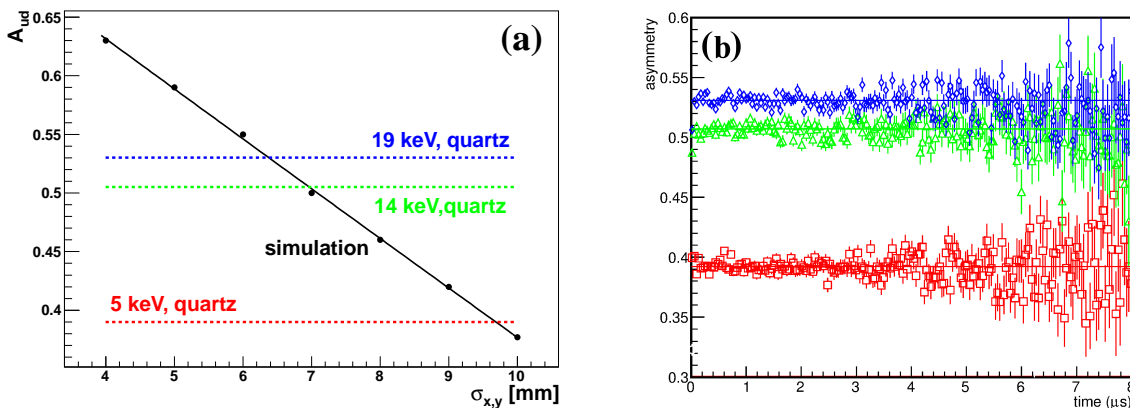
Figure 4.2: *(a) Simulated A_{ud} values for various μ^+ beam sizes parametrized with $\sigma_{x,y}$. The horizontal dashed lines are the experimentally determined A_{ud} values for various implantation energies. (b) Measured A_{ud} for a fused quartz sample (no emission of Mu in vacuum) at 5 keV (red), 14 keV (green) and 19 keV (blue) μ^+ implantation energies.*

This "calibration curve" is used to determine the experimental μ^+ beam size at the sample position. The μ^+ beam size is determined by comparing the experimental A_{ud}
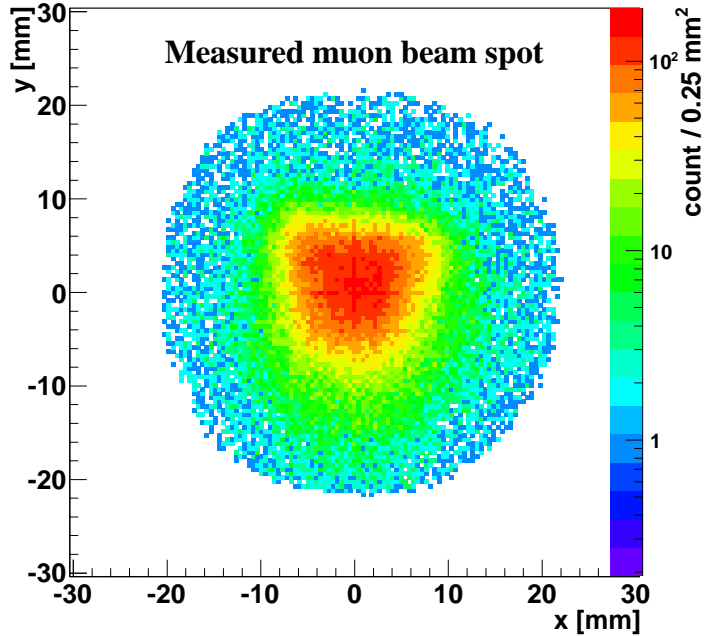
Figure 4.3: μ^+ *beam spot for 14 keV implantation energy ($\sigma_x = 5.6$ mm, $\sigma_y = 6.0$ mm) measured using a MCP detector 17.5 mm downstream of the position of the nose sample plate.*

value of a fused quartz reference sample with simulations. From the measured A_{ud} at 5, 14 and 19 keV, the RMS values ($\sigma_{x,y}$) of the beam were determined to be 9.7 mm, 7.0 mm and 6.4 mm, respectively.

The validity of this calibration method is supported by the fact that these beam sizes agree well with the values from the full μ^+ beam transport simulations done using musrSim [107] and also with a beam spot measurement at 14 keV implantation energy done with a MCP plate installed at a position 17.5 mm downstream of the position of the nose sample plate (see Figure 4.3). The ∼1 mm smaller μ^+ beam spot in the beam spot measurement is due to the fact that the μ^+ beam size was optimized for the usual μSR sample plate which is 16 mm downstream of the position of the nose sample plate. Hence a larger beam size is expected at the nose sample plate position.

4.3 Muonium yield in vacuum

In order to determine the fraction of Mu emitted into vacuum, simulated and measured time spectra in the downstream detector are compared. In Figure 4.4(a), simulated time
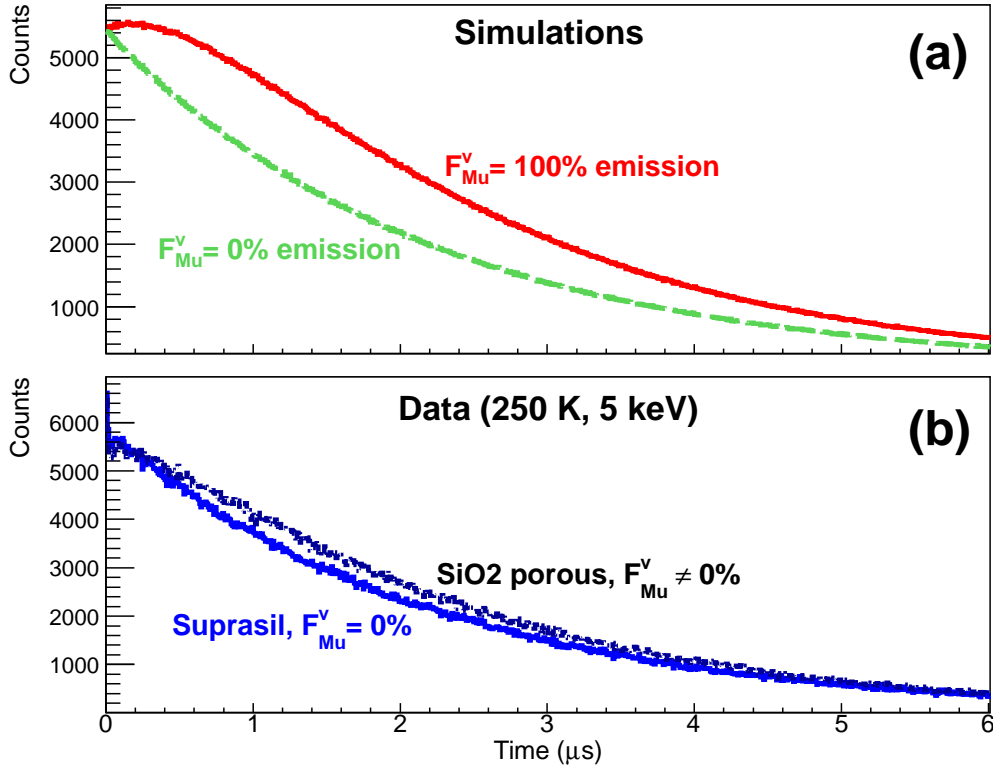
Figure 4.4: *(a) Simulated time spectra for the PST in the downstream detector for 0% (dashed green) and 100% (solid red). (b) Measured time spectra for the F-sample porous material (dotted black) and the fused quartz sample (solid blue). Mu vacuum yield is extracted by fitting the positron spectra of the downstream detector to the linear combination of the simulated positron time spectra of 0% and 100% Mu emission. Reproduced from [108].*

spectra in the downstream detector using Geant4 [109] for 0% (f_0) and 100% (f_{100}) Mu yield in vacuum are shown. In Figure 4.4(b), the measured data for suprasil (where there is no emission into vacuum and thus corresponds to 0% emission) and for SiO_2 porous material where emission into vacuum is expected are shown.

In order to extract the fraction of Mu emission into vacuum (F_{Mu}^v), the measured time spectra is fitted with

$$f_{\text{fit}}(t) = n\{(1 - F_{Mu}^v)f_0(t) + F_{Mu}^v f_{100}(t)\} + n_{pp}f_{pp}(t) \ . \tag{4.2}$$

where n is the normalization, $f_{pp}(t)$ the distribution of a prompt peak and n_{pp} the normalization of the prompt peak. This prompt peak which occurs in the first bins of the time spectra is originated from μ^+ decaying in flight before reaching the target

and from backscattered μ^+ [110]. The shape of the prompt peak $f_{pp}(t)$ is determined experimentally using the suprasil sample. Summarizing, the measured time spectra are fit with three free parameters: n, n_{pp} and F_{Mu}^v.

Fits of $f_{\text{fit}}(t)$ to the experimental data which have been taken for various implantation energies and film temperatures typically give χ^2 of 1.1-1.4, after optimizing the range (30-500 ns) in which the peak distribution $f_{pp}(t)$ is used. The fluctuation of the fitting values is about 10% and is assigned as a systematic error to F_{Mu}^v. In the simulations Mu is assumed to be emitted from the surface of the sample with a $\cos\theta$ angular distribution [58, 111] and an energy spectrum corresponding to a Maxwell-Boltzmann at the target temperature. Fitting the data with an isotropic angular distribution or a different temperature worsens the reduced χ^2 by more than 0.2.
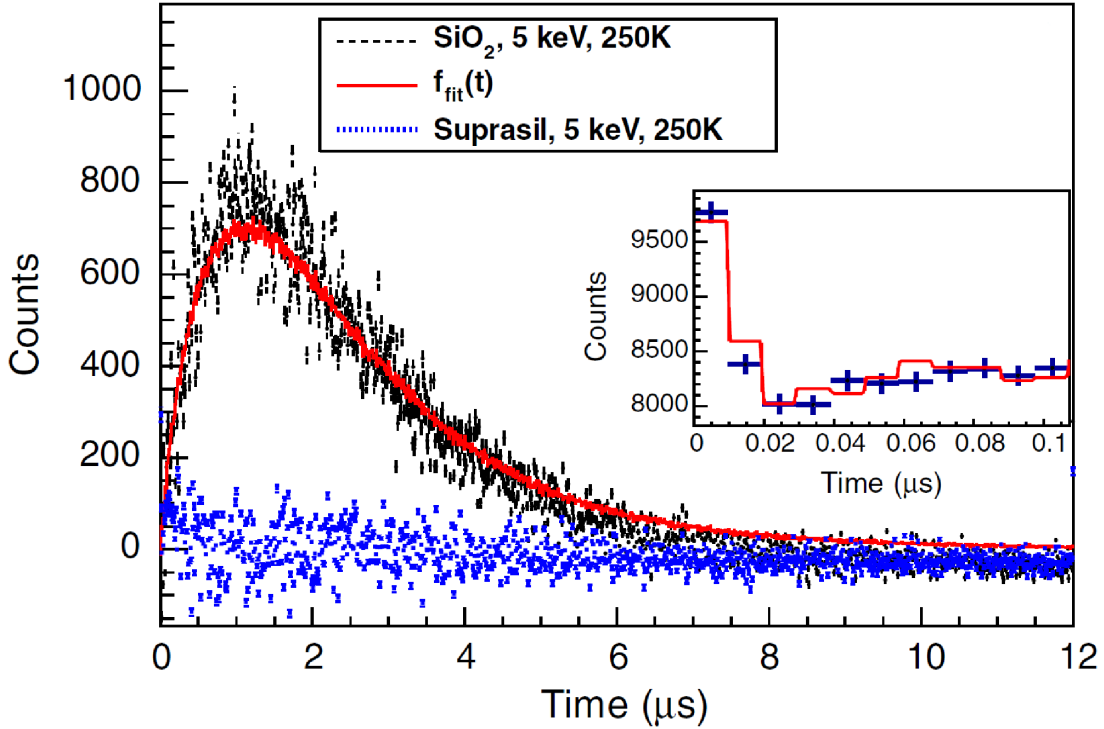
Figure 4.5: *Data after subtraction of the exponential muon decay distribution fit with $f_{\text{fit}}(t)$. The inset shows the prompt peak (without subtraction). Reproduced from [108].*

In order to better visualize the comparison between simulations and measurements (Figure 4.5) the time spectra (data and fit) are shown after subtraction of the exponential μ^+ decay. The fused quartz data give a constant value (beside the prompt peak) as expected due to the absence of Mu emission from this sample. On the contrary, for
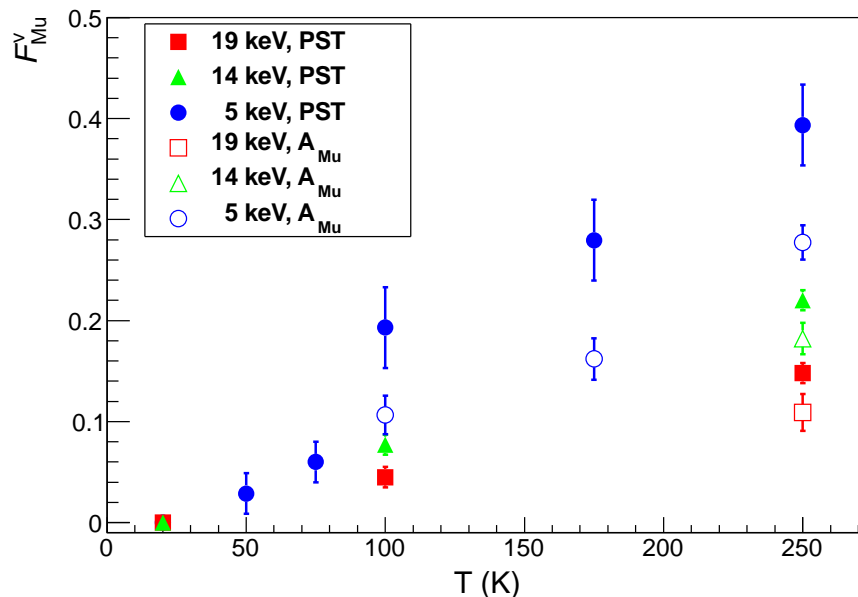
Figure 4.6: F_{Mu}^v *versus the temperature determined with PST for a F-sample. For comparison, the results of the direct method (using A_{Mu}) from μSR measurements in Section 3.5 are shown. Reproduced from [108].*

the mesoporous thin film there is bump caused by the increased positron detection efficiency when Mu is emitted into vacuum. The values of F_{Mu}^v extracted from the fit are presented in Figure 4.6. The best results have been obtained from the F-samples which showed a Mu yield in vacuum of $(38\pm4)\%$ at 250 K and is $(20\pm4)\%$ at 100 K for 5 keV implantation energy. The abrupt change of F_{Mu}^v visible around 75 K is due to absorption of Mu at the pore walls as already reported for silica powders [112, 113]. For 20 K F_{Mu}^v is compatible with zero.

For comparison, in Figure 4.6, the fraction of Mu determined directly from the measurement of the Mu asymmetry A_{Mu} with μSR technique is also presented. As one can see, these points are systematically lower than F_{Mu}^v obtained with PST. This is because PST, in contrast to the μSR direct method, is also sensitive to the fraction of Mu that depolarizes fast. Nevertheless, both methods give consistent results in terms of dependence on the sample temperature and μ^+ implantation energy (E).
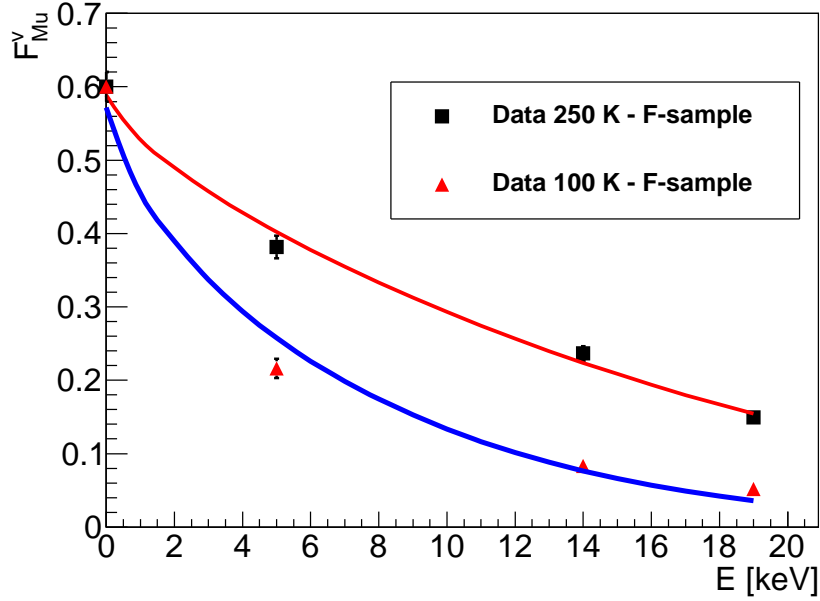
Figure 4.7: *F_{Mu}^{v} versus the implantation energy for the F-sample. The curves are fits with the diffusion model described in the text.*

4.4 Determination of the diffusion constant

In Figure 4.7, F_{Mu}^{v} versus implantation energy E at 100 and 250 K is fitted with a one-dimensional diffusion model originally developed for Ps [114, 115]. The Mu fraction diffusing into vacuum is given by

$$F_{\mathrm{Mu}}^{v}(E) = F_{\mathrm{Mu}}^{0}(E)J(E) \tag{4.3}$$

$$J(E) = \int_{0}^{l} e^{-\beta x} P(x, E) dx . \tag{4.4}$$

where l is the film thickness, $\beta = 1/\sqrt{D_{\mathrm{Mu}}\tau}$ the inverse of the diffusion length and D_{Mu} the diffusion coefficient. The initial Mu fraction F_{Mu}^{0} is taken from Figure 3.8. The μ^{+} implantation profile $P(x, E)$ was calculated using the TrimSP simulation validated for μ^{+} with experimental data [86]. The only free parameter used to fit the data is the Mu diffusion constant D_{Mu} and the resulting values determined from the fit are summarized in Table 4.1. The Mu yield in vacuum as a function of the implantation energy for F-sample is shown in Figure 4.7.

The good agreement between fit and data implies that D_{Mu} does not depend on the implantation energy. This means that the Mu thermalization time is much shorter than

Table 4.1: *Diffusion constants, D_{Mu} and number of collision in the pores, N_C for mesoporous silica F-sample.*

Sample	T (K)	$D_{Mu}(cm^2s^{-1})$	N_C
F	100	$(4.2\pm0.4)\times10^{-5}$	2050 ± 390
F	250	$(1.9\pm0.2)\times10^{-4}$	710 ± 150
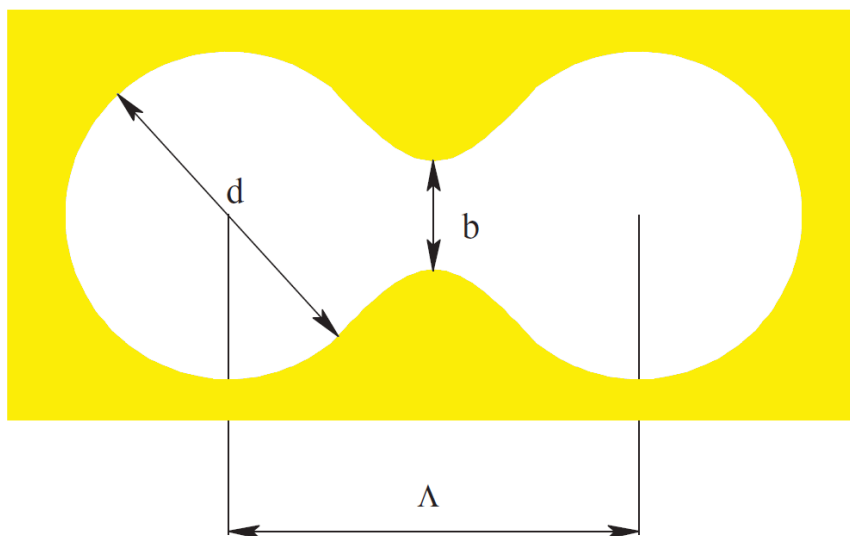
Figure 4.8: *A schematic representation of two interconnected pores in the mesoporous SiO_2. The nearly spherical pores have a diameter d and are connected to other pores via holes of diameter b. The separation between pores Λ is simply the pore diameter plus the wall thickness.*

the diffusion time. A further argument that Mu thermalizes quickly is given by the worsening of the χ^2 when fitting the data of Figure 4.5 with distributions simulated at temperatures different from the sample temperature. Therefore, the diffusion coefficient as a function of the mean kinetic energy E_{Mu} of thermalized Mu in the pores can be written as [111]

$$D_{Mu} = \Lambda/(3N_C)\sqrt{2E_{Mu}/m_{Mu}} \ . \tag{4.5}$$

where N_C is the mean number of collisions that Mu undergoes in one pore before reaching the next one, m_{Mu} the Mu mass and Λ the mean distance between the pores.

Similar to [111], the mesoporous silica has a microscopic structure consisting of approximately spherical pores interconnected via short channels, as shown in Figure 4.8. This figure shows only two spherical pores of diameter d connected by a hole of diameter b. If the porous films retain their hexagonal close packing (HCP) structure (at least over

a short range) then it is expected that each pore has 12 nearest neighbors, all of them connected in a manner similar to that shown in Figure 4.8. Thus, for pores connected by channels of diameter b, the mean number of collisions per pore is expected to be

$$N_C \approx \frac{4\pi(d/2)^2}{12\pi(b/2)^2} = \frac{d^2}{3b^2} \ , \tag{4.6}$$

which is the inverse of the escape probability per collision, from a simple geometrical calculation.

The spacing between pores Λ, is the mean free path for Mu atoms that tunnel from pore to pore. This is given by the pore diameter plus the wall thickness and may be determined from the mean density of the porous material. For hollow spheres of diameter d and nearest neighbor distance Λ in a HCP arrangement within a material of density ρ_0, the average density is approximately given by

$$\rho = \rho_0(1 - \pi d^3/\Lambda^3\sqrt{18}) \ . \tag{4.7}$$

Using a silica bulk density of $\rho_0 = 2.2$ g/cm^3 and porous film density of $\rho = 1.1$ g/cm^3, $\Lambda = 5.7$ nm was obtained for a pore diameter of $d = 5$ nm. Using the experimentally determined D_{Mu}, the mean number of collisions in each pore is $N_C = 2050 \pm 390$ at 100 K and $N_C = 710 \pm 150$ at 250 K for F-sample. These values confirm that Mu thermalization is fast ($\sim$ns) compared to the time scale of the diffusion process ($\sim \mu$s). In fact, from the mass difference of Mu and SiO$_2$ [116], one expects that in order to reach thermal energy Mu needs $\sim$500 collisions.

4.5   Quantum mechanical tunneling

The obtained D_{Mu} values are three orders of magnitude smaller than expected from a classical diffusion model [57]. Moreover, N_C should not be depending on the temperature based on the geometrical argument in previous section. In order to explain these disagreements, the Mu diffusion process in the porous material is interpreted as quantum mechanical tunneling from pore to pore through a step potential barrier of (0.6±0.2) nm width (corresponding to the pore walls thickness). From the mean number of collisions N_C, which is the inverse of the pore-to-pore tunneling probability, a height of the potential barrier of (0.3±0.1) eV can be deduced. The uncertainty is dominated by the poor knowledge of the material structure. With this quantum mechanical model the observed dependence of $D_{\mathrm{Mu}}(T)$ versus the temperature T can be reproduced. Since in the regime of the measurements the tunneling probability scales approximately linearly with T

$$D_{\mathrm{Mu}}(T) \sim \sqrt{E_{Mu}}/C) \sim \sqrt{T}/T^{-1} \sim T^{3/2} \tag{4.8}$$

is obtained. The measured ratio $D_{Mu}^{250K}/D_{Mu}^{100K} \approx 3.81$ compares well with the expected value from the $T^{3/2}$ dependence of 3.95 supporting the validity of the model.

To check if the value of the potential barrier height obtained above can be identified with the Mu work-function (W), Density Functional Theory calculations within GAUS-SIAN 98 [117] were performed on clusters of SiO_2 containing up to eight silicon atoms and terminated by oxygen, capped with hydrogen atoms. We compute the total energy $E_{SiO2+Mu}^{tot}$ of the SiO_2 matrix with a Mu atom and the total energy of the SiO_2 fragment alone E_{SiO2}^{tot}. These computations yield $W = E_{SiO2+Mu}^{tot} - E_{SiO2}^{tot} - 13.6eV = (-0.6\pm0.3)\,eV$. The main error for W originates from the uncertainty to locate the exact position of the interstitial Mu site with respect the Si and O atoms. Considering the over-simplification of the quantum diffusion model, it can be concluded that the experimental determination of the work-function is consistent with the theoretical estimation. Further experiments using other techniques and more precise measurements for Mu and Ps will be useful to gain a deeper understanding of this intriguing diffusion process in mesoporous films.

4.6   Possible improvement

From Figure 4.7, according to the model, the Mu yield in vacuum should be even higher at lower muon implantation energy, e.g. 40% at 2 keV at 100 K for F-sample (blue curve). Even though 40% of Mu yield in vacuum at 250 K is already a factor of two better compared to the previous measurements [58], for precision measurements like Mu spectroscopy, it is more desirable to have Mu at very low temperature as the exciting probability is proportional to the square of the interaction time between the Mu atom and the laser. The attempt to produce Mu at low temperature at even lower μ^+ implantation energies was done in summer 2012 using an upgraded LEM beam line. This is discussed in the next chapter.

Chapter 5

Muonium production at very low muon implantation energy

The Mu vacuum yield should increase with decreasing implantation depth. This hypothesis has been confirmed by the prediction of the quantum mechanical diffusion model, as shown in Figure 4.7. According to this model that was fitted to the previously measured data at higher energies, the Mu yield in vacuum is expected to be 40% for 2 keV implantation energy and a temperature of 100 K (for mesoporous silica F-sample). For next generation Mu experiments, it is desirable to have high vacuum yield at low temperature. Therefore measurements at low implantation energies have been performed in 2012 with the aim to explicitly measure the vacuum yield for low implantation energies. Moreover, in the same beam time period new mesoporous samples were tested. The data have been analyzed as previously using μSR and PST techniques. However the analysis of the data taken was complicated by the upgrade of the LEM beam line which was completed during the 2012 accelerator shut-down. This upgrade significantly affected the beam size and other features of the LEM beam line and the LEM spectrometer that will be discussed in this chapter.

5.1 The upgraded LEM beam line

In 2012, the PSI low-energy μ^+ beam line with μSR spectrometer [73] was upgraded. The major changes include the installation of a spin rotator [118] (Figure 5.1) after the electrostatic mirror and repositioning of the start detector closer to the sample region (c.f. Figure 2.2). In the spin rotator the μ^+ spin is rotated by 20° counter-clockwise. The spin rotator was installed to improve the background rejection (mainly proton) and to enable longitudinal μSR measurements (the μ^+ spin has to be rotated by 80°
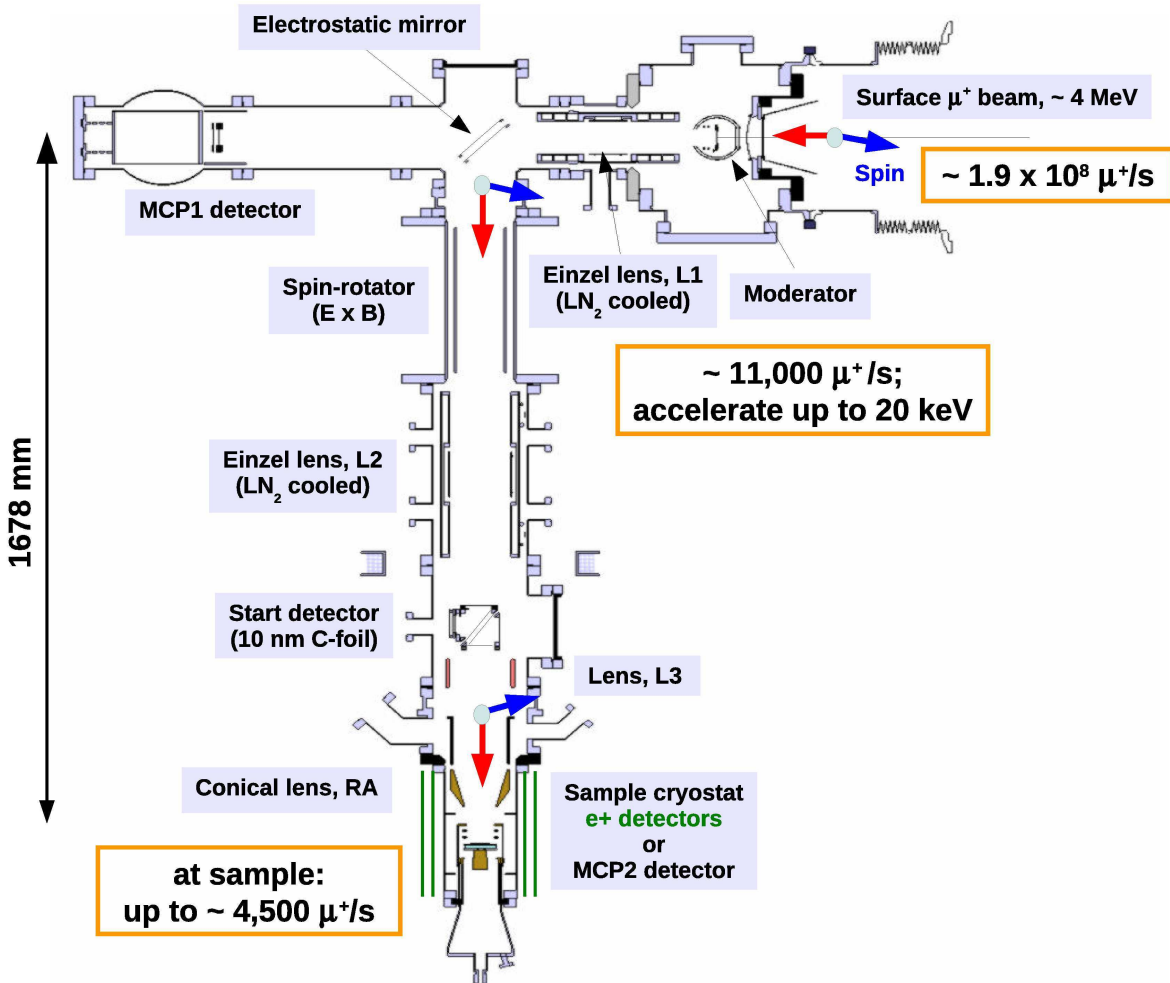
Figure 5.1: *A schematic of the new LEM beam line. The 4 MeV surface μ^+ is moderated at an efficiency of about 0.01% to an energy of about 15 eV before being re-accelerated again to energies up to 20 keV. The μ^+ beam is then bent by 90° at an electrostatic mirror before going through the spin rotator and the start detector and arriving at the sample plate mounted to the cold finger of the cryostat.*

clockwise or 100° anti-clockwise). After leaving the spin rotator the beam is refocused with an einzel lens (L2) before hitting the 10 nm thick carbon foil (≈ 2.2 μg/cm^2) of the start detector. After a slight refocus via the L3 lens, the beam is strongly focused by a conical lens before being implanted into the sample. The sample chamber of the μSR spectrometer was not modified.

5.2 Muon spin rotation measurements

μSR measurements were done for a mesoporous silica F14 sample (an improved version of the F-sample characterized in 2011 beam time) and a B-sample. The mesoporous silica samples were pre-selected with the ETHZ slow positron beam. Most of the data contained 8 million events. Data sets used for the data analysis are summarized in Appendix E.

The fraction of Mu formed in the mesoporous sample is determined from μSR measurements using the indirect way, that is, by measuring the muon A_μ and the total A_{tot} asymmetries and by accounting for correction related with the fraction of μ^+ hitting the sample. Both, the total decay asymmetries and the fraction of μ^+ hitting the sample were obtained differently compared with previous measurements described in Chapter 4.

5.2.1 Total decay asymmetry

As explained in Section 3.4, in order to determine the Mu formation probability, first the total decay asymmetry A_{tot} at various implantation energies are required. Due to the limited time allocated for the beam time 2012, another approach was taken to determine A_{tot}. This is done by coating the Cu nose sample plate with a thin layer ($\sim$500 nm) of Ag. Ag was chosen because of its large decay asymmetry A_μ and because there is no Mu formation in this material [86]. Moreover, A_μ of silver has been measured to be temperature independent [86]. A_{tot} at different μ^+ implantation energies measured using a Ag sputtered sample plate is shown in Figure 5.2. Since A_{tot} does not depend on temperature as shown in Figure 5.2, the average values for each implantation energy in analysis are:

$$A_{\text{tot}}(2 \text{ keV}, \text{Ag}) = 0.157(1) \tag{5.1}$$

$$A_{\text{tot}}(3 \text{ keV}, \text{Ag}) = 0.170(1) \tag{5.2}$$

$$A_{\text{tot}}(5 \text{ keV}, \text{Ag}) = 0.186(1) \tag{5.3}$$

$$A_{\text{tot}}(10 \text{ keV}, \text{Ag}) = 0.198(1) \tag{5.4}$$

$$A_{\text{tot}}(14 \text{ keV}, \text{Ag}) = 0.204(1) \ . \tag{5.5}$$
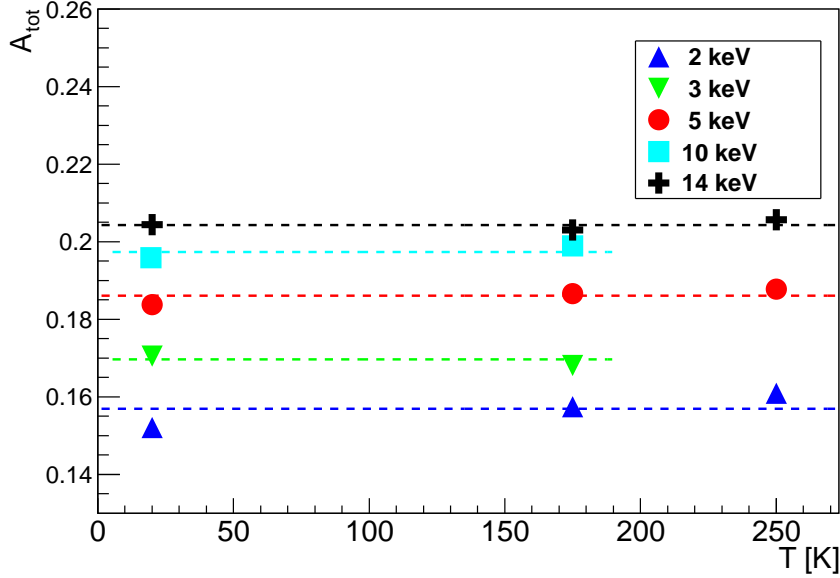
Figure 5.2: *Total decay asymmetry A_{tot} versus temperature for various μ^+ implantation energies of the Ag measurements. There is no strong temperature dependence. The energy dependence is due to the backscattered μ^+ that form Mu which quickly depolarize in the applied magnetic field and move rapidly to the thermo-shield surrounding the sample region. The dotted lines are guides to the eyes.*

From Figure 5.3, for the Ag measurements, a smaller value at lower implantation energy is expected due to the backscattered μ^+ which forms Mu and lost its polarization immediately. It is also important to note that these values are much lower compared to the measurements done on a fused quartz sample in 2011 (c.f. Equations 3.29 to 3.31). This difference, as will be explained later, is probably due to larger contamination of the time spectra with the so called "foil Mu": muonium atoms formed in the carbon foil of the start detector and transported into the spectrometer. In the LEM upgrade, the start detector was moved considerably closer to the sample region. Hence, the "foil Mu" plays a more important role after the beam line upgrade. A 10-15% of "foil Mu" formation in the carbon foil is enough to explain the observed decrease.

5.2.2   Mu formation probability

To determine the Mu formation probability for F14- and B-samples, the indirect method discussed in Section 3.5 was used. Accounting for the fraction x of μ^+ hitting the sample,
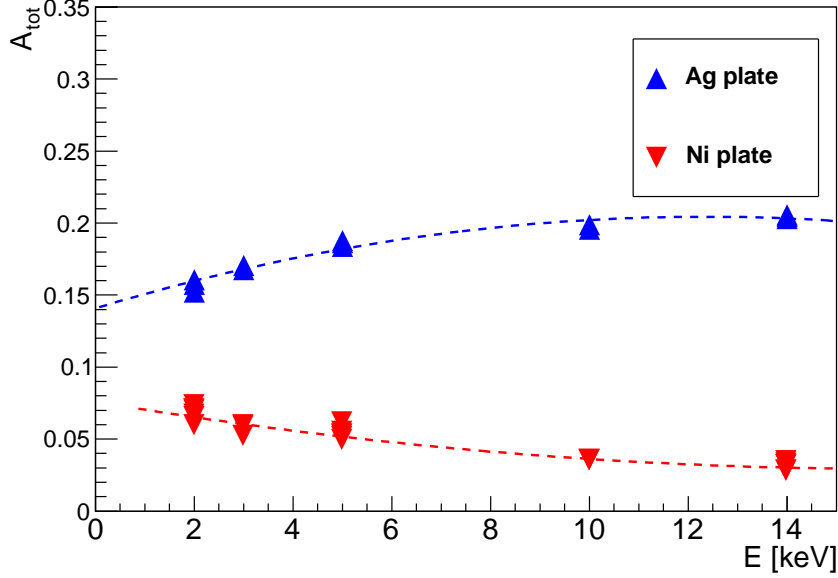
Figure 5.3: *Total observable asymmetry A_{tot} versus implantation energy for the Ag coated nose sample plate and the same nose sample plate with an additional 20×20 mm^2 area of Ni coating at the sample position. For the Ag measurements, a smaller value at lower implantation energy is expected due to the backscattered μ^+ which forms Mu and loose its polarization immediately. A higher value at lower implantation energy for the Ni measurements means that the μ^+ beam is hitting the region outside the 20×20 mm^2 area coated with Ni.*

the corrected Mu formation probability is then given by

$$F_{\mathrm{Mu}}^{0,\mathrm{cor}} = \frac{1 - F_\mu}{x} \ . \tag{5.6}$$

Determination of x, as explained in Appendix C.2, relies on the measurements with a Ni sputtered nose sample plate. This 500 nm thick Ni is coated on the same area occupied by the sample (20×20 mm^2). In Ni, the fraction of μ^+ that hits the sample experiences a broad distribution of static internal magnetic fields (≈ 64 mT) [119], and hence exhibits a fast relaxation during the first 100 ns [120]. Therefore the residual precession signal $A_\mu^{\mathrm{res}}(\mathrm{Ni})$ observed in the LEM apparatus is coming from those μ^+ which are stopping outside the 20×20 mm^2 sample region. Hence the fraction x of μ^+ hitting the sample is given by

$$x = 1 - \frac{A_\mu^{\mathrm{res}}(\mathrm{Ni})}{A_{\mathrm{tot}}(\mathrm{Ag})} \ , \tag{5.7}$$

where $A_\mu^{\mathrm{res}}(\mathrm{Ni})$ is coming from the Ni coated plate measurement and $A_{\mathrm{tot}}(\mathrm{Ag})$ coming from the Ag coated plate measurement described in previous section. Since no strong temperature dependence of $A_\mu^{\mathrm{res}}(\mathrm{Ni})$ has been observed, the averages at various implantation energies can be used:

$$A_\mu^{\mathrm{res}}(2 \text{ keV}, \mathrm{Ni}) = 0.069(1) \tag{5.8}$$

$$A_\mu^{\mathrm{res}}(3 \text{ keV}, \mathrm{Ni}) = 0.060(1) \tag{5.9}$$

$$A_\mu^{\mathrm{res}}(5 \text{ keV}, \mathrm{Ni}) = 0.053(1) \tag{5.10}$$

$$A_\mu^{\mathrm{res}}(10 \text{ keV}, \mathrm{Ni}) = 0.036(1) \tag{5.11}$$

$$A_\mu^{\mathrm{res}}(14 \text{ keV}, \mathrm{Ni}) = 0.031(1) \ . \tag{5.12}$$

A higher value at lower implantation energy for the Ni measurements means that the μ^+ beam is hitting the region outside the $20 \times 20 \text{ mm}^2$ area where the Ni is sputtered. Measurements of Ag and Ni coated plates are summarized in Figure 5.3.

Combining Equation 5.6 and Equation 5.7, the corrected Mu formation probability $F_{\mathrm{Mu}}^{0,\mathrm{cor}}$ in the sample is obtained:

$$F_{\mathrm{Mu}}^{0,\mathrm{cor}} = \frac{1 - F_\mu}{x} = \frac{1 - \dfrac{A_\mu}{A_{tot}(\mathrm{Ag})}}{1 - \dfrac{A_\mu^{\mathrm{res}}(\mathrm{Ni})}{A_{\mathrm{tot}}(\mathrm{Ag})}} = \frac{A_{tot}(\mathrm{Ag}) - A_\mu}{A_{tot}(\mathrm{Ag}) - A_\mu^{\mathrm{res}}(\mathrm{Ni})} \ . \tag{5.13}$$

For the mesoporous silica F14 sample at 20 K, the corrected Mu formation probabilities at various μ^+ implantation energies are

$$F_{\mathrm{Mu}}^{0,\mathrm{cor}}(14\mathrm{keV}) = \frac{A_{tot}(\mathrm{Ag}) - A_\mu}{A_{tot}(\mathrm{Ag}) - A_\mu^{\mathrm{res}}(\mathrm{Ni})}$$

$$= \frac{0.204(1) - 0.090(2)}{0.204(1) - 0.031(1)} = 0.66(1) \tag{5.14}$$

$$F_{\mathrm{Mu}}^{0,\mathrm{cor}}(5\mathrm{keV}) = \frac{0.186(1) - 0.102(2)}{0.186(1) - 0.053(1)} = 0.63(2) \tag{5.15}$$

$$F_{\mathrm{Mu}}^{0,\mathrm{cor}}(2\mathrm{keV}) = \frac{0.157(1) - 0.100(2)}{0.157(1) - 0.069(1)} = 0.65(3) \ , \tag{5.16}$$

whereas for the B sample at 20 K and at 14 keV implantation energy, it is

$$F_{\mathrm{Mu}}^{0,\mathrm{cor}}(14\mathrm{keV}) = \frac{0.204(1) - 0.089(2)}{0.204(1) - 0.031(1)} = 0.66(1) \ . \tag{5.17}$$

The Mu formation probabilities for B and F-14 samples measured in low magnetic field (5 G) are shown in Figure 5.4. As mentioned before in Section 3.5, measurements at
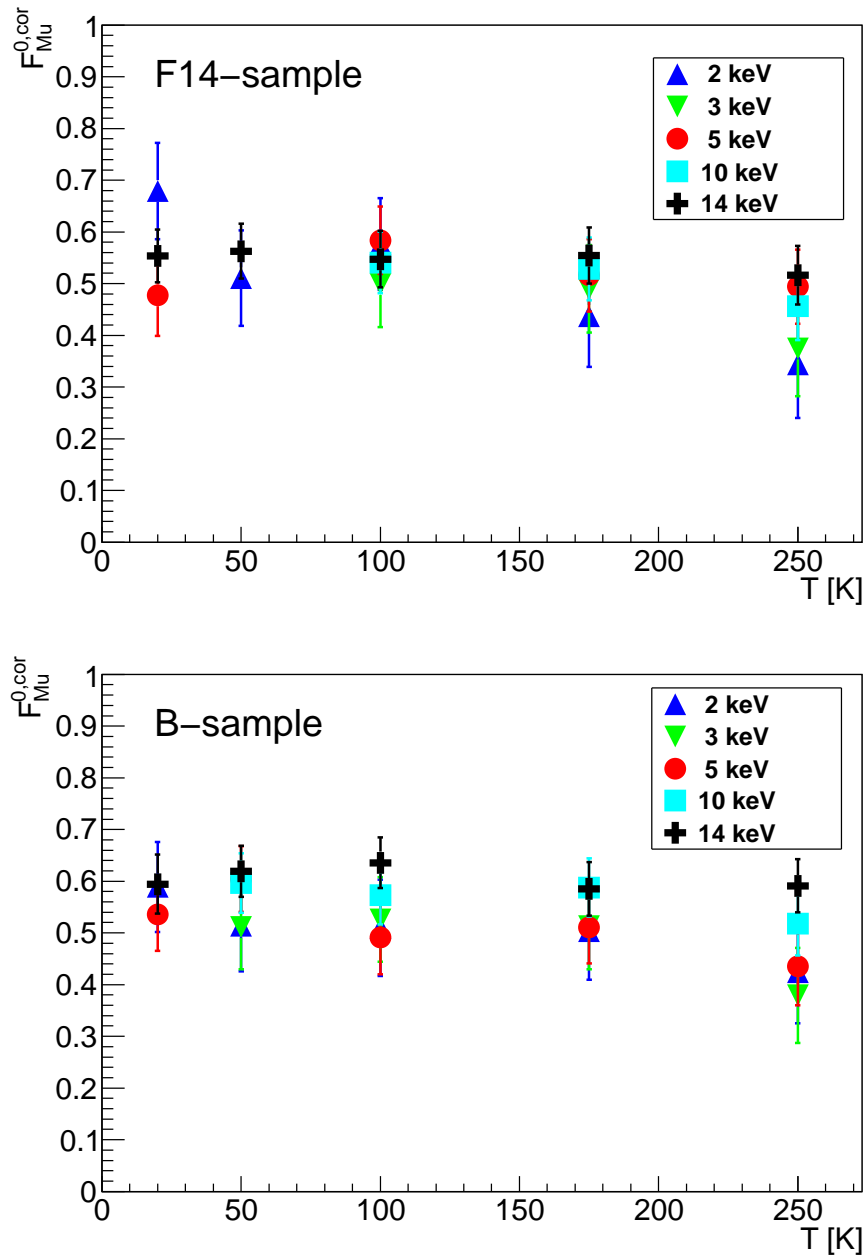
Figure 5.4: *Mu formation probability versus temperature for the mesoporous silica F14-sample (a) and the B-sample (b), at a 5 G magnetic field. These values are just for reference and are not used in the final calculation.*

low magnetic fields suffer from systematic fit problems and hence Figure 5.4 is only for reference. By considering only measurements from 100 G, the Mu formation probability for F14-sample and B-sample are then 0.65(1) and 0.66(1), respectively. These values are slightly higher but in good agreement with the C-sample [0.60(2)] and F-sample [0.64(2)] measured in beam time 2011.

5.3 Positron-shielding-technique measurements

As previously explained, to determine the fraction of Mu emitted into vacuum, simulated and measured time spectra of the downstream detectors have to be compared. These time spectra depend strongly on the beam size. In previous measurements the beam size was determined from upstream-downstream asymmetry A_{ud}. A_{ud} after the insertion of the spin rotator and the re-placement of the start detector decreased, as seen by comparing the horizontal lines of Figure 5.5 with Figure 4.2. This implies that the upgrade of the LEM beam line has lead to an increased μ^+ beam at the sample position. In Figure 5.5, the very small measured asymmetries for low implantation energies indicate that the beam size is strongly increasing with decreasing energy. The beam size for 11 keV implantation energy measured with a MCP at the standard plate position was about 6 mm as shown in Figure 5.5. However the corresponding size determined from the asymmetry measurement has yielded a value of 9.0 mm. This disagreement and the fact that A_{ud} measurements were indicating a large blow up of the beam for low implantation energies motivated a more exact study of the beam propagation in the LEM beam line, and a detailed study of the A_{ud} dependence on the various beam line parameters.

5.4 Simulation of the LEM beam line

A Geant4-based (version 9.4 patch04) simulation of the beam propagation has been accomplished. Low energy physics processes currently not available in Geant4 were implemented to describe the energy losses and formation processes in the thin C-foil of the start detector. Figure 5.6 shows the geometry implemented in the Geant4 simulation. Most of the crucial parts of the apparatus are included, from the L1 einzel lens, spin rotator (SR) to the sample chamber. The detailed geometry including radiation shield, sample holder and cold finger of the cryostat are also implemented.

Precise electric and magnetic field maps are inputs to the Geant4 Monte Carlo simulation. The magnetic field map of the spin-rotator was calculated using the commercial OPERA finite element programs (TOSCA/OPERA-3D) [121], and the electric field
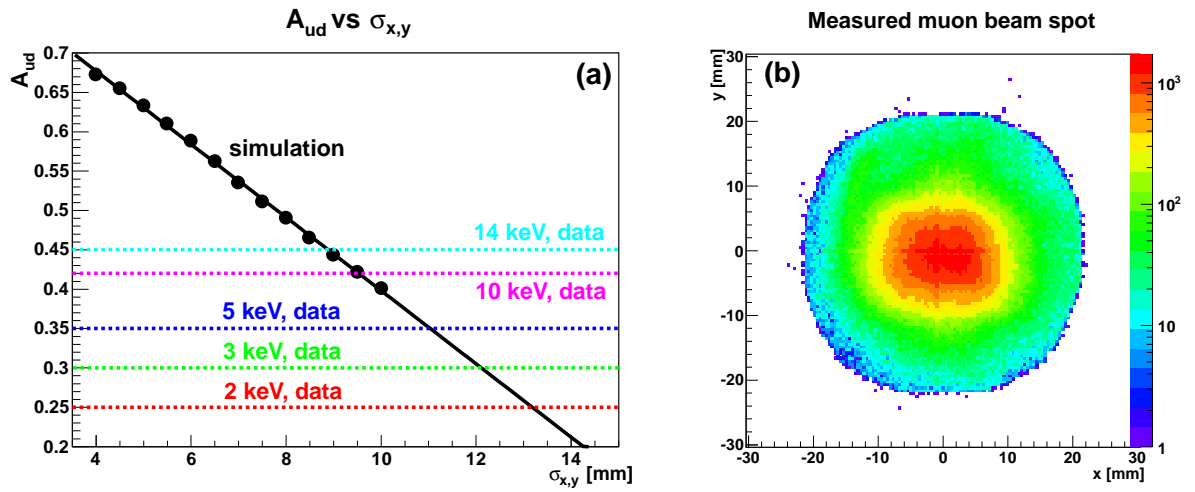
Figure 5.5: *(a) Simulated upstream-downstream asymmetry A_{ud} for various values of the muon beam size $\sigma_{x,y}$ for the 2012 measurement. The horizontal dashed lines are the measured asymmetries using the Ag coated sample nose plate. This plot is used to determine the μ^+ beam size at the sample position. (b) Measured μ^+ beam spot at 11 keV implantation energy using a MCP detector. The measured values of $\sigma_x = 6.4$ mm and $\sigma_y = 6.0$ mm disagree with the simulated values of $\sigma_{x,y} \approx 9.0$ mm obtained via the comparison of measured and simulated A_{ud}.*
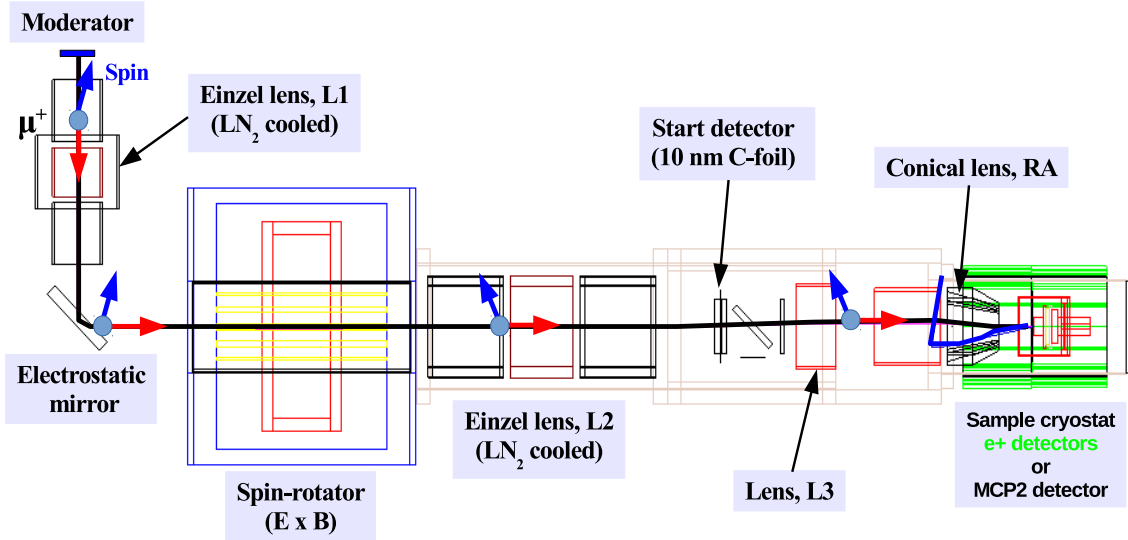
Figure 5.6: *Schematic view of the LEM beam line as implemented in the Geant4 simulation. The beam which is given by the black solid line is simulated starting after the moderator. The arrows indicate spin (blue) and momentum (red) directions.*
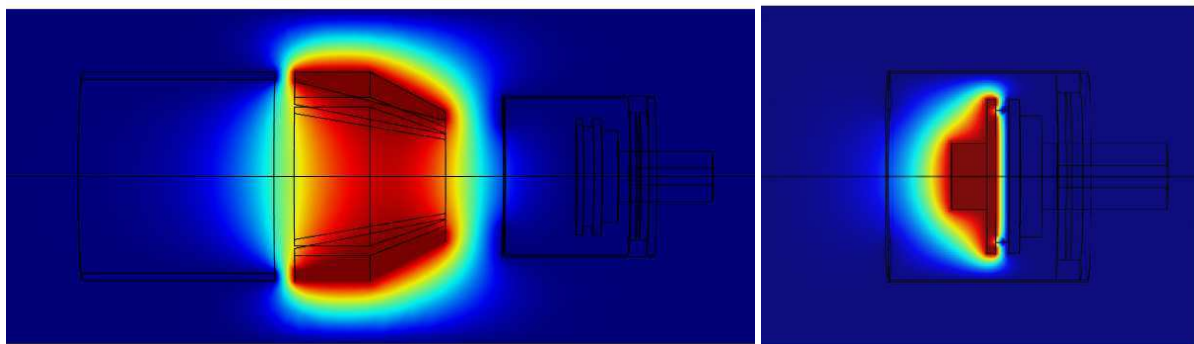
Figure 5.7: *Electric potential in the conical lens regions (left) and in the sample nose plate region (right), calculated with COMSOL multiphysics. Maximum electric potential (red) is 1 kV in both figures. They are then scaled to match the values in the LEM beam line.*

66

maps were calculated with the finite element software COMSOL [122]. Due to the modified sample plate setup in this work, the electric field maps of the conical lens (RA) and the copper sample plate with cylindrical nose were re-calculated. The electrostatic module of COMSOL was used and a fine mesh was applied for higher accuracy calculations. The results are shown in Figure 5.7. The electrostatic potential at the nose sample plate shows a strong curvature also in the region of the muon propagation. Because of this, the corresponding electric field (gradient of the potential) has a radial component which leads to a defocusing of the beam. Therefore the sample nose plate which leads to a strong z-position dependence of the positron detection also distort significantly the muon beam. This is especially severe for lower implantation energies.

Implementation of low energy muon physics
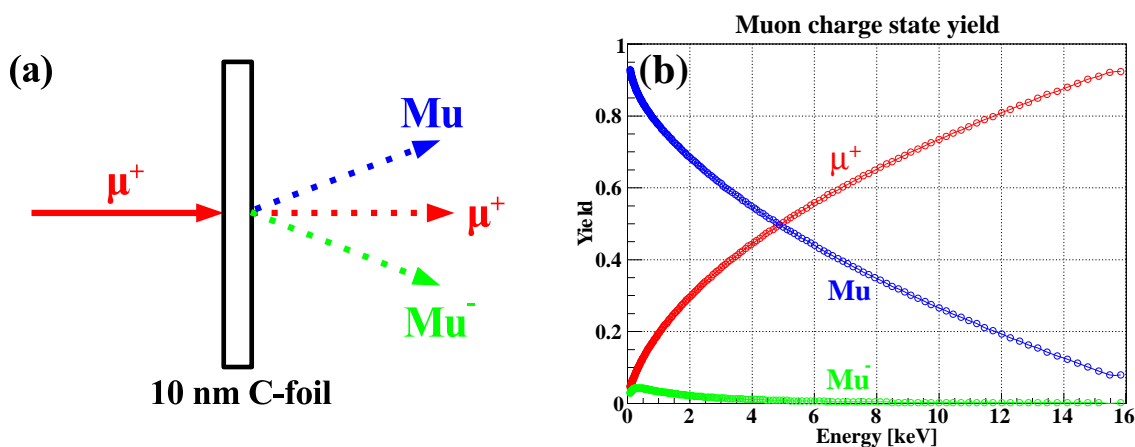
Figure 5.8: *(a) Formation of Mu and Mu$^-$ in the carbon foil due to the charge exchange process. (b)* **The charge state yields of the μ^+ exiting the carbon foil as a function of incoming muon energy at the foil surface***, according to a velocity scaling of the proton data parameterizations [1].*

The current version of Geant4 has a vast amount of libraries for physics processes. However, several low energy processes are still missing and need to be implemented into the simulation code. For example, "fast" Mu generation at the thin carbon foil is implemented by velocity scaling of existing data from proton-carbon foil collisions [1, 80, 110]. These "fast" Mu will be stopped when they reach a material interface. The energy loss of the μ^+ passing through the carbon foil is not correctly generated by the physics library G4MuIonisation for two reasons: first because not all physics processes
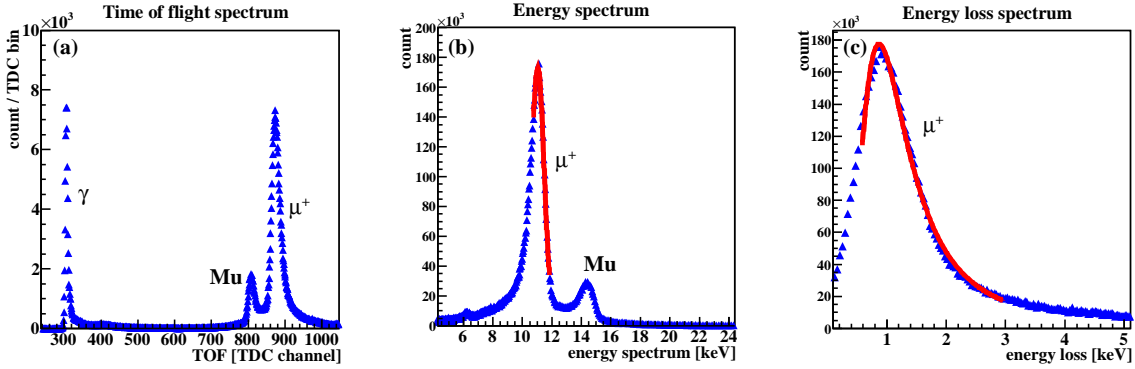
Figure 5.9: *(a) Time of flight distribution of the μ^+ from the start detector to a micro-channel plate detector placed at the sample plate position for 12 kV μ^+ beam transport energy. The peaks are corresponding to the prompt photons, the foil "fast" Mu and the μ^+, respectively. (b) Energy distribution of μ^+ and Mu after passing through the 10 nm carbon foil of the start detector, determined from the time-of-flight spectrum. The μ^+ energy after the moderator was set to 12 keV. (c) Energy loss distribution of μ^+, calculated from the energy spectrum. The energy loss distribution is fitted with a Landau distribution which gives a most probable value of 0.9 keV.*

have been implemented and second because the foil is very thin (tens of carbon layers).

Time-of-flight (TOF) data have been used to measure the energy loss in the thin C-foil and to validate the Geant4 simulations. Before commenting and showing the measured TOF distribution, the various processes occurring in the C-foil have to be introduced. μ^+ crossing the C-foils lose energy due to elastic and ionization processes. Some electrons usually leave the foil together with the μ^+. Additionally the muon can exit the foil at various charge states: μ^+, Mu and Mu$^-$. The yield versus energy for these processes are given in Figure 5.8.

To precisely quantify the energy loss of the μ^+ in the C-foil, TOF distributions between the signals recorded in the start detector and a MCP placed at the sample position (MCP2, see Figure 5.1) have been recorded. Energy of the Mu can be calculated by utilizing the fast Mu formed at the carbon foil which also reaches the MCP2 and from the drift distance $d_{\mathrm{TD-MCP2}}$. Since the energy of the Mu is not affected by the electric fields in the start detector, it is equal to the energy of the Mu or μ^+ coming out from the carbon foil, E_{CFoil}.

A measured TOF spectrum is shown in Figure 5.9. The start signal, which is the time zero of the measurement, is given by a click in the entrance detector usually from electrons ejected by the μ^+ from the C-foil (see Figure 2.3 of start detector). Three

peaks are well distinguishable. They are produced by γ, Mu and μ^+ leaving the C-foil. The γ are the first to reach the MCP2. The last are the μ^+ which have to overcome the negative potential applied at the C-foil. The neutral Mu atoms, on the contrary, do not feel the electrostatic potential and therefore arrive earlier than the μ^+.

From the TOF spectrum, the energy spectrum can be obtained as shown in Figure 5.9(b) as explained in Appendix D. Subtracting from this energy spectrum the energy of the μ^+ prior to the entrance into the C-foil, which is given by the moderator HV, it is possible to deduce the energy losses E_{loss} in the foil itself as shown in Figure 5.9(c).

The measured TOF spectra can be compared with the results of the simulations as shown in Figure 5.10. A good matching has been achieved. However in order to reach this good matching a small fraction of so called "unmoderated muons" have to be included in the simulations. These are muons of slightly higher kinetic energy that are leaving the moderator Ag foil even in the absence of the rare gas solid. The TOF distribution produced by these "unmoderated muons" has been measured and is shown in Figure 5.11. Differently to the situation in Figure 5.10 this measurements has been performed with non-zero voltage at the conical lens. Therefore the distances between the Mu peak and the μ^+ for this unmoderated muons have to be adapted from Figure 5.11 to Figure 5.10. The resulting good agreement between simulation and measurements confirms the validity of the velocity scaling of proton data for the formation of "fast" Mu in the carbon foil.

In order to extract the Mu vacuum yield, it is essential to know very precisely the muon beam size, which can be inferred from the upstream-downstream asymmetry A_{ud}. Hence to study the the beam size at various implantation energies, measurements and simulations of the A_{ud} were performed. Several parameters (whose initial values are summarized in Table 5.1) in the beam line and μSR apparatus that could possibly alter the μ^+ beam size are studied in detail:

- **Implantation energy of the muon beam**

  As the bias on the sample plate increases at lower implantation energy, the beam becomes defocused and reduces A_{ud}. This is confirm experimentally as shown in Figure 5.12 and via simulations given in Figure 5.13(a).

- **Initial phase space of the muon beam**

  Initial phase space (vertex and tilt angle) after the acceleration section of the moderator is taken to be $\sigma_x^{\text{vertex}} = \sigma_y^{\text{vertex}} = 7.5$ mm and $\sigma_x^{\text{tilt}} = \sigma_y^{\text{tilt}} = 2.0°$ from a recent simulation [80]. The initial polarization vector is chosen as $\mathbf{P}_\mu = (0.9848, 0, 0.17365)$ since the μ^+ spin is rotated by 10° clockwise after traversing the
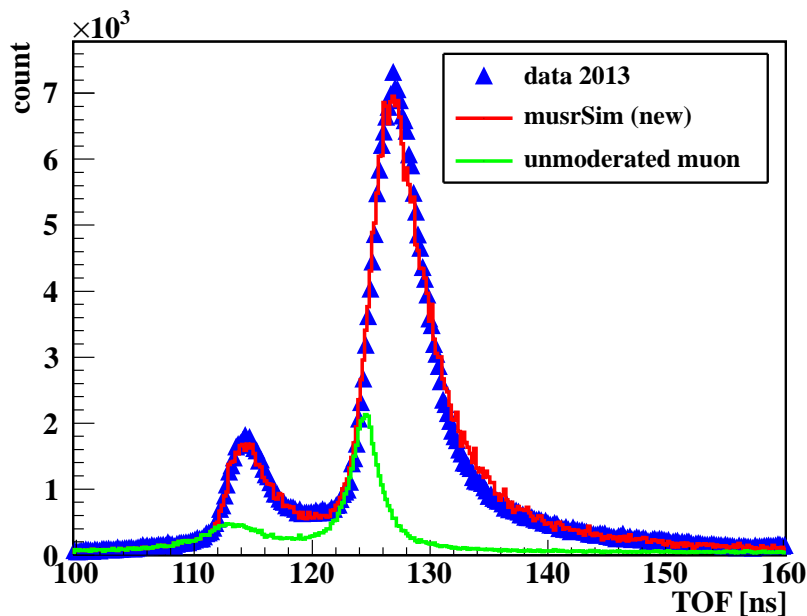
Figure 5.10: *Measured and simulated time-of-flight spectra from the start detector to the sample plate, at 12 keV transport energy and $V_{RA} = 0$ kV and $V_{L3} = 0$ kV. Good agreement is reached when including also the "unmoderated muon" contribution shown in green and the formation of "fast" Mu in the carbon foil.*

Table 5.1: *LEM beam line settings during the experiment and for the Geant4 simulation.*

	High voltage setting (kV)	
	12 kV	15 kV
Moderator	12	15
Einzel lens, L1	7.19	8.99
Mirror	12	15
Spin rotator, SR (E)	2.09	2.29
Spin rotator, SR (B)	62.3 G	69.7 G
Einzel lens, L2	8.38	10.484
Lens, L3	8.99	11.483
Conical lens, RA	9.15	11.9
Sample plate	-2.9 to 10.1	-4.7 to 9.3

70
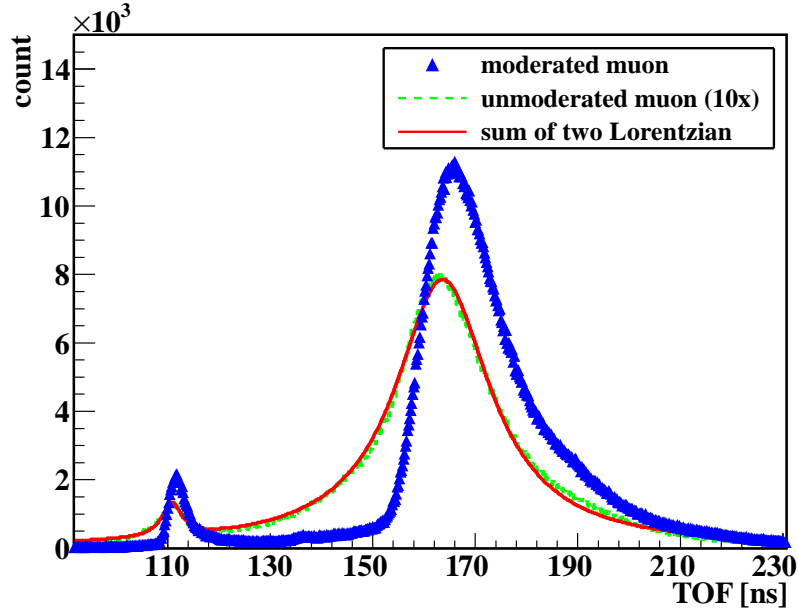
Figure 5.11: *TOF spectra of the unmoderated μ^+ determined from a measurement without solid rare gas deposition. The measured distribution (green) is fitted with the sum of two 2 Lorentzian functions.*

electrostatic separator of the μE4 beam line before entering the LEM instrument. The vertex sigma varied between 5.5 mm and 9.5 mm while the tilt sigma was varied between 0° and 4.0°. The effect of vertex sigma and tilt sigma on A_{ud} are shown in Figure 5.13(b,c). There is no strong dependence of A_{ud} on $\sigma_{x,y}^{\mathrm{vertex}}$ and $\sigma_{x,y}^{\mathrm{tilt}}$ in the simulation. But there should be an effect on the beam transmission: when vertex sigma or tilt sigma is too large the transmission should rapidly decrease.

- **Electric and magnetic field of the spin rotator**

  The magnetic field of the spin rotator was fixed to $B_z = -62.3(-69.7)$ G for 12(15) keV transport energy to obtain the experimental μ^+ spin rotation of 20° counterclockwise. The spin angle with respect to the μE4 beam direction (corresponding to -x direction in the simulation) is then changed from +10° (the angle after the separator in the μE4 beam line) to -10°. The electric field was varied from $E_x = 1.85$ to 2.25 kV/mm and is chosen such that the beam is centered on the original sample plate position (16 mm downstream of the nose sample plate) as shown in Figure 5.14. From Figure 5.13(d), A_{ud} reaches maximum at around 2 kV/mm. This is when the beam is centered on the sample plate and most of the positrons are shielded from the downstream detectors. However, for a fair

71
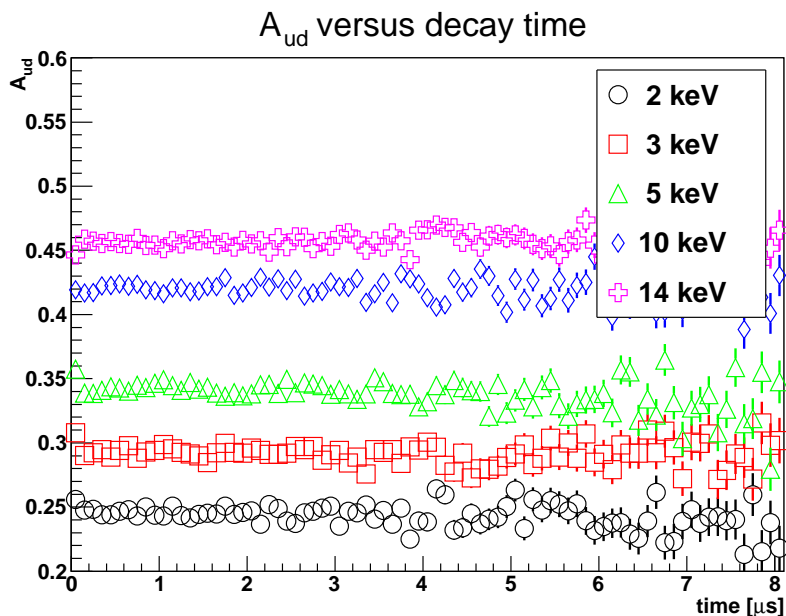
Figure 5.12: A_{ud} *versus μ^+ implantation energy for the measurements with implantation energy from 2 keV to 14 keV. The spectra are flat and are as expected from measurements without Mu emission into vacuum.*

comparison between simulation and measurement, the beam spot is centered on the usual μSR sample position as is in the actual measurement. Hence this is why the value of E_x is 2.09 in Table 5.1.

- **Electric potential of the conical lens (RA)** When the high voltage (HV) is too small or too large, the beam is not properly focused on the sample position. This causes a reduction in the A_{ud}. A comparison with simulation is given in Figure 5.13(e), and is experimentally confirmed.

- **Offset of the sample plate position**

  It is very obvious that there is a strong dependence of the A_{ud} on the offset (in the downstream direction) of the nose sample plate position. Moving the sample plate downstream, in z-direction, will decrease the A_{ud} as the positrons will be less shielded from the downstream detector. The dependence of the A_{ud} on the offset is shown in Figure 5.13(f).
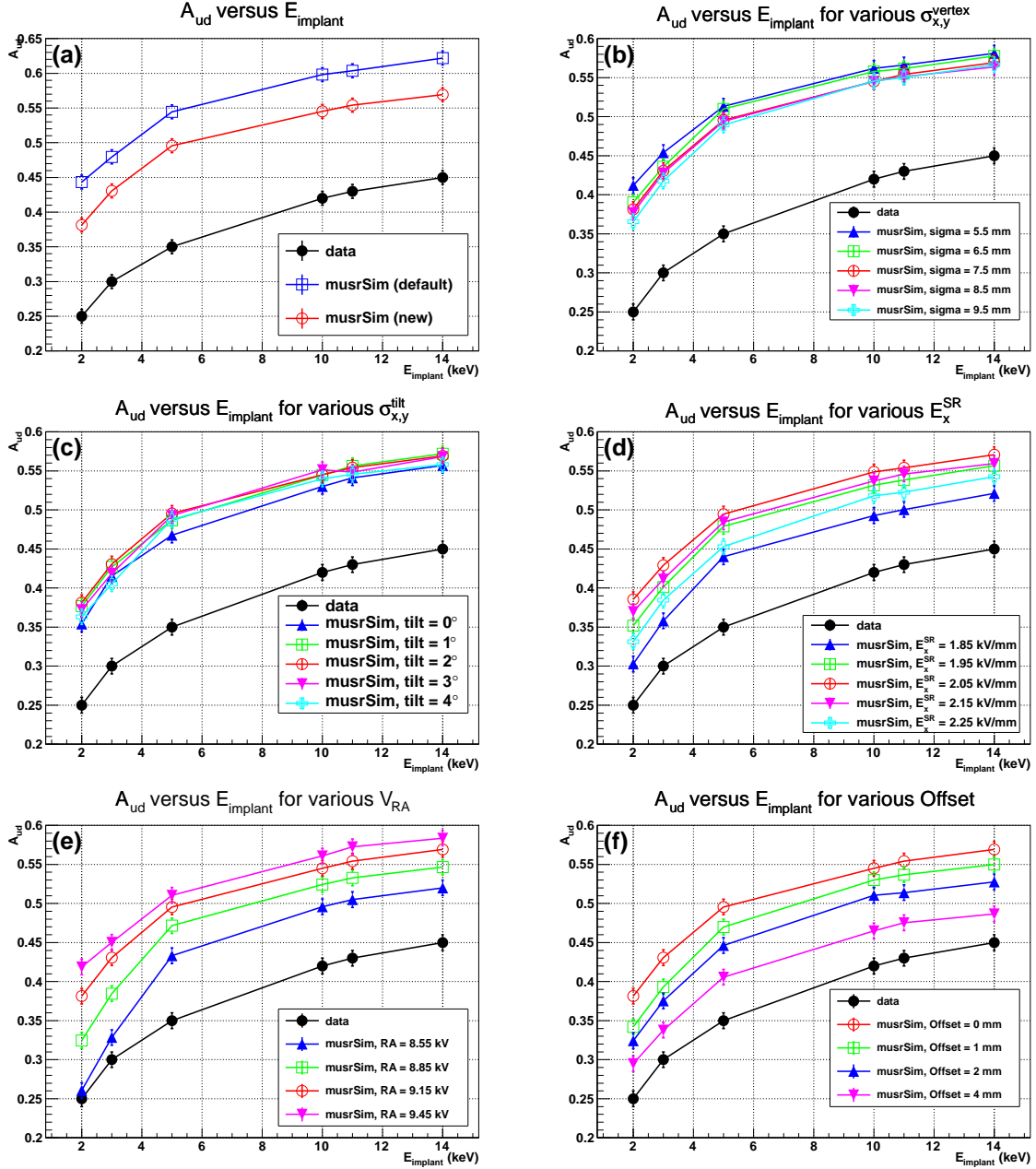
Figure 5.13: A_{ud} *versus* μ^+ *implantation energy for the measurements and the simulations. The discrepancies between the experimental data and the musrSim simulations are reduced after implementing detailed processes explained in the text.*
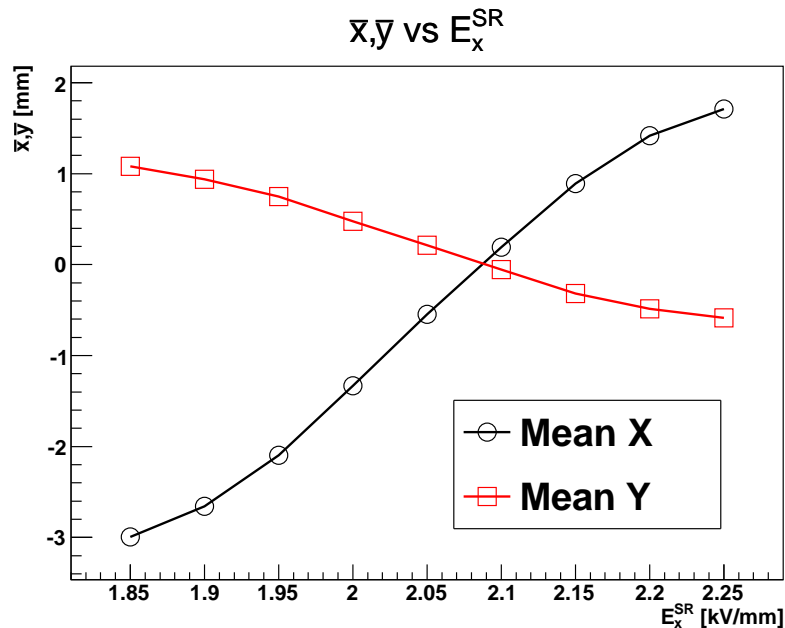
Figure 5.14: *Mean μ^+ beam position ($\overline{x}$,$\overline{y}$) as a function of the E_x^{SR}. The E_x^{SR} value is chosen such that the beam is centered on the original sample plate position (16 mm downstream of the nose sample plate).*

5.5 Sources of discrepancy

After implementing foil Mu formation in the carbon foil of the start detector and introducing Landau energy loss distribution in the carbon foil, the μ^+ and Mu energy spectra on the sample plate at different μ^+ implantation energies were reproduced. However, to explain the discrepancy in the A_{ud} between the experiment and the simulation, several possibilities are discussed in this section.

Unmoderated muons

It has been shown in [82] that about 87% of the incoming surface μ^+ beam is stopped in the 125-μm thick Ag foil where the solid layer of Ar and Ne are deposited on or in the copper frame surrounding it. About 13% of them will go through the moderator as unmoderated μ^+, whereas about 0.01% will be moderated and becomes slow μ^+. The measured and simulated energy spectrum of the unmoderated μ^+ both agree with each other and the fitted mean energy and the width are respectively about 485 keV and 235 keV. Even though a large fraction of them will not be reflected by the electrostatic mirror, they contribute about 10% of the event rate as shown in Figure 5.11.

74

This is because, as visible from Figure 5.11, the unmoderated μ^+ which has energy close to the re-accelerated moderated slow μ^+ (12 keV) can go through the spin rotator and reaches the sample chamber. The event rate of this unmoderated μ^+ is about 10% of the moderated μ^+.

Disagreements in the A_{ud} between the simulations and the measurements are probably coming from the contribution of particles other than the moderated slow μ^+. Unmoderated μ^+ is one of the more likely candidates as they have a larger beam spot (x_{RMS} and y_{RMS}) as shown in Table 5.2 and hence a lower value of A_{ud}.

Table 5.2: *Measured values of the μ^+ beam spot x_{RMS} and y_{RMS} for the unmoderated μ^+ and moderated μ^+. It should be noted that due to the finite size of the active region of the MCP detector (42 mm in diameter) the actual x_{RMS} and y_{RMS} could be larger, especially for the unmoderated μ^+.*

Energy (keV)	Spin rotator	Moderator	x_{RMS} (mm)	y_{RMS} (mm)	μ^+ type
15	No	No	6.1	6.0	unmoderated
15	No	Yes	5.3	4.9	moderated
15	Yes	No	7.2	7.2	unmoderated
15	Yes	Yes	6.2	6.0	moderated

The reason why there was a good agreement between simulation and experiment for the 2011 setup (without SR, $x_{RMS} = 6.1$ mm) is probably because the beam spot for the unmoderated μ^+ was not as large as the one for the 2012 setup (with SR, $x_{RMS} = 7.2$ mm). The ≈ 1.2 mm larger RMS values is sufficient to cause the observed deviation. Indeed, from a recent measurement as shown in Figure 5.15, A_{ud} is smaller for the one without moderator.

Electric and magnetic fields of the spin rotator

Even though the trajectory of the μ^+ with the velocity $v = \frac{E}{B}$ will not be altered when it is traversing the spin rotator, imperfectness of the electric and magnetic fields will cause the μ^+ to deviate from its original path. Such a situation obviously exists in the current LEM setup. The electric field of the SR has to be tuned from its applied value of 2.68 kV/mm to 2.09 kV/mm in order to center the beam on the original sample plate position.
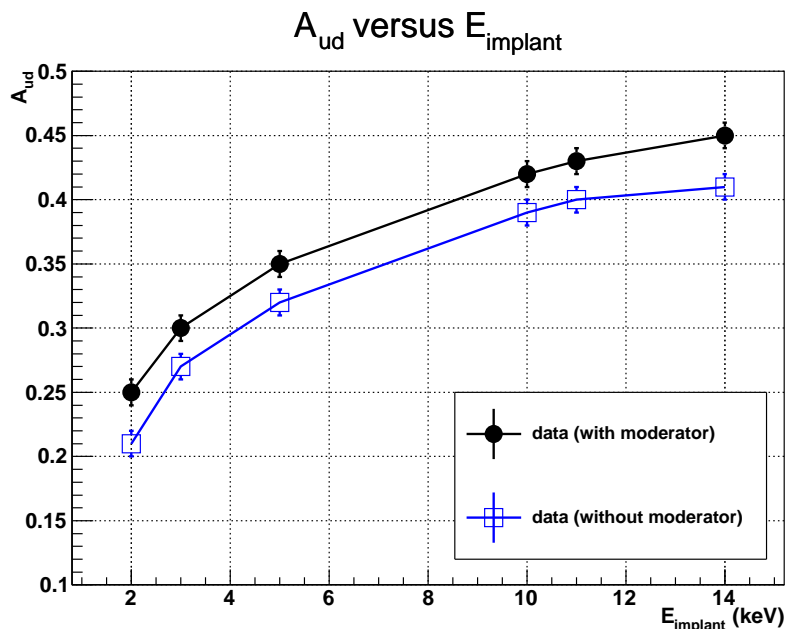
Figure 5.15: A_{ud} *versus* μ^+ *implantation energy for the measurements with moderator and without moderator.* A_{ud} *of the latter is smaller as expected from a larger beam size.*

Scattering of muons on the carbon foil

Scattering of μ^+ on the carbon foil is simulated using G4MuMultipleScattering of the Geant4 package. Even though the agreement in terms of transmission was shown in [118], the distribution of the scattering angle can not be measured experimentally and a larger uncertainty is expected due to the inhomogeneity of the density of the thin carbon foil.

Conclusion

The accuracy of the simulation of the new LEM beam line and μSR spectrometer is improved by including several processes such as Mu formation in the carbon foil and the Landau energy loss distribution into the musrSim package. The time of flight spectra are reproduced to very high accuracy. Disagreement between simulation and experiment in the A_{ud} is mainly due to the unmoderated μ^+ which has a larger beam spot, although the uncertainty in the spin rotator field map and the uncertainty in the scattering angle of the μ^+ in the thin carbon foil also contributes.

Extraction of precise values of the Mu emission into vacuum is not possible due to

uncertainties related with the muon beam size at the sample plate, especially for low implantation energies. However the detailed investigation have lead to implementation and understanding of the various processes and energy losses occurring in the thin C-foil.

Moreover, a large fraction of polarized Mu was observed using μSR technique, indicating that the samples investigated in 2012 could have even a better performance than the sample of 2011 in term of Mu yield in vacuum.

Chapter 6

Confinement of muonium for the 1S-2S transition frequency measurement

As summarized at the end of Chapter 4, a sizable fraction of thermalized Mu is emitted into vacuum from mesoporous thin SiO_2 films per implanted μ^+. At 250 K the Mu vacuum yield is 0.38(4) and at 100 K it is 0.20(4). The high Mu vacuum yield, even at low temperatures, is an important step towards a more precise measurement of the Mu 1S-2S transition frequency planned at PSI. Such a source of cold Mu opens the possibility of performing continuous wave (CW) laser spectroscopy of this transition. This decreases both statistical and systematical uncertainties compared to the previous measurement [31] as the power broadening and residual first order Doppler shift related to pulsed laser spectroscopy could be eliminated. Utilizing a μ^+ beam similar to the one used for the μSR and PST measurements described in this thesis, an improvement of about an order of magnitude can be achieved. This will provide a stringent test of bound-state QED, the best verification of charge equality in the first two generations of particles and the best determination of the muon mass. The next generation Mu spectroscopy experiment will make use of this improved Mu production from mesoporous materials studied in this thesis, and also gives rise to the possibility of confining Mu in a hollow cylinder.

6.1   Principle of the muonium confinement

The principle of the Mu confinement in a hollow cylinder is sketched in Figure 6.1. Low energy μ^+ cross a SiN entrance window and finally stop in the mesoporous thin-film.
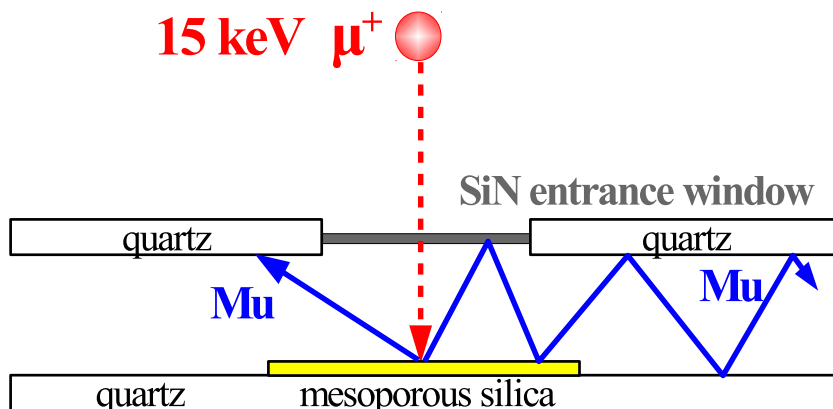
Figure 6.1: *Confinement of Mu inside a hollow volume with inner walls made of quartz. After crossing the thin SiN entrance window the μ^+ stop in the mesoporous SiO_2 thin film. Mu exiting the thin film into the vacuum are confined because of reflections at the SiN and quartz walls.*

TrimSP simulations show that about 96% of the μ^+ with initial energy of 15 keV are transmitted through a 50 nm SiN window with a mean energy of 4.1 keV (0.9 keV RMS) and implanted in the mesoporous silica. The formed Mu atoms then drift to the thin-film surface, emitted into vacuum and move freely in vacuum till they hit the walls surrounding the target. These walls are made of SiO_2 (quartz) which has a negative work function for Mu. Hence, Mu reflection at the walls occur in the same way as during the drift through the network of pores in the mesoporous silica target. When reflected they bounce back into the free space towards the laser beam which is positioned along the axis of the cylinder. Therefore, the reflections at the target walls increase the number of Mu atoms crossing the laser beam. The probability to laser excite a Mu atom is substantially increased leading to an improvement in signal rate by about one order of magnitude.

Another merit of using this kind of configuration is that a smaller beam size of μ^+ hitting the Mu production target can be achieved. As mentioned previously in Chapter 4 and Appendix C, a higher μ^+ implantation energy corresponds to a smaller μ^+ beam size on the sample plate position. By removing the start detector which consists of a thin carbon foil to reduce the scattering effect (one could instead use the secondary electrons coming from μ^+ hitting the SiN window for this purpose like in [123]) and increasing the bias voltage applied on the moderator substrate to achieve higher transportation energy, a μ^+ beam size of less than 8 mm can be realized for an implantation energy of 20-30 keV. The final μ^+ implantation energy on the mesoporous silica sample can be
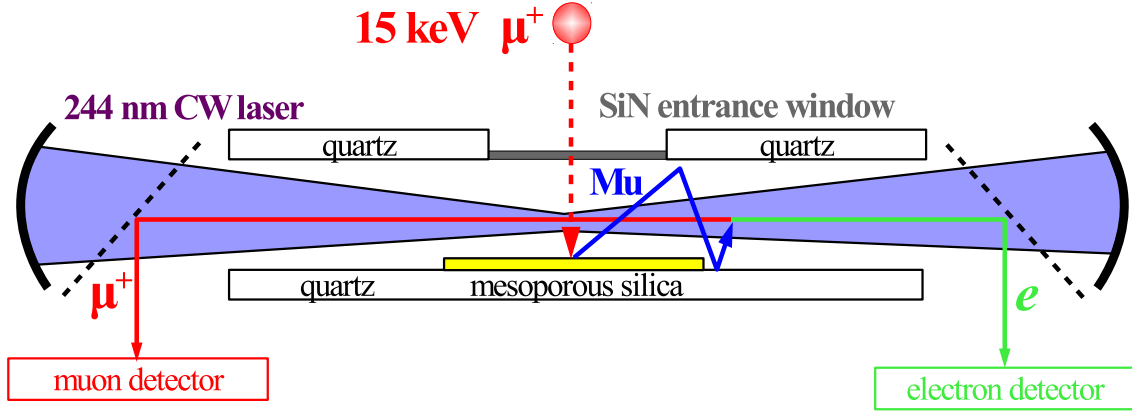
Figure 6.2: *The Mu emitted into vacuum from the mesoporous thin film are confined inside a hollow volume. In this way the probability to cross the laser beam before muon decay occurs is substantially improved. An enhancement cavity is used to guarantee Doppler-free excitation of the 1S-2S transition. The same laser beam is used to ionize the 2S-state. The charged particles are then transported to the corresponding particle detectors using electrostatic or pulsed electric fields.*

tuned using SiN entrance windows of different thickness.

Next generation measurement of Mu 1S-2S transition frequency

Figure 6.2 depicts a possible schematic setup for the 1S-2S spectroscopy experiment of Mu. The muon beam from a low energy beam line crosses the entrance window and is stopped in the mesoporous thin-film where Mu is formed and ejected into vacuum. Transversally to the muon direction there is a cw laser beam with a wavelength of 244 nm exciting the Doppler-free two-photon transitions from the 1S to the 2S state. The laser that is being used for the Ps spectroscopy [123] will be upgraded with an commercially available second harmonic generation (SHG) stage to deliver 100 mW at 244 nm [124]. A build up cavity will be used in order to get a circulating power of the order of 5-8 W. Such an enhancement factor of 50-80 is achievable with current available mirrors [125].

The Mu atoms crossing the laser beam either come directly from the Mu production target or after reflection at the walls surrounding the target. If the laser frequency is resonant with the 1S-2S transition, the Mu atom can be excited from the ground state to the metastable 2S-state. To determine the number of atoms which have been excited into the 2S-state the idea is to ionize the 2S-state atoms. This may be achieved either

using a second laser beam tuned to be resonant with the 2S-to-continuum transition or to use the same 244 nm laser beam which was used to excite the 1S-2S transition. If the 2S-state is ionized, the Mu atom dissolves leaving a free electron and a free μ^+ which can be detected after acceleration and transport to the corresponding particle detectors. A resonance curve is obtained by plotting the number of μ^+ detected in time coincidence with an electron versus the laser frequency.

The optimization of μ^+ to Mu conversion from mesoporous silica and the possibility to confine Mu are essential to improve the accuracy of the Mu 1S-2S transition measurement because of the low estimated signal rate which is of the order of only one event/h (including the "confinement" factor).

6.2 Setup to test muonium confinement
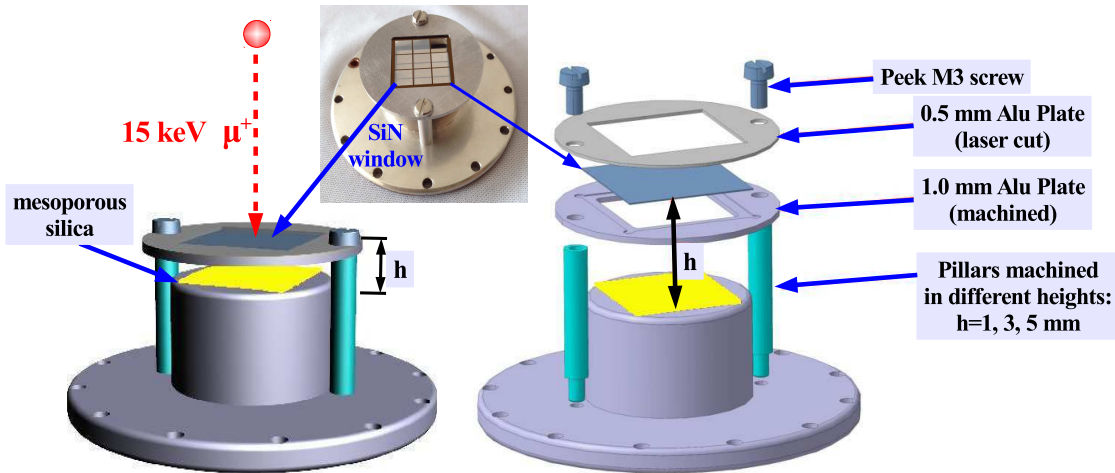
Figure 6.3: *(Left) Schematic view of the SiN membrane support and the nose sample plate for testing Mu confinement. The SiN membrane is held by two aluminum thin plates of 0.5 mm and 1.0 mm in thickness. (Right) Blow-up view of the SiN membrane support. Pillars of various heights enable studies of confinement between mesoporous silica and SiN membrane for various distances (h = 1, 3, 5 mm). (Inset) Picture of the SiN membrane mounted on the nose sample plate.*

The ability to confine the formed Mu atoms in a hollow volume is an essential requirement for next generation Mu spectroscopy. To test that Mu atoms are really confined

and reflected at the walls, a measurement was performed at the LEM beam line of the μE4 area at PSI. A setup as sketched in Figure 6.3(Left) was used to demonstrate the effect of Mu reflecting between the walls. This effect can be investigated by studying the time spectra of the downstream detectors using PST explained in Chapter 4.

Two aluminum thin plates of 0.5 mm and 1.0 mm are sandwiching a 3×3 array of 50 nm-thick 5.6×5.6 mm^2 SiN membranes (Silson, Blisworth, U.K.) that have 0.2 mm support ribs (see Figure 6.3(Inset)). This gives a SiN membrane with overall area of 17.6×17.6 mm^2 and an average transmission of $> 80\%$. The membrane is installed in front of the mesoporous SiO$_2$ thin-film, which is glued to the nose sample plate. Pillars with different heights are used to vary the distance between mesoporous silica and SiN window as shown in Figure 6.3(Right). This membrane was cooled with a cryocooler down to 4 K without any observable mechanical damage.

The produced Mu atoms will be emitted into the vacuum space between the mesoporous material and the SiN entrance window. If reflections at the walls occur while bouncing, the Mu atoms will diffuse from the center of the setup in radial direction. Therefore with increasing time, they will approach the scintillators which are surrounding the sample plate. The scintillators are used to detect the positrons from muon decays. The positrons emitted by Mu that have moved a large distance radially have a considerable larger probability to reach the downstream positron detector. This is due to the reduced shielding by the nose sample plate made of Cu which is illustrated in Figure 6.4(a). Therefore, if Mu reflection and diffusion occurs, the time spectra of the downstream detector are distorted as a consequence of the position-dependent detection probability reflecting the space evolution of Mu as shown in Figure 6.4(b). These are the typical PST time spectra discussed in Chapter 4.

In order to better visualize the effects of Mu atoms emitted into vacuum and reflecting between the SiN window and the mesoporous SiO$_2$, the Geant4 simulated positron time spectra is divided by e^{-t/τ_μ} to eliminate the muon lifetime effect as shown in Figure 6.4(c). Such "normalized" time spectra can be interpreted as the time evolution of the detection efficiency of the positron detector. For μ^+ or Mu stationary on the sample plate, the detection efficiency of the decay positron as seen from the downstream detector remains unchanged at any instance. Hence a straight horizontal line is expected (black histogram). For Mu emission into vacuum without SiN entrance window, an increase in the "normalized" spectra is expected due to the larger detection probability (red histogram). For simplicity, this "normalized" time spectra will be denoted as time spectra from here onwards.

When a SiN window is installed, the time evolution is more complicated. First, Mu propagate freely till it reaches the SiN wall. Thus the time spectra at the beginning are "identical" with the histograms computed without SiN wall (red histogram). But
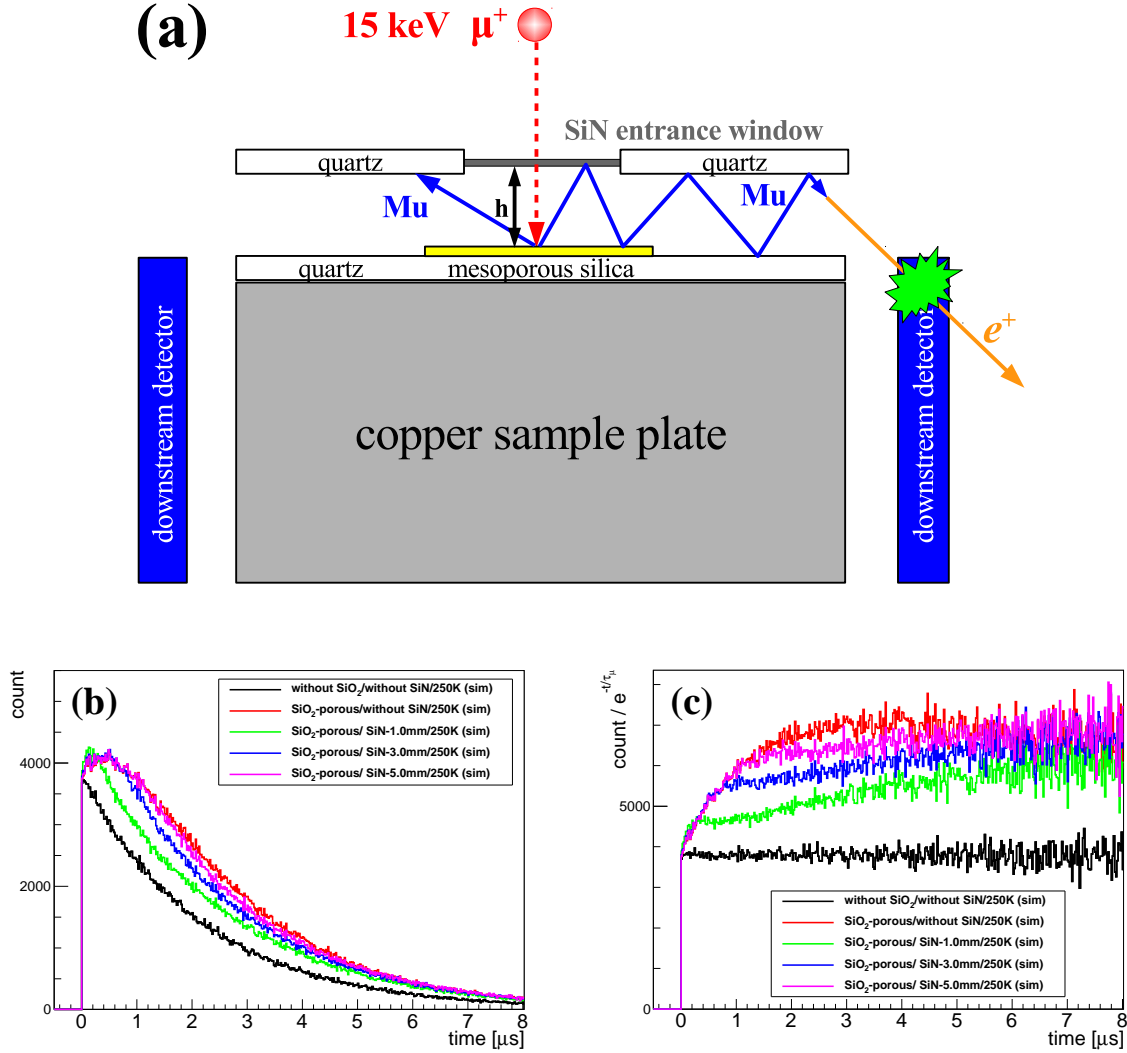
Figure 6.4: *(a) Confinement of Mu in between the SiN entrance window and the mesoporous SiO_2 thin film. After crossing the thin SiN entrance window the μ^+ stop in the mesoporous SiO_2 thin film. Mu emitted into vacuum are confined because of reflections at the SiN and quartz. The reflection probability can be investigated by studying the time spectra of the downstream detectors. (b) Time spectra of the downstream detectors simulated with Geant4 for various separations h between the SiN entrance window and the mesoporous SiO_2 thin film. (c) "Normalized" time spectra. Same time spectra as in (b) but with cancellation of the muon-decay related effects.*

when the SiN wall is reached, this increase in the detection probability stops because the Mu are either adsorbed at the wall or back-reflected. Back-reflection causes the Mu to radially drift towards the surrounding positron detectors. The slow increase of the time spectra at late time is related with this slow diffusion. The various curves in Figure 6.4(c) have been simulated for various distances between the mesoporous silica and the SiN window. The time when the Mu hits the SiN window is visible in the time spectra and increases, as expected, with the distance. This time also depends on the sample temperature as will be discussed later.

6.3   Does muonium stick at the SiN wall? (Preliminary)

The positron time spectra of the downstream detectors for measurements done at $h = 1$ mm separation and various temperatures are shown in Figure 6.5(a). For comparison, the simulated time spectra are shown in Figure 6.5(b). As was reported in Section 4.3 and visible in Figure 4.6, Mu emission into vacuum increases with temperature. The time spectra of Figure 6.5(a) for times $t \in [0; 0.5]$ μs show a fast increase till a "plateau". This "plateau" level is proportional to the Mu emission into vacuum F_{Mu}^{vac}, whereas the slopes depend on the kinetic energy distribution of the emitted Mu, therefore on the sample temperature. For later times $t \in [1; 8]$ μs, the histograms show slow increases due to radial diffusion of the Mu atoms. The slopes of these increases depend not only on the Mu kinetic energy distribution but also on the type of reflection (specular, isotropic etc.) and on the reflection probability. Thus the slope at delayed times contains information on the reflection probability R. For the 20 K simulation it is assumed that Mu do not diffuse out of the sample and hence the time distribution is flat. This assumption, based on results from Figure 4.6, has been confirmed by the measured time spectra (black histogram) in Figure 6.5(a). If Mu adsorption to the SiN window occurs, the spectra becomes flat after 0.5 μs, whereas for the reflection scenario, the histogram is still increasing gradually. The data down to temperature of 100 K clearly indicate Mu bouncing between the two walls and thus the feasibility of confinement.

The positron time spectra of the downstream detectors for measurements performed at $h = 5$ mm separation are shown in Figure 6.5(c). For comparison, the simulated time spectra are shown in Figure 6.5(d). As seen in the figures the larger separation is causing larger "plateau" levels (the shadowing effects of the mechanics decreases with distance) and longer times before the "plateau" is reached as expected.

The simulations start with the Mu emission from the mesoporous sample with the vacuum yield F_{Mu}^{vac} of Figure 4.6, with a $\cos\theta$ angular distribution and a Maxwell-Boltzmann
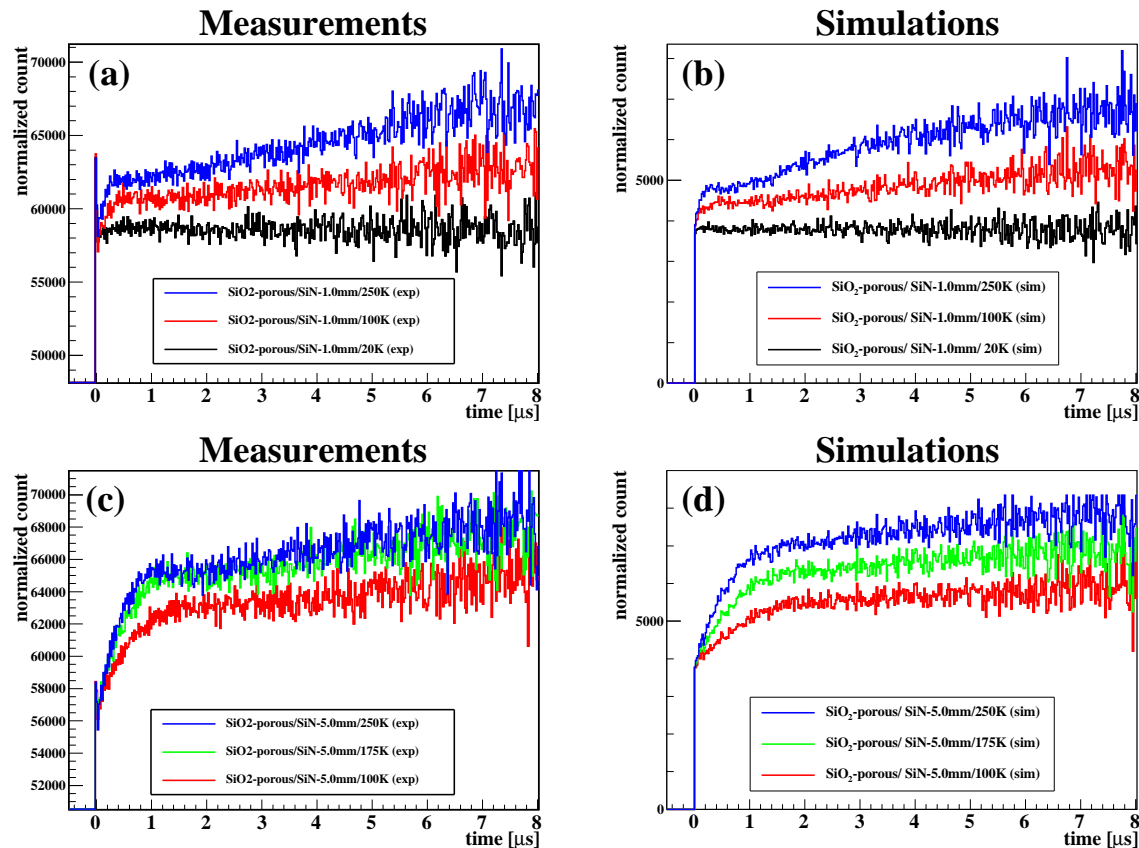
Figure 6.5: *(a) Measured time spectra at $T = 20$, 100 and 250 K for a SiN window height of 1 mm (a) and of 5 mm (c). The corresponding simulated time spectra are shown in (b) and (d), respectively. The time spectra are divided by a factor of e^{-t/τ_μ}.*

kinetic energy distribution according to the sample temperature. For the reflection at the walls, a Knudsen reflection from a rough surface is assumed. A reflectivity of 100% is assumed for T=250 K, 175 K and 100 K and 0% at 20 K far the values reported in the table.

The measured flat background level significantly depends on the height h in as much as a non-negligible fraction of the μ^+ beam stops in the SiN windows holder and the positron detection efficiency strongly depends on the height h. Thus a precise comparison between measurements and simulation requires precise knowledge of the μ^+ beam and precise knowledge of the relative positioning between sample holder and positron detectors, including effects related with the thermal contraction of the sample mount.

However a simple estimate of the reflection probability can be evinced from the slope

Table 6.1: *Summary of the gradients extract from the time spectra. a_0 and a_1 are the coefficients of the fit function $f(t) = a_0 + a_1t$, and $r_a = a_1(T)/a_1(250 \text{ K})$. In the simulation it is assumed 100% reflectivity except at $T = 20$ K where 0% reflection probability was assumed.*

Fit parameters	Measurements			Simulations		
	a_0	a_1	r_a	a_0	a_1	r_a
SiN-1.0mm/250K	61113(68)	837(16)	1	4983(20)	266(5)	1
SiN-1.0mm/100K	60168(67)	363(15)	0.43(2)	4309(18)	143(4)	0.54(2)
SiN-1.0mm/20K	58497(70)	19(18)	0.02(2)	3797(16)	-3(4)	-0.01(2)
SiN-5.0mm/250K	64134(75)	614(18)	1	6759(22)	162(5)	1
SiN-5.0mm/175K	63724(65)	542(15)	0.88(4)	6053(23)	127(6)	0.78(4)
SiN-5.0mm/100K	62319(64)	322(16)	0.52(3)	5351(20)	74(5)	0.46(3)

of the time spectra at late times. The measured and simulated time spectra are fitted from $t = 2$ μs to $t = 6$ μs with the fit function $f(t) = a_0 + a_1t$. The results are summarized in Table 6.1. The ratio

$$r_a = \frac{a_1(T)}{a_1(250 \text{ K})} \tag{6.1}$$

can be used to match simulations with data and to extract the Mu reflection probability. This ratio does not depend on the above mentioned complications related with the flat background level, but depends only on the physics occurring in the confinement volume. A ratio $r_a^{\text{exp}} < r_a^{\text{sim}}$ indicates that there is additional Mu adsorption at the walls compared to the 250 K case. From Table 6.1, it can be seen that at $h = 1$ mm, $r_a^{\text{exp}} < r_a^{\text{sim}}$ but at $h = 5$ mm, $r_a^{\text{exp}} > r_a^{\text{sim}}$. Considering the 10% uncertainties in the $F_{\text{Mu}}^{\text{vac}}$ assumed in the simulation and a very primitive analysis method (slope comparison), it can be concluded that the reflection effect is significant and the Mu confinement is feasible. The observed reflectivity is compatible with 100% within 20% of accuracy.

The demonstration of Mu reflection from SiN wall can also be done by using a qualitative comparison between measured and simulated time spectra as shown in Figure 6.6 and Figure 6.7. In Figure 6.6(a) where $h = 1$ mm and $T = 250$ K, the scenarios of 100% reflectivity (reflection) and 0% reflectivity (adsorption) are simulated. It is expected that in the scenario of adsorption, once the Mu is sticking to the SiN wall, there will be no change in the detection efficiency of the downstream detector. Hence the time spectra will reach a "plateau" as soon as the Mu is reaching the SiN wall. However in the measured time spectra of Figure 6.6(b), such effect, has not been observed and
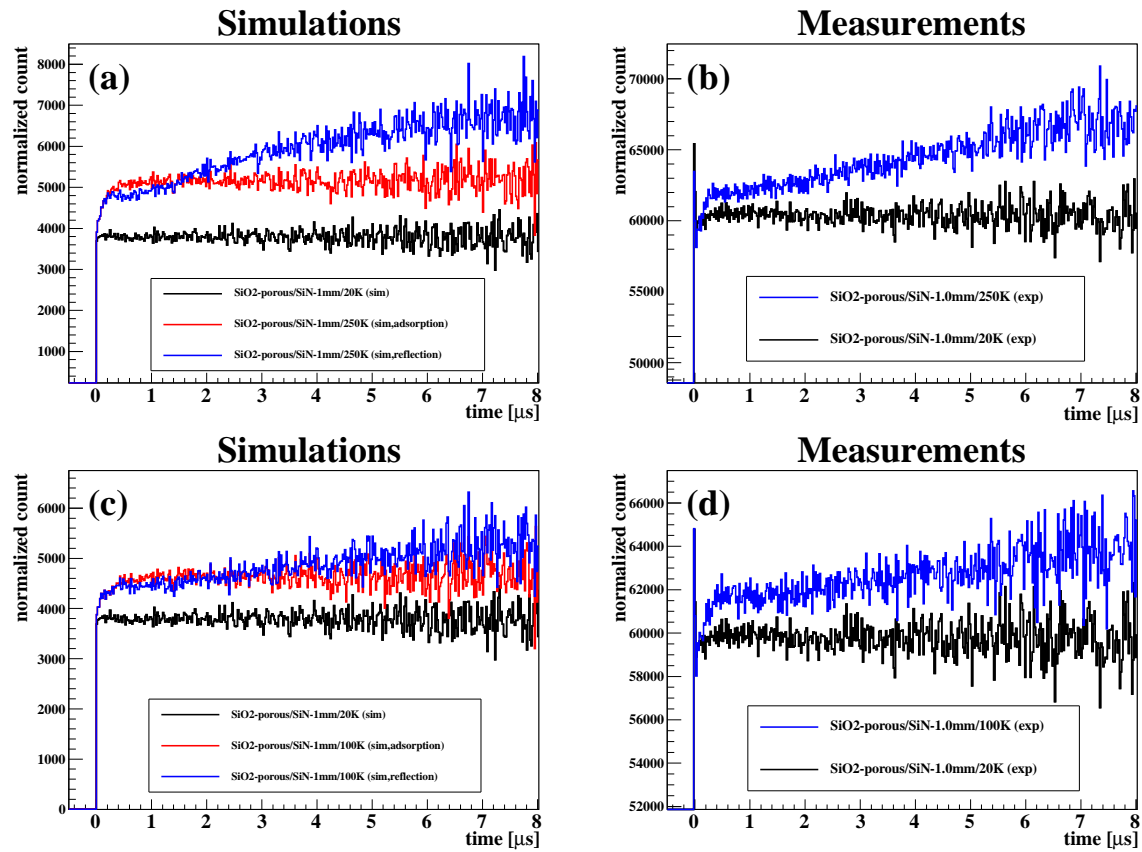
Figure 6.6: *Simulated (a+c) and measured (b+d) time spectra for reflection and sticking scenarios, $h = 1$ mm and various temperatures. The time spectra are divided by a factor of e^{-t/τ_μ}.*
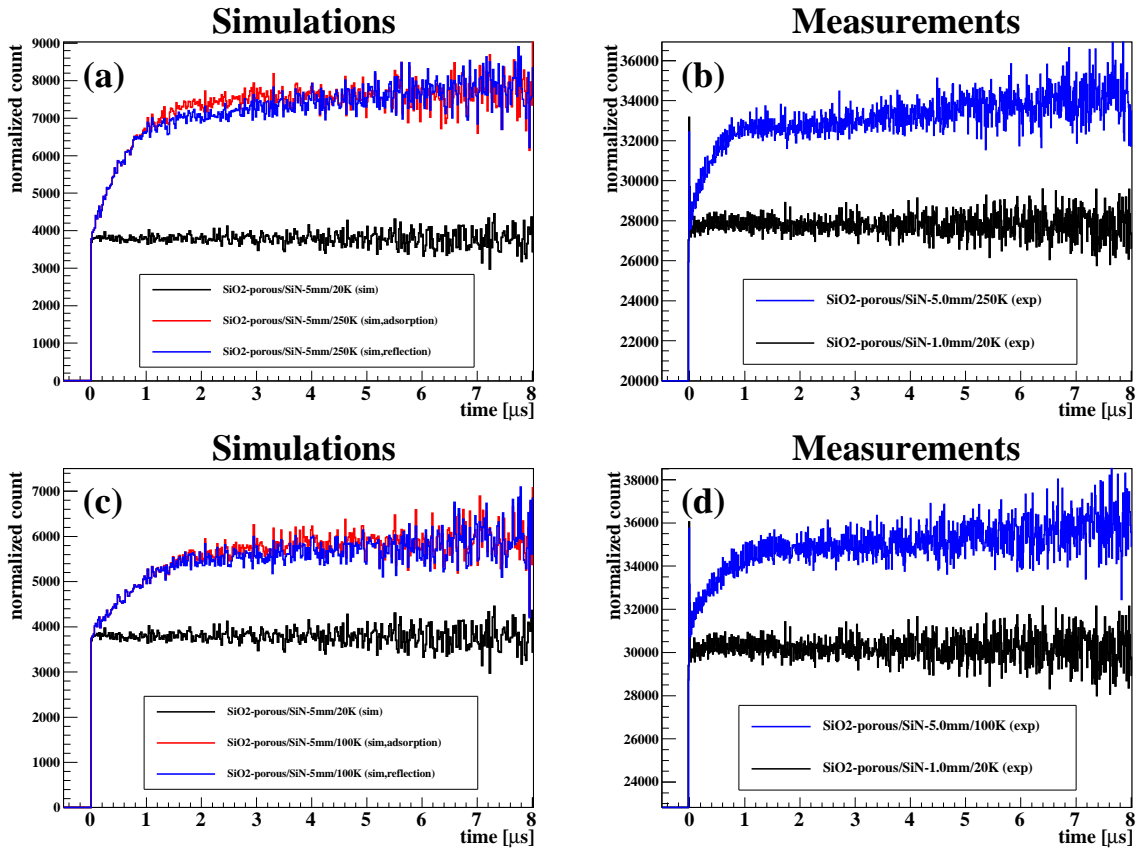
Figure 6.7: *Simulated (a+c) and measured (b+d) time spectra for reflection and sticking scenarios, $h = 5$ mm and various temperatures. The time spectra are divided by a factor of e^{-t/τ_μ}.*

hence again validating the claim that the reflection effect is very significant. It is very clear that the Mu atoms are bouncing between top and bottom plates even at cold temperatures and thus confinement can be realized. In addition to this second method, there is also another way to distinguish between the reflection and adsorption scenario. This method, called the "two-frequency method", is explained in next section.

6.4   Two-frequency method

Adsorption of the muonium atoms on the surface can be observed via the frequency shift of the Mu hyperfine splitting (HFS) [126]. If Mu atoms are adsorbed to the surface of a material, this implies a bond between the atoms and the surface mediated by a surface electric field. Such an electric field mixes the s- and the p-waves of the atom. Thus the HFS is reduced as the overlapping of the e^- wave function with the μ^+ is reduced. Such a distortion in the hyperfine interaction causes the μ^+ spin precession in the Mu bound at the surface to be different from the precession of the free Mu.

   Measurements were performed in transverse magnetic field of 33 G. The HFS for isotropic Mu can be expressed in terms of the Mu triplet frequencies ν_{12} and ν_{23} (two-frequency method [127]) and the muon Larmor precession frequency ν_μ by [112, 128]

$$\nu_0 = \frac{1}{2}\left[\frac{(\nu_{12} + \nu_{23} + 2\nu_\mu)^2}{\nu_{23} - \nu_{12}} + \nu_{12} - \nu_{23}\right] \ . \tag{6.2}$$

A derivation of this equation is given in Appendix A.6. In vacuum, the HFS is $\nu_0 = $ 4464 MHz. The splitting of the ν_{12} and ν_{23} lines at 33 G for a fused quartz sample shown in Figure 6.9(a) yields $\nu_0 = 4531(173)$ MHz, in agreement with the value obtained in [55] of $\nu_0 = 4509(3)$ MHz. This value is slightly higher than the one in vacuum due to the "compression" of the Mu atom in the crystalline environment. Due to the limited statistical accuracy, unfortunately it is not possible to distinguish Mu embedded in a crystalline quartz from a free Mu. However the taken data is analyzed with this "two-frequency method" because Mu adsorbed at the surface may feel a stronger and asymmetric field that causes an observable shift of the HFS.

   The frequency $\nu_{12}(B)$ and $\nu_{23}(B)$ are functions of the magnetic field and are given by the Breit-Rabi equation explained in Appendix A. For small magnetic fields this two frequencies reduces to the $\nu_{\text{Mu}} = \nu_e/2$ as described by Equations A.58 and A.61. With increasing magnetic field a splitting of the two frequencies occurs. For small magnetic field the Mu precession frequency can be approximated by an average value of $\nu_{12}(B)$ and $\nu_{23}(B)$ but for larger fields both components need to be considered separately. To fit the time spectra of the measurements which have been conducted at 33 G, the following

asymmetry function was used

$$A(t) = A_\mu(t) + A_{\mathrm{Mu}}^{12}(t) + A_{\mathrm{Mu}}^{23}(t) \tag{6.3}$$

where both Mu precession frequencies with amplitude $A_{\mathrm{Mu}}(\nu_{12})$ and $A_{\mathrm{Mu}}(\nu_{23})$ have been accounted for. A typical fit for two different time scales is shown in Figure 6.8. Fitting the μSR time spectra with Equation 6.3 yields the frequencies ν_{12} and ν_{23} which are needed to determine the HFS via Equation 6.2.
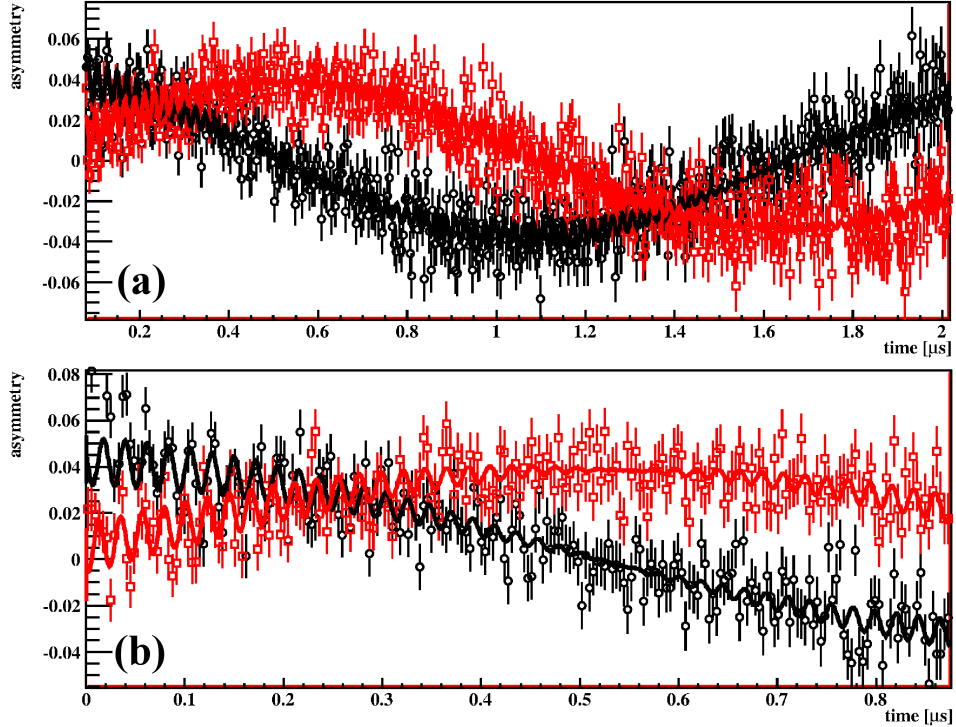
Figure 6.8: *A typical asymmetry spectra for a 33 G μSR measurement. (a) For a longer time scale, the slowly varying μ^+ spin precession is visible. (b) For a shorter time scale, the "beat" of the two Mu precession frequencies ν_{12} and ν_{23} are visible.*

To cross check the correctness of the fitted ν_{12} and ν_{23} values, the power spectrum of the Fast Fourier Transform (FFT) of the time distribution is considered. Typical power spectra in the region of interest are shown in Figure 6.9. The dots arise from a Fourier transform of the measured data, whereas the solid lines arises from the Fourier transform of the function $A(t)$ fitted to the time spectrum. It has to be stressed that the solid line do not represent a fit to the power spectrum. But in the resonances region strong

91
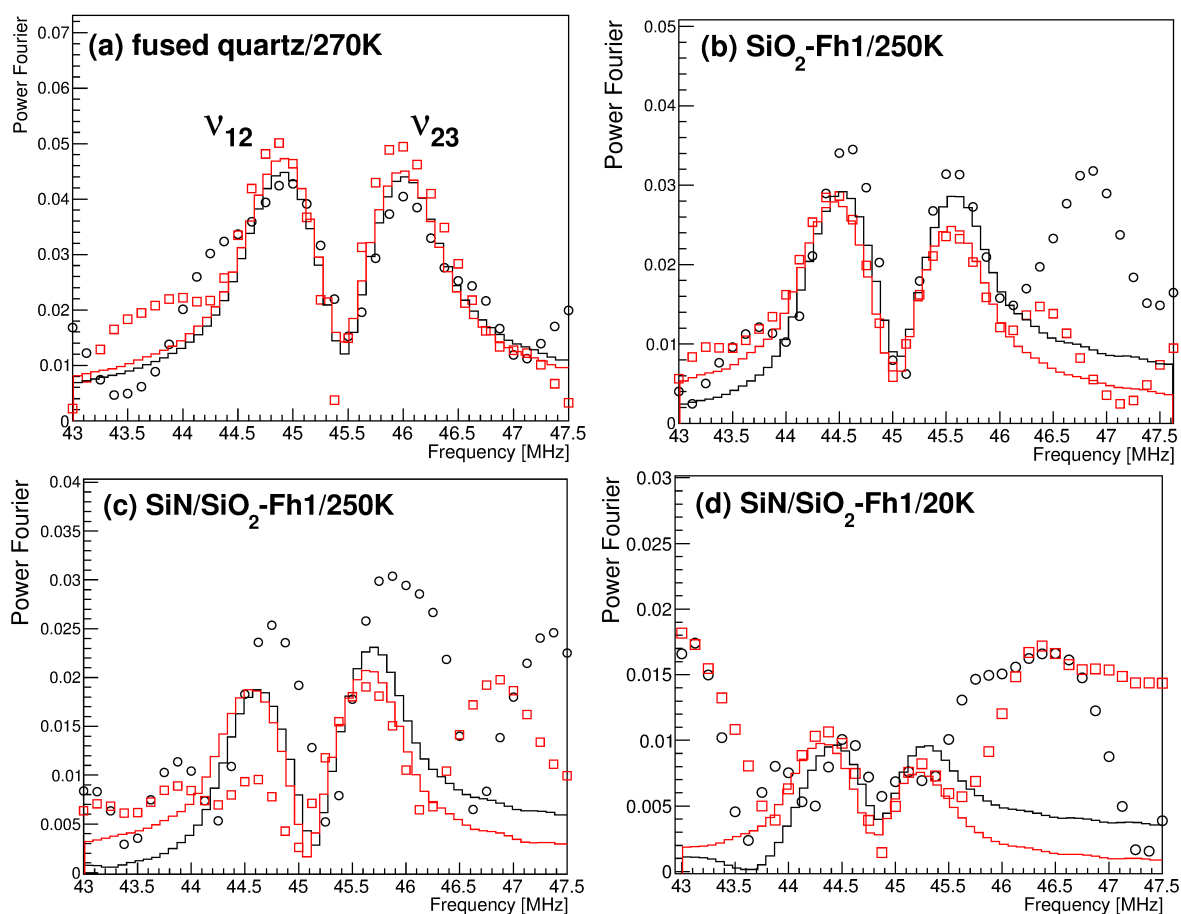
Figure 6.9: *The splitting of the ν_{12} and ν_{23} lines at 33 G for (a) a fused quartz sample at $T = 270$ K, (b) a mesoporous silica (Fh1) sample at $T = 250$ K, (c) a mesoporous silica (Fh1) sample with Si_3N_4 window at $T = 250$ K and (d) a mesoporous silica (Fh1) sample at $T = 20$ K. The solid lines do not represents fits. They are obtained from the Fourier transform of the asymmetry fit to their respective time spectra.*

Table 6.2: *Summary of the measurements of the Mu HFS ν_0. At 100 K, the ν_0 value for the SiO_2 porous with SiN window is in agreement with the one of SiO_2 porous, implying that no extra surface interaction is happening with the configuration with a SiN entrance window. The vacuum value of ν_0 is 4463 MHz.*

Configuration	T [K]	ν_{12} [MHz]	ν_{23} [MHz]	B [G]	ν_0 [MHz]
Fused quartz	270	44.974(23)	45.903(27)	32.411(98)	4531(173)
SiO_2 porous	100	44.620(13)	45.535(30)	32.538(57)	4528(160)
SiO_2 porous	175	44.567(29)	45.502(27)	32.534(57)	4423(188)
SiO_2 porous	250	44.531(24)	45.466(22)	32.501(45)	4415(154)
SiO_2 porous/SiN-5mm	100	44.749(17)	45.685(56)	32.386(72)	4454(274)
SiO_2 porous/SiN-5mm	175	44.702(20)	45.625(15)	32.536(69)	4506(123)
SiO_2 porous/SiN-5mm	250	44.553(31)	45.519(21)	32.455(69)	4281(167)
SiO_2 porous/SiN-1mm	20	44.384(32)	46.019(57)	32.612(73)	2548(188)
SiO_2 porous/SiN-1mm	100	44.787(31)	45.708(22)	32.588(68)	4533(100)
SiO_2 porous/SiN-1mm	250	44.636(15)	45.587(15)	32.440(65)	4363(97)
SiO_2 porous/SiN-1mm-SiO_2	100	44.760(23)	45.680(11)	32.557(69)	4532(544)
SiO_2 porous/SiN-1mm-SiO_2	175	44.732(22)	45.684(20)	32.526(60)	4377(137)
SiO_2 porous/SiN-1mm-SiO_2	250	44.586(19)	45.501(20)	32.490(55)	4521(136)

correlation between data and solid lines should be visible. The fitted ν_{12} and ν_{23} values are summarized in Table 6.2 and the dependence of ν_0 on the temperature for various configurations are plotted in Figure 6.10. The measured values are in agreement with the vacuum value. More statistics are needed to investigate the effect of Mu adsorption on the SiN surface. The only exception is represented by the 20 K measurement which shows a very strong shift of the HFS. This has to be ascribed to Mu sticking at the pore walls of the mesoporous material as no emission into vacuum has been observed. The power spectrum at 20 K is shown in Figure 6.9(d). Due to strong depolarization effects the Mu precession is basically not visible in the time spectrum but the power spectrum of the fit shows a peak suitable to the observed power spectrum.
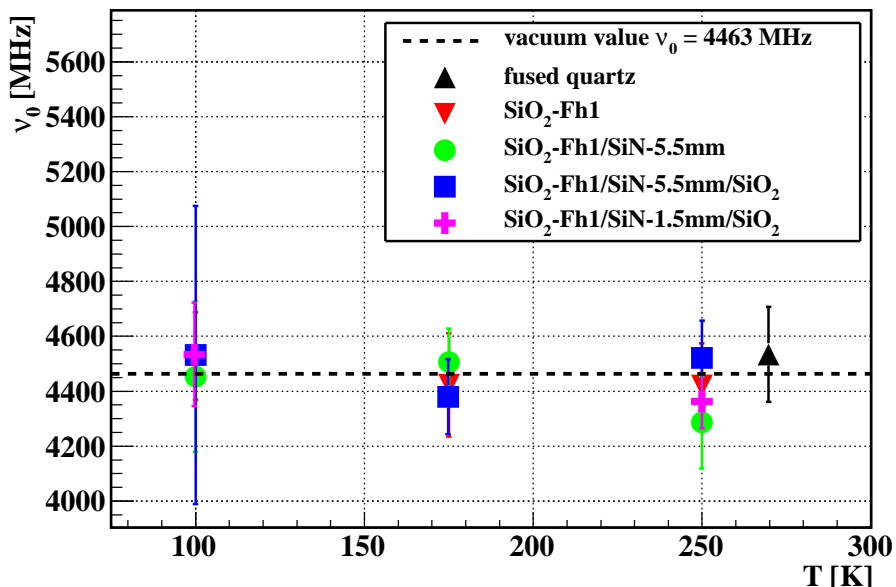
Figure 6.10: *Hyperfine splitting of muonium at the ground state versus temperature for various configurations.*

6.5   Summary and conclusion

Improvement of the μ^+ to Mu conversion using mesoporous material, and the possibility of Mu confinement which has been demonstrated here open the way to a more precise measurement of the Mu 1S-2S transition frequency. Very preliminary analyses using gradient ratio and qualitative comparison show that the reflection effect of Mu on the

SiN wall is very significant compared to the adsorption effect. The measured time spectra showed that Mu atoms are reflected from the SiN or SiO_2 surface even at 100 K. The actual enhancement factor achievable with this reflectivity is strongly depends on the final setup design and cannot be given at this stage.

Mu two-frequency method has also been used to study the effect of adsorption to the surface but no strong evidence has found for the case of surface adsorption due to limited statistics. Only measurements at 20 K have shown a very strong shift of the HFS indicating (for this temperature) Mu sticking at the pore walls of the mesoporous material.

Chapter 7

Phase-space compression of a muon beam

As explained before in Section 1.4, an improved μ^+ beam is essential to the next generation precision measurements involving μ^+ and Mu. As standard μ^+ beams have a relatively high energy and poor phase space quality, several ideas have been proposed [62, 63] to produce a low energy and high quality μ^+ beam. Among them, a new scheme [63] making use of stopped μ^+ in a cryogenic He gas target is under development at PSI. Through the stopping process, a high intrinsic phase-space compression can be achieved. The remaining challenge is to extract the μ^+ fast enough into vacuum. This can be done by compressing the stopped μ^+ swarm with electric fields and guiding it to a small extraction hole.

Related schemes have been used in the field of rare isotope investigations [129, 130]. High energy ion beams are stopped in He gas and manipulated with DC and RF electric fields to induce drift, radial compression and extraction from a gas target. Typical manipulation and extraction times are 5-200 ms. Due to the short lifetime of the μ^+, which is about 2 μs, much faster techniques are needed.

The new concept for fast μ^+ beam compression is based on a position-dependent μ^+ drift velocity $\vec{v}_D$ in a gas. In a long He gas target placed in a longitudinal high magnetic field, the stopped μ^+ beam are first transversely, then longitudinally compressed and finally extracted into vacuum through 1 mm^2 extraction holes in transverse direction (see Figure 7.1). The whole operation takes place in less than 10 μs and should lead to a phase-space compression of 10^{10}. An intense slow μ^+ beam can then be obtained with a 10 ns time resolution at a few eV energy or a micro-beam can be focused into a beam spot of 10 μm diameter at 10 keV. Such a beam can be applied to μSR measurements for micro-sized samples and thin films, to precision measurements like Mu spectroscopy, and to new physics searches like μ^+ EDM and Mu $- \overline{\text{Mu}}$ conversion.
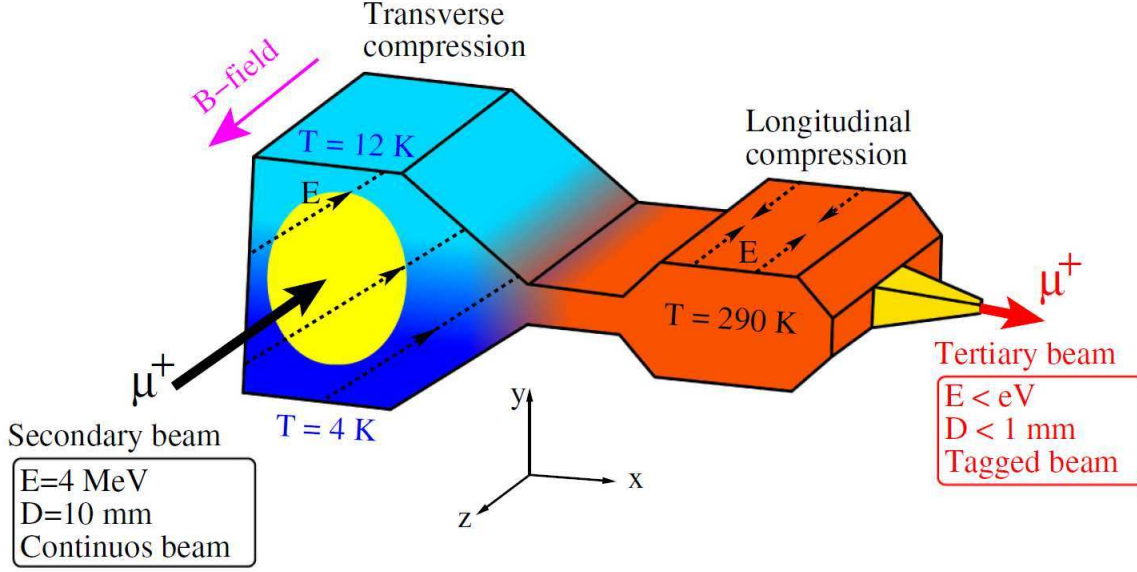
Figure 7.1: *Schematic of the phase space compression of the μ^+ beam proposed in [63]. μ^+ traveling in the $-z$ direction are stopped in 5 mbar He gas at cryogenic temperatures. First, transverse (y direction) compression occurs within a density gradient in He gas (blue region). Then at room temperature the longitudinal z direction) compression takes place (red region). In the yellow region a mixed transverse-longitudinal compression precedes before extraction into vacuum. Reproduced from [131].*

The principle of the fast μ^+ beam compression [63, 131, 132] is explained in the subsequent sections.

7.1   Principle of the experiment

The drift velocity of charged particles in gas in the presence of electric $\vec{E}$ and magnetic $\vec{B}$ fields is [133]

$$\vec{v}_D = \frac{\mu E}{1 + \omega^2 \tau_c^2} \left[\hat{E} + \omega \tau_c \hat{E} \times \hat{B} + \omega^2 \tau_c^2 (\hat{E} \cdot \hat{B}) \hat{B} \right] \tag{7.1}$$

where $\hat{E}$ and $\hat{B}$ are the unit vectors along $\vec{E}$ and $\vec{B}$, $\omega = eB/m$ the cyclotron frequency with m the μ^+ mass, μ the μ^+ mobility in the gas and τ_c the mean time between collisions. For small $\omega \tau_c$ the μ^+ drift is along the electric field lines. This is the regime of high gas density where the collision rate is large. For large $\omega \tau_c$ the third term dominates

98

and μ^+ follow the magnetic lines. The second term that is proportional to $\hat{E} \times \hat{B}$ is largest for $\omega\tau_c \approx 1$, whereas it vanishes for for $\omega\tau_c \to 0$ and $\omega\tau_c \to \infty$.

μ^+ compression can be achieved by making the drift velocity position dependent. For example, by producing a gas density gradient via a temperature (T) gradient and by using an electric field configuration with spatially dependent magnitude and direction,

$$\vec{v}_D(\vec{x}) = \vec{v}_D(\tau(\vec{x}), \vec{E}(\vec{x})) = \vec{v}_D(T(\vec{x}), \vec{E}(\vec{x})) \ . \tag{7.2}$$

The beam line that will be developed is composed of a sequence of stages as shown in Figure 7.1. In the initial **transverse compression** stage a μ^+ beam is stopped in He gas at 5 mbar pressure inside a 5 T longitudinal magnetic field $\vec{B}$ and a transverse electric field $\vec{E}$. The gas temperature in this first stage has a vertical gradient from 4 to 12 K. At lower densities (top part) τ_c is large and $\vec{v_D}$ is dominated by the $\hat{E} \times \hat{B}$ term. Hence, the μ^+ drift diagonally in the y direction and in the $+x$ direction. By contrast, at larger densities (bottom part) the first term of Equation 7.1 dominates and the resulting drift velocity is along $\hat{E}$. Therefore, μ^+ originating from the upper (lower) part of the stop distribution while drifting in the $+x$ direction are moving downwards (upwards) giving rise to a compression in the transverse (y) direction. The 10 mm wide stopping volume in the y direction is thereby reduced to a swarm of μ^+ moving in the x direction with a height of 0.5 mm (in the y direction) and a length (in the z direction) of 50 cm or more [63].

The μ^+ swarm is then entering a second stage at room temperature (low density) where **longitudinal compression** (in the direction of $\hat{B}$ or z) takes place. Hence, the μ^+ are directed towards the exit hole as shown in Figure 7.1. The third term of Equation 7.1 is here dominant. The electric fields are designed such that E_z changes sign in the center of this region. Thus, μ^+ drift to the center along the magnetic field lines, which gives rise to longitudinal compression. This method depends crucially on whether μ^+ undergo a "runaway effect" in the gas target [134]. A non-vanishing E_y component guarantees that the μ^+ swarm drifts also along the $+x$ axis because of the $\hat{E} \times \hat{B}$ term. An additional μ^+ swarm compression in both the y and z direction occurs in a third stage followed by vacuum extraction through small holes at particular locations of the gas target.

7.1.1   Transverse compression

In the initial transverse compression stage a μ^+ beam is stopped in He gas at 5 mbar pressure inside a 5 T longitudinal magnetic field $\hat{B} = (0, 0, 1)$ and a transverse electric field $\hat{E} = 1/\sqrt{2}\,(1, 1, 0)$. The gas temperature in this first stage has a vertical gradient from 4 K to 12 K corresponding to an average STP pressure of about 200 mbar. Hence a
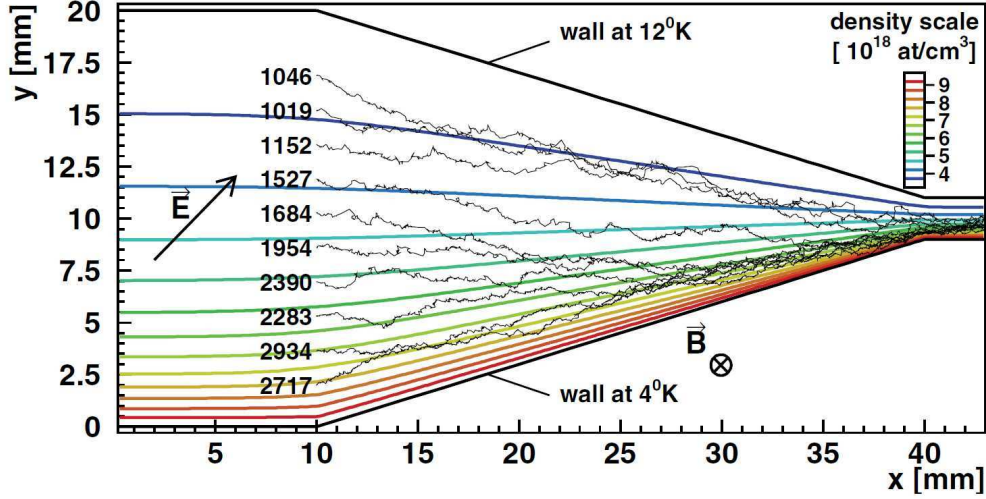
Figure 7.2: *Transverse compression stage based on density gradient in helium gas at 4.6 mbar, 5 T magnetic field and an electric field of 1800 V/cm. μ^+ coming along the z-axis are stopped in the gas. Several μ^+ trajectories for μ^+ "stopped" in the gas are simulated starting 10 mm away from the left target wall. The drift time up to the "throat" is given in ns near the starting point of each μ^+ trajectory. Constant density lines are shown together with the density scale (colored lines). Taken from [63].*

standard surface μ^+ beam can be stopped in such a gas target within a length of about 1 m. A high intrinsic phase space compression is achieved through the stopping process. The remaining challenge is to compress and extract the μ^+ into vacuum.

A density gradient is created in the y direction by having the lower wall of the target at lower temperature and the upper wall at higher temperature, with the density at the center of the target ($y = 0$) such as $\omega\tau_c = 1$. At lower densities (top part) τ_c is large and $\vec{v}_D$ is dominated by the $\hat{E} \times \hat{B}$ term. Hence the μ^+ drift diagonally in $-y$ direction and in $+x$ direction. By contrast, at larger densities (bottom part) the first term of Equation 7.1 dominates and the resulting drift velocity is along $\hat{E}$. Therefore, as shown in Figure 7.2 μ^+ originating from the upper (lower) part of the stop distribution while drifting along the $+x$ direction are moving downwards (upwards) giving rise to a compression in transverse (y) direction. Simulations of the process indicate that the 15 mm wide stopping volume in the y-direction is thereby reduced to a swarm of μ^+ moving in x-direction with an height of 0.5 mm (in y-direction) and a large (1 m) length (in the z direction) in an average time of 2 μs.

The μ^+ flow, which has been transversely compressed but extends over a long length

in the z direction enters a second stage at room temperature (low density) where longitudinal compression (in the direction of $\hat{B}$ or z) takes place.

7.1.2 Longitudinal compression

Following transverse compression, the μ^+ swarm then enters a second stage at room temperature (low density) where longitudinal compression (in the direction of $\hat{B}$ or z) takes place to direct the μ^+ towards the exit hole as shown in Figure 7.1. The third term of Equation 7.1 is here dominant because $\omega\tau \gg 1$.

The compression is achieved by implementing an E_z field that alternates in direction. The whole z-range is thus divided in sections of length d. In each section, the E_z changes sign in the center of this region (taken to be at $z = 0$ in what follows) and the μ^+ are compressed towards it. Thus, μ^+ drift to the center following the magnetic field lines giving rise to longitudinal compression. A non-vanishing E_y component guarantees that the μ^+ swarm drift also along the $+x$ axis because of the $\hat{E} \times \hat{B}$ term.

Longitudinal compression occurs over a relatively large length of the μ^+ swarm. This is possible only if at sufficiently high E_z/N, where N is the gas density, "runaway" occurs [134]. As shown by [134] for protons, when the kinetic energy T of the charged particle reaches values greater than 1 eV, the momentum transfer cross-section σ_{mt} for elastic scattering (p-He scattering) decreases with T like $1/T$ or faster. The energy loss due to collisions is not compensating for the energy gain from the electric field and the proton can accelerate to high energies till other processes comes into play. The onset of "runaway" has been demonstrated for protons drifting in He gas [135]. Fast longitudinal compression of the μ^+ swarm within 10-15 cm length requires the μ^+ to be accelerated at "runaway" conditions. Figure 7.3 shows some simulated μ^+ trajectories in the transverse and longitudinal compression stages. Efficient extraction of the μ^+ into vacuum requires further compression from the few mm into the sub-mm regime. This is achieved in the next stage.

Efficient extraction of the μ^+ into vacuum requires further compression from the few mm into the sub-mm regime. This is achieved in the next stage.

7.1.3 Extraction into vacuum

The longitudinal compression is followed by an additional compression along both y and z axis, again at cryogenic temperature as shown in Figure 7.4. The cold temperature yields the necessary density and also guarantees a low μ^+ energy when extracted into vacuum.

μ^+ are extracted from the region (filled with He gas) where compression occurs in
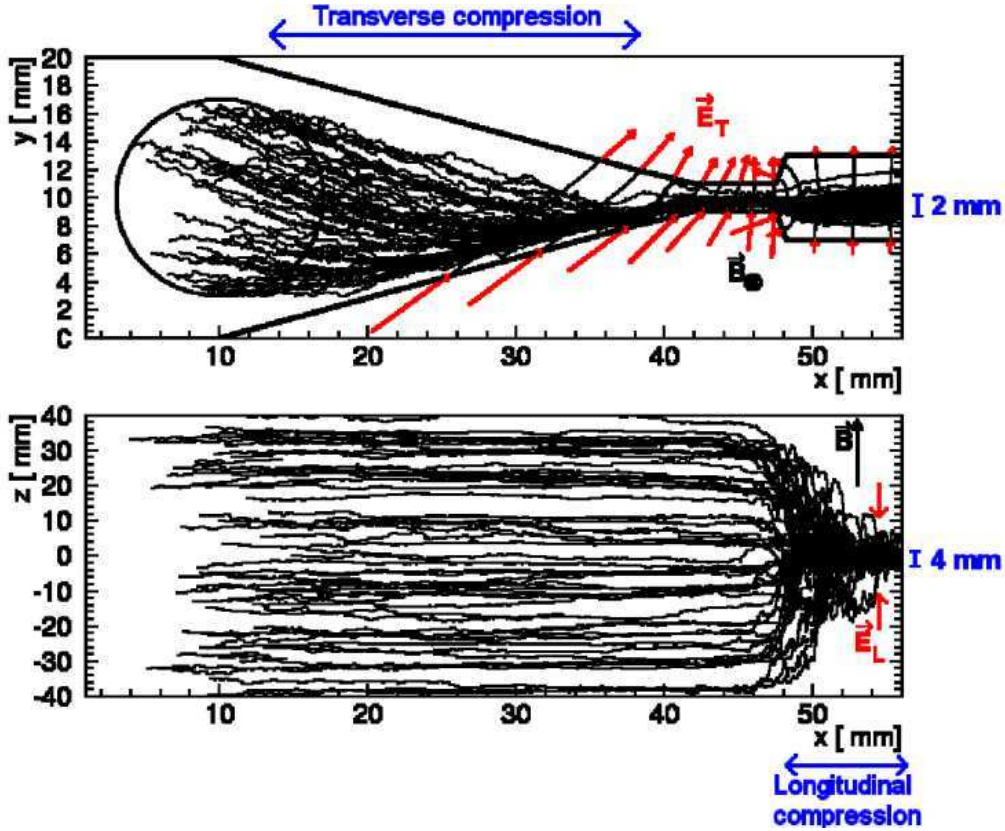
Figure 7.3: μ^+ *trajectories in the transverse and longitudinal compression stages projected in the $y - x$ and $z - x$ planes. The circle indicates the μ^+ stop area. Reproduced from [132].*

vacuum via a small orifice of 1 mm diameter. As a consequence, He gas also exits this orifice. Therefore to guarantee the required 5 mbar pressure over the various compression regions helium gas needs to be continuously injected into the gas cell. To avoid turbulence that would destroy the necessary temperature gradients, the He gas is injected with radial symmetry along the y-z plane at the end of the third stage as shown in Figure 7.5 (left).

Preliminary simulations of the gas stream, using ANSYS and shown in Figure 7.5 (Right), have demonstrated that the 5 mbar pressure can be sustained without turbulence in the compression regions [132]. The simulations suggest the plausibility of the gas injection concept. The experimental verification of an injection and differential pumping scheme will be part of the next steps.

As a final stage, μ^+ drifting into the vacuum at random times (quasi-continuously) are re-accelerated along the z-direction (magnetic field direction) with a pulsed electric field
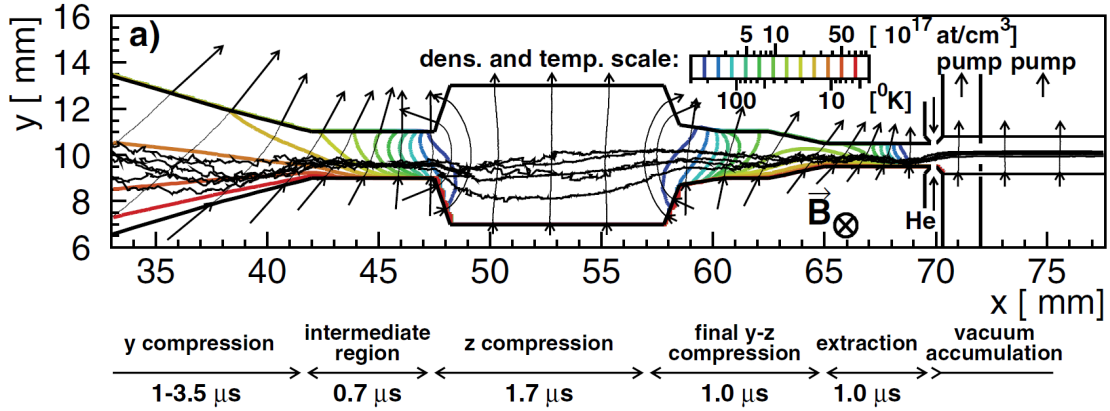
Figure 7.4: *Schematic view of the whole compression scheme in the $x - y$ plane. The colored lines represent density and temperature contour lines, the arrows the electric field lines. The thin black irregular lines are simulated μ^+ trajectories. Taken from [63].*

producing μ^+ bunches. This results in a micro-beam with a well-defined time structure. For many applications (for example Mu spectroscopy) it is necessary to extract the μ^+ from the 5 T magnetic field into a field-free region. Efficient extraction is not easy but quasi divergence-free non-adiabatic extraction can be achieved by introducing a ferromagnetic grid [136] at the exit of the beam into the field free region.

7.2 Demonstration of the longitudinal compression

Demonstration of the longitudinal compression was achieved in 2011 using PSI's πE1 beam line tuned at a momentum of 10 MeV/c. μ^+ coming from the beam line enter the gas target, cross the entrance detector and a part of them stop in the He gas. The stopped μ^+ can then be compressed longitudinally along the μ^+ beam and the magnetic field. The μ^+ stop volume, where compression occurs, is 160 mm long and has a cross section of 6×10 mm^2. The walls of the gas target have several strips to define the electric fields as shown in Figure 7.6.

   To attract the μ^+ to the center, a negative high voltage (HV) was applied at the $z = 0$ mm strip whereas the strips at $z = \pm 80$ mm were grounded. S1 is the 30 μm thick entrance detector read out by G-APDs. It provides the "start time" (t_{start}) of the measurement. S2 is used to align the target along the beam and provides anti-coincidences to identify μ^+ stops in the gas. P1 and P2 are two positron counters made of 1 mm thick 8×8 mm^2 scintillators readout with 3×3 mm^2 G-APDs. The waveforms of these four detectors were recorded by a DRS4 [137] based waveform digitizer developed
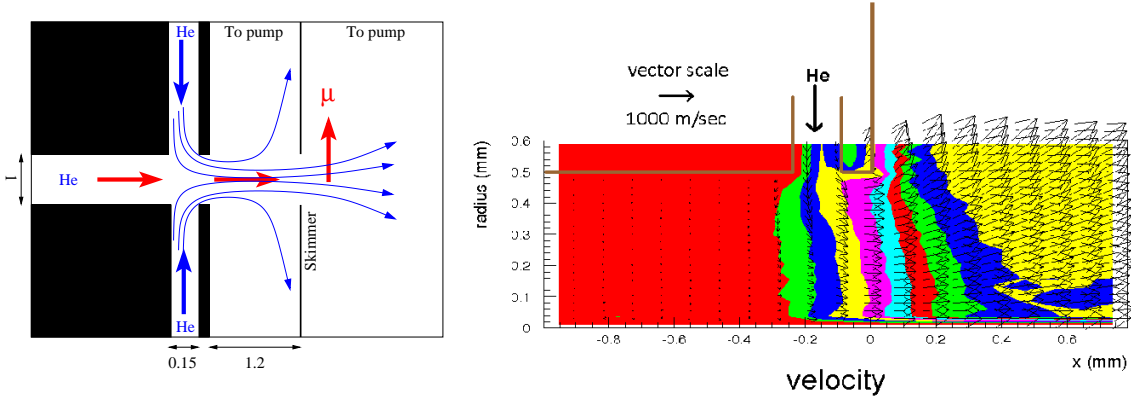
Figure 7.5: *(Left) Sketch of the μ^+ extraction region which encompasses the He gas injection, the orifice and skimmer for differential pumping. Lengths are in mm. (Right) Simulated velocity vectors of the helium gas. Reproduced from [132].*

at PSI. The positron counters are shielded by thick brass collimators in order to detect only positrons originating from decays around $z = 0$.

A special program using ROOT framework [96] was developed for the waveform analysis. As the DRS4 data file is written in a binary format as shown in Figure 7.7 for maximal readout rate, it is first converted to decimal prior to waveform analysis. The position of the peak minimum in the recorded waveform is giving the "stop time" (t_{stop}) of the event. This t_{stop} approach is sufficient for this measurement because the μ^+ drift occurs on a μs time scale whereas the rise time of the pulses are of the order of ns.

By plotting the number of events in the positron counters (P1 and P2) versus time ($t_{\text{stop}} - t_{\text{start}}$), a time histogram as shown in Figure 7.8 is obtained. Events with multiple peaks have been discarded. The histograms were multiplied with e^{t/τ_μ} to remove the μ^+ lifetime effect. The resulting plots given in Figure 7.8 show that all curves become flat at times larger than 500 ns. This means that after 500 ns compression is finished and a pure exponential decay with the μ^+ lifetime is observed. The "prompt" peaks originate from the higher energy μ^+ decaying in flight in the acceptance region of P_1 and P_2.

When a negative HV is applied, the μ^+ are attracted close to P_1 and P_2. The resulting e^+ time distribution (blue curve) shows an increase caused by the μ^+ drift into a region with higher positron detection efficiency. On the contrary, by applying a positive HV, the μ^+ are pushed to a region with smaller detection efficiency resulting in a decrease of detected positrons (green curve).

The curve for large positive HV at delayed time essentially corresponds to a background measurement. Its flat asymptotic behavior (after multiplication with $\exp(t/\tau)$) reveals that this background is μ^+-correlated. It arises from μ^+ stopping in the target
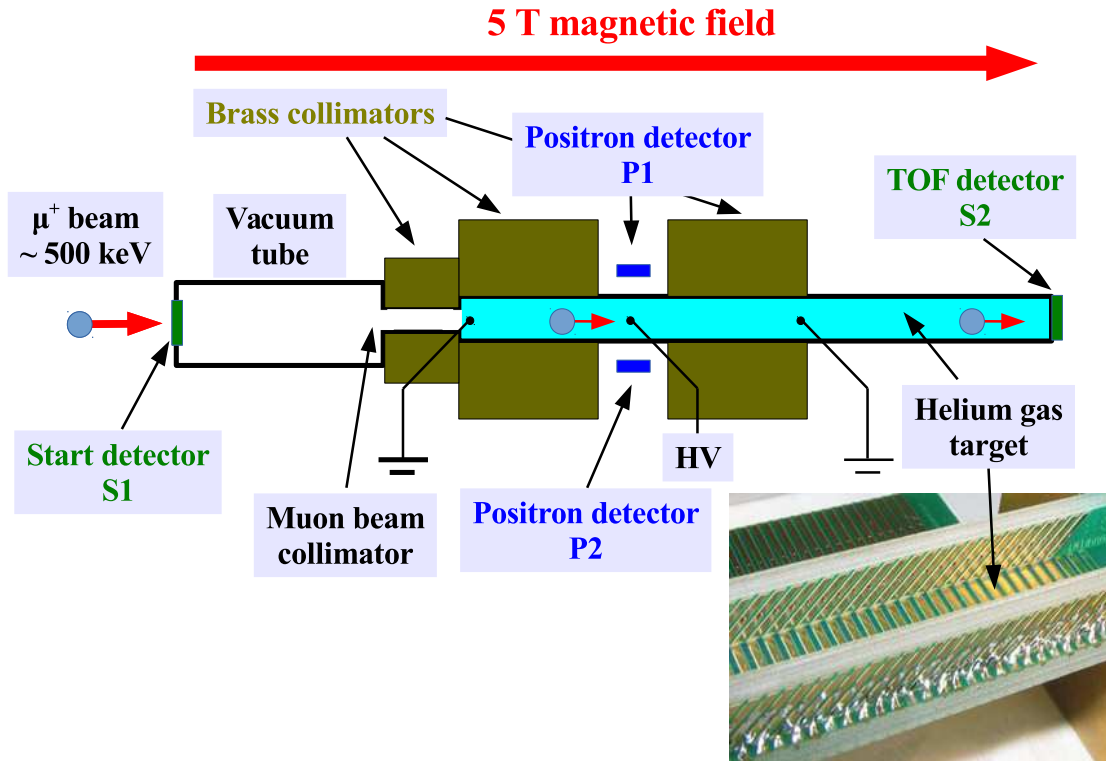
Figure 7.6: *Scheme of the setup used to test longitudinal compression. μ^+ from $\pi E1$ beam line crosses the entrance detector S1 producing the "start signal" (t_{start}) of the event. The μ^+ beam is collimated before entering the 5-12 mbar helium gas target at room temperature. μ^+ stopping inside the target will be drifting towards the central region where P1 and P2 are located. The event is ended when a positron from the μ^+ decay is hitting P1 or P2 giving the "stop signal" (t_{stop}). (Inset) Picture of the inner walls of the target. The various metallic strips are set at different high voltages (HV).*

Word	Byte 0	Byte 1	Byte 2	Byte 3	Contents
0	'T'	'I'	'M'	'E'	Time Header
1	'B'	'#'	Board number		Board serial number
2	'C'	'0'	'0'	'1'	Channel 1 header
3	Time Bin Width #0				Effective time bin width in ns for channel 1 encoded in 4-Byte floating point format
4	Time Bin Width #1				
...	...				
1026	Time Bin Width #1023				
1027	'C'	'0'	'0'	'2'	Channel 2 header
1028	Time Bin Width #0				Effective time bin width in ns for channel 2 encoded in 4-Byte floating point format
1029	Time Bin Width #1				
...	...				
2051	Time Bin Width #1023				
2052	'E'	'H'	'D'	'R'	Event Header
2053	Event Serial Number				Serial number starting with 1
2054	Year		Month		Event date/time 16-bit values
2055	Day		Hour		
2056	Minute		Second		
2057	Millisecond		*reserved*		
2058	'B'	'#'	Board number		Board serial number
2059	'T'	'#'	Trigger cell		Number of first readout cell
2060	'C'	'0'	'0'	'1'	Channel 1 header
2061	Voltage Bin #0		Voltage Bin #1		Channel 1 waveform data encoded in 2-Byte integers. 0=-0.5V and 65535=+0.5V
2062	Voltage Bin #2		Voltage Bin #3		
...	...		...		
2572	Voltage Bin #1022		Voltage Bin #1023		
2573	'C'	'0'	'0'	'2'	Channel 2 header
2574	Voltage Bin #0		Voltage Bin #1		Channel 2 waveform data encoded in 2-Byte integers. 0=-0.5V and 65535=+0.5V
2575	Voltage Bin #2		Voltage Bin #3		
...	...		...		
3085	Voltage Bin #1022		Voltage Bin #1023		
3086	'E'	'H'	'D'	'R'	Next Event Header
	...				

Figure 7.7: *DRS4 data format. Example of the binary file when two out of four channels are switched on. Taken from [138].*
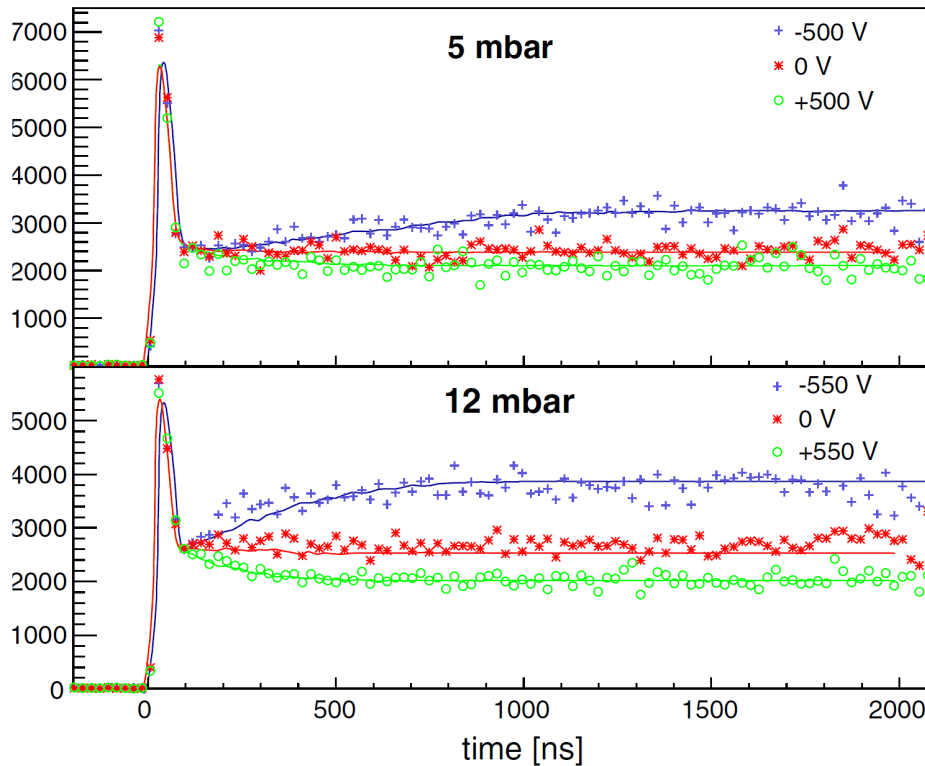
Figure 7.8: *Measured and simulated (continuous lines) positron time spectra multiplied with $e^{t/2200}$ for two different pressures, where t is the time in ns. The simulations account for μ^+ chemical capture with a rate of $40 \times 10^6 \ s^{-1}$ and a misalignment between the target and the magnetic field of 1 mrad (see text). Reproduced from [131].*

walls, in the beam collimators, in the beam dump and in the inactive region of the target. It was observed that the background was reduced by only 20% when emptying the gas cell (relative to 5 mbar and HV=0).

7.2.1   Geant4 Monte Carlo simulation

Geant4 [109] Monte Carlo simulations with the geometry shown in Figure 7.9 were done in order to analyze the measured time spectra (which include prompt peak, background, slowing down, and compression) and to quantify the μ^+ beam compression. However, the μ^+ physics in a standard Geant4 package at low energy (0.1-1000 eV) does not correctly reflect the reality where the elastic collision is dominant instead of the inelastic one.

In the standard Geant4 package, the energy loss process and the scattering process are handled independently. The energy loss of a particle is handled by the ionization

process according to the stopping power provided by NIST down to particle energy of 1 keV. Below 1 keV and down to 10 eV, the model of a free electron gas [139] is used. In this model, the energy loss is proportional to particle velocity. When the particle energy is below 10 eV, it is treated as "stopped" and is set to zero energy. Tracking of the particle will be terminated if there is no "at rest" processes such as decay of a particle. On the other hand, the scattering of a particle is handled by the scattering process according to the multiple scattering model based on Lewis theory [140].

Hence, the standard package is extended to include μ^+ physics processes in the 0.1 eV$-$1 keV energy range [141]. Below 1 keV energy standard Geant4 processes are replaced with the elastic μ^+-He collision, Mu formation and Mu ionization processes. Data available for protons were scaled to be used for μ^+: velocity scaling is used for the charge-transfer processes [142] and energy scaling for the elastic collisions [143]. Among these processes the elastic μ^+-He scattering is the decisive interaction that controls the μ^+ compression. It has been included in the Geant4 Monte Carlo simulation starting from the proton differential cross sections calculated in [144].

Elastic scattering

Collisions are usually characterized by the differential cross section defined as the ratio of the number of particle N scattered into direction (θ, ϕ) per unit time per unit solid angle $d\Omega = \sin\theta d\theta d\phi$, divided by incident flux j_I,

$$\frac{d\sigma(\theta, \phi)}{d\Omega} = \frac{N}{j_\mathrm{I}} \ . \tag{7.3}$$

In case of Coulomb potential which is a central potential $V(r)$, i.e. a potential energy that depends only on the distance r from the origin, the differential cross section is only a function of the scattering angle θ for particle with velocity v [144]:

$$\left.\frac{d\sigma(\theta, \phi)}{d\Omega}\right|_v = |f(\theta)|^2 \tag{7.4}$$

where $f(\theta)$ is the scattering amplitude of the scattered wave.

The total elastic scattering cross section, which is the flux of particle scattered in all directions σ_el [144], is defined as

$$\sigma_\mathrm{el} = \int d\Omega \, \frac{d\sigma(\theta, \phi)}{d\Omega} = \int_0^{2\pi} d\phi \int_0^\pi d\theta \, \sin\theta \, \frac{d\sigma(\theta, \phi)}{d\Omega} \tag{7.5}$$

$$= 2\pi \int_0^\pi d\theta \, \sin\theta \, |f(\theta)|^2 \ , \tag{7.6}$$
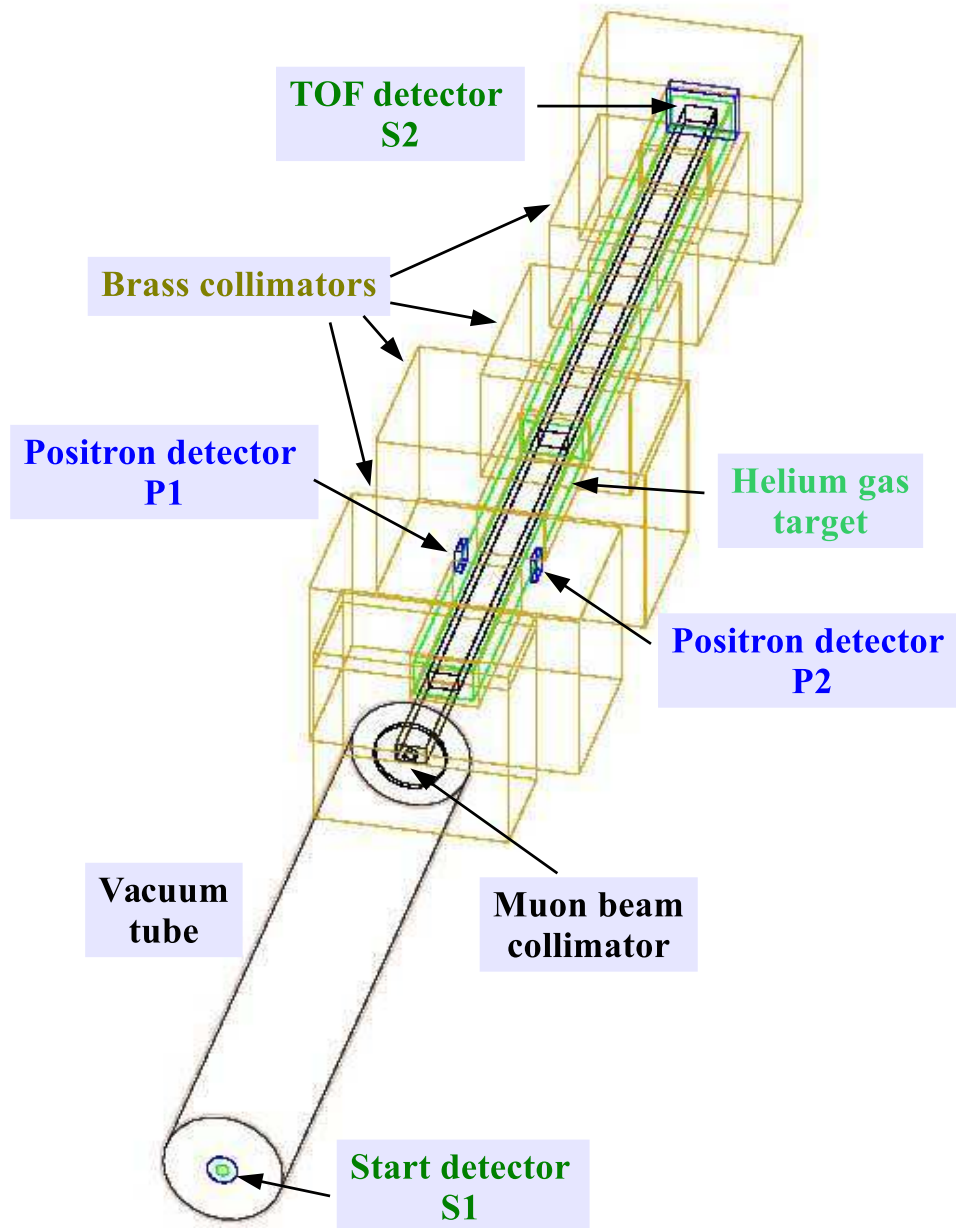
Figure 7.9: *Details of the simulated section. The whole geometry is inside a 5 T PST solenoid. The μ^+ is simulated starting from the left bottom corner. After registering a start signal at S1, the μ^+ is collimated before entering the 5-12 mbar helium gas target at room temperature. μ^+ is stopped inside the target and will be drifting towards the region where P1 and P2 are located. The measurement is ended when a positron from the μ^+ decay is hitting P1 or P2.*

109

and the momentum-transfer cross section, which is an effective scattering cross section describing the average momentum transferred from a particle to a target is defined as

$$\sigma_{\mathrm{mt}} = \int d\Omega \, \frac{d\sigma(\theta, \phi)}{d\Omega} \, (1 - \cos\theta) = \int_0^{2\pi} d\phi \int_0^{\pi} d\theta \, \sin\theta \, \frac{d\sigma(\theta, \phi)}{d\Omega} \, (1 - \cos\theta) \qquad (7.7)$$

$$= 2\pi \int_0^{\pi} d\theta \, \sin\theta \, |f(\theta)|^2 \, (1 - \cos\theta) \ . \qquad (7.8)$$

The scattering amplitude $f(\theta)$ and the cross sections σ_{el} and σ_{mt} are being calculated with very high precision in the center of mass (CM) frame [144].

Both cross sections can be used for the simulation of the transport of the particle depending on the situation. Due to the $1 - \cos\theta$ term in Equation 7.8, the σ_{mt} is much smaller than the σ_{el} because the importance of forward scattering is suppressed ($\sigma_{\mathrm{el}} \approx 5\sigma_{\mathrm{mt}}$ at 0.1 eV and $\sigma_{\mathrm{el}} \approx 200\sigma_{\mathrm{mt}}$ at 100 eV). σ_{el} represents a more precise description of the scattering process but it costs in computational power. For longitudinal compression where the density is low (10^{17} atom/cm^3), it is affordable to use the σ_{el} but for transverse compression where the density is much higher (5×10^{18} atom/cm^3), σ_{mt} is a better choice considering the trade-off between the precision and computational time.

In the Geant4 simulation, the elastic scattering process between μ^+ and He is implemented in the following way:

(I) The kinetic energy of the μ^+ is transformed into the center of mass (CM) collision energy T_{CM}.

(II) The mean free path of a step is calculated using the total elastic cross section:

$$\lambda_{\mathrm{el}} = \frac{1}{\sigma_{\mathrm{el}} N} \ , \qquad (7.9)$$

where N is the number of atom per unit volume (density). The step length is then given by λ_{el} multiplied by a random number with an exponential distribution.

(III) A second random number is generated to select the scattering angle of the μ^+ according to the differential cross section. The scattering angle θ in the CM reference frame is sampled according to the differential cross sections $\dfrac{d\sigma(\theta, \phi)}{d\Omega}$ given in [144]. θ is then transformed into the scattering angle ϕ in the laboratory frame:

$$\tan\phi = \frac{\sin\theta}{\cos\theta + m/M} \ , \qquad (7.10)$$

where M is the He mass and m the μ^+ mass.
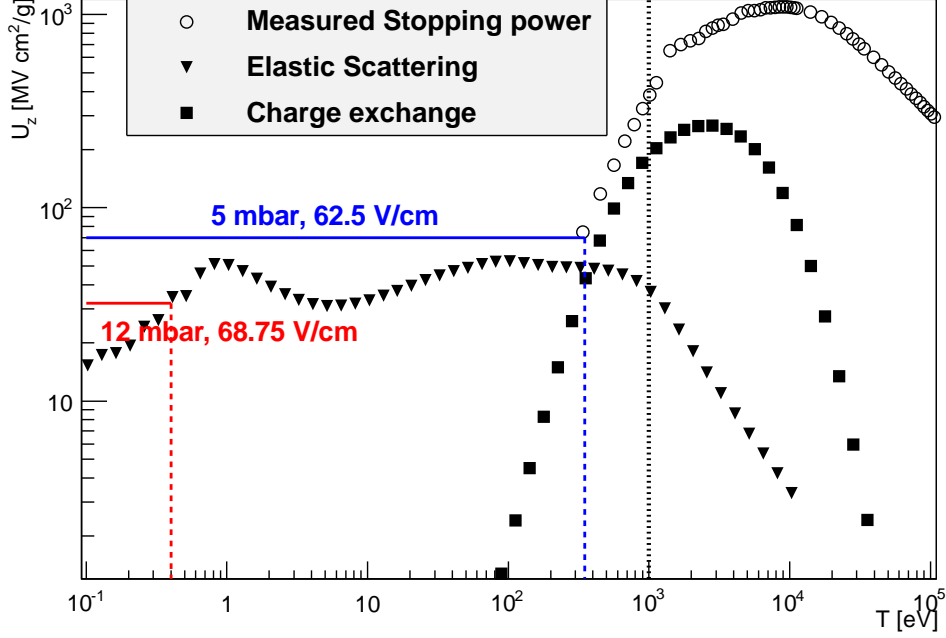
Figure 7.10: *Energy loss processes of μ^+ at low energy. The hollow circles show the stopping power $(dT/(N\,ds))$ where ds is the path length) caused by ionization, excitation and charge exchange processes. The curve with triangles represents the energy loss $(dT/(N\,dz))$ caused by elastic scattering per unit length in a fixed direction (z, electric field direction). The vertical blue and red lines are the resulting equilibrium energies at the experimental conditions.*

(IV) Another angle φ is randomly generated to obtain the scattering angle in another dimension. This initial direction is then rotated to the new direction ($\sin\phi\cos\varphi$, $\sin\phi\sin\varphi$, $\cos\phi$).

(V) The energy loss of this step in the lab frame is then calculated using

$$dT = \frac{2m}{m+M}(1-\cos\theta)T_{\mathrm{CM}}\ . \tag{7.11}$$

Note that for the implementation of the momentum transfer cross section σ_{mt}, σ_{el} in step (II) is simply replace by σ_{mt} and in (III) the θ angle is generated isotropically in the CM frame.

111

Charge exchange

When a μ^+ crosses matter in the keV energy regime, it undergoes charge exchange, that is electron-capture and electron-loss processes. Both processes have been accounted for separately in the simulation using the velocity scaled cross sections of [142] with 11 eV energy loss in the electron-capture process, and 13.6 eV in the electron-loss process and no change in direction for both processes.

Energy loss of μ^+ at low energy

The stopping power caused by these processes is given in Figure 7.10 where for simplicity only the net μ^+ energy losses caused by the full charge exchange cycle is represented without separating electron-capture and electron-loss. The μ^+ stopping power given by the circles in Figure 7.10 which results from velocity scaling the measured proton stopping power [145] deviates from the stopping power given by the charge exchange. This is because it also includes non-negligible processes as ionization and excitation of the target helium atom. Because no cross sections are available for these processes, between 300 eV and 1 keV the energy losses of the charge exchange processes is deliberately increased to reproduce the measured stopping power. Such an approximation is sufficient as simulations show that the drift of the μ^+ is insensitive to the precise implementation of these processes, as they spend only a small amount of time in this energy range.

The curve shown with triangles in Figure 7.10 illustrates the approximate energy loss of diffusive motion per unit length along a given direction (dz) when only elastic scattering takes place. For a given energy T it amounts to [134]

$$\frac{1}{N}\frac{dT}{dz} \approx 2T\sigma_{\mathrm{mt}}(T)\Big(\frac{m}{m+M}\Big)^{1/2} . \tag{7.12}$$

By equating energy loss with energy gain due to the applied electric field E,

$$\frac{1}{N}\frac{dT}{dz} \approx \frac{E}{N} , \tag{7.13}$$

one can estimate the average μ^+ equilibrium energy at the corresponding field and density conditions. For example, as shown in Figure 7.10 at $E = 69$ V/cm and a pressure of 12 mbar the average kinetic energy is 0.8 eV. As E/N and the average energy increase, there is an energy region where the product $T\sigma_{mt}(T)$ (see right side of Equation 7.12) does not increase anymore. At this point Equation 7.13 can no more be fulfilled and runaway occurs. This is shown in Figure 7.10 for 5 mbar, where the limiting process is the charge exchange at 200 eV.

The simulation allows for tracking μ^+ without averaging the angular distribution in terms of a momentum transfer cross section as used in Equation 7.12. A time evolution
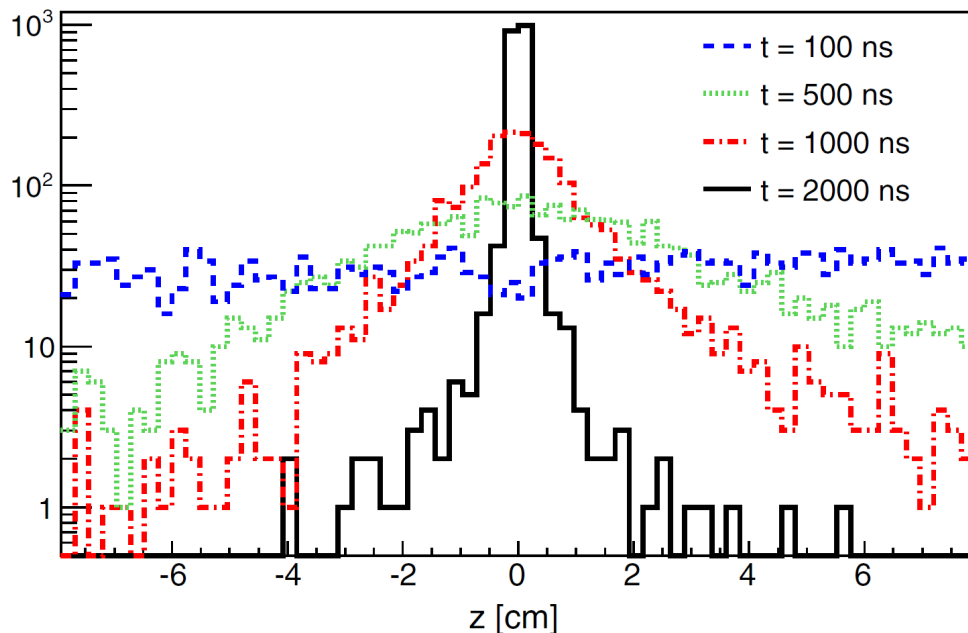
Figure 7.11: *μ^+ distribution at various times during the compression for 5 mbar and HV = 550 V. Reproduced from [131].*

of the μ^+ spatial distribution during compression in the target is given in Figure 7.11. Starting from an approximately flat stop distribution (blue curve), the μ^+ are compressed in the center. Some broadening of the peak at intermediate times is caused by μ^+ which have already reached the center but are still oscillating while thermalizing around the minimum of the V-shape potential. Figure 7.11 shows that it takes less than 2 μs to compress the stopping μ^+ in the gas target within ± 2 mm.

The positron time spectra of P_1 and P_2 simulated with the Geant4 are shown in Figure 7.12. The 12 mbar (blue continuous) curve has a fast and a slow component. The slow component which become visible at times later than 700 ns arises from slow μ^+ drifting at the equilibrium energy of 0.8 eV. The fast component results from compressing μ^+ while having several hundreds eV energy, thus still in the process of slowing down to the equilibrium energy. For 5 mbar no fast and slow component can be distinguished since the equilibrium drift energy is higher (around 200 eV). Hence most μ^+ arrive at the center of the target before they slow down.

The measured time spectra of Figure 7.8 do not show any hint of a slow component. At 12 mbar the measured compression is completed at about 500 ns. According to simulations, at this time the μ^+ energy ranges from 1 eV to 10 eV. The explanation for the absence of the slow component is that at these energies the μ^+ interacts with impurities, organic molecules or water, to form muonic ions or to replace a proton of

113
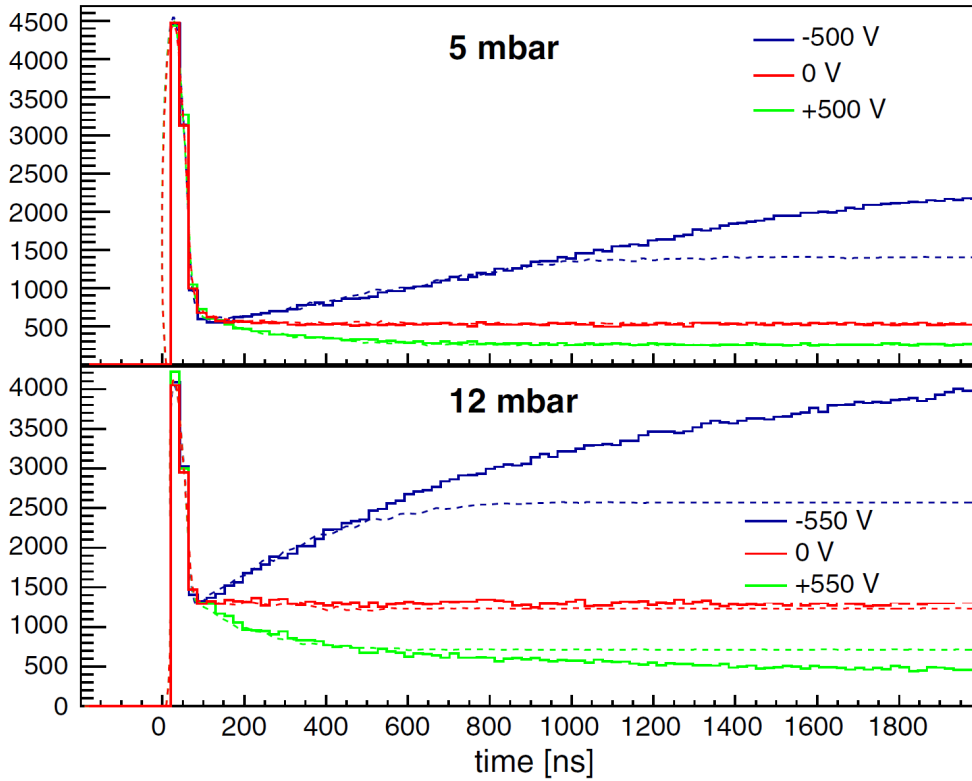
Figure 7.12: *Simulated positron time spectra without (continuous lines) and with (dashed lines) μ^+ chemical capture to impurities with $R = 40 \times 10^6 \ s^{-1}$ and 10 eV cutoff. Reproduced from [131].*

these molecules (isotopic exchange).

This interaction originates from the polarization potential between the μ^+ and the He atom. It attracts the μ^+ from a far distance into the atom with a cross section varying as 1/velocity at low energies. This results in an interaction rate independent on the energy. Above a certain energy the μ^+ may interact with the molecule without "chemical capture". Therefore, a constant loss rate R in the low energy range up to a cut-off energy is introduced into the simulation and is taken to be 10 eV. Large desorption rates have been measured in the target (PCB glued with Araldite) giving rise to impurities of about 10^{14} molecules/cm^3 corresponding to few atomic mono-layers when integrated over the active target length. It is known that few mono-layers of impurities on the Ar-moderator surface of the LEM beam line [71] are sufficient to reduce by one order of magnitude the number of μ^+ with energy between 0 to 30 eV emerging from the surface [84].

The dotted curves in Figure 7.12 show the effect of this "chemical capture" assuming

a rate of $R = 40 \times 10^6$ s^{-1}. The measured time distributions show a larger flat (μ^+ correlated) background than the simulations. This increased background can be explained by a small (within experimental uncertainties) misalignment between the magnetic field lines and the target that causes an increased number of μ^+ stopping in the target walls in front of the positron detectors. Adjusting the simulations to include misalignment and "chemical capture", results in a complete agreement with the measured spectra as shown in Figure 7.8.

7.2.2   Realization of longitudinal compression

In conclusion, the compression of stopping μ^+ in the magnetic field direction has been demonstrated for the first time. It is an essential part in the realization of the beam line proposed in [63]. This demonstration relies on the agreement between the experimental results and simulations based on Geant4 extended to account for low energy processes. While the cross sections at low energy in He gas are known only for protons, cross sections scaled from protons are used for μ^+. Variation of the elastic μ^+-He cross section by a factor of 2 leads to simulated time spectra that disagrees strongly with the measurements. Therefore these measurements confirm the correctness of the used cross sections. Applying the simulation to μ^+ starting the longitudinal compression process at low energy as in [63], a compression process with almost no losses in walls or Mu formation is predicted. The compression of the 160 mm wide μ^+ swarm to a 4 mm width takes place in less than 2 μs. Hence, no physical unknown process seems to prevent the realization of this part of the beam line.

7.3   Towards test of the transverse compression

Transverse compression has been be tested at the end of year 2014 at PSI πE1 beam line. A simplified schematic setup of the target and the detector system required for this experiment is shown in Figure 7.13.

A surface μ^+ beam of 28 MeV/c crosses a μ^+ entrance detector and then stops in a cold He gas target at a pressure of 5 mbar, inside a 5 T longitudinal (along the μ^+ stopping axis) magnetic field. The gas target has a gradient in temperature from 4 K (bottom) to 12 K (top) as shown in Figure 7.1 and Figure 7.2. μ^+ drift along the x-axis and the swarm is compressed in the y-direction if suitable electric fields are applied as detailed in Section 7.1.1.

To demonstrate μ^+ drift and transverse μ^+ compression, some long (along z-axis) scintillators (S$_i$) are placed around the target preferentially close to the target cell "throat". The time spectra (relative to a μ^+ entrance detector) of the positron hits in the various
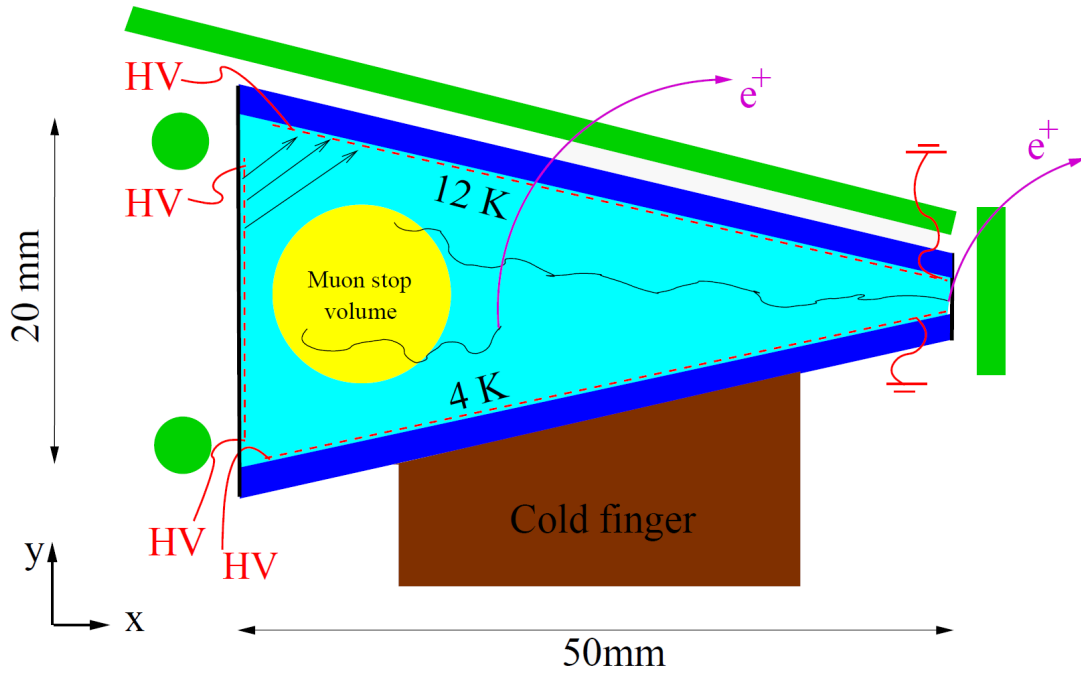
Figure 7.13: *Schematic view of the gas-cell and a simplified positron detection system to test the transverse compression stage. The scintillators (green) are used to detect the decay positrons. The target is made by two quartz plates (blue) with lateral walls made of Kapton foils. The electric field is defined by about hundred metallic strips (red) arranged on the inner walls of the target set at various HV. μ^+ drift from the stopping volume (yellow) in x-direction while compressing in y-direction towards the cell "throat".*

scintillators carry the information regarding the μ^+ swarm compression and drift. In this simplified scheme the S_3 time spectrum increases with time while μ^+ drift towards it. Furthermore, an anti-coincidence with S_6 can be used to clean-up this spectrum and more precisely disentangle μ^+ which have drifted from the stopping volume to the "throat" without impinging into the target walls. In addition, the scintillators S_1 and S_2 carry information about the secondary μ^+ beam alignment relative to the target.

In order to better disentangle between drift-with-compression and drift-without- compression the μ^+ beam will be collimated to about 4 mm diameter, and directed to various vertical positions in the gas cell.

7.3.1   Preliminary simulations of the positron detection system

Geant4 simulations are performed to optimize the positron detection system taking into account the space at disposal in the bore hole ($\phi = 200$ mm) of the PSC solenoid, the various constraints given by the thermal shield while minimizing the amount of material to guarantee fast cooling at cryogenic temperatures. At the current development stage, a sophisticated positron tracker is not needed. One of the various geometries investigated is given in Figure 7.14.
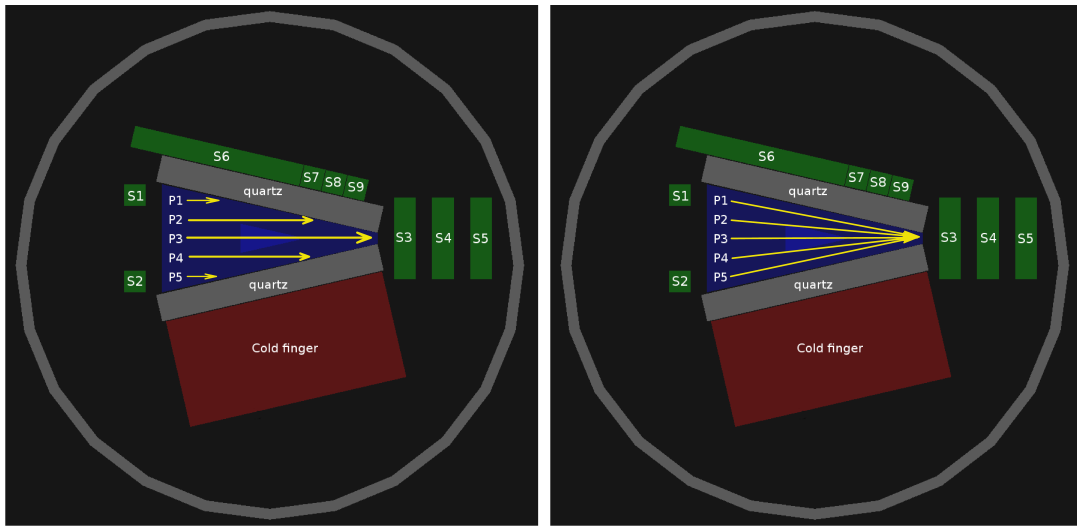
Figure 7.14: *Scheme of a detector-target geometry simulated using Geant4. The various scintillators are given by S_i. The particle trajectories starting at various initial positions (P_i) are given by the arrows for two simplified cases: drift without compression (left), drift with compression (right).*

The time spectra recorded in the various positron detectors for μ^+ starting at various vertical position P_i drifting in x-direction with constant speed are given in Figure 7.15. When drifting to the right, the detection efficiency for S_3 increases and for S_1 decreases, giving rise to the corresponding variation of the time spectra. μ^+ that ultimately stop on the walls can be distinguish from μ^+ compressed in the "throat". Disentangling a simple drift (bottom plots) from a drift accompanied by compression (top plots) is thus feasible, given the large differences in the time spectra. Note that these time spectra consider the simplified situation of particles drifting along the indicated arrows with constant speed. However in reality the time spectra will be smeared out due to random diffusion, and extended stop and energy distributions of the μ^+.

These preliminary simulations indicate the feasibility of a simple detection scheme to demonstrate transverse compression. Variations of the experimental parameters such
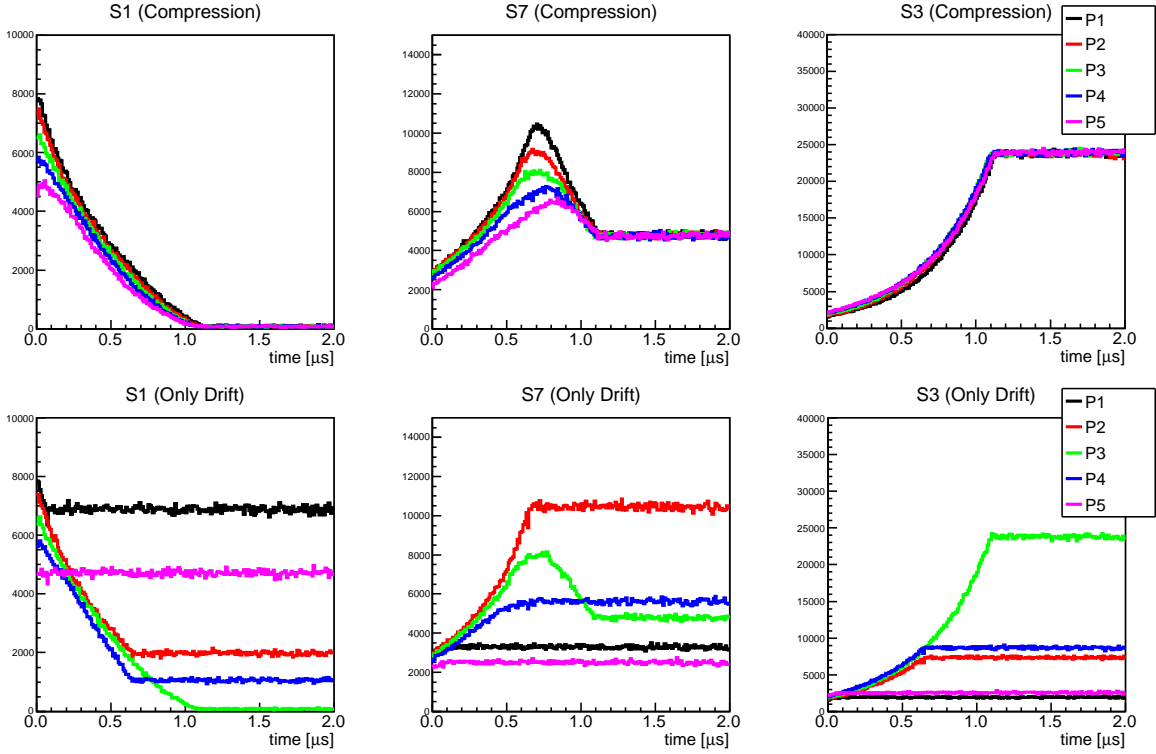
Figure 7.15: *Simulated time spectra for three scintillators (S_1, S_7, S_3) for μ^+ moving with constant speed for various initial vertical positions (P_i) for the two cases shown in Figure 7.14: (Top row) only drift in x-direction, (Bottom row) drift in x-direction accompanied by compression in y-direction. The time spectra have been multiplied by $e^{t/2.2}$ where t is the time in μs.*

as electric field, pressure and stopping position will allow us to switch from a drift mode, to a compression mode, to measurements of background. Detailed investigations are ongoing, where ratios between detectors, placement of collimators and so on are considered. One must consider the background, but the test of longitudinal compression made in 2011 at the πE1 beam line demonstrated that it is well under control and that it is basically only μ^+ correlated.

7.3.2   Optimization of the muon beam momentum

Simulation of the last part of the beam line has been accomplished using Geant4. The aim of this simulation was to optimize the momentum of the beam for maximal stopping probability in the cold He gas target accounting for the various foils, collimators, entrance detector, target window that the μ^+ needs to cross. An event display of the

simulation which include also the positron detection system is shown in Figure 7.16. The corresponding evolution of the kinetic energy and beam size is shown in Figure 7.17.

The momentum of 17.2 MeV/c has been found to be optimized - to have the maximal stopping probability in the He gas cell (20%) for the foils and scintillator thickness given in the Table 7.1.

Table 7.1: *An example of the optimized positions of the elements for the demonstration of the transverse compression. The positions are optimized such that the μ^+ stopping probability in the He gas cell is maximized.*

Element	Geometry	Dimension	Position
PSC Magnet	cylinder(r_{in}, r_{out}, z)	(150, 200, 1000)	(0,0,0)
Foil F1	disk(r, z)	(15,0.02)	(0,0,-470)
Flange CF1	cylinder(r_{in}, r_{out}, z)	(15,150,10)	(0,0,-465)
Entrance detector	disk(r, z)	(15,0.09)	(0,0,-447)
Foil F2	disk(r, z)	(40,0.02)	(0,0,-200)
Flange CF2	cylinder(r_{in}, r_{out}, z)	(40,100,20)	(0,0,-190)
Foil F3	disk(r, z)	(40,0.02)	(0,0,-150)
Flange CF3	cylinder(r_{in}, r_{out}, z)	(40,90,10)	(0,0,-145)
Collimator	disk(r, z)	(35,20)	(0,0,-120)
Collimator hole 1	disk(r, z)	(2,20)	(16,5,-120)
Collimator hole 2	disk(r, z)	(2,20)	(0,0,-120)
Collimator hole 3	disk(r, z)	(2,20)	(16,-5,-120)
Target foil front	trapezium(y_{min}, y_{max}, z)	(2,24.2,0.025)	(0,0,-100.0125)
Collimator top T1	box(x, y, z)	(50,20,30)	(-2.7,20.5,-85)
Helium gas target	trapezium(y_{min}, y_{max}, z)	(2,24.2,300)	(0,0,50)
Collimator top T2	box(x, y, z)	(50,20,30)	(-2.7,20.5,185)
Target foil back	trapezium(y_{min}, y_{max}, z)	(2,24.2,0.025)	(0,0,200.0125)

7.3.3   Simulation of transverse compression

In order to simulate the transverse compression stage, beside the low-energy processes explained in Section 7.2.1, a gas density gradient has to be implemented. In the G4Material class of the Geant4 package, the density of a material in a given volume is constant. Parameterization of the volume in the G4DetectorConstruction is one of the easiest solution but it is expensive in terms of computational time. A fast solution given here is to explicitly implement the position dependent gas density into the mean
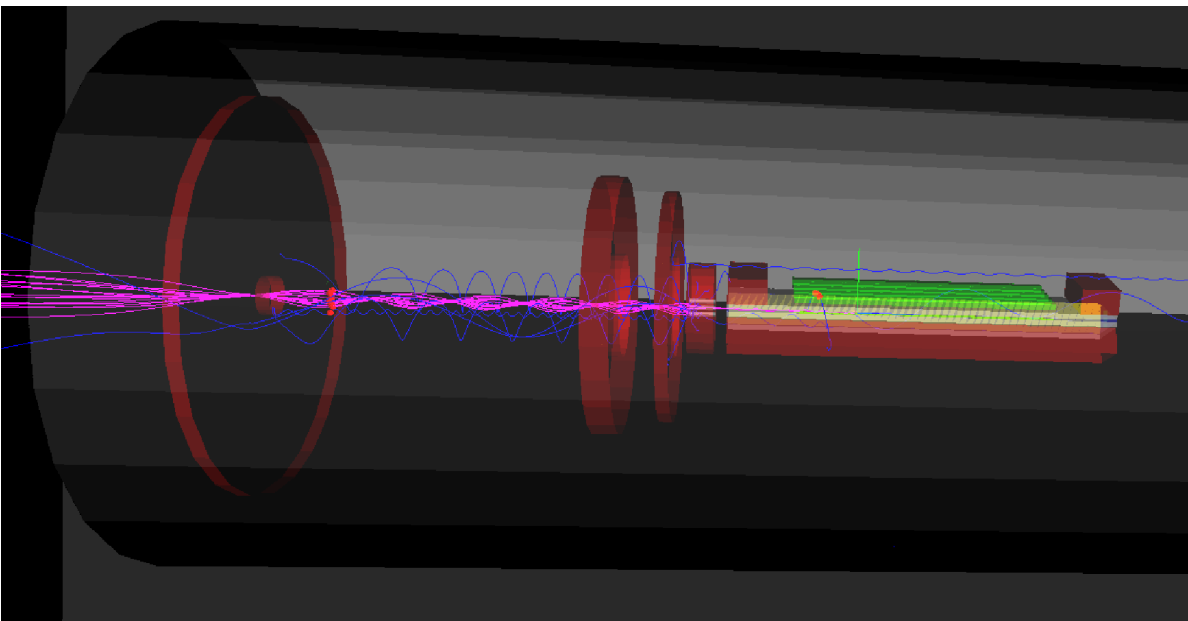
Figure 7.16: *An event display from the Geant4 simulation of the transverse compression. The μ^+ beam is coming in from the left. The foils are attached to the front part of the flanges (brown) and their positions are optimized. The positions of the scintillators (green) are also optimized to have less background from the positrons originated from the μ^+ stopping on the front target foil.*
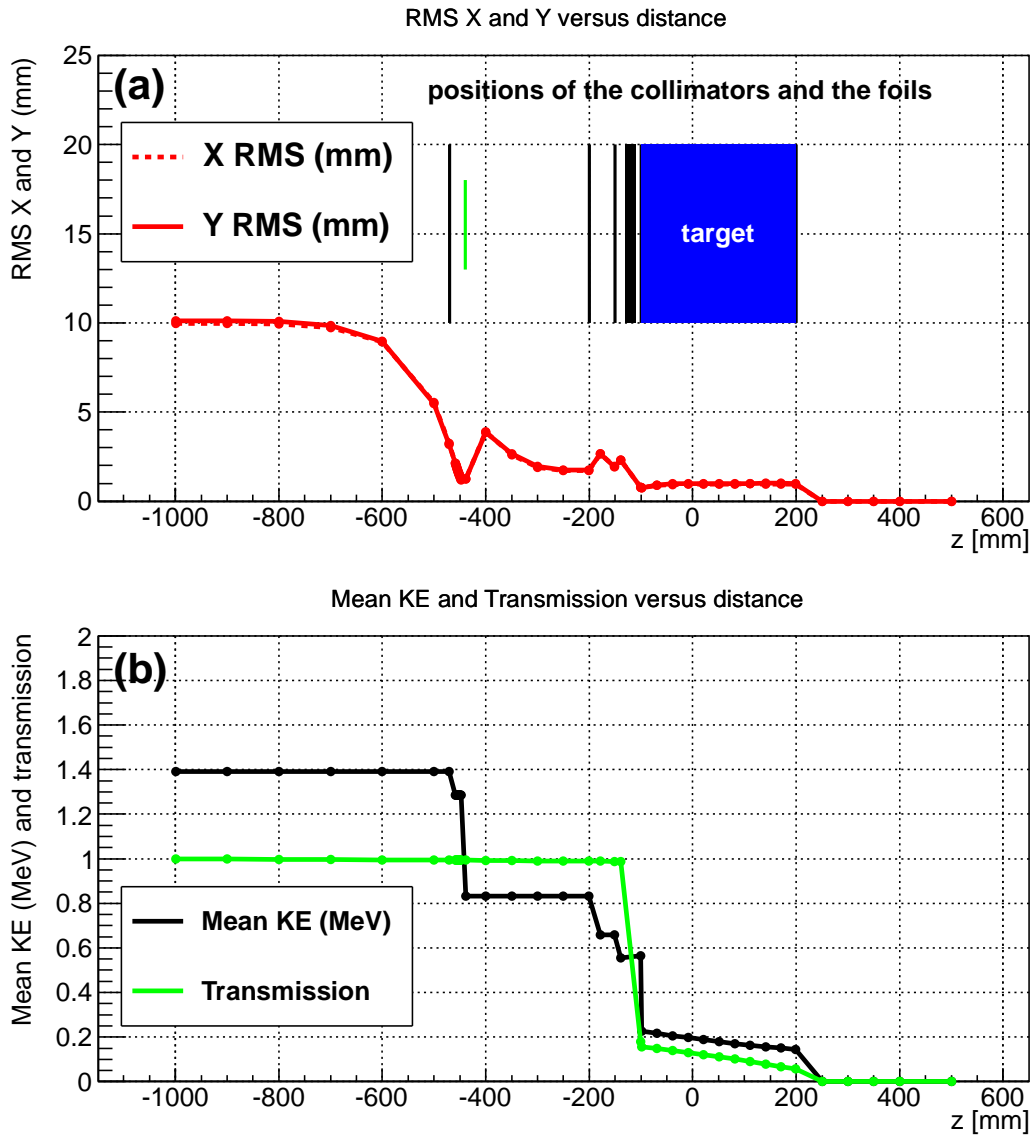
Figure 7.17: *Geant4 simulation of the (a) beam size (x_{rms}, y_{rms}), and (b) kinetic energy and beam transmission, of the μ^+ in the last part of the beam line. The step-wise change in kinetic energy are due to the μ^+ crossing vacuum foils or the plastic scintillator.*
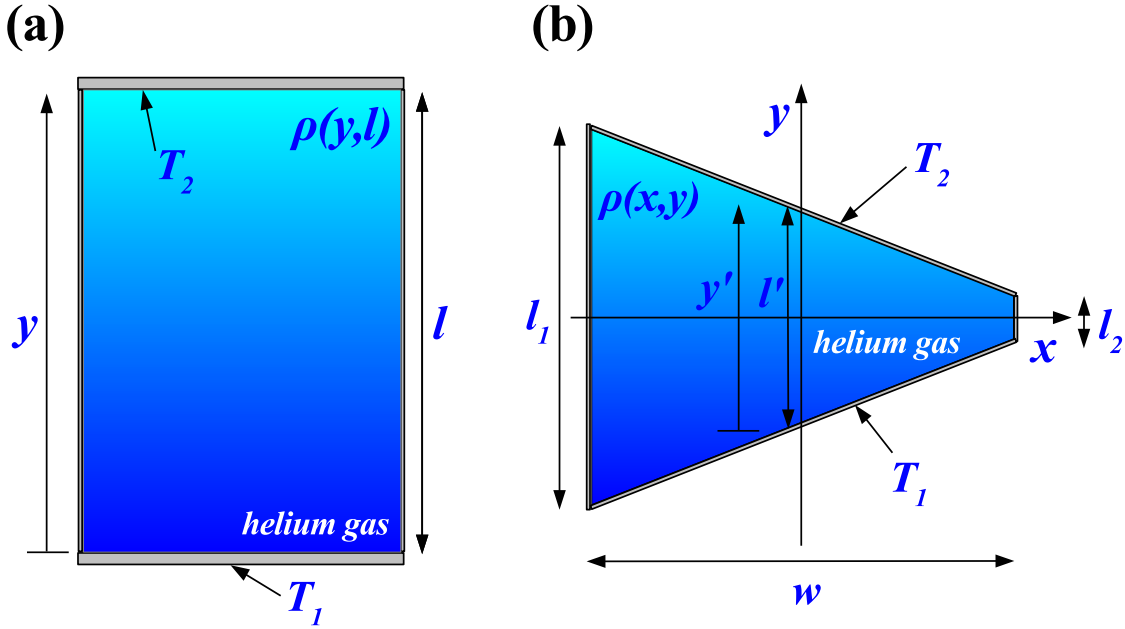
Figure 7.18: *Geometries and variables used in deriving position-dependent gas densities. (a) Gas density in a cylindrical cell given by $\rho(y,l)$ according to Equation 7.15. (b) Gas density of a triangular helium gas cell given by $\rho(x,y)$ according to according to Equation 7.18. The bottom plate is cooled to a temperature T_1 and the top plate is warmed to a temperature T_2. The colors do not reflect the actual gas density gradient and are only for illustration.*

free path calculation of the transportation. This can be achieved by substituting in N of Equation 7.9 with $N(x,y)$ where x, y correspond to the transverse coordinates.

The local density can be calculated using a thermal conductivity model of the He gas. Assuming that the thermal conductivity of the He [146] is

$$k(T) = aT^n \tag{7.14}$$

where $a = 1/\sqrt{M}$, M the mass of the He atom and n is gas dependent ($n = 0.5$ for an ideal gas and $n = 0.68$ for ^{4}He.). Then the particle density distribution (ρ) in the vertical direction y for the He gas in a cylindrical cell as shown in Figure 7.18(a) with bottom plate at a temperature T_1 and the top plate at a temperature T_2 with $\Delta T = T_2 - T_1 > 0$ is given by

$$\rho(y,l) \propto \frac{p}{R \cdot \left[\left(\frac{\Delta T}{l^{\frac{1}{1+n}}} \right) \cdot y^{\frac{1}{1+n}} + T_1 \right]} , \tag{7.15}$$

where p is the gas pressure, R the gas constant and l the height of the cell. Detailed derivation of the formula can be found in [146]. This formula assumes that there is no convection. The applicability of this formula to the test setup of transverse compression has been confirmed by performing a neutron radiography experiment using cells filled with ^{3}He [147]. At the same time, neutron radiography has also demonstrated the feasibility to sustain the gas density gradient needed for the transverse compression.

In the setup for the test of transverse compression as shown in Figure 7.18(b), the distance between top and bottom plates of the cell is x-position dependent and has to be modified according to

$$l'(x) = l_+ - \frac{2xl_-}{w} \ ,$$

(7.16)

where $l_+ = (l_1+l_2)/2$ and $l_- = (l_1-l_2)/2$, while l_1, l_2 and w are as given in Figure 7.18(b). The vertical distance from the bottom plate as shown in Figure 7.18(b), has also x-position dependent and is modified according to

$$y'(x) = y - \frac{l'(x)}{2} \ ,$$

(7.17)

where y is the coordinate in the y-axis. Substituting Equation 7.16 and Equation 7.17 into Equation 7.15, the final gas density is given by

$$\rho(x,y) \propto \frac{p}{R \cdot \left\{ \left[\dfrac{\Delta T}{(l_+ - \frac{2xl_-}{w})^{\frac{1}{1+n}}} \right] \cdot \left(y - \dfrac{l_+ - \frac{2xl_-}{w}}{2} \right)^{\frac{1}{1+n}} + T_1 \right\}} \ .$$

(7.18)

7.3.4 Simulations with the gas density gradient

Geant4 simulations were performed using $\rho(x,y)$ from Equation 7.18 to calculate the gas density $N(x,y)$ which is needed to calculate the mean free path $\lambda_{\mathrm{mt}} = 1/\sigma_{\mathrm{mt}}N(x,y)$. Instead of the elastic scattering differential cross section from [144], the momentum transfer differential cross section was used. The reason is that unlike longitudinal compression where the setup is held at room temperature, transverse compression is done at cryogenic temperature with the same gas pressure. This means that the gas density is about 50 times higher in this first stage and hence much frequent elastic scattering (at least 30×10^6 steps per event and hence very expensive in terms of computing cost). Instead of generating a random number to select the scattering angle of the μ^+ according to the differential cross section, the scattering angle is generated randomly in 4π direction.

In Figure 7.19, a typical simulation of the transverse compression stage is shown. Only the elastic μ^+-He collision process has been accounted using the momentum transfer

cross section. Effects such as charge exchange process can be implemented for improved precision. By comparing the simulated and measured time spectra, it is possible to determine the μ^+ drift velocity, the compression efficiency and to investigate the validity of the various cross sections assumed.

7.4 Conclusion and outlook

Ongoing research and development (R&D) of the new μ^+ beam compression scheme at ETH and PSI are very encouraging. The second part of the scheme, longitudinal compression was successfully demonstrated in 2011. This demonstration relies on the agreement between the experimental results and simulation based on Geant4, after implementing μ^+ physics processes at low energy such as elastic collision and charge exchange.

A neutron radiography experiment has demonstrated the feasibility to sustain the necessary density gradient for the transverse compression stage. An engineering run towards test of the transverse compression was complete in Dec 2014. A gas density gradient was implemented into Geant4 simulation by the means of recalculating the gas density and hence the mean free path of the μ^+ in the low energy physics process. With this, the simulated time spectra and the experimental data can be compared when data will available.
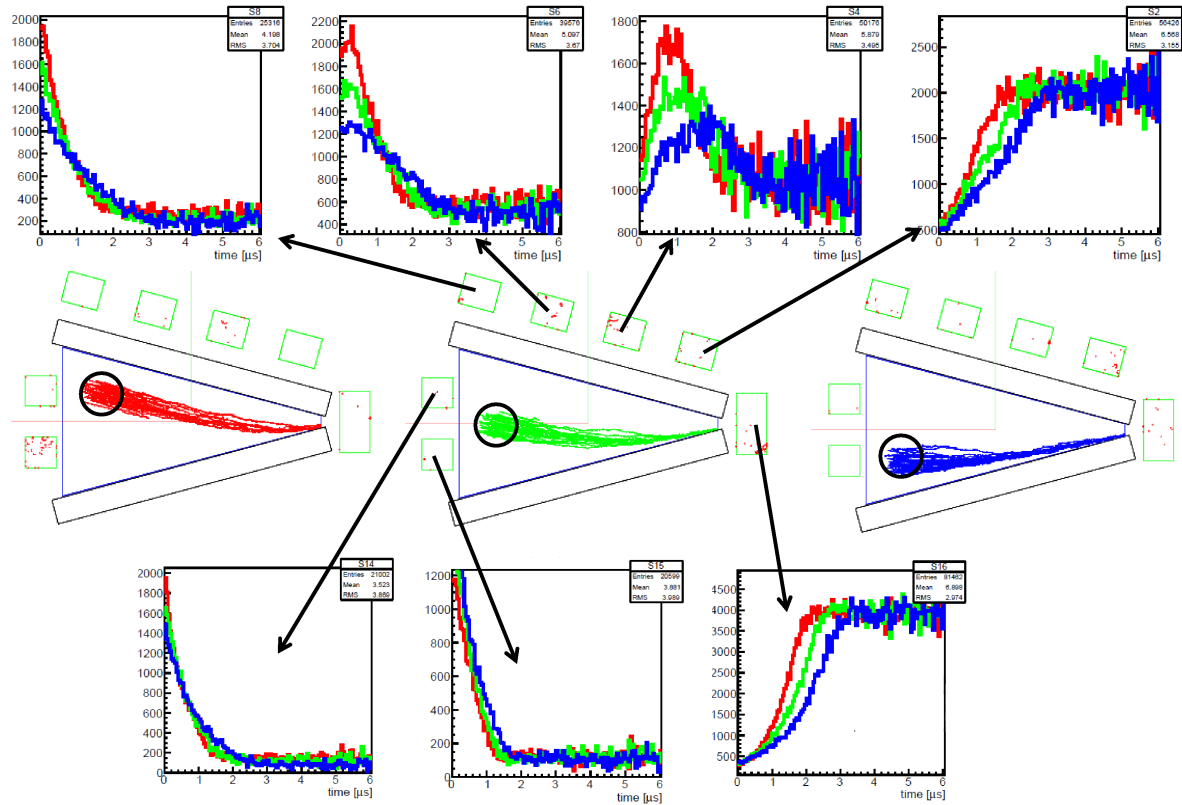
Figure 7.19: *Simulated time spectra for the positron detectors installed at various positions around the target for the test of transverse compression. Each of them is showing distinctive behavior due to the drift of the μ^+ beam. The red, green and blue lines represent the time spectra for various initial μ^+ positions given by the black hollow circles. These simulations have been done at 5 mbar He gas pressure and top-bottom temperature of $T_2 = 12$ K and $T_1 = 4$ K, respectively, starting for μ^+ at rest and using only the momentum transfer cross section.*

Chapter 8

Conclusions

During the course of this thesis, the requirements for next generation fundamental precision measurements with muons have been studied in detail through various experimental campaigns and simulations.

A factor of two improvement in muonium vacuum yield has been achieved using mesoporous silica materials at room temperature, but also high vacuum yield at cryogenic temperatures has been observed for the first time: 20% at a temperature of 100 K. Moreover muonium reflection at walls has also been investigated. A preliminary analysis of the taken data shows high reflection probability which implies that muonium can be confined in a small hollow volume which could be illuminated efficiently by a laser beam. These two achievements, high vacuum yield and confinement, represent important steps towards next generation muonium spectroscopy.

The first steps towards the development of a novel, low-energy, high-brilliance positive muon beam have been very encouraging. This new beam line makes use of a phase-space compression of muons stopping and drifting in a helium gas within suitable electric and magnetic fields. The feasibility of the longitudinal compression stage has been tested and no unknown limiting process which would hinder the beam line realization has been observed. Cross sections for low energy processes scaled from proton data have been validated. An engineering run towards the test of transverse compression was completed in Dec 2014. The realization of this novel tertiary beam line will enable one to produce a micro-beam of muons having several applications, especially for the μSR and precision particle physics community.

These results have been achieved by developing several new techniques. First, a positron shielding technique was developed to monitor the muonium yield in vacuum, by modifying the existing LE-μSR apparatus. Second, the Geant4 simulation package has been extended down to 0.1 eV by implementing μ^+ physics at low energy such as elastic collision and charge exchange. The concept of density gradient has also been explicitly

implemented into the Geant4 simulation enabling comparison between simulated time spectra and experimental time spectra of the transverse compression.

Appendix A

Muonium precession

In order to understand the time evolution of the μ^+ polarization in Mu atom in a magnetic field discussed in Section 3.2, a minimal theoretical treatment of this system is given in this chapter. This requires some knowledge of the Mu energy levels in the magnetic field. Therefore this chapter begins with a description of the energy eigenstates of the Mu atom placed in a magnetic field. Then the time evolution of the μ^+ in Mu atom in a longitudinal and a transverse magnetic field is explained. Finally the two-frequency method used to determine the Mu ground-state hyperfine structure (HFS) in Section 6.4 is discussed.

A.1   Energy eigenstates of muonium

The energy levels of Mu calculated using non-relativistic Schrödinger equation are similar to the one of hydrogen except for the difference in the reduced mass factor. The discrete energy levels of Mu in first approximation are given by $E_n = -R_\infty(1 - \frac{m_e}{m_\mu})/n^2$, where n is the principal quantum number and R_∞ is the Rydberg constant. The ground state HFS interval of Mu is given in first approximation by the Fermi formula [148]

$$\nu_0 = \frac{\Delta W}{h} = \frac{16}{3}\alpha^2 cR_\infty \frac{\mu_\mu}{\mu_B^e} \approx 4.463 \times 10^9 \text{ Hz} \tag{A.1}$$

where α is the fine-structure constant, c the velocity of the light, ΔW the singlet-triple energy difference, μ_μ the muon magnetic moment and $\mu_B^e = \dfrac{e\hbar}{2m_ec}$ the electron Bohr magneton. Higher order corrections to this Fermi formula can be found in [3, 36] and is out of the scope of this thesis.

A.2 One-particle spin-1/2 system

Consider a spin-1/2 particle like an electron or a muon. The eigenfunctions of $\hat{J}_z$, $|\alpha\rangle$ and $|\beta\rangle$, are the spin-up and spin-down states of the particle

$$\hat{J}_z |\alpha\rangle = \frac{1}{2} |\alpha\rangle \tag{A.2}$$

$$\hat{J}_z |\beta\rangle = -\frac{1}{2} |\beta\rangle \ . \tag{A.3}$$

The matrix elements of the $\hat{J}_z$ in this bases are

$$\langle \alpha | \hat{J}_z |\alpha\rangle = \frac{1}{2} \tag{A.4}$$

$$\langle \alpha | \hat{J}_z |\beta\rangle = -\frac{1}{2} \langle \alpha|\beta\rangle = 0 \tag{A.5}$$

$$\langle \beta | \hat{J}_z |\alpha\rangle = \frac{1}{2} \langle \beta|\alpha\rangle = 0 \tag{A.6}$$

$$\langle \beta | \hat{J}_z |\beta\rangle = -\frac{1}{2} \ . \tag{A.7}$$

Hence the matrix representation of $\hat{J}_z$ is

$$\hat{J}_z = \begin{pmatrix} \langle \alpha | \hat{J}_z |\alpha\rangle & \langle \alpha | \hat{J}_z |\beta\rangle \\ \langle \beta | \hat{J}_z |\alpha\rangle & \langle \beta | \hat{J}_z |\beta\rangle \end{pmatrix} = \frac{1}{2} \begin{pmatrix} 1 & 0 \\ 0 & -1 \end{pmatrix} \ . \tag{A.8}$$

Similarly, it can be derived that

$$\hat{J}_x = \frac{1}{2} \begin{pmatrix} 0 & 1 \\ 1 & 0 \end{pmatrix} \tag{A.9}$$

$$\hat{J}_y = \frac{1}{2} \begin{pmatrix} 0 & -i \\ i & 0 \end{pmatrix} \ . \tag{A.10}$$

These operators obey the permutation relations

$$[\hat{J}_i, \hat{J}_j] = i\hbar\epsilon_{ijk}\hat{J}_k \ . \tag{A.11}$$

A.3 Muonium: Two-particle spin-1/2 system

The interaction of the Mu atom (two bound particles with spin-1/2) with an external magnetic field is described by the following Hamiltonian

$$\hat{H} = \Delta W \hat{\mathbf{I}} \cdot \hat{\mathbf{J}} + g_e \mu_B^e \hat{\mathbf{J}} \cdot \mathbf{B} + g_\mu \mu_B^\mu \hat{\mathbf{I}} \cdot \mathbf{B} \ , \tag{A.12}$$

where ΔW is the hyperfine splitting, $\hat{\mathbf{I}} = (\hat{I}_x, \hat{I}_y, \hat{I}_z)$ the muon spin operator, $\hat{\mathbf{J}} = (\hat{J}_x, \hat{J}_y, \hat{J}_z)$ the electron angular momentum operator, $\mu_B^\mu = \dfrac{e\hbar}{2m_e c}$ the muon magnetons, $g_e \approx +2$, $g_\mu \approx -2$ the electron and muon g-factors, and $\mathbf{B}$ is the external static magnetic field. Under a magnetic field along the z-direction $\mathbf{B} = (0, 0, B_z)$, $\hat{H}$ (in the unit of Planck constant, h) can be rewritten as

$$\hat{H} = \nu_0 \hat{\mathbf{J}} \cdot \hat{\mathbf{I}} + \nu_e \hat{J}_z - \nu_\mu \hat{I}_z , \tag{A.13}$$

where the first term account for the hyperfine interaction between the electron and the muon, and the last two terms are the electron and muon Zeeman interactions with frequencies $\nu_e = g_e \mu_B^e B_z$ and $\nu_\mu = g_\mu \mu_B^\mu B_z$, respectively. By defining

$$\hat{J}_+ = \hat{J}_x + i\hat{J}_y \tag{A.14}$$
$$\hat{J}_- = \hat{J}_x - i\hat{J}_y , \tag{A.15}$$

the term $\hat{\mathbf{J}} \cdot \hat{\mathbf{I}}$ can be rewritten as

$$\hat{\mathbf{J}} \cdot \hat{\mathbf{I}} = \hat{J}_x \hat{I}_x + \hat{J}_y \hat{I}_y + \hat{J}_z \hat{I}_z \tag{A.16}$$
$$= \frac{1}{2}(\hat{J}_+ \hat{I}_- + \hat{J}_- \hat{I}_+) + \hat{J}_z \hat{I}_z . \tag{A.17}$$

Considering a basis set of product spin functions $|m_J, m_I\rangle = |\alpha\alpha\rangle$, $|\alpha\beta\rangle$, $|\beta\alpha\rangle$ and $|\beta\beta\rangle$, it can be calculated that

$$\hat{H} |\alpha\alpha\rangle = (\nu_e \hat{J}_z - \nu_\mu \hat{I}_z + \nu_0 \hat{\mathbf{J}} \cdot \hat{\mathbf{I}}) |\alpha\alpha\rangle \tag{A.18}$$
$$= \left[\nu_e \hat{J}_z - \nu_\mu \hat{I}_z + \frac{1}{2}\nu_0(\hat{J}_+ \hat{I}_- + \hat{J}_- \hat{I}_+) + \nu_0 \hat{J}_z \hat{I}_z \right] |\alpha\alpha\rangle \tag{A.19}$$
$$= \left(\frac{\nu_e}{2} - \frac{\nu_\mu}{2} + \frac{\nu_0}{4} \right) |\alpha\alpha\rangle \tag{A.20}$$
$$\hat{H} |\alpha\beta\rangle = \left[\nu_e \hat{J}_z - \nu_\mu \hat{I}_z + \frac{1}{2}\nu_0(\hat{J}_+ \hat{I}_- + \hat{J}_- \hat{I}_+) + \nu_0 \hat{J}_z \hat{I}_z \right] |\alpha\beta\rangle \tag{A.21}$$
$$= \left(\frac{\nu_e}{2} + \frac{\nu_\mu}{2} - \frac{\nu_0}{4} \right) |\alpha\beta\rangle + \frac{\nu_0}{2} |\beta\alpha\rangle . \tag{A.22}$$

It is clear that $|\alpha\alpha\rangle$ is an eigenfunction while $|\alpha\beta\rangle$ is not. By defining

$$\nu_+ = \frac{\nu_e + \nu_\mu}{2} \tag{A.23}$$
$$\nu_- = \frac{\nu_e - \nu_\mu}{2} , \tag{A.24}$$

the Hamiltonian $\hat{H}$ can be expressed in terms of matrix, with the $|\alpha\alpha\rangle$, $|\alpha\beta\rangle$, $|\beta\alpha\rangle$ and $|\beta\beta\rangle$ bases,

$$
\hat{H} = \begin{pmatrix} \dfrac{\nu_0}{4} + \nu_- & 0 & 0 & 0 \\ 0 & -\dfrac{\nu_0}{4} + \nu_+ & \dfrac{\nu_0}{2} & 0 \\ 0 & \dfrac{\nu_0}{2} & -\dfrac{\nu_0}{4} - \nu_+ & 0 \\ 0 & 0 & 0 & \dfrac{\nu_0}{4} - \nu_- \end{pmatrix} . \tag{A.25}
$$

If we label the states $|m_e, m_\mu\rangle$ as

$$
|1'\rangle = |\alpha\alpha\rangle \, ; \ |2'\rangle = |\alpha\beta\rangle \, ; \ |3'\rangle = |\beta\alpha\rangle \, ; \ |4'\rangle = |\beta\beta\rangle \, , \tag{A.26}
$$

then the two eigenvalues are

$$
\nu_{1'} = \frac{\nu_0}{4} + \nu_- ; \ \nu_{4'} = \frac{\nu_0}{4} - \nu_- . \tag{A.27}
$$

Since $|1'\rangle$ and $|4'\rangle$ are already eigenfunctions of $\hat{H}$, to get eigenvalues $\nu_{2'}$ and $\nu_{3'}$, we have to diagonalize the central part of the matrix $\hat{H}$. The characteristic polynomial of the central 2×2 matrix is

$$
(-\frac{\nu_0}{4} + \nu_+ - \nu)(-\frac{\nu_0}{4} - \nu_+ - \nu) - \frac{\nu_0^2}{4} = 0 \, , \tag{A.28}
$$

where the solutions are

$$
\nu_{2,3} = -\frac{\nu_0}{4} \pm \frac{\sqrt{\nu_+^2 + \nu_0^2}}{2} \, . \tag{A.29}
$$

The conventional notation for the Mu eigenstates is

$$
|1\rangle = |\alpha\alpha\rangle \tag{A.30}
$$

$$
|2\rangle = c \, |\alpha\beta\rangle + s \, |\beta\alpha\rangle \tag{A.31}
$$

$$
|3\rangle = |\beta\beta\rangle \tag{A.32}
$$

$$
|4\rangle = c \, |\beta\alpha\rangle - s \, |\alpha\beta\rangle \, , \tag{A.33}
$$

where $c^2 = \dfrac{1}{2}\left(1 + \dfrac{x_B}{\sqrt{1 + x_B^2}}\right)$, $s^2 = \dfrac{1}{2}\left(1 - \dfrac{x_B}{\sqrt{1 + x_B^2}}\right)$ and $x_B = \dfrac{2\nu_+}{\nu_0}$. The corresponding eigenvalues are given by

$$
\nu_1 = \frac{\nu_0}{4} + \nu_- \tag{A.34}
$$

$$
\nu_2 = -\frac{\nu_0}{4} + \frac{\sqrt{\nu_+^2 + \nu_0^2}}{2} = -\frac{\nu_0}{4} + \frac{\nu_0\sqrt{1 + x_B^2}}{2} \tag{A.35}
$$

$$
\nu_3 = \frac{\nu_0}{4} - \nu_- \tag{A.36}
$$

$$
\nu_4 = -\frac{\nu_0}{4} - \frac{\sqrt{\nu_+^2 + \nu_0^2}}{2} = -\frac{\nu_0}{4} - \frac{\nu_0\sqrt{1 + x_B^2}}{2} \, . \tag{A.37}
$$

The energy levels described by Equation A.34 to Equation A.37 are shown in Figure A.1. The weak-field quantum numbers (F, m_F) corresponding to the zero or weak magnetic fields (ν_+, $\nu_- \to 0$ and c, $s \to 1/\sqrt{2}$) hyperfine states, and the strong field quantum numbers (m_J, m_μ) corresponding to the strong field limits (ν_+/ν_0, $\nu_-/\nu_0 \gg 1$ and $c \to 1$, $s \to 0$) are indicated for the four states labeled from 1 to 4.
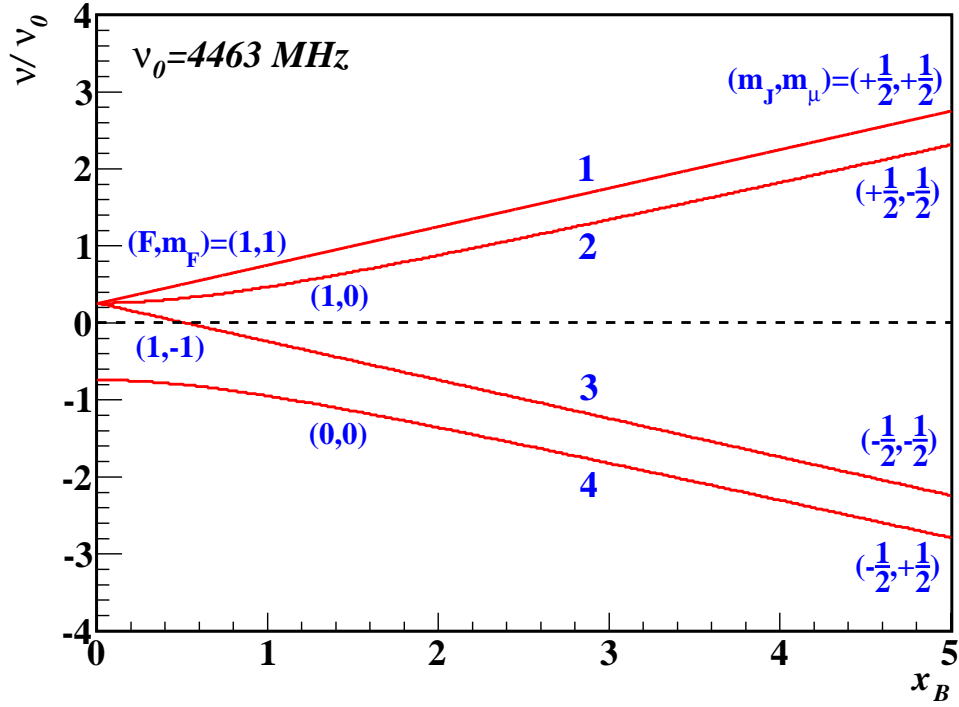
Figure A.1: *Breit-Rabi diagram of Mu in the ground-state, as given by Equation A.34 to A.37. At zero magnetic field, the energy difference between the $F = 0$ and $F = 1$ states is the HFS splitting $\Delta W = h\nu_0$. At weak magnetic fields, (F, m_F) are good quantum numbers whereas at strong magnetic fields, (m_J, m_μ) are the good quantum numbers.*

A.4 Muonium in a longitudinal magnetic field

If the muon ensemble is initially polarized and the electrons are not, then the initial state of the system is

$$|\phi(0)\rangle = \frac{1}{\sqrt{2}} |\alpha\alpha\rangle + \frac{1}{\sqrt{2}} |\beta\alpha\rangle \ . \tag{A.38}$$

This initial state can be represented in terms of $\hat{H}$ eigenstates

$$|\phi(0)\rangle = \frac{1}{\sqrt{2}}|\alpha\alpha\rangle + \frac{1}{\sqrt{2}}|\beta\alpha\rangle = \frac{1}{\sqrt{2}}|1\rangle + \frac{1}{\sqrt{2}}(s|2\rangle + c|4\rangle) . \tag{A.39}$$

How does this system evolve in time? The $|\alpha\alpha\rangle = |1\rangle$ state being eigenstate of $\hat{H}$ will remain static while the mixed state $|\beta\alpha\rangle$ oscillates between the states $|2\rangle$ and $|4\rangle$ at a frequency $\nu_{24} = \nu_0\sqrt{1 + x_B^2}$. To understand this oscillation, only the time evolution of the $|\beta\alpha\rangle$ state is considered. To simplify the notation, we re-define $|\phi\rangle = |\beta\alpha\rangle$. Thus its time evolution is given by

$$|\phi(t)\rangle = \frac{1}{\sqrt{2}}(se^{-iE_2t/\hbar}|2\rangle + ce^{-iE_4t/\hbar}|4\rangle) . \tag{A.40}$$

The probability of finding the $|\phi(t)\rangle$ state with the μ^+ spin state in $+z$ direction is then

$$P_{+z} = |\langle\alpha\alpha|\phi(t)\rangle|^2 + |\langle\beta\alpha|\phi(t)\rangle|^2 \tag{A.41}$$
$$= |\langle 1|\phi(t)\rangle|^2 + |(s\langle 2| + c\langle 4|)|\phi(t)\rangle|^2 . \tag{A.42}$$

The first term is

$$|\langle 1|\phi(t)\rangle|^2 = \left|\frac{1}{\sqrt{2}}(se^{-iE_2t/\hbar}\langle 1|2\rangle + ce^{-iE_4t/\hbar}\langle 1|4\rangle)\right|^2 \tag{A.43}$$
$$= 0 , \tag{A.44}$$

because the $|1\rangle$, $|2\rangle$, $|3\rangle$, $|4\rangle$ states are orthogonal. The second term is

$$|(s\langle 2| + c\langle 4|)|\phi(t)\rangle|^2 = \left|\frac{1}{\sqrt{2}}(s^2 e^{-iE_2t/\hbar}\langle 2|2\rangle + cse^{-iE_4t/\hbar}\langle 2|4\rangle\right.$$
$$\left. + cse^{-iE_2t/\hbar}\langle 4|2\rangle + c^2 e^{-iE_4t/\hbar}\langle 4|4\rangle)\right|^2 \tag{A.45}$$

$$= \frac{1}{2}|(s^2 e^{-iE_2t/\hbar} + c^2 e^{-iE_4t/\hbar})|^2 \tag{A.46}$$

$$= \frac{1}{2}|e^{-i(E_2+E_4)t/2\hbar}(s^2 e^{-i(E_2-E_4)t/2\hbar} + c^2 e^{-i(E_4-E_2)t/2\hbar})|^2 \tag{A.47}$$

$$= \frac{1}{2}|(s^2 e^{-i2\pi\nu_{24}t/2} + c^2 e^{i2\pi\nu_{24}t/2})|^2 \tag{A.48}$$

$$= \frac{1}{2}(s^2 e^{-i2\pi\nu_{24}t/2} + c^2 e^{i2\pi\nu_{24}t/2})(s^2 e^{i2\pi\nu_{24}t/2} + c^2 e^{-i\omega_{24}t/2}) \tag{A.49}$$

$$= \frac{1}{2}\left[s^4 + c^4 + c^2 s^2(e^{-i2\pi\nu_{24}t} + e^{i2\pi\nu_{24}t})\right] \tag{A.50}$$

$$= \frac{1}{2}\left[s^4 + c^4 + 2c^2 s^2\cos 2\pi\nu_{24}t\right] , \tag{A.51}$$

where $\nu_{24} = \dfrac{E_2 - E_4}{h} = \nu_0\sqrt{1 + x_B^2}$ as mentioned before. Substituting c^2 and s^2 into Equation A.51, the muon polarization in the z-direction is obtained:

$$P_{+z} = \frac{1}{2}\left(\frac{1 + 2x_B^2 + \cos 2\pi\nu_{24}t}{1 + x_B^2}\right)\ . \tag{A.52}$$

The μ^+ polarization has a component precessing with a frequency ν_{24} which is usually too high to be resolved experimentally ($\nu_0 \approx 4.5$ GHz).

A.5   Muonium in a transverse magnetic field

Similar calculation can be applied to the Mu in a transverse magnetic field configuration even though it is much more complex in this situation and requires a transformation of the basis as the initial polarization is perpendicular to the magnetic field. As the final result, the muon polarization along the transverse direction is given by [98, 149]

$$P_\perp = \frac{1}{2}\left[c^2(e^{i2\pi\nu_{12}t} + e^{i2\pi\nu_{43}t}) + s^2(e^{i2\pi\nu_{14}t} + e^{i2\pi\nu_{23}t})\right]\ , \tag{A.53}$$

where ν_{12}, ν_{43}, ν_{14} and ν_{23} are frequencies defined as

$$\nu_{12} = \frac{E_1 - E_2}{h} = \nu_- + \frac{\nu_0}{2} - \frac{\nu_0\sqrt{1 + x_B^2}}{2} \tag{A.54}$$

$$\nu_{43} = \frac{E_4 - E_3}{h} = \nu_- - \frac{\nu_0}{2} - \frac{\nu_0\sqrt{1 + x_B^2}}{2} \tag{A.55}$$

$$\nu_{14} = \frac{E_1 - E_4}{h} = \nu_- + \frac{\nu_0}{2} + \frac{\nu_0\sqrt{1 + x_B^2}}{2} \tag{A.56}$$

$$\nu_{23} = \frac{E_2 - E_3}{h} = \nu_- - \frac{\nu_0}{2} + \frac{\nu_0\sqrt{1 + x_B^2}}{2}\ . \tag{A.57}$$

For a low magnetic field, $x_B \to 0$ and these equations simplify to

$$\nu_{12} \to \nu_- \tag{A.58}$$

$$\nu_{43} \to \nu_- - \nu_0 \approx -\nu_0 \tag{A.59}$$

$$\nu_{14} \to \nu_- + \nu_0 \approx +\nu_0 \tag{A.60}$$

$$\nu_{23} \to \nu_-\ . \tag{A.61}$$

Thus for weak magnetic fields the transverse polarization $P_\perp$ becomes

$$P_\perp \approx \frac{1}{2}\left[c^2(e^{i2\pi\nu_-t} + e^{-i2\pi\nu_0t}) + s^2(e^{i2\pi\nu_0t} + e^{i2\pi\nu_-t})\right]\ . \tag{A.62}$$

Note that $\nu_0 \approx 4.5$ GHz is much larger than ν_- for small magnetic fields ($\nu_- = 1.4$ MHz/-Gauss). ν_0 is also not resolvable by the LEM apparatus because of the limited time resolution (≈ 5 ns). Because of this, Equation A.62 can be simplified to

$$P_\perp \approx \frac{1}{2}(e^{i2\pi\nu_- t}) \ . \tag{A.63}$$

This shows why only half of the polarization of the Mu in the LEM apparatus is observable. Furthermore, from Equation A.24 we have that

$$\nu_- = \frac{\nu_e - \nu_\mu}{2} \approx \frac{\nu_e}{2} \ , \tag{A.64}$$

because the muon mass is much larger than the electron mass. Hence the muon spin in the Mu atom is precessing at a frequency given by Equation A.64 which is half the electron precession frequency.

A.6   Two-frequency precession of muonium

At intermediate magnetic field strength, the precession of μ^+ in Mu is described by two frequencies ν_{12} and ν_{23} defined in Figure A.2. The frequencies of the hyperfine splitting ν_0 of Mu in a material environment can be found by using two-frequency precession method (see for example [150]). By studying the ν_0, the "condition" of Mu atom, whether it is being "compressed" or being "tear apart" can be investigated. The ν_0 expressed in terms of ν_{12} and ν_{23} can be derived using the knowledge from previous sections.

By taking the sum and the difference of Equation A.54 and Equation A.57, we get

$$\nu_{12} + \nu_{23} = 2\nu_- \tag{A.65}$$

$$\nu_{12} - \nu_{23} = -\nu_0 + \nu_0\sqrt{1 + x_B^2} \tag{A.66}$$

$$= -\nu_0 + \nu_0\sqrt{1 + (2\nu_+/\nu_0)^2} \tag{A.67}$$

$$= -\nu_0 + \sqrt{\nu_0^2 + (2\nu_+)^2} \ . \tag{A.68}$$

Rearranging Equation A.68 we obtain

$$\sqrt{\nu_0^2 + (2\nu_+)^2} = \nu_{12} - \nu_{23} + \nu_0 \tag{A.69}$$

$$\nu_0^2 + (2\nu_+)^2 = \nu_{12}^2 + \nu_{23}^2 + \nu_0^2 - 2\nu_{12}\nu_{23} + 2\nu_0(\nu_{23} - \nu_{12}) \ . \tag{A.70}$$
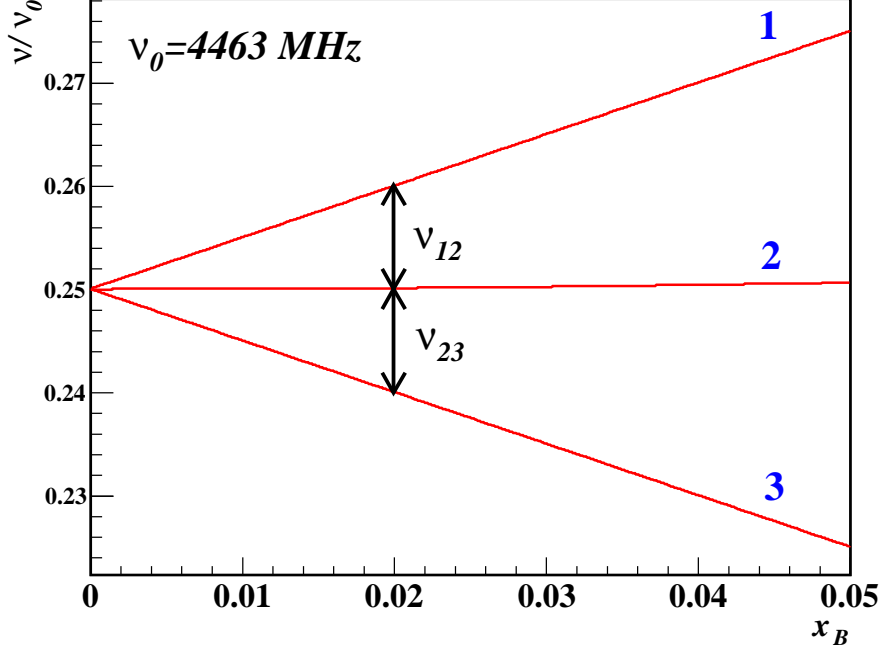
Figure A.2: *Energy-level diagram for Mu in the eigenstates labeled 1, 2 and 3. The Mu splitting frequencies ν_{12} and ν_{23} can be used to determine the Mu hyperfine splitting ν_0 via Equation A.74.*

Solving for ν_0 using Equation A.23, Equation A.24 and Equation A.65, we get

$$\nu_0 = \frac{(2\nu_+)^2 - (\nu_{23} - \nu_{12})^2}{2(\nu_{23} - \nu_{12})} \tag{A.71}$$

$$= \frac{(2\nu_- + 2\nu_\mu)^2 - (\nu_{23} - \nu_{12})^2}{2(\nu_{23} - \nu_{12})} \tag{A.72}$$

$$= \frac{(\nu_{12} + \nu_{23} + 2\nu_\mu)^2 - (\nu_{23} - \nu_{12})^2}{2(\nu_{23} - \nu_{12})} \ . \tag{A.73}$$

This means that the Mu hyperfine splitting ν_0 can be calculated by measuring the Mu splitting frequencies ν_{12} and ν_{23} and the muon Larmor precession frequency ν_μ via

$$\nu_0 = \frac{1}{2} \left[\frac{(\nu_{12} + \nu_{23} + 2\nu_\mu)^2}{\nu_{23} - \nu_{12}} + \nu_{12} - \nu_{23} \right] \ . \tag{A.74}$$

A more detailed treatment is given in [112, 128]. Assuming that all the frequencies are independent variables, then the error propagation is as follows:

$$\sigma_{\nu_0}^2 = \left(\frac{\partial \nu_0}{\partial \nu_{12}} \right)^2 \sigma_{\nu_{12}}^2 + \left(\frac{\partial \nu_0}{\partial \nu_{23}} \right)^2 \sigma_{\nu_{23}}^2 + \left(\frac{\partial \nu_0}{\partial \nu_\mu} \right)^2 \sigma_{\nu_\mu}^2 \ , \tag{A.75}$$

where

$$\left(\frac{\partial \nu_0}{\partial \nu_{12}}\right) = \frac{2\nu_{23}^2 + 4\nu_{23}\nu_\mu + 2\nu_\mu^2}{(\nu_{12} - \nu_{23})^2} \tag{A.76}$$

$$\left(\frac{\partial \nu_0}{\partial \nu_{23}}\right) = \frac{-2\nu_{12}^2 - 4\nu_{12}\nu_\mu - 2\nu_\mu^2}{(\nu_{12} - \nu_{23})^2} \tag{A.77}$$

$$\left(\frac{\partial \nu_0}{\partial \nu_\mu}\right) = 2\left(\frac{2\nu_{12} + \nu_{23} + 2\nu_\mu}{\nu_{23} - \nu_{12}}\right) . \tag{A.78}$$

Appendix B

The growth of mesoporous thin silica films

In this appendix, recipes used to prepare mesoporous silica thin films relevant to this thesis are provided. They are based on [151] and [152] and have been optimized by L. Liskay from CEA Saclay for positronium yield in vacuum.

B.1   CTACl-based (C) film

Materials

- CTACl (Hexadecyl trimethyl ammonium chloride, $CH_3(CH_2)_{15}NCl\,(CH_3)_3$) (m=364.45) (Sigma-Aldrich 52366-10G)

- TEOS (tetraethyl orthosilicate) $m = 208.33$ (Sigma-Aldrich 86578-1L)

- HCl 30% 9.45 mol/l (Sigma-Aldrich 17077-1L)

- distilled water

- glass or Si substrate (e.g. standard microscope cover glass)

Recipe

- global composition: 25 H_2O : 5 x 10^{-3} HCl : 1 TEOS : 0.22 CTACl

- reference: Cohen et. al., Advance Materials 15, 572 (2003)

- 1 g CTACl

- 2.959 g TEOS

- 6.406 g [H$_2$O + HCl] where [H$_2$O + HCl] is 851.6 ml H$_2$O + 1 ml 30% HCl

Procedure

- mix [H$_2$O + HCl] (851.6 ml/1 ml)

- take 6.406g from the HCl solution and mix with 2.959 g TEOS; keep stirred

- add CTACl to the mixture when stirring vigorously

- cover it with Parafilm and let stirred overnight (16 h)

- mount the substrate on the spin coater (surface perpendicular to the axis; use sticky tape)

- put a drop of gel in the middle with a glass rod and smear it over the surface; it should cover the whole surface

- run spin coating (1000 rpm) for 2 min

- take the sample from the spin coater

- wait 1-5 hours at room temperature and then put the samples on the heating plate; heat it to 130°

- keep at 130° for about two days

- store at room temperature

- heat at 450° for 15 min in air just before mounting in the vacuum (heating up with the plate)

Remark

The resulting film will be around 800 nm thick (to be confirmed again), although the viscosity is not controlled so this value may change from preparation to preparation.

  It seems that the 130° heating phase might not be essential.

B.2 Pluronic F-127-based (F) film

Materials

- Pluronic F-127 (triblock copolymer, 9003-11-6 Sigma-Aldrich), m=13336

- TEOS (tetraethyl orthosilicate) $m = 208.33$ (Sigma-Aldrich 86578-1L)

- HNO_3 concentrated

- distilled water

- glass or Si substrate (e.g. standard microscope cover glass)

Recipe

- reference: Yantasee et al, The Analyst 128, 899 (2003)

- global recipe (molar ratio): TEOS : water : ethanol : HNO_3 : Pluronic F-127 = 1 : 8 : 8 : 0.05 : 0.016

- 5.16 g F-127

- 3.430 g H_2O

- 8.846 g EtOH

- 0.108 g HNO_3 concentrated ($\approx$69%)

- 5.0 g TEOS

Procedure

- dissolve F-127 in water + alcohol

- add HNO_3

- add TEOS

- mix and keep stirring a day (max 200 rpm to prevent bubble formation)

- put a drop of gel in the middle of the silicon wafer with a glass rod and smear it over the surface; it should cover the whole surface

- run spin coating (3000 rpm) for 1 min

- take the sample from the spin coater

- put the samples on the heating plate; heat it to 250°

- store at room temperature

- heat at 450° for 15 min in air just before mounting in the vacuum (heating up with the plate)

Remark

It seems that fast heating (dropping the sample on the pre-heated heating plate (results in higher o-Ps emission from the deeper region (presumably the porosity is more open due to the destruction of some of the walls).

Appendix C

Fraction of muons hitting the sample

To determine the Mu production probability per implanted μ^+ we need to know the fraction of the μ^+ really hitting the mesoporous silica sample. This fraction is denoted as x and is used to correct for the F_{Mu}^0 obtained in Section 3.5. Two different approaches have been used to determine x for the 2011 and the 2012 beam times and will be explained in the following sections.

C.1   Beam time 2011

To determine the fraction of μ^+ hitting the sample x, the muon decay asymmetries (only the ones of the upstream detectors) for a 20×20 mm^2 fused quartz sample mounted on the nose sample plate is compared with a fused quartz reference sample with a diameter of 50 mm mounted on the regular LEM sample plate (which is 16 mm downstream in the z-direction compared to the nose sample plate). Note that the muon decay asymmetries (A_μ, A_{Mu}) of the upstream detector do not depend on the exact position (in z-direction) of the sample. From the reference measurement which was done at 19 keV implantation energy [106], the fraction of implanted μ^+ which remains as free μ^+ (not bound to form Mu) can be determined from the fitted asymmetries

$$F_\mu^{\mathrm{ref}}(19 \text{ keV}) = \frac{A_\mu^{\mathrm{ref}}}{A_{\mathrm{tot}}^{\mathrm{ref}}} = 0.150(1) \ . \tag{C.1}$$

C.1.1   30 mm nose sample plate

From a μSR measurement done using a 20×20 mm^2 fused quartz sample mounted on the 30 mm nose sample plate, the fraction of μ^+ on the sample can be determined:

$$F_\mu(19 \text{ keV}) = \frac{A_\mu}{A_{\text{tot}}} = \frac{0.045(1)}{0.246(6)} = 0.18(1) \ . \tag{C.2}$$

This result is slightly higher compared to the reference measurement $F_\mu^{\text{ref}}(19 \text{ keV}) = 0.150(1)$. This is due to μ^+ stopping outside of the sample as these μ^+ do not form
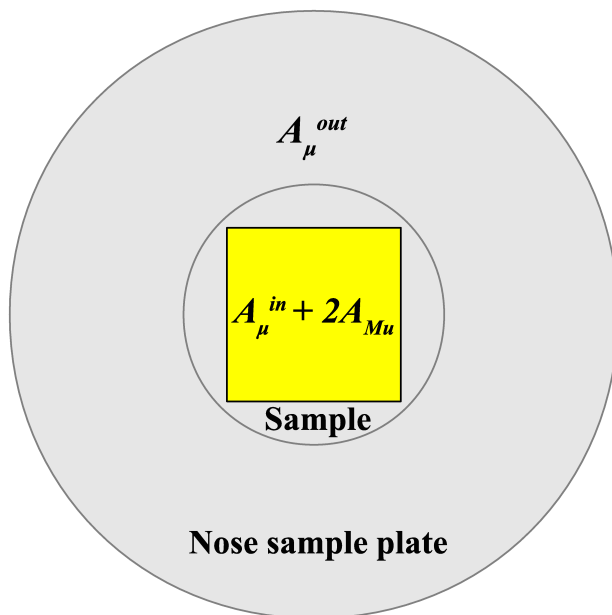
Figure C.1: *The 30 mm nose sample plate as seen along the z-axis with a 20×20 mm^2 sample in the center. The nose plate is coated with 1 μm of Ag.*

Mu because they are implanted in Ag. Figure C.1 is showing the 30 mm nose sample plate seen along the z-axis with a 20×20 mm^2 sample in the center. The nose plate was coated with about 1 μm of Ag. Thus μ^+ which miss the sample are implanted into Ag. We assume that in Ag, $F_\mu = 1$ and $F_{\text{Mu}} = 0$ which is a good approximation of the measured values [81]. Therefore we can write

$$A_\mu = A_\mu^{\text{in}} + A_\mu^{\text{out}} \tag{C.3}$$

$$A_{\text{Mu}} = A_{\text{Mu}}^{\text{in}} \tag{C.4}$$

$$A_{\text{tot}} = A_\mu^{\text{in}} + A_\mu^{\text{out}} + 2A_{\text{Mu}} \ . \tag{C.5}$$

The fraction x of μ^+ hitting the sample is then given by

$$x = \frac{A_\mu^{\text{in}} + 2A_{\text{Mu}}}{A_{\text{tot}}} = \frac{A_{\text{tot}} - A_\mu^{\text{out}}}{A_{\text{tot}}} \ . \tag{C.6}$$

The fraction of μ^+ after implantation (normalizing correctly to the number of μ^+ which really hit the sample) is thus given by

$$F_\mu^{\text{cor}} = \frac{A_\mu^{\text{in}}}{A_{\text{tot}} - A_\mu^{\text{out}}} \ . \tag{C.7}$$

Since F_μ^{cor} has to be the same as F_μ^{ref} we get

$$\frac{A_\mu^{\text{in}}}{A_{\text{tot}} - A_\mu^{\text{out}}} = F_\mu^{\text{ref}} \ . \tag{C.8}$$

Substituting $A_\mu^{\text{in}} = A_\mu - A_\mu^{\text{out}}$ into Equation C.8 and rearranging the terms, we obtain

$$A_\mu^{\text{out}} = \frac{F_\mu^{\text{ref}} A_{\text{tot}} - A_\mu}{F_\mu^{\text{ref}} - 1} \ . \tag{C.9}$$

Finally after substituting Equation C.9 into Equation C.6 and rearranging the terms, we find

$$x = \frac{A_{\text{tot}} - A_\mu^{\text{out}}}{A_{\text{tot}}} = \frac{A_{\text{tot}} - A_\mu}{(1 - F_\mu^{\text{ref}}) \cdot A_{\text{tot}}} \ . \tag{C.10}$$

For 19 keV muon implantation energy, the fraction of μ^+ hitting the sample is

$$x = \frac{A_{\text{tot}} - A_\mu}{(1 - F_\mu^{\text{ref}}) \cdot A_{\text{tot}}} = \frac{0.246 - 0.045}{(1 - 0.150) \cdot 0.246} = 0.96(4) \ . \tag{C.11}$$

This means that for 19 keV implantation energy only about $4(4)\%$ of the μ^+ are missing the 20×20 mm^2 sample. Repeating the calculation for 5 keV and 14 keV, we find $x = 0.75(4)$ and $x = 0.92(4)$, respectively. The results are summarized in Table C.1. These values are used to correct the fraction of Mu formed in the sample as the following equation:

$$F_{\text{Mu}}^{0,\text{cor}} = \frac{F_{\text{Mu}}^0}{x} = \frac{1 - F_\mu}{x} \ . \tag{C.12}$$

where $F_\mu = \dfrac{A_\mu}{A_{\text{tot}}}$ as explained in Chapter 3.4.

145

Table C.1: *Total asymmetry A_{tot} and fraction of μ^+ beam hitting the sample x for various implantation energies E. Values at 5, 14 and 19 keV were calculated from the 30 mm nose sample plate measurements. Values at 3 and 10 keV were deduced from an empirical fit to the x values of 5, 14 and 19 keV shown in Figure C.2.*

E (keV)	3	5	10	14	19
A_{tot}	0.225(36)	0.233(5)	0.243(45)	0.238(4)	0.240(4)
x	0.68(5)	0.75(4)	0.87(4)	0.92(4)	0.96(4)

C.1.2   45 mm nose sample plate

No fused quartz measurements have been done for the 45 mm nose sample plate. Thus the data for the measurements performed with the 45 mm nose sample plate were corrected in an approximate way using the 30 mm nose sample plate measurements. To check the validity of this approximative correction, $F_{\text{Mu}}^{0,\text{cor}}$ for C-sample measured with the 45 mm nose sample plate for various implantation energies using the x extracted from the 30 mm nose sample plate have been calculated:

$$F_{\text{Mu}}^{0,\text{cor}}(5 \text{ keV}) = \frac{1 - F_\mu}{x} = \frac{1 - \frac{0.127(2)}{0.233(5)}}{0.75(4)} = 0.61(3) \tag{C.13}$$

$$F_{\text{Mu}}^{0,\text{cor}}(14 \text{ keV}) = \frac{1 - F_\mu}{x} = \frac{1 - \frac{0.111(2)}{0.238(4)}}{0.92(4)} = 0.58(3) \ . \tag{C.14}$$

Both values of F_{Mu}^0 agree well with each other confirming the validity of the correction. In fact it was demonstrated with the F-sample using the 30 mm nose sample plate that F_{Mu}^0 is energy independent. This means that the correction of the energy-dependent beam size was correct because it reproduces the observation that F_{Mu}^0 do not depend on the μ^+ implantation energy. By assuming again that the fraction of μ^+ beam missing the sample is identical for the same implantation energy for both sample plates, the fraction $(1-x)$ of μ^+ missing the sample for 3 keV and 10 keV can be obtained from an educated empirical fit of $(1-x)$ versus μ^+ implantation energy for 30 mm plate with an exponential function

$$1 - x = e^{a+bE} \ , \tag{C.15}$$

where a and b are the constants and E is the implantation energy. The fit results are a=-0.74 and b=-0.13 as shown in Figure C.2. The deduced implanted fraction x at 3 keV and 10 keV are $x = 0.68(5)$ and $x = 0.87(4)$, respectively. Since $F_{\text{Mu}}^0 = 0.60(2)$ (the average of $F_{\text{Mu}}^{0,\text{cor}}(5 \text{ keV})$ and $F_{\text{Mu}}^{0,\text{cor}}(14 \text{ keV})$ at all implantation energies, the total
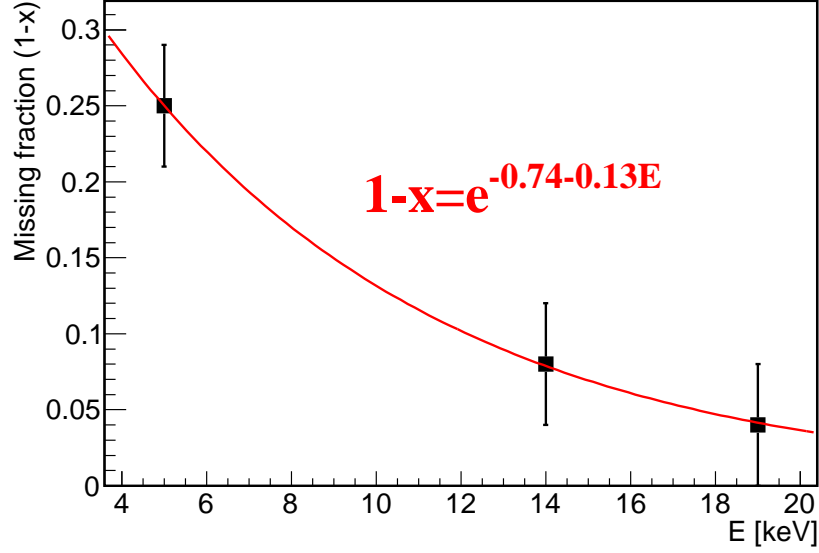
Figure C.2: *Fraction of μ^+ missing the sample $1 - x$ for the measurements done on a 20×20 mm^2 fused quartz mounted on the 30 mm nose sample plate. The line is an educated fit with an exponential function.*

asymmetries at 3 keV and 10 keV for C-sample can be determined:

$$F_{\mathrm{Mu}}^{0,\mathrm{cor}}(3 \text{ keV}) = \frac{1 - F_\mu}{x} = \frac{1 - \frac{0.133(2)}{A_{\mathrm{tot}}(3 \text{ keV})}}{0.68(5)} = 0.60(2) \tag{C.16}$$

$$\Rightarrow A_{\mathrm{tot}}(3 \text{ keV}) = 0.225(36) \tag{C.17}$$

$$F_{\mathrm{Mu}}^{0,\mathrm{cor}}(10 \text{ keV}) = \frac{1 - F_\mu}{x} = \frac{1 - \frac{0.116(2)}{A_{\mathrm{tot}}(10 \text{ keV})}}{0.87(4)} = 0.60(2) \tag{C.18}$$

$$\Rightarrow A_{\mathrm{tot}}(10 \text{ keV}) = 0.243(45) \ . \tag{C.19}$$

$A_{\mathrm{tot}}(10 \text{ keV})$ is comparable with $A_{\mathrm{tot}}(14 \text{ keV})$ and $A_{\mathrm{tot}}(19 \text{ keV})$ in Table C.1 indicating the backscattering effect is negligible, while the smaller values of $A_{\mathrm{tot}}(3 \text{ keV})$ and $A_{\mathrm{tot}}(5 \text{ keV})$ show that the backscattering effect increases with decreasing implantation energy. All obtained values of A_{tot} are "reasonable" thus strengthening the validity of the correction.

Another consistency check can be done by comparing A_μ for various implantation energies measured from C- and F-samples. Based on Table 3.1, for C-sample (on the

45 mm nose sample plate) at 250 K, the following ratios can be obtained:

$$\frac{A_\mu(3\text{ keV}, 100\text{ G})}{A_\mu(14\text{ keV}, 100\text{ G})} = \frac{0.133(2)}{0.111(2)} = 1.20(3) \tag{C.20}$$

$$\frac{A_\mu(5\text{ keV}, 100\text{ G})}{A_\mu(14\text{ keV}, 100\text{ G})} = \frac{0.127(2)}{0.111(2)} = 1.14(3) \ , \tag{C.21}$$

whereas for the F-sample (on the 30 mm nose sample plate)

$$\frac{A_\mu(5\text{ keV}, 100\text{ G})}{A_\mu(14\text{ keV}, 100\text{ G})} = \frac{0.115(3)}{0.102(2)} = 1.13(4) \ . \tag{C.22}$$

The equality of the numerical values of Equation C.21 and Equation C.22 implies that the ratio of the fraction of μ^+ hitting the sample is the same for both sample plates (30 mm nose and 45 mm nose). Note that for 14 keV implantation energy they are about the same for both plates because there are no bias voltages applied on the nose sample plates.

Comparing Equation C.20 with Equation C.21 it can be seen that A_μ increases with decreasing energy. This means that at low implantation energy a higher fraction of μ^+ is hitting the Ag where no Mu formation occurs. This means that the beam size increases at lower implantation energy. Results from Appendix C.1 are summarized in Table C.1.

C.2 Beam time 2012

For the measurements of beam time 2012, another approach is used to estimate the fraction x of μ^+ hitting the sample plate. The values estimated in beam time 2011 are not valid anymore due to the changes in the LEM beam line.

First, the total decay asymmetry $A_{\text{tot}}(\text{Ag})$ is measured using a silver-coated nose sample plate. Silver was chosen because of its large decay asymmetry A_μ and because there is no Mu formation in this material [86]. Moreover, A_μ of silver has been measured to be temperature independent [81]. Next, the central part of the nose sample plate corresponding to the area occupied by the sample is coated with a 500 nm-thick 20×20 mm^2 Ni layer. In a ferromagnetic material like Ni, the fraction of μ^+ that hits the sample experiences a broad distribution of static internal magnetic fields (≈ 64 mT) [119], and hence exhibits a fast relaxation during the first 100 ns [120]. Therefore the residual precession signal $A_\mu^{\text{res}}(\text{Ni})$ which is observed in the LEM apparatus is coming from those μ^+ which are stopping outside the 20×20 mm^2 sample region. Hence the fraction x of μ^+ hitting the sample is given by

$$x = 1 - \frac{A_\mu^{\text{res}}(\text{Ni})}{A_{\text{tot}}(\text{Ag})} \ . \tag{C.23}$$

The results from the data taken in summer 2012 are summarized in Table C.2 .

Table C.2: *Fraction of μ^+ implanted into the sample.*

E (keV)	2	3	5	10	14
$A_{\mathrm{tot}}(\mathrm{Ag})$	0.157(1)	0.170(1)	0.186(1)	0.198(1)	0.204(1)
$A_{\mathrm{res}}(\mathrm{Ni})$	0.069(1)	0.060(1)	0.053(1)	0.036(1)	0.031(1)
x	0.57(3)	0.65(2)	0.72(2)	0.82(1)	0.85(1)

Appendix D

Energy loss of muons in the carbon foil from time of flight measurements
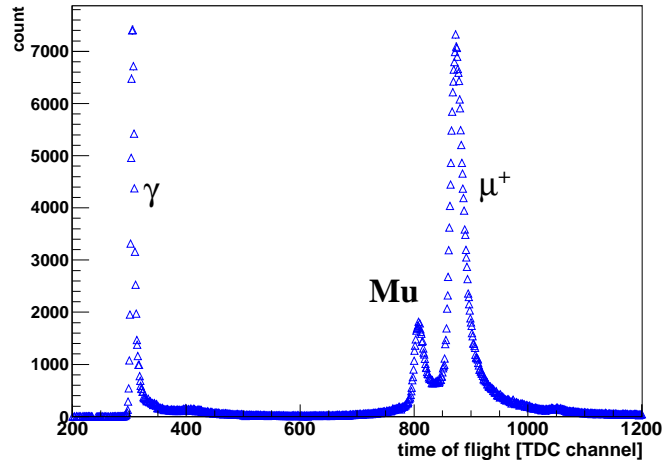
Figure D.1: *Time of flight distribution for various particles from the start detector to a MCP detector placed at the sample plate position ($z = 18.5$ mm) for 12 kV μ^+ beam transport energy. The peaks are corresponding to the prompt photons, the foil "fast" Mu and the μ^+, respectively.*

Energy loss of the μ^+ in the carbon foil of the start detector (TD) was determined using the data from run 321 to 327 (summer 2013). The time-of-flight (TOF) between TD and the MCP2 detector located at the sample plate location (see Figure 5.1) was measured

with different HV settings at the moderator (V_{mod}) between 8.5 kV and 18.0 kV. The L3 and RA were set to 0 kV so that μ^+ has a "field-free" region to drift to the MCP2 and also to ease the calculation of the TOF for the charged particle. In Figure D.1, an example of the time of flight distribution is shown.

By utilizing the fast Mu formed at the carbon foil which also reaches the MCP2 and from the drift distance $d_{\mathrm{TD-MCP2}}$, energy of the Mu can be calculated. Since the energy of the Mu is not affected by the electric fields in the start detector, it is equal to the energy of the μ^+ coming out from the carbon foil, E_{CFoil}. To get an accurate result for the TOF, the drift distance $d_{\mathrm{TD-MCP2}}$ has to be determined. Its value is 563 mm from the technical drawing and has to be cross checked using the TOF measured at different HV settings.

The time zero t_0 for a TOF measurement is given by:

$$t_0 = t_{pp} - t_{\mathrm{FE}} - t_c \ , \tag{D.1}$$

where t_{pp} is the position of the prompt γ peak, t_{FE} is the TOF of the foil electrons from the carbon foil to MCP3 in the TD and can be determined from the time difference of the two prompt peaks in the μ^+ decay spectra, and t_c is the TOF of a particle with the speed of light from TD to MCP2. For run 321 to 327,

$$t_0 = 305 - 69 - 10 = 226 \ , \tag{D.2}$$

in the unit of TDC bin (1 TDC bin = 0.1953125 ns). Peak positions t_P of the Mu and μ^+ are determined by fitting a Gaussian to the TOF peaks. Mean TOF of each particle is calculated using

$$t_{\mathrm{TOF}}^{\mathrm{peak}} = t_P - t_0 \ . \tag{D.3}$$

By substituting the distance between TD and MCP2 $d_{\mathrm{TD-MCP2}} = 563$ mm into the equation below,

$$E_{\mathrm{CFoil}} = \frac{m_{\mathrm{Mu}}}{2} \left(\frac{d_{\mathrm{TD-MCP2}}}{t_{\mathrm{TOF}}^{\mathrm{Mu,peak}}} \right)^2 \ , \tag{D.4}$$

where E_{CFoil} is the Mu energy after exiting the carbon foil can be calculated. Since the Mu is gaining 3.38 kV due to the negative bias applied to the carbon foil, and since it is not decelerated due to its neutral charge state downstream side of the TD, the energy loss in the carbon foil can be calculated using

$$E_{\mathrm{loss}} = \mathrm{HV} + 3.38 - E_{\mathrm{CFoil}} \ . \tag{D.5}$$

All the results are summarized in Table D.1. To check if the assumed drift distance $d_{TD-MCP2}$ is consistent with the experimental results, $t_{\mathrm{TOF}}^{\mu^+,\mathrm{peak}}$ is compared to the $t_{\mathrm{TOF}}^{\mu^+,\mathrm{calc}}$ which is calculated based on simple kinematic calculations.

Table D.1: *Mean TOF of μ^+ and Mu from TD to MCP2. The energy E_{CFoil} of the particle after the carbon foil is determined from Mu TOF peak. From E_{CFoil}, energy loss E_{loss} in the carbon foil can be calculated.*

V_{mod}	8.5	10.0	12.0	13.5	15.0	16.5	18.0
$t_{TOF}^{\mathrm{Mu,peak}}$ (ns)	131.4(2)	123.0(2)	113.7(2)	107.8(2)	102.9(2)	98.8(2)	94.9(2)
E_{CFoil} (keV)	10.84(4)	12.37(4)	14.49(5)	16.11(6)	17.67(7)	19.17(8)	20.78(9)
$t_{\mathrm{TOF}}^{\mu^+,\mathrm{peak}}$ (ns)	152.7(2)	139.8(2)	126.4(2)	118.6(2)	112.1(2)	106.8(2)	101.6(2)
$t_{\mathrm{TOF}}^{\mu^+,\mathrm{calc}}$ (ns)	152.9(3)	140.0(3)	126.5(3)	118.4(3)	112.0(3)	106.7(3)	101.8(3)
E_{loss} (keV)	1.04(4)	1.01(4)	0.89(5)	0.77(6)	0.71(7)	0.71(8)	0.60(9)
E_{in} (keV)	7.46(4)	8.99(4)	11.11(5)	12.73(6)	14.29(7)	15.79(8)	17.40(9)
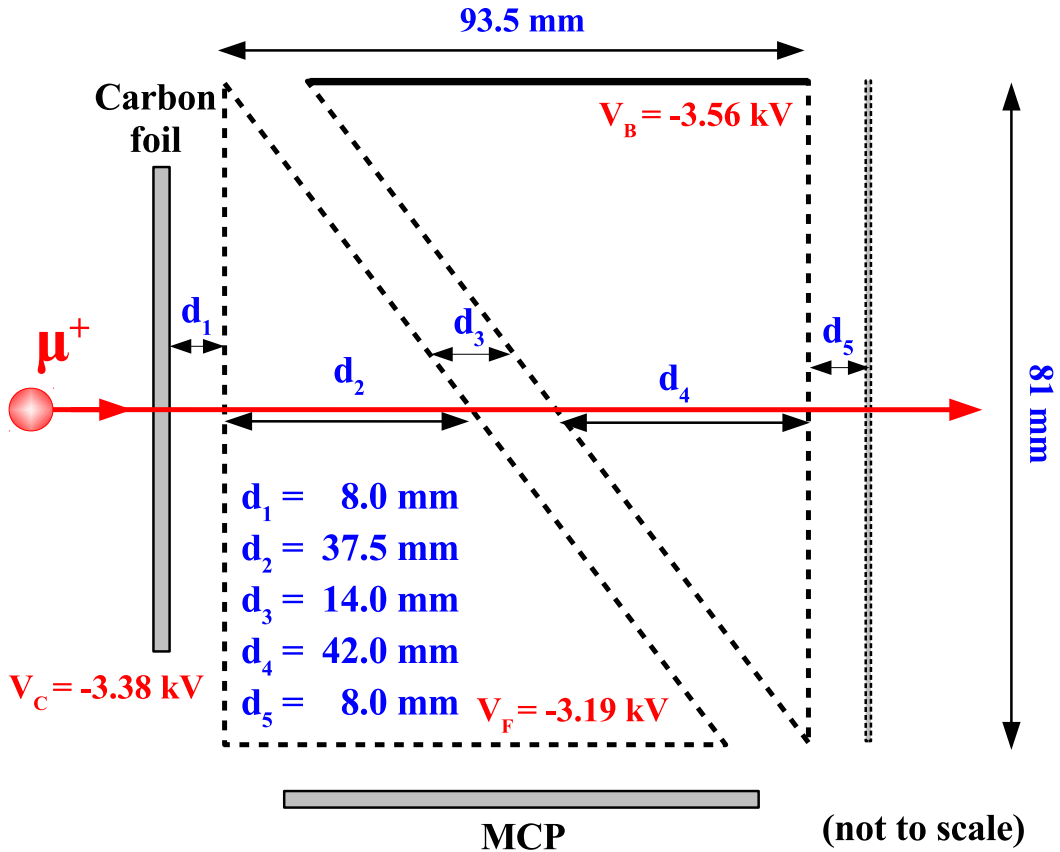
Figure D.2: *Schematic of the start detector. Starting from the left, the μ^+ traversing through the carbon foil and several grids held at different electric potentials before exiting the TD.*

The time-of-flight of μ^+ for the drift from the carbon foil to the MCP2 is calculated by dividing the start detector into several regions based on the electric potentials. $d_{\text{TD}-\text{MCP2}}$ and E_{CFoil} are the inputs to the calculation. The electric potentials V_C, V_F and V_B (at carbon foil, front and back "triangle") are set to -3.38, -3.19 and -3.56 kV respectively. The drift lengths d_1 to d_5 on the beam axis are taken from the technical drawings (see Figure D.2). The kinematics of the particle in the TD is calculated according to the particle mass, the potential V_C, V_F, V_B and the drift distances d_1 to d_5. The non-relativistic equations of motions for the separate drift lengths are given by:

$$d_1 = \frac{1}{2}a_1 t_1^2 + v_1 t_1 \ , \quad v_1 = \sqrt{\frac{2E_1}{m}} \ , \quad \Delta V_1 = (V_C - V_F) \ , \qquad a_1 = \frac{q}{m}\frac{\Delta V_1}{d_1} \ , \quad \text{(D.6)}$$

$$d_2 = v_2 t_2 \ , \qquad v_2 = \sqrt{\frac{2E_2}{m}} \ , \quad E_2 = E_1 + \text{sign}(q)\Delta V_1, \quad a_2 = 0 \ , \qquad \text{(D.7)}$$

$$d_3 = \frac{1}{2}a_3 t_3^2 + v_3 t_3 \ , \quad v_3 = v_2, \qquad \Delta V_3 = (V_F - V_B) \ , \qquad a_3 = \frac{q}{m}\frac{\Delta V_3}{d_3} \ , \quad \text{(D.8)}$$

$$d_4 = v_4 t_4 \ , \qquad v_4 = \sqrt{\frac{2E_4}{m}} \ , \quad E_4 = E_2 + \text{sign}(q)\Delta V_3 \ , \quad a_4 = 0 \ , \qquad \text{(D.9)}$$

$$d_5 = \frac{1}{2}a_5 t_5^2 + v_5 t_5 \ , \quad v_5 = v_4 \ , \qquad \Delta V_5 = (V_B - 0) \ , \qquad a_5 = \frac{q}{m}\frac{\Delta V_5}{d_5} \ . \quad \text{(D.10)}$$

Here m is the μ^+ mass, a_i, v_i and t_i the acceleration, initial velocity, q the charge of the particle and TOF in the five regions of the TD and $E_1 = E_{CFoil}$ the energy at the exit of the carbon foil. The drift time in each region can be written as

$$t_i \ = \ \frac{d_i}{v_i} \qquad \text{for } a_i = 0 \qquad\qquad\qquad \text{(D.11)}$$

$$t_i \ = \ -\frac{v_i}{a_i} + \text{sign}(a_i)\sqrt{\left(\frac{v_i}{a_i}\right)^2 + \frac{2d_i}{a_i}} \qquad\qquad \text{(D.12)}$$

and the total TOF t_{TD} through the TD is finally given by the sum

$$t_{\text{TD}} = \sum_{i=1}^{5} t_i \ . \qquad\qquad\qquad\qquad\qquad \text{(D.13)}$$

Appendix E

Dataset used for the data analysis

E.1   List of the datasets

All the data taken from 2011 to 2014 in preparation for this thesis are summarized in
Tables E.1 to E.3 and can be downloaded from [153].

Table E.1: *Data below are taken during the beam time in summer 2011 from 23.06.2011 to 26.06.2011. Run is the run number, Stat is the number of events recorded, Sample is the sample description, Nose is the diameter of the nose sample plate, T is the temperature, B is the magnetic field, E is the muon implantation energy, Mod is the high voltage on the moderator, Sa is the high voltage on the sample plate and SR is the angle of the muon spin at $t = t_0$.*

Run	Stats	Sample	Nose [mm]	T [K]	B [G]	E [keV]	Mod [kV]	Sa [kV]	SR [°]
1418	2504.6k	SiO$_2$-f	30mm	100	100	5.0	15.0	9.1	10
1419	2502.2k	SiO$_2$-f	30mm	100	100	14.1	15.0	0.0	10
1420	2502.6k	SiO$_2$-f	30mm	100	100	19.1	15.0	-5.0	10
1421	2506.3k	SiO$_2$-f	30mm	250	100	5.0	15.0	9.1	10
1422	2505.2k	SiO$_2$-f	30mm	250	100	14.1	15.0	0.0	10
1423	2506.6k	SiO$_2$-f	30mm	250	100	19.1	15.0	-5.0	10
1424	12007.6k	SiO$_2$-f	30mm	250	100	5.0	15.0	9.1	10
1425	12003.4k	SiO$_2$-f	30mm	175	100	5.0	15.0	9.1	10
1426	12008.8k	SiO$_2$-f	30mm	100	100	5.0	15.0	9.1	10
1427	12006.7k	SiO$_2$-f	30mm	50	100	5.0	15.0	9.1	10
1428	1004.3k	SiO$_2$-f	30mm	50	1498	14.1	15.0	0.0	10
1429	1006.9k	SiO$_2$-f	30mm	50	1498	5.0	15.0	9.1	10
1430	60.9k	SiO$_2$-f	30mm	250	1498	5.0	15.0	9.1	10
1431	8008.3k	SiO$_2$-f	30mm	250	6	5.0	15.0	9.1	10
1432	8000.4k	SiO$_2$-f	30mm	250	6	19.1	15.0	-5.0	10
1433	8007.7k	SiO$_2$-f	30mm	250	6	14.1	15.0	0.0	10
1434	8006.6k	SiO$_2$-f	30mm	175	6	5.0	15.0	9.1	10
1435	8004.2k	SiO$_2$-f	30mm	100	6	5.0	15.0	9.1	10
1436	8005.6k	SiO$_2$-f	30mm	50	6	5.0	15.0	9.1	10
1437	8003.1k	SiO$_2$-f	30mm	20	6	20.4	15.0	-6.3	10

Run	Stats	Sample	Nose [mm]	T [K]	B [G]	E [keV]	Mod [kV]	Sa [kV]	SR [°]
1438	8004.2k	SiO_2-f	30mm	20	6	14.1	15.0	0.0	10
1439	8004.8k	SiO_2-f	30mm	20	6	5.0	15.0	9.1	10
1440	4447.8k	SiO_2-f	30mm	20	6	19.1	15.0	-5.0	10
1441	259.1k	SiO_2-f	30mm	250	6	2.0	12.0	9.0	10
1442	5002.8k	SiO_2-f	30mm	250	6	2.0	12.0	9.0	10
1443	2505.5k	SiO_2-f	30mm	250	100	2.0	12.0	9.0	10
1444	2505.3k	SiO_2-f	30mm	250	100	14.0	12.0	-3.0	10
1445	8003.6k	SiO_2-f	30mm	250	6	5.0	15.0	9.1	10
1446	20004.3k	SiO_2-f	30mm	75	6	5.0	15.0	9.1	10
1447	14618.9k	SiO_2-f	30mm	50	6	5.0	15.0	9.1	10
1448	2503.5k	SiO_2-c	45mm	250	100	5.0	12.0	6.0	10
1449	3001.1k	SiO_2-c	45mm	250	100	3.0	12.0	8.0	10
1450	2501.3k	SiO_2-c	45mm	250	100	10.0	12.0	1.0	10
1451	2503.3k	SiO_2-c	45mm	250	100	14.0	12.0	-3.0	10
1452	8002.2k	SiO_2-c	45mm	250	6	3.0	12.0	8.0	10
1453	8002.4k	SiO_2-c	45mm	250	6	5.0	12.0	6.0	10
1454	8003.9k	SiO_2-c	45mm	250	6	10.0	12.0	1.0	10
1455	8004.8k	SiO_2-c	45mm	250	6	14.0	12.0	-3.0	10
1456	8002.3k	SiO_2-c	45mm	100	6	3.0	12.0	8.0	10
1457	4161.0k	SiO_2-c	45mm	100	6	5.0	12.0	6.0	10
1458	8000.7k	SiO_2-c	45mm	250	6	6.1	15.0	8.0	10
1459	8003.1k	SiO_2-c	45mm	175	6	3.0	12.0	8.0	10
1460	8002.8k	SiO_2-c	45mm	175	6	2.0	12.0	9.0	10
1461	408.5k	SiO_2-c	45mm	175	6	5.0	12.0	6.0	10
1462	6002.9k	SiO_2-c	45mm	175	6	5.0	12.0	6.0	10
1463	6002.9k	SiO_2-c	45mm	50	6	5.0	12.0	6.0	10

Run	Stats	Sample	Nose [mm]	T [K]	B [G]	E [keV]	Mod [kV]	Sa [kV]	SR [°]
1464	6003.8k	SiO$_2$-c	45mm	50	6	3.0	12.0	8.0	10
1631	2002.0k	Suprasil	30mm	50	100	5.0	15.0	9.1	10
1632	2001.3k	Suprasil	30mm	50	100	14.1	15.0	0.0	10
1633	2005.0k	Suprasil	30mm	50	100	19.1	15.0	-5.0	10
1634	8003.4k	Suprasil	30mm	50	6	5.0	15.0	9.1	10
1635	8004.0k	Suprasil	30mm	50	6	14.1	15.0	0.0	10
1636	8003.6k	Suprasil	30mm	50	6	19.1	15.0	-5.0	10
1637	8002.7k	Suprasil	30mm	100	6	5.0	15.0	9.1	10
1638	8003.3k	Suprasil	30mm	100	6	14.1	15.0	0.0	10
1639	8002.0k	Suprasil	30mm	100	6	19.1	15.0	-5.0	10
1640	8002.6k	Suprasil	30mm	175	6	5.0	15.0	9.1	10
1641	8002.8k	Suprasil	30mm	175	6	14.1	15.0	0.0	10
1642	8003.8k	Suprasil	30mm	175	6	19.1	15.0	-5.0	10
1643	8005.0k	Suprasil	30mm	250	6	5.0	15.0	9.1	10
1644	8004.1k	Suprasil	30mm	250	6	14.1	15.0	0.0	10
1645	8005.2k	Suprasil	30mm	250	6	19.1	15.0	-5.0	10
1646	12002.6k	Suprasil	30mm	250	100	5.0	15.0	9.1	10
1647	8004.8k	Suprasil	30mm	270	6	5.0	15.0	9.1	10
1648	6754.9k	Suprasil	30mm	270	6	14.1	15.0	0.0	10
1649	8004.3k	Suprasil	30mm	270	6	19.1	15.0	-5.0	10
1650	25002.0k	Suprasil	30mm	270	33	19.1	15.0	-5.0	10
1651	8005.6k	Suprasil	30mm	20	6	19.1	15.0	-5.0	10
1652	8006.1k	Suprasil	30mm	20	6	14.1	15.0	0.0	10
1653	8004.2k	Suprasil	30mm	20	6	5.0	15.0	9.1	10

Table E.2: *Data below are taken during the beam time in summer 2012 from 24.07.2012 to 28.07.2012. Run is the run number, Stat is the number of events recorded, Sample is the sample description, Nose is the diameter of the nose sample plate, T is the temperature, B is the magnetic field, E is the muon implantation energy, Mod is the high voltage on the moderator, Sa is the high voltage on the sample plate and SR is the angle of the muon spin at $t = t_0$.*

Run	Stats	Sample	Nose [mm]	T [K]	B [G]	E [keV]	Mod [kV]	Sa [kV]	SR [°]
3427	5004.7k	SiO_2-f	30mm	250	100	14.3	15.0	0.0	-10
3428	4143.7k	SiO_2-f	30mm	250	5	14.3	15.0	0.0	-10
3429	4232.4k	SiO_2-f	30mm	250	5	5.0	15.0	9.3	-10
3430	8004.1k	SiO_2-f14	30mm	250	5	2.0	12.0	9.1	-10
3431	8005.9k	SiO_2-f14	30mm	250	5	3.0	12.0	8.1	-10
3432	8007.8k	SiO_2-f14	30mm	250	5	5.0	12.0	6.1	-10
3433	8007.8k	SiO_2-f14	30mm	250	5	10.0	12.0	1.1	-10
3434	8007.0k	SiO_2-f14	30mm	250	5	14.0	12.0	-2.9	-10
3435	8005.5k	SiO_2-f14	30mm	175	5	14.0	12.0	-2.9	-10
3436	8003.2k	SiO_2-f14	30mm	175	5	10.0	12.0	1.1	-10
3437	8008.6k	SiO_2-f14	30mm	175	5	5.0	12.0	6.1	-10
3438	8007.0k	SiO_2-f14	30mm	175	5	3.0	12.0	8.1	-10
3439	8005.2k	SiO_2-f14	30mm	175	5	2.0	12.0	9.1	-10
3440	8005.3k	SiO_2-f14	30mm	100	5	2.0	12.0	9.1	-10
3441	8002.2k	SiO_2-f14	30mm	100	5	3.0	12.0	8.1	-10
3442	8002.4k	SiO_2-f14	30mm	100	5	5.0	12.0	6.1	-10
3443	8002.8k	SiO_2-f14	30mm	100	5	10.0	12.0	1.1	-10
3444	8002.4k	SiO_2-f14	30mm	100	5	14.0	12.0	-2.9	-10
3445	3007.3k	SiO_2-f14	30mm	20	5	14.0	12.0	-2.9	-10
3446	3004.7k	SiO_2-f14	30mm	20	100	14.0	12.0	-2.9	-10

Run	Stats	Sample	Nose [mm]	T [K]	B [G]	E [keV]	Mod [kV]	Sa [kV]	SR [°]
3447	3004.4k	SiO$_2$-f14	30mm	20	5	5.0	12.0	6.1	-10
3448	3003.1k	SiO$_2$-f14	30mm	20	100	5.0	12.0	6.1	-10
3449	3007.7k	SiO$_2$-f14	30mm	20	5	2.0	12.0	9.1	-10
3450	3006.9k	SiO$_2$-f14	30mm	20	100	2.0	12.0	9.1	-10
3451	8005.2k	SiO$_2$-f14	30mm	50	5	2.0	12.0	9.1	-10
3452	8005.9k	SiO$_2$-f14	30mm	50	5	5.0	12.0	6.1	-10
3453	8007.0k	SiO$_2$-f14	30mm	50	5	14.0	12.0	-2.9	-10
3454	8005.8k	SiO$_2$-b	30mm	250	5	2.0	12.0	9.1	-10
3455	8004.4k	SiO$_2$-b	30mm	250	5	3.0	12.0	8.1	-10
3456	8003.2k	SiO$_2$-b	30mm	250	5	5.0	12.0	6.1	-10
3457	8007.7k	SiO$_2$-b	30mm	250	5	10.0	12.0	1.1	-10
3458	8005.5k	SiO$_2$-b	30mm	250	5	14.0	12.0	-2.9	-10
3459	8004.5k	SiO$_2$-b	30mm	175	5	14.0	12.0	-2.9	-10
3460	8003.1k	SiO$_2$-b	30mm	175	5	10.0	12.0	1.1	-10
3461	8006.6k	SiO$_2$-b	30mm	175	5	5.0	12.0	6.1	-10
3462	8008.3k	SiO$_2$-b	30mm	175	5	3.0	12.0	8.1	-10
3463	8008.2k	SiO$_2$-b	30mm	175	5	2.0	12.0	9.1	-10
3464	8008.0k	SiO$_2$-b	30mm	100	5	2.0	12.0	9.1	-10
3465	8009.5k	SiO$_2$-b	30mm	100	5	3.0	12.0	8.1	-10
3466	8003.1k	SiO$_2$-b	30mm	100	5	5.0	12.0	6.1	-10
3467	8002.8k	SiO$_2$-b	30mm	100	5	10.0	12.0	1.1	-10
3468	8006.5k	SiO$_2$-b	30mm	100	5	14.0	12.0	-2.9	-10
3469	8005.4k	SiO$_2$-b	30mm	50	5	14.0	12.0	-2.9	-10
3470	8007.0k	SiO$_2$-b	30mm	50	5	10.0	12.0	1.1	-10
3471	8006.5k	SiO$_2$-b	30mm	50	5	5.0	12.0	6.1	-10
3472	8001.1k	SiO$_2$-b	30mm	50	5	3.0	12.0	8.1	-10

Run	Stats	Sample	Nose [mm]	T [K]	B [G]	E [keV]	Mod [kV]	Sa [kV]	SR [°]
3473	8006.3k	SiO$_2$-b	30mm	50	5	2.0	12.0	9.1	-10
3474	8003.2k	SiO$_2$-b	30mm	20	5	2.0	12.0	9.1	-10
3475	8006.4k	SiO$_2$-b	30mm	20	5	5.0	12.0	6.1	-10
3476	8002.2k	SiO$_2$-b	30mm	20	5	14.0	12.0	-2.9	-10
3477	4004.5k	SiO$_2$-b	30mm	20	20	14.0	12.0	-2.9	-10
3478	4007.0k	SiO$_2$-b	30mm	20	35	14.0	12.0	-2.9	-10
3479	4003.9k	SiO$_2$-b	30mm	20	50	14.0	12.0	-2.9	-10
3480	4006.0k	SiO$_2$-b	30mm	20	100	14.0	12.0	-2.9	-10
3481	3005.0k	Ag	30mm	250	5	2.0	12.0	9.1	-10
3482	3003.7k	Ag	30mm	250	5	3.0	12.0	8.1	-10
3483	3004.9k	Ag	30mm	250	5	5.0	12.0	6.1	-10
3484	3007.3k	Ag	30mm	250	5	10.0	12.0	1.1	-10
3485	3005.2k	Ag	30mm	250	5	14.0	12.0	-2.9	-10
3486	3008.0k	Ag	30mm	250	100	14.0	12.0	-2.9	-10
3487	3005.3k	Ag	30mm	250	100	5.0	12.0	6.1	-10
3488	3005.7k	Ag	30mm	250	100	2.0	12.0	9.1	-10
3489	3004.3k	Ag	30mm	100	5	14.0	12.0	-2.9	-10
3490	3006.4k	Ag	30mm	100	5	10.0	12.0	1.1	-10
3491	3006.0k	Ag	30mm	100	5	5.0	12.0	6.1	-10
3492	3008.4k	Ag	30mm	100	5	3.0	12.0	8.1	-10
3493	3004.4k	Ag	30mm	100	5	2.0	12.0	9.1	-10
3494	3007.7k	Ag	30mm	20	5	2.0	12.0	9.1	-10
3495	3006.4k	Ag	30mm	20	5	3.0	12.0	8.1	-10
3496	3007.8k	Ag	30mm	20	5	5.0	12.0	6.1	-10
3497	3005.8k	Ag	30mm	20	5	10.0	12.0	1.1	-10
3498	3006.1k	Ag	30mm	20	5	14.0	12.0	-2.9	-10

Run	Stats	Sample	Nose [mm]	T [K]	B [G]	E [keV]	Mod [kV]	Sa [kV]	SR [°]
3499	3004.7k	Ag	30mm	20	100	14.0	12.0	-2.9	-10
3500	3005.2k	Ag	30mm	20	100	10.0	12.0	1.1	-10
3501	3001.8k	Ag	30mm	20	100	5.0	12.0	6.1	-10
3502	3001.6k	Ag	30mm	20	100	3.0	12.0	8.1	-10
3503	3004.8k	Ag	30mm	20	100	2.0	12.0	9.1	-10
3504	3005.0k	Ag	30mm	20	20	14.0	12.0	-2.9	-10
3505	3007.2k	Ag	30mm	20	35	14.0	12.0	-2.9	-10
3506	3008.2k	Ag	30mm	20	50	14.0	12.0	-2.9	-10
3507	3006.0k	Ag	30mm	175	100	14.0	12.0	-2.9	-10
3508	2704.9k	Ag	30mm	175	100	10.0	12.0	1.1	-10
3509	2009.7k	Ag	30mm	175	100	5.0	12.0	6.1	-10
3510	2019.3k	Ag	30mm	175	100	3.0	12.0	8.1	-10
3511	2029.6k	Ag	30mm	175	100	2.0	12.0	9.1	-10
4032	3005.0k	Ag/Ni	30mm	250	100	3.0	12.0	8.1	-10
4033	3005.2k	Ag/Ni	30mm	250	99	2.0	12.0	9.1	-10
4034	3007.6k	Ag/Ni	30mm	250	100	2.0	12.0	9.1	10
4035	3003.6k	Ag/Ni	30mm	250	99	5.0	12.0	6.1	10
4036	3004.6k	Ag/Ni	30mm	250	99	5.0	12.0	6.1	-10
4037	3007.7k	Ag/Ni	30mm	250	99	10.0	12.0	1.1	-10
4038	3002.7k	Ag/Ni	30mm	250	99	14.0	12.0	-2.9	-10
4039	3003.5k	Ag/Ni	30mm	250	99	14.0	12.0	-2.9	10
4040	3002.8k	Ag/Ni	30mm	175	100	14.0	12.0	-2.9	-10
4041	3005.2k	Ag/Ni	30mm	175	99	10.0	12.0	1.1	-10
4042	3005.7k	Ag/Ni	30mm	175	99	5.0	12.0	6.1	-10
4043	3003.9k	Ag/Ni	30mm	175	100	3.0	12.0	8.1	-10
4044	3009.9k	Ag/Ni	30mm	175	100	2.0	12.0	9.1	-10

Run	Stats	Sample	Nose [mm]	T [K]	B [G]	E [keV]	Mod [kV]	Sa [kV]	SR [°]
4045	3006.8k	Ag/Ni	30mm	100	99	2.0	12.0	9.1	-10
4046	3006.9k	Ag/Ni	30mm	100	99	5.0	12.0	6.1	-10
4047	2044.6k	Ag/Ni	30mm	100	99	14.0	12.0	-2.9	-10
4048	3007.9k	Ag/Ni	30mm	50	100	14.0	12.0	-2.9	-10
4049	3004.6k	Ag/Ni	30mm	50	99	5.0	12.0	6.1	-10
4050	3008.2k	Ag/Ni	30mm	50	99	2.0	12.0	9.1	-10
4051	3007.6k	Ag/Ni	30mm	20	100	2.0	12.0	9.1	-10
4052	3005.6k	Ag/Ni	30mm	20	100	3.0	12.0	8.1	-10
4053	3001.2k	Ag/Ni	30mm	20	99	5.0	12.0	6.1	-10
4054	3005.6k	Ag/Ni	30mm	20	99	10.0	12.0	1.1	-10
4055	3004.7k	Ag/Ni	30mm	20	100	14.0	12.0	-2.9	-10

Table E.3: *Data below are taken during the beam time in summer 2014 from 04.07.2014 to 09.07.2014. Run is the run number, Stat is the number of events recorded, Sample is the sample description, Nose is the diameter of the nose sample plate, T is the temperature, B is the magnetic field, E is the muon implantation energy, Mod is the high voltage on the moderator, Sa is the high voltage on the sample plate and SR is the angle of the muon spin at $t = t_0$.*

Run	Stats	Sample	Nose [mm]	T [K]	B [G]	E [keV]	Mod [kV]	Sa [kV]	SR [°]
1068	3005.3k	Ag	30mm	250	100	14.27	15.0	0.0	-10
1069	3003.7k	Ag	30mm	250	100	14.27	15.0	0.0	-10
1070	3005.1k	Ag	30mm	250	100	14.27	15.0	0.0	-10
1071	3002.0k	Ag	30mm	250	100	11.09	12.0	0.0	-10
1072	3004.6k	Ag	30mm	250	100	11.09	12.0	0.0	-10
1073	3003.2k	Ag	30mm	250	100	11.09	12.0	0.0	-10
1074	21945.1k	SiO_2-fh1	30mm	100	33	4.97	15.0	9.30	-10
1076	25009.1k	SiO_2-fh1	30mm	250	33	4.97	15.0	9.30	-10
1077	17011.8k	SiO_2-fh1	30mm	175	33	4.97	15.0	9.30	-10
1078	8001.5k	MOF5	30mm	100	33	4.97	15.0	9.30	-10
1079	8003.2k	MOF5	30mm	150	33	4.97	15.0	9.30	-10
1080	8002.5k	MOF5	30mm	175	33	4.97	15.0	9.30	-10
1081	8003.4k	MOF5	30mm	250	33	4.97	15.0	9.30	-10
1082	8003.1k	MOF5	30mm	250	33	1.99	12.0	9.10	-10
1083	5273.6k	MOF5	30mm	175	33	1.99	12.0	9.10	-10
1084	25006.9k	SiN/SiO_2-fh1	30mm	100	33	14.27	15.0	0.0	-10
1085	25011.0k	SiN/SiO_2-fh1	30mm	100	33	16.96	15.0	-2.70	-10
1086	25008.2k	SiN/SiO_2-fh1	30mm	20	33	14.26	15.0	0.0	-10
1087	25005.6k	SiN/SiO_2-fh1	30mm	250	33	14.26	15.0	0.0	-10
1088	8572.0k	SiN/SiO_2-fh1	30mm	250	33	16.96	15.0	-2.70	-10

Run	Stats	Sample	Nose [mm]	T [K]	B [G]	E [keV]	Mod [kV]	Sa [kV]	SR [°]
1089	25005.3k	SiN-5.5mm/SiO$_2$-fh1	30mm	100	33	14.26	15.0	0.0	-10
1090	25003.3k	SiN-5.5mm/SiO$_2$-fh1	30mm	175	33	14.26	15.0	0.0	-10
1091	22558.8k	SiN-5.5mm/SiO$_2$-fh1	30mm	250	33	14.26	15.0	0.0	-10
1092	25007.3k	SiN/SiO$_2$-1.5mm/SiO$_2$-fh1	30mm	100	33	14.26	15.0	0.0	-10
1093	25006.6k	SiN/SiO$_2$-1.5mm/SiO$_2$-fh1	30mm	175	33	14.26	15.0	0.0	-10
1094	25000.9k	SiN/SiO$_2$-1.5mm/SiO$_2$-fh1	30mm	250	33	14.26	15.0	0.0	-10
1095	13006.2k	SiN/SiO$_2$-1.5mm/SiO$_2$-fh1	30mm	250	33	16.96	15.0	-2.70	-10
3663	1056.6k	Ag/Ni	30mm	250	100	5.27	15.02	9.00	-10
3664	1010.1k	Ag/Ni	30mm	250	100	14.27	15.02	-0.00	-10
3665	1007.4k	Ag/Ni	30mm	250	100	9.98	12.02	1.10	-10
3666	1002.1k	Ag/Ni	30mm	250	100	4.99	12.02	6.10	-10
3667	1003.2k	Ag/Ni	30mm	250	100	1.99	12.02	9.10	-10
3668	1000.4k	Ag/Ni (no moderator)	30mm	250	100	5.27	15.02	9.00	-10
3669	1000.8k	Ag/Ni (no moderator)	30mm	250	100	14.27	15.02	-0.00	-10
3670	1000.8k	Ag/Ni (no moderator)	30mm	250	100	9.98	12.02	1.10	-10
3671	1001.2k	Ag/Ni (no moderator)	30mm	250	100	4.99	12.02	6.10	-10
3672	1000.7k	Ag/Ni (no moderator)	30mm	250	100	1.99	12.02	9.10	-10
3673	1000.5k	Ag/Ni (no moderator)	30mm	250	100	2.99	12.02	8.09	-10
3674	1708.7k	Ag/Ni (no moderator)	30mm	250	100	11.09	12.02	-0.00	-10

Dataset used for the data analysis

Bibliography

[1] M. Gonin, R. Kallenbach, and P. Bochsler, *Charge exchange of hydrogen atoms in carbon foils at 0.4-120 keV*, Review of Scientific Instruments **65**, 648 (1994), URL: http://scitation.aip.org/content/aip/journal/rsi/65/3/10.1063/1.1145132.

[2] M. I. Eides, H. Grotch, and V. A. Shelyuto, *Theory of light hydrogenlike atoms*, Physics Reports **342**, 63 (2001), URL: http://www.sciencedirect.com/science/article/pii/S0370157300000776.

[3] M. I. Eides, H. Grotch, and V. A. Shelyuto, *Theory of Light Hydrogenic Bound States (Springer Tracts in Modern Physics)* (Springer-Verlag New York, Inc., Secaucus, NJ, USA, 2006), ISBN 3540452699.

[4] S. G. Karshenboim, *Precision physics of simple atoms: QED tests, nuclear structure and fundamental constants*, Physics Reports **422**, 1 (2005), URL: http://www.sciencedirect.com/science/article/pii/S0370157305003637.

[5] M. E. Peskin and D. V. Schroeder, *An Introduction To Quantum Field Theory* (1995), URL: http://CERN.eblib.com/patron/FullRecord.aspx?p=729240.

[6] T. Kinoshita, editor., *Quantum Electrodynamics*, vol. 7 of *Advanced Series on Directions in High Energy Physics* (World Scientific Publishing Co. Pte. Ltd., 1990).

[7] C. Audoin and G. Bernard, *The Measurement of Time: Time, Frequency, and the Atomic Clock* (Cambridge University Press, Cambridge, 2001), 1st ed.

[8] E. M. Purcell, R. V. Pound, and N. Bloembergen, *Nuclear Magnetic Resonance Absorption in Hydrogen Gas*, Phys. Rev. **70**, 986 (1946), URL: http://link.aps.org/doi/10.1103/PhysRev.70.986.

[9] S. A. Diddams, D. J. Jones, J. Ye, S. T. Cundiff, J. L. Hall, J. K. Ranka, R. S. Windeler, R. Holzwarth, T. Udem, and T. W. Hänsch, *Direct Link between Microwave and Optical Frequencies with a 300 THz Femtosecond Laser*

Comb, Phys. Rev. Lett. **84**, 5102 (2000), URL: http://link.aps.org/doi/10.1103/PhysRevLett.84.5102.

[10] R. Holzwarth, T. Udem, T. W. Hänsch, J. C. Knight, W. J. Wadsworth, and P. S. J. Russell, *Optical Frequency Synthesizer for Precision Spectroscopy*, Phys. Rev. Lett. **85**, 2264 (2000), URL: http://link.aps.org/doi/10.1103/PhysRevLett.85.2264.

[11] S. Karshenboim, F. Pavone, F. Bassani, M. Inguscio, and T. Hänsch, editors., *The Hydrogen Atom*, vol. 570 of *Lecture Notes in Physics* (Springer-Verlag Berlin and Heidelberg GmbH & Co. K, 2001).

[12] A. P. Mills and S. Chu, *Precision Measurements in Positronium* (Adv. Ser. Direct. High Energy Phys., 1990), chap. 15, pp. 774–821, http://www.worldscientific.com/doi/pdf/10.1142/9789814503273_0015.

[13] V. W. Hughes and G. zu Putlitz, *MUONIUM* (Adv. Ser. Direct. High Energy Phys., 1990), chap. 16, pp. 822–904, http://www.worldscientific.com/doi/pdf/10.1142/9789814503273_0016.

[14] H. Martyn, *TEST OF QED BY HIGH-ENERGY ELECTRON - POSITRON COLLISIONS*, Adv. Ser. Direct. High Energy Phys. **7**, 92 (1990), URL: http://www.worldscientific.com/doi/abs/10.1142/9789814503273_0005.

[15] K. P. Jungmann, *Spectroscopy of the Muonium Atom*, in *The Hydrogen Atom*, edited by S. Karshenboim, F. Bassani, F. Pavone, M. Inguscio, and T. Hänsch (Springer Berlin Heidelberg, 2001), vol. 570 of *Lecture Notes in Physics*, pp. 81–102, ISBN 978-3-540-41935-8.

[16] G. W. Bennett, B. Bousquet, H. N. Brown, G. Bunce, R. M. Carey, P. Cushman, G. T. Danby, P. T. Debevec, M. Deile, H. Deng, *et al.* (Muon (g-2) Collaboration), *Final report of the E821 muon anomalous magnetic moment measurement at BNL*, Phys. Rev. D **73**, 072003 (2006), URL: http://link.aps.org/doi/10.1103/PhysRevD.73.072003.

[17] R. Pohl, A. Antognini, F. Nez, F. D. Amaro, F. Biraben, J. M. R. Cardoso, D. S. Covita, A. Dax, S. Dhawan, L. M. P. Fernandes, *et al.*, *The size of the proton*, Nature **466**, 213 (2010), URL: http://dx.doi.org/10.1038/nature09250.

[18] A. Antognini, F. Kottmann, F. Biraben, P. Indelicato, F. Nez, and R. Pohl, *Theory of the 2S-2P Lamb shift and 2S hyperfine splitting in muonic hydrogen*, An-

nals of Physics **331**, 127 (2013), URL: http://www.sciencedirect.com/science/article/pii/S0003491612002102.

[19] R. Carey, K. Lynch, J. Miller, B. Roberts, W. Morse, *et al.*, *The New (g-2) Experiment: A proposal to measure the muon anomalous magnetic moment to* ± 0.14 *ppm precision* (2009).

[20] J. Imazato, *Particle and nuclear physics at J-PARC*, Nuclear Physics B - Proceedings Supplements **129130**, 81 (2004), lattice 2003, URL: http://www.sciencedirect.com/science/article/pii/S092056320302509X.

[21] K. Shimomura, *Possibility of precise measurements of muonium HFS at J-PARC MUSE*, AIP Conference Proceedings **1382**, 245 (2011), URL: http://scitation.aip.org/content/aip/proceeding/aipcp/10.1063/1.3644324.

[22] T. Nebel, F. Amaro, A. Antognini, F. Biraben, J. Cardoso, D. Covita, A. Dax, L. Fernandes, A. Gouvea, T. Graf, *et al.*, *The Lamb-shift experiment in Muonic helium*, Hyperfine Interactions **212**, 195 (2012), URL: http://dx.doi.org/10.1007/s10751-012-0637-0.

[23] M. Herrmann, M. Haas, U. D. Jentschura, F. Kottmann, D. Leibfried, G. Saathoff, C. Gohle, A. Ozawa, V. Batteiger, S. Knünz, *et al.*, *Feasibility of coherent xuv spectroscopy on the* $1S$-$2S$ *transition in singly ionized helium*, Phys. Rev. A **79**, 052505 (2009), URL: http://link.aps.org/doi/10.1103/PhysRevA.79.052505.

[24] A. Beyer, J. Alnis, K. Khabarova, A. Matveev, C. G. Parthey, D. C. Yost, R. Pohl, T. Udem, T. W. Hänsch, and N. Kolachevsky, *Precision spectroscopy of the 2S-4P transition in atomic hydrogen on a cryogenic beam of optically excited 2S atoms*, Annalen der Physik **525**, 671 (2013), URL: http://dx.doi.org/10.1002/andp.201300075.

[25] D. Z. Kandula, C. Gohle, T. J. Pinkert, W. Ubachs, and K. S. E. Eikema, *XUV frequency-comb metrology on the ground state of helium*, Phys. Rev. A **84**, 062512 (2011), URL: http://link.aps.org/doi/10.1103/PhysRevA.84.062512.

[26] R. van Rooij, J. S. Borbely, J. Simonet, M. D. Hoogerland, K. S. E. Eikema, R. A. Rozendaal, and W. Vassen, *Frequency Metrology in Quantum Degenerate Helium: Direct Measurement of the* $2^3S_1 \rightarrow 2^1S_0$ *Transition*, Science **333**, 196 (2011), URL: http://www.sciencemag.org/content/333/6039/196.abstract.

[27] O. Arnoult, F. Nez, L. Julien, and F. Biraben, *Optical frequency measurement of the 1S-3S two-photon transition in hydrogen*, Eur. Phys. J. D **60**, 243 (2010), URL: http://dx.doi.org/10.1140/epjd/e2010-00249-6.

[28] A. Vutha, N. Bezginov, I. Ferchichi, M. George, V. Isaac, C. Storry, A. Weatherbee, M. Weel, and E. Hessels, *Progress towards a new microwave measurement of the hydrogen n=2 Lamb shift: a measurement of the proton charge radius*, Bull. Am. Phys. Soc. **57**, Q1.138 (2012), URL: http://meetings.aps.org/link/BAPS.2012.DAMOP.D1.138.

[29] W. Liu, M. G. Boshier, S. Dhawan, O. van Dyck, P. Egan, X. Fei, M. Grosse Perdekamp, V. W. Hughes, M. Janousch, K. Jungmann, *et al.*, *High Precision Measurements of the Ground State Hyperfine Structure Interval of Muonium and of the Muon Magnetic Moment*, Phys. Rev. Lett. **82**, 711 (1999), URL: http://link.aps.org/doi/10.1103/PhysRevLett.82.711.

[30] S. Chu, A. P. Mills, A. G. Yodh, K. Nagamine, Y. Miyake, and T. Kuga, *Laser Excitation of the Muonium 1S-2S Transition*, Phys. Rev. Lett. **60**, 101 (1988), URL: http://link.aps.org/doi/10.1103/PhysRevLett.60.101.

[31] V. Meyer, S. N. Bagayev, P. E. G. Baird, P. Bakule, M. G. Boshier, A. Breitrück, S. L. Cornish, S. Dychkov, G. H. Eaton, A. Grossmann, *et al.*, *Measurement of the 1S-2S Energy Interval in Muonium*, Phys. Rev. Lett. **84**, 1136 (2000), URL: http://link.aps.org/doi/10.1103/PhysRevLett.84.1136.

[32] V. W. Hughes and T. Kinoshita, *Muon Physics I* (Academic Press, 1977).

[33] K. Nagamine, *Introductory Muon Science* (Cambridge University Press, 2003), ISBN 9780511470776, cambridge Books Online.

[34] K. P. Jungmann, *Muonium - Physics of a most Fundamental Atom*, Nuclear Physics B - Proceedings Supplements **155**, 355 (2006), proceedings to the 7th International Workshop on Neutrino Factories and Superbeams Proceedings to the 7th International Workshop on Neutrino Factories and Superbeams, URL: http://www.sciencedirect.com/science/article/pii/S0920563206001915.

[35] V. W. Hughes, D. W. McColm, K. Ziock, and R. Prepost, *Muonium. I. Muonium Formation and Larmor Precession*, Phys. Rev. A **1**, 595 (1970), URL: http://link.aps.org/doi/10.1103/PhysRevA.1.595.

[36] J. M. Bailey, W. E. Cleland, V. W. Hughes, R. Prepost, and K. Ziock, *Muonium. II. Observation of the Muonium Hyperfine-Structure Interval*, Phys. Rev. A **3**, 871 (1971), URL: http://link.aps.org/doi/10.1103/PhysRevA.3.871.

[37] W. E. Cleland, J. M. Bailey, M. Eckhause, V. W. Hughes, R. Prepost, J. E. Rothberg, and R. M. Mobley, *Muonium. III. Precision Measurement of the Muonium Hyperfine-Structure Interval at Strong Magnetic Field*, Phys. Rev. A **5**, 2338 (1972), URL: http://link.aps.org/doi/10.1103/PhysRevA.5.2338.

[38] P. A. Thompson, P. Crane, T. Crane, J. J. Amato, V. W. Hughes, G. zu Putlitz, and J. E. Rothberg, *Muonium. IV. Precision Measurement of the Muonium Hyperfine-Structure Interval at Weak and Very Weak Magnetic Fields*, Phys. Rev. A **8**, 86 (1973), URL: http://link.aps.org/doi/10.1103/PhysRevA.8.86.

[39] C. D. Anderson and S. H. Neddermeyer, *Cloud Chamber Observations of Cosmic Rays at 4300 Meters Elevation and Near Sea-Level*, Phys. Rev. **50**, 263 (1936), URL: http://link.aps.org/doi/10.1103/PhysRev.50.263.

[40] S. H. Neddermeyer and C. D. Anderson, *Note on the Nature of Cosmic-Ray Particles*, Phys. Rev. **51**, 884 (1937), URL: http://link.aps.org/doi/10.1103/PhysRev.51.884.

[41] K. Olive and P. D. Group, *Review of Particle Physics*, Chinese Physics C **38**, 090001 (2014), URL: http://stacks.iop.org/1674-1137/38/i=9/a=090001.

[42] A. Pifer, T. Bowen, and K. Kendall, *A high stopping density μ^+ beam*, Nuclear Instruments and Methods **135**, 39 (1976), URL: http://www.sciencedirect.com/science/article/pii/0029554X76908235.

[43] K. H. Luetkens, Ph.D. thesis, Technische Universität Braunschweig (2003).

[44] U. of Fribourg (Group Bernhard), *μSR on organic semiconductors* (2014), URL: http://physics.unifr.ch/en/page/133/.

[45] R. L. Garwin, L. M. Lederman, and M. Weinrich, *Observations of the Failure of Conservation of Parity and Charge Conjugation in Meson Decays: the Magnetic Moment of the Free Muon*, Phys. Rev. **105**, 1415 (1957), URL: http://link.aps.org/doi/10.1103/PhysRev.105.1415.

[46] J. I. Friedman and V. L. Telegdi, *Nuclear Emulsion Evidence for Parity Nonconservation in the Decay Chain $\pi^+ - \mu^+ - e^+$*, Phys. Rev. **105**, 1681 (1957), URL: http://link.aps.org/doi/10.1103/PhysRev.105.1681.2.

[47] B. D. Patterson, *Muonium states in semiconductors*, Rev. Mod. Phys. **60**, 69 (1988), URL: http://link.aps.org/doi/10.1103/RevModPhys.60.69.

[48] W. H. Koppenol, *Names for muonium and hydrogen atoms and their ions (IUPAC Recommendations 2001)*, Pure Appl. Chem. **73**, 377 (2001), URL: http://iupac.org/publications/pac/73/2/0377/.

[49] L. Willmann, P. V. Schmidt, H. P. Wirtz, R. Abela, V. Baranov, J. Bagaturia, W. Bertl, R. Engfer, A. Großmann, V. W. Hughes, *et al.*, *New Bounds from a Search for Muonium to Antimuonium Conversion*, Phys. Rev. Lett. **82**, 49 (1999), URL: http://link.aps.org/doi/10.1103/PhysRevLett.82.49.

[50] K. Kirch, *Testing Gravity with Muonium*, ArXiv Physics e-prints (2007), URL: http://arxiv.org/abs/physics/0702143.

[51] D. M. Kaplan, D. C. Mancini, T. J. Phillips, T. J. Roberts, J. Terry, *et al.*, *Measuring Antimatter Gravity with Muonium* (2013).

[52] K. Kirch and K. S. Khaw, *Testing antimatter gravity with muonium*, International Journal of Modern Physics: Conference Series **30**, 1460258 (2014), URL: http://www.worldscientific.com/doi/abs/10.1142/S2010194514602580.

[53] A. H. Gomes, V. A. Kostelecký, and A. J. Vargas, *Laboratory tests of Lorentz and CPT symmetry with muons*, Phys. Rev. D **90**, 076009 (2014), URL: http://link.aps.org/doi/10.1103/PhysRevD.90.076009.

[54] K. P. Jungmann, *Past, present and future of muonium*, pp. 134–153 (2004).

[55] J. Brown, S. Dodds, T. Estle, R. Heffner, M. Leon, and D. Vanderwater, *A precision determination of the hyperfine splitting of muonium in quartz*, Solid State Communications **33**, 613 (1980), URL: http://www.sciencedirect.com/science/article/pii/0038109880907358.

[56] A. P. Mills, J. Imazato, S. Saitoh, A. Uedono, Y. Kawashima, and K. Nagamine, *Generation of Thermal Muonium in Vacuum*, Phys. Rev. Lett. **56**, 1463 (1986), URL: http://link.aps.org/doi/10.1103/PhysRevLett.56.1463.

[57] G. Marshall, J. Warren, D. Garner, G. Clark, J. Brewer, and D. Fleming, *Production of thermal muonium in the vacuum between the grains of fine silica powders*, Physics Letters A **65**, 351 (1978), URL: http://www.sciencedirect.com/science/article/pii/0375960178907272.

[58] A. C. Janissen, G. A. Beer, G. R. Mason, A. Olin, T. M. Huber, A. R. Kunselman, T. Bowen, P. G. Halverson, C. A. Fry, K. R. Kendall, *et al.*, *Muonium production from fine silica powder*, Phys. Rev. A **42**, 161 (1990), URL: http://link.aps.org/doi/10.1103/PhysRevA.42.161.

[59] W. Schwarz, V. Ebert, H. Geerds, K. Jungmann, S. Kirches, S. Koppe, F. Maas, H.-J. Mundinger, G. zu Putlitz, J. Rosenkranz, *et al.*, *Thermal muonium in vacuo from silica aerogels*, Journal of Non-Crystalline Solids **145**, 244 (1992), proceedings of the Third International Symposium on Aerogels, URL: http://www.sciencedirect.com/science/article/pii/S002230930580465X.

[60] P. Bakule, G. Beer, D. Contreras, M. Esashi, Y. Fujiwara, Y. Fukao, S. Hirota, H. Iinuma, K. Ishida, M. Iwasaki, *et al.*, *Measurement of muonium emission from silica aerogel*, Progress of Theoretical and Experimental Physics **2013** (2013), URL: http://ptep.oxfordjournals.org/content/2013/10/103C01.abstract.

[61] G. A. Beer, G. M. Marshall, G. R. Mason, A. Olin, Z. Gelbart, K. R. Kendall, T. Bowen, P. G. Halverson, A. E. Pifer, C. A. Fry, *et al.*, *Emission of Muonium into Vacuum from a Silica-Powder Layer*, Phys. Rev. Lett. **57**, 671 (1986), URL: http://link.aps.org/doi/10.1103/PhysRevLett.57.671.

[62] A. Toyoda, Y. Fujiwara, Y. Fukao, O. Kamigaito, N. Kawamura, Y. Matsuda, T. Mibe, T. Ogitsu, N. Saito, K. Sasaki, *et al.*, *J-PARC MUSE H-line optimization for the g-2 and Mu HFS experiments* (2011), URL: http://arxiv.org/abs/1110.1125.

[63] D. Taqqu, *Compression and Extraction of Stopped Muons*, Phys. Rev. Lett. **97**, 194801 (2006), URL: http://link.aps.org/doi/10.1103/PhysRevLett.97.194801.

[64] P. Crivelli, U. Gendotti, A. Rubbia, L. Liszkay, P. Perez, and C. Corbel, *Measurement of the orthopositronium confinement energy in mesoporous thin films*, Phys. Rev. A **81**, 052703 (2010), URL: http://link.aps.org/doi/10.1103/PhysRevA.81.052703.

[65] G. A. Beer, Y. Fujiwara, S. Hirota, K. Ishida, M. Iwasaki, S. Kanda, H. Kawai, N. Kawamura, R. Kitamura, S. Lee, *et al.*, *Enhancement of muonium emission rate from silica aerogel with a laser-ablated surface*, Progress of Theoretical and Experimental Physics **2014** (2014), URL: http://ptep.oxfordjournals.org/content/2014/9/091C01.abstract.

[66] M. Aoki, P. Bakule, B. Bassalleck, G. Beer, A. Deshpande, S. Eidelman, D. E. Fields, M. Finger, M. F. Jr., Y. Fujirawa, *et al.*, Tech. Rep., J-PARC (2009).

[67] G. W. Bennett, B. Bousquet, H. N. Brown, G. Bunce, R. M. Carey, P. Cushman, G. T. Danby, P. T. Debevec, M. Deile, H. Deng, *et al.* (Muon (g-2) Collaboration), *Improved limit on the muon electric dipole moment*, Phys. Rev. D **80**, 052008 (2009), URL: http://link.aps.org/doi/10.1103/PhysRevD.80.052008.

[68] R. Abela, D. Herlach, E. Morenzoni, G. Solt, U. Zimmermann, F. N. Gygax, A. Schenck, D. G. Eshchenko, E. P. Krasnoperov, and E. E. Meillikhov, *Muonium in liquid helium isotopes*, JETP Letters **57**, 157 (1993), URL: http://www.jetpletters.ac.ru/ps/1176/article_17753.shtml.

[69] E. Kosarev and E. Krasnoperov, *Kinetics of muonium formation in liquid helium*, Journal of Experimental and Theoretical Physics Letters **69**, 273 (1999), URL: http://dx.doi.org/10.1134/1.568017.

[70] M. Saarela and E. Krotscheck, *Hydrogen isotope and ^3He impurities in liquid ^4He*, Journal of Low Temperature Physics **90**, 415 (1993), URL: http://dx.doi.org/10.1007/BF00681890.

[71] T. Prokscha, E. Morenzoni, K. Deiters, F. Foroughi, D. George, R. Kobler, A. Suter, and V. Vrankovic, *The new beam at PSI: A hybrid-type large acceptance channel for the generation of a high intensity surface-muon beam*, Nuclear Instruments and Methods in Physics Research Section A: Accelerators, Spectrometers, Detectors and Associated Equipment **595**, 317 (2008), URL: http://www.sciencedirect.com/science/article/pii/S016890020801067X.

[72] M. Luthy, W. Burkert, and T. Rauber, *The PSI experimental hall and High Intensity Proton Accelerator (HIPA)* (2014), URL: http://www.psi.ch/num/FacilitiesEN/HallenplanPSI.png.

[73] T. Prokscha, A. Suter, and Z. Salman, *Low Energy Muons: Overview of the Experimental Setup* (accessed Dec 2014), URL: http://www.psi.ch/low-energy-muons/experimental-setup.

[74] E. Morenzoni, T. Prokscha, A. Suter, H. Luetkens, and R. Khasanov, *Nanoscale thin film investigations with slow polarized muons*, Journal of Physics: Condensed Matter **16**, S4583 (2004), URL: http://stacks.iop.org/0953-8984/16/i=40/a=010.

[75] T. Prokscha, K. H. Chow, E. Stilp, A. Suter, H. Luetkens, E. Morenzoni, G. J. Nieuwenhuys, Z. Salman, and R. Scheuermann, *Photo-induced persistent inversion of germanium in a 200-nm-deep surface region*, Sci. Rep. **3**, (2013), URL: http://dx.doi.org/10.1038/srep02569.

[76] I. McKenzie, Z. Salman, S. R. Giblin, Y. Y. Han, G. W. Leach, E. Morenzoni, T. Prokscha, and A. Suter, *Polymer dynamics near the surface and in the bulk of poly(tetrafluoroethylene) probed by zero-field muon-spin-relaxation spectroscopy*, Phys. Rev. E **89**, 022605 (2014), URL: http://link.aps.org/doi/10.1103/PhysRevE.89.022605.

[77] T. Prokscha, R. Khasanov, H. Luetkens, E. Morenzoni, A. Suter, and H.-P. Weber, *Low Energy Muon Developments*, Scientific Report 2001: Particle and Matter **1**, 91 (2002), URL: http://www.iaea.org/inis/collection/NCLCollectionStore/_Public/33/046/33046483.pdf.

[78] E. Morenzoni, H. Glckler, T. Prokscha, H. Weber, E. Forgan, T. Jackson, H. Luetkens, C. Niedermayer, M. Pleines, M. Birke, *et al.*, *Low-energy SR at PSI: present and future*, Physica B: Condensed Matter **289-290**, 653 (2000), URL: http://www.sciencedirect.com/science/article/pii/S0921452600003033.

[79] G. D. Morris, *Epithermal muons from solid rare-gas moderators*, Master's thesis, University of British Columbia (1990).

[80] A. Hofer, Ph.D. thesis, Universitt Konstanz (1998).

[81] T. Prokscha, E. Morenzoni, C. David, A. Hofer, H. Glckler, and L. Scandella, *Moderator gratings for the generation of epithermal positive muons*, Applied Surface Science **172**, 235 (2001), URL: http://www.sciencedirect.com/science/article/pii/S0169433200008576.

[82] T. Prokscha, E. Morenzoni, M. Meyberg, T. Wutzke, B. E. Matthias, A. Fachat, K. Jungmann, and G. zu Putlitz, *Muonium formation by collisions of muons with solid rare-gas and solid nitrogen layers*, Phys. Rev. A **58**, 3739 (1998), URL: http://link.aps.org/doi/10.1103/PhysRevA.58.3739.

[83] E. Morenzoni, F. Kottmann, D. Maden, B. Matthias, M. Meyberg, T. Prokscha, T. Wutzke, and U. Zimmermann, *Generation of very slow polarized positive muons*, Phys. Rev. Lett. **72**, 2793 (1994), URL: http://link.aps.org/doi/10.1103/PhysRevLett.72.2793.

[84] E. Morenzoni, M. Birke, H. Glckler, A. Hofer, J. Litterst, M. Meyberg, C. Niedermayer, T. Prokscha, G. Schatz, and T. Wutzke, *Generation of very slow polarized muons by moderation*, Hyperfine Interactions **106**, 229 (1997), URL: http://dx.doi.org/10.1023/A%3A1012610528798.

[85] W. Eckstein, *Computer Simulation of Ion-Solid Interactions*, vol. 10 of *Springer Series in Materials Science* (Springer Berlin Heidelberg, 1991).

[86] E. Morenzoni, H. Glückler, T. Prokscha, R. Khasanov, H. Luetkens, M. Birke, E. Forgan, C. Niedermayer, and M. Pleines, *Implantation studies of keV positive muons in thin metallic layers*, Nuclear Instruments and Methods in Physics Research Section B: Beam Interactions with Materials and Atoms **192**, 254 (2002), URL: http://www.sciencedirect.com/science/article/pii/S0168583X01011661.

[87] P. Bakule, Y. Matsuda, Y. Miyake, K. Nagamine, M. Iwasaki, Y. Ikedo, K. Shimomura, P. Strasser, and S. Makimura, *Pulsed source of ultra low energy positive muons for near-surface SR studies*, Nuclear Instruments and Methods in Physics Research Section B: Beam Interactions with Materials and Atoms **266**, 335 (2008), URL: http://www.sciencedirect.com/science/article/pii/S0168583X07016734.

[88] P. Bakule, Y. Matsuda, Y. Miyake, K. Nagamine, K. Shimomura, P. Strasser, S. Makimura, and M. Iwasaki, *Prospects for ultra-low-energy muon beam at J-PARC*, Nuclear Instruments and Methods in Physics Research Section A: Accelerators, Spectrometers, Detectors and Associated Equipment **600**, 35 (2009), URL: http://www.sciencedirect.com/science/article/pii/S0168900208016513.

[89] D. H. Everett, *Manual of Symbols and Terminology for Physicochemical Quantities and Units, Appendix II: Definitions, Terminology and Symbols in Colloid and Surface Chemistry*, Pure Appl. Chem. **31**, 577 (1972).

[90] T. Yanagisawa, T. Shimizu, K. Kuroda, and C. Kato, *The Preparation of Alkyltriinethylaininonium-Kaneinite Complexes and Their Conversion to Microporous Materials*, Bulletin of the Chemical Society of Japan **63**, 988 (1990).

[91] C. T. Kresge, M. E. Leonowicz, W. J. Roth, J. C. Vartuli, and J. S. Beck, *Ordered mesoporous molecular sieves synthesized by a liquid-crystal template mechanism*, Nature **359**, 710 (1992), URL: http://dx.doi.org/10.1038/359710a0.

[92] Y. Cohen, K. Landskron, N. Ttreault, S. Fournier-Bidoz, B. Hatton, and G. Ozin, *A Silicon-Silica Nanocomposite Material*, Advanced Functional Materials **15**, 593 (2005), URL: http://dx.doi.org/10.1002/adfm.200400069.

[93] A. Schenk, *Muon Spin Rotation Spectroscopy: Principles and Applications in Solid State Physics* (Adam Hilger, Bristol, 1985).

[94] M. M. Hossain, Ph.D. thesis, University of British Columbia (2012).

[95] N. Alberola, T. Anthonioz, A. Badertscher, C. Bas, A. Belov, P. Crivelli, S. Gninenko, N. Golubev, M. Kirsanov, A. Rubbia, *et al.*, *Development of a high-efficiency pulsed slow positron beam for measurements with orthopositronium in vacuum*, Nuclear Instruments and Methods in Physics Research Section A: Accelerators, Spectrometers, Detectors and Associated Equipment **560**, 224 (2006), URL: http://www.sciencedirect.com/science/article/pii/S0168900206000702.

[96] R. Brun and F. Rademakers, *ROOT – An object oriented data analysis framework*, Nuclear Instruments and Methods in Physics Research Section A: Accelerators, Spectrometers, Detectors and Associated Equipment **389**, 81 (1997), new Computing Techniques in Physics Research V, URL: http://www.sciencedirect.com/science/article/pii/S016890029700048X.

[97] A. Suter and B. Wojek, *Musrfit: A Free Platform-Independent Framework for SR Data Analysis*, Physics Procedia **30**, 69 (2012), 12th International Conference on Muon Spin Rotation, Relaxation and Resonance (SR2011), URL: http://www.sciencedirect.com/science/article/pii/S187538921201228X.

[98] M. Senba, *Spin dynamics of positive muons during cyclic charge exchange and muon slowing down time*, Journal of Physics B: Atomic, Molecular and Optical Physics **23**, 1545 (1990), URL: http://stacks.iop.org/0953-4075/23/i=9/a=024.

[99] D. P. Spencer, Ph.D. thesis, University of British Columbia (1985).

[100] D. Fleming, D. Arseneau, D. Garner, M. Senba, and R. Mikula, *Muonium formation and the missing fraction in vapors*, Hyperfine Interactions **18**, 655 (1984), URL: http://dx.doi.org/10.1007/BF02064885.

[101] R. E. Turner and M. Senba, *On the pressure dependence of the polarization of diamagnetic muons and muonium in pure noble gases: Is there a missing fraction?*, The Journal of Chemical Physics **84**, 3776 (1986), URL: http://scitation.aip.org/content/aip/journal/jcp/84/7/10.1063/1.450087.

[102] T. Prokscha, *Change to Konti-2/Ag-coated sample plate: energy and B scan*, LEM Experimental ELOG: 4834 (2010), URL: http://lmu.web.psi.ch/docu/LEM_Memo/LEM_Asymmetry/Ag_Asym_asFunctionOf_EandB_July2010.pdf.

[103] S. F. J. Cox, *Implanted muon studies in condensed matter science*, Journal of Physics C: Solid State Physics **20**, 3187 (1987), URL: http://stacks.iop.org/0022-3719/20/i=22/a=005.

[104] R. Kiefl and T. Estle, *Chapter 15 Muonium in Semiconductors*, in *Hydrogen in Semiconductors*, edited by J. I. Pankove and N. M. Johnson (Elsevier, 1991), vol. 34 of *Semiconductors and Semimetals*, pp. 547 – 584.

[105] K. Woodle, K.-P. Arnold, M. Gladisch, J. Hofmann, M. Janousch, K. Jungmann, H.-J. Mundinger, G. Putlitz, J. Rosenkranz, W. Schfer, *et al.*, *Measurement of the polarization of thermal muonium in vacuum*, Zeitschrift fr Physik D Atoms, Molecules and Clusters **9**, 59 (1988), URL: http://dx.doi.org/10.1007/BF01384448.

[106] T. Prokscha, E. Morenzoni, D. G. Eshchenko, N. Garifianov, H. Glückler, R. Khasanov, H. Luetkens, and A. Suter, *Formation of Hydrogen Impurity States in Silicon and Insulators at Low Implantation Energies*, Phys. Rev. Lett. **98**, 227401 (2007), URL: http://link.aps.org/doi/10.1103/PhysRevLett.98.227401.

[107] K. Sedlak, R. Scheuermann, T. Shiroka, A. Stoykov, A. Raselli, and A. Amato, *MusrSim and MusrSimAna - Simulation Tools for µSR Instruments*, Physics Procedia **30**, 61 (2012), 12th International Conference on Muon Spin Rotation, Relaxation and Resonance (µSR2011), URL: http://www.sciencedirect.com/science/article/pii/S1875389212012266.

[108] A. Antognini, P. Crivelli, T. Prokscha, K. S. Khaw, B. Barbiellini, L. Liszkay, K. Kirch, K. Kwuida, E. Morenzoni, F. M. Piegsa, *et al.*, *Muonium Emission into Vacuum from Mesoporous Thin Films at Cryogenic Temperatures*, Phys. Rev. Lett. **108**, 143401 (2012), URL: http://prl.aps.org/abstract/PRL/v108/i14/e143401.

[109] S. Agostinelli, J. Allison, K. Amako, J. Apostolakis, H. Araujo, P. Arce, M. Asai, D. Axen, S. Banerjee, G. Barrand, *et al.*, *Geant4 - a simulation toolkit*, Nuclear Instruments and Methods in Physics Research Section A: Accelerators, Spectrometers, Detectors and Associated Equipment **506**, 250 (2003), URL: http://www.sciencedirect.com/science/article/pii/S0168900203013688.

[110] T. Paraïso, E. Morenzoni, T. Prokscha, and A. Suter, *Geant4 simulation of low energy experiments at PSI*, Physica B: Condensed Matter **374 - 375**, 498 (2006), proceedings of the Tenth International Conference on Muon Spin Rotation, Relaxation and Resonance Proceedings of the Tenth International Conference on Muon Spin Rotation, Relaxation and Resonance, URL: http://www.sciencedirect.com/science/article/pii/S0921452605013608.

[111] D. B. Cassidy, P. Crivelli, T. H. Hisakado, L. Liszkay, V. E. Meligne, P. Perez, H. W. K. Tom, and A. P. Mills, *Positronium cooling in porous silica measured via*

Doppler spectroscopy, Phys. Rev. A **81**, 012715 (2010), URL: http://link.aps.org/doi/10.1103/PhysRevA.81.012715.

[112] R. Kiefl, B. Patterson, E. Holzschuh, W. Odermatt, and D. Harshman, *Hyperfine splitting of muonium in SiO_2 powder*, Hyperfine Interactions **18**, 563 (1984), URL: http://dx.doi.org/10.1007/BF02064868.

[113] D. Harshman, R. Keitel, M. Senba, R. Kiefl, E. Ansaldo, and J. Brewer, *Diffusion and trapping of muonium on silica surfaces*, Physics Letters A **104**, 472 (1984), URL: http://www.sciencedirect.com/science/article/pii/0375960184900252.

[114] K. G. Lynn and H. Lutz, *Slow positrons in single-crystal samples of Al and Al-Al_xO_y*, Phys. Rev. B **22**, 4143 (1980), URL: http://link.aps.org/doi/10.1103/PhysRevB.22.4143.

[115] J. Xu, J. Moxom, S. Yang, R. Suzuki, and T. Ohdaira, *Dependence of porosity in methyl-silsesquioxane thin films on molecular weight of sacrificial triblock copolymer*, Chemical Physics Letters **364**, 309 (2002), URL: http://www.sciencedirect.com/science/article/pii/S0009261402013696.

[116] G. W. Ford, L. M. Sander, and T. A. Witten, *Lifetime Effects of Positronium in Powders*, Phys. Rev. Lett. **36**, 1269 (1976), URL: http://link.aps.org/doi/10.1103/PhysRevLett.36.1269.

[117] M. J. Frisch, G. W. Trucks, H. B. Schlegel, G. E. Scuseria, M. A. Robb, J. R. Cheeseman, V. G. Zakrzewski, J. A. M. Jr., R. E. Stratmann, J. C. Burant, *et al.*, *Gaussian 98 (Gaussian, Inc., Pittsburgh, PA, 1998)* (1998).

[118] Z. Salman, T. Prokscha, P. Keller, E. Morenzoni, H. Saadaoui, K. Sedlak, T. Shiroka, S. Sidorov, A. Suter, V. Vrankovic, *et al.*, *Design and Simulation of a Spin Rotator for Longitudinal Field Measurements in the Low Energy Muons Spectrometer*, Physics Procedia **30**, 55 (2012), 12th International Conference on Muon Spin Rotation, Relaxation and Resonance (μSR2011), URL: http://www.sciencedirect.com/science/article/pii/S1875389212012254.

[119] K. Nagamine, S. Nagamiya, O. Hashimoto, N. Nishida, T. Yamazaki, and B. Patterson, *Temperature-independent hyperfine field on μ^+ in nickel in the temperature range of* $0.12-300$ *K*, Hyperfine Interactions **1**, 517 (1975), URL: http://dx.doi.org/10.1007/BF01022481.

[120] R. F. Kiefl, M. D. Hossain, B. M. Wojek, S. R. Dunsiger, G. D. Morris, T. Prokscha, Z. Salman, J. Baglo, D. A. Bonn, R. Liang, *et al.*, *Direct measurement*

of the London penetration depth in $YBa_2Cu_3O_{6.92}$ *using low-energy* μSR, Phys. Rev. B **81**, 180502 (2010), URL: http://link.aps.org/doi/10.1103/PhysRevB.81.180502.

[121] *OPERA, Magnetic Field Solver, Vector Fields Ltd., Oxford, England* (2014), URL: http://operafea.com/.

[122] *COMSOL Multiphysics: The Platform for Physics-Based Modeling and Simulation* (accessed Dec 2014), URL: http://www.comsol.com.

[123] P. Crivelli, D. A. Cooke, and S. Friedreich, *Experimental considerations for testing antimatter antigravity using positronium 1S-2S spectroscopy*, International Journal of Modern Physics: Conference Series **30**, 1460257 (2014), URL: http://www.worldscientific.com/doi/abs/10.1142/S2010194514602579.

[124] *TOPTICA photonics* (accessed Dec 2014), URL: http://www.toptica.com/.

[125] *Advanced Thin Films* (accessed Dec 2014), URL: http://www.atfilms.com/.

[126] D. Harshman, *Muon/muonium surface interactions*, Hyperfine Interactions **32**, 847 (1986), URL: http://dx.doi.org/10.1007/BF02394994.

[127] I. Gurevich, I. Ivanter, E. Meleshko, B. Nikol'skii, V. Roganov, V. Selivanov, V. Smilga, B. Sokolov, and V. Shestakov, *Two-frequency Precession of Muonium in a Magnetic Field*, ZhETF (1971), URL: http://www.jetp.ac.ru/cgi-bin/e/index/e/33/2/p253?a=list.

[128] E. Holzschuh, W. Kündig, and B. Patterson, *Direct measurement of the muonium hyperfine frequencies in quartz*, Helvetica Physica Acta **54**, 552 (1981), URL: http://retro.seals.ch/digbib/view?pid=hpa-001:1981:54::558.

[129] G. Bollen, C. Campbell, S. Chouhan, C. Gunaut, D. Lawton, F. Marti, D. Morrissey, J. Ottarson, G. Pang, S. Schwarz, *et al.*, *Manipulation of rare isotope beams - from high to low energies*, Nuclear Instruments and Methods in Physics Research Section B: Beam Interactions with Materials and Atoms **266**, 4442 (2008), proceedings of the {XVth} International Conference on Electromagnetic Isotope Separators and Techniques Related to their Applications, URL: http://www.sciencedirect.com/science/article/pii/S0168583X08007532.

[130] G. Savard, *Ion manipulation with cooled and bunched beams*, The European Physical Journal A - Hadrons and Nuclei **25**, 713 (2005), URL: http://dx.doi.org/10.1140/epjad/i2005-06-206-x.

[131] Y. Bao, A. Antognini, W. Bertl, M. Hildebrandt, K. S. Khaw, K. Kirch, A. Papa, C. Petitjean, F. M. Piegsa, S. Ritt, *et al.*, *Muon Cooling: Longitudinal Compression*, Phys. Rev. Lett. **112**, 224801 (2014), URL: http://link.aps.org/doi/10.1103/PhysRevLett.112.224801.

[132] A. Antognini, A. Eggenberger, K. S. Khaw, K. Kirch, F. Piegsa, D. Taqqu, G. Wichmann, W. Bertl, M. Hildebrandt, A. Knecht, *et al.*, *High-brightness ultracold muon beam: Test of transverse compression*, Proposal for an experiment at PSI (BV 2014) (2014).

[133] F. Sauli, *Instrumentation in High Energy Physics*, Advanced Series on Directions in High Energy Physics: Volume 9 (World Scientific Publishing Co. Pte. Ltd., 1992).

[134] E. A. Mason, S. L. Lin, and I. R. Gatland, *Mobility and diffusion of protons and deuterons in helium-a runaway effect*, Journal of Physics B: Atomic and Molecular Physics **12**, 4179 (1979), URL: http://stacks.iop.org/0022-3700/12/i=24/a=023.

[135] F. Howorka, F. C. Feshsenfeld, and D. L. Albritton, *H^+ and D^+ ions in He: observations of a runaway mobility*, Journal of Physics B: Atomic and Molecular Physics **12**, 4189 (1979), URL: http://stacks.iop.org/0022-3700/12/i=24/a=024.

[136] D. Gerola, W. B. Waeber, M. Shi, and S. J. Wang, *Quasidivergency-free extraction of a slow positron beam from high magnetic fields*, Review of Scientific Instruments **66**, 3819 (1995), URL: http://scitation.aip.org/content/aip/journal/rsi/66/7/10.1063/1.1145443.

[137] S. Ritt, R. Dinapoli, and U. Hartmann, *Application of the DRS chip for fast waveform digitizing*, Nuclear Instruments and Methods in Physics Research Section A: Accelerators, Spectrometers, Detectors and Associated Equipment **623**, 486 (2010), 1st International Conference on Technology and Instrumentation in Particle Physics, URL: http://www.sciencedirect.com/science/article/pii/S0168900210006091.

[138] S. Ritt, *DRS4 Evaluation Board Users Manual* (accessed Jan 2015), URL: http://www.psi.ch/drs/DocumentationEN/manual_rev50.pdf.

[139] J. Lindhard and A. Winther, *Stopping power of electron gas and equipartition rule*, Mat. Fys. Medd. Dan. Wid. Selsk **34** (1964), URL: http://www.sdu.dk/media/bibpdf/Bind%2030-39%5CBind%5Cmfm-34-4.pdf.

[140] L. Urbán (GEANT4 Collaboration), Tech. Rep. CERN-OPEN-2006-077, CERN, Geneva (2006).

[141] *LOW-ENERGY p-He AND mu-He SIMULATION IN GEANT4* (Paper presented at the 11th International Computational Accelerator Physics Conference (ICAP 2012), 2012).

[142] Y. Nakai, T. Shirai, T. Tabata, and R. Ito, *Cross sections for charge transfer of hydrogen atoms and ions colliding with gaseous atoms and molecules*, Atomic Data and Nuclear Data Tables **37**, 69 (1987), URL: http://www.sciencedirect.com/science/article/pii/0092640X87900052.

[143] M. Senba, *Charge exchange collisions in the presence of competing processes: an integral equation approach*, Journal of Physics B: Atomic, Molecular and Optical Physics **22**, 2027 (1989), URL: http://stacks.iop.org/0953-4075/22/i=12/a=018.

[144] P. Krstic and D. Schultz, *Elastic and related transport cross sections for collisions among isotopomers of $H^+ + H$, $H^+ + H^2$, $H^+ + He$, $H + H$, and $H + H^2$*, Atomic and Plasma-Material Data for Fusion 8 **1** (1998).

[145] J. F. Ziegler, M. Ziegler, and J. Biersack, *SRIM – The stopping and range of ions in matter (2010)*, Nuclear Instruments and Methods in Physics Research Section B: Beam Interactions with Materials and Atoms **268**, 1818 (2010), 19th International Conference on Ion Beam Analysis, URL: http://www.sciencedirect.com/science/article/pii/S0168583X10001862.

[146] G. Wichmann, *Stationary Density Gradient in a Helium Gas Cell at Low Temperature*, Master's thesis, ETH Zurich (2013).

[147] G. Wichmann, *Neutron radiography of a helium gas density gradient at cryogenic temperatures for a novel muon beam line*, Poster presentation at Swiss Physical Society (SPS) annual meeting 2014 (2014).

[148] E. Fermi, *Ueber die magnetischen Momente der Atomkerne*, Zeitschrift fuer Physik **60**, 320 (1930), URL: http://dx.doi.org/10.1007/BF01339933.

[149] D. G. Fleming, R. J. Mikula, and D. M. Garner, μ^+ *charge exchange and muonium formation in low-pressure gases*, Phys. Rev. A **26**, 2527 (1982), URL: http://link.aps.org/doi/10.1103/PhysRevA.26.2527.

[150] E. Holzschuh, *Direct measurement of muonium hyperfine frequencies in Si and Ge*, Phys. Rev. B **27**, 102 (1983), URL: http://link.aps.org/doi/10.1103/PhysRevB.27.102.

[151] Y. Cohen, B. Hatton, H. Mguez, N. Coombs, S. Fournier-Bidoz, J. Grey, R. Beaulac, C. Reber, and G. Ozin, *Spin-on Nanostructured SiliconSilica Film Displaying Room-Temperature Nanosecond Lifetime Photoluminescence*, Advanced Materials **15**, 572 (2003), URL: http://dx.doi.org/10.1002/adma.200304491.

[152] W. Yantasee, Y. Lin, X. Li, G. E. Fryxell, T. S. Zemanian, and V. V. Viswanathan, *Nanoengineered electrochemical sensor based on mesoporous silica thin-film functionalized with thiol-terminated monolayer*, Analyst **128**, 899 (2003), URL: http://dx.doi.org/10.1039/B303973K.

[153] Z. Salman, *Search PSI μSR Runs* (accessed Dec 2014), URL: http://musruser.psi.ch/cgi-bin/SearchDB.cgi.

Kim Siang Khaw

Curriculum Vitae

Institute for Particle
Physics (IPP)
HPK G 27
Otto-Stern-Weg 5
8093 Zurich
☎ *+41 44 633 71 95*
✉ *khaw@phys.ethz.ch*

Education

Tertiary

2011 - 2015 **Ph.D. (Physics)**, *ETH Zurich*, Zurich, Switzerland.

2009 - 2011 **Master of Science (Physics)**, *University of Tokyo*, Tokyo, Japan, *Grade : 3.9/4.0*.

2005 - 2009 **Bachelor of Science (Physics)**, *Kyoto University*, Kyoto, Japan, *Grade : 3.5/4.0*.

Secondary

2004 - 2005 **Japanese Pre-U Course**, *Osaka University of Foreign Studies*, Osaka, Japan.

2002 - 2003 **Malaysian Higher School Certificate (STPM)**, *Chung Ling High School*, Penang, Malaysia.

Scholarships and grants

2010 **Participation Grant**, *CSC School Grant*, Brunel University and STFC.
Grant for the participation to the CERN School of Computing (CSC) 2010 to London.

2010 **Program for Young Researcher Overseas Visits**, *Department of Physics*, University of Tokyo.
Travel allowance for the participation to the CERN School of Computing (CSC) 2010 to London.

2009 -2011 **Master Scholarship**, *Monbukagakusho Scholarship*, Japanese Government.
Scholarship for master course for a duration of two years.

2004 -2009 **Undergraduate Scholarship**, *Monbukagakusho Scholarship*, Japanese Government.
Scholarship for undergraduate studies for a duration of five years.

Research and Teaching Experience

Research

2011 - Present   **Graduate Research Assistant**, *ETH Zurich*, Switzerland.
Supervisor : **Klaus Kirch** (ETH Zurich and PSI)
- Muonium production with mesoporous silica
- Phase space compression of muon beam
- Charged particle detection with plastic scintillating fibers and Geiger-mode APD

2011   **Internship**, *Paul Scherrer Institute (PSI)*, Switzerland.
Supervisor : **Klaus Kirch** (ETH Zurich and PSI)
- Muonium production with mesoporous silica

2009 - 2011   **Master Research**, *University of Tokyo*, Japan.
Supervisors : **Tomio Kobayashi, Shoji Asai and Toshio Namba** (University of Tokyo)
- Test of CPT symmetry with positronium
- Search for NMSSM Higgs bosons in the LHC-ATLAS experiment (Master thesis)

2008 - 2009   **Undergraduate Research (Final year)**, *Kyoto University*, Japan.
Supervisor : **Koichiro Tanaka** (Kyoto University)
- External Cavity Laser Diode (ECLD) with Littrow configuration (Bachelor thesis)
- Rubidium Saturated Absorption Spectroscopy

2007 - 2008   **Undergraduate Research (Third year second semester)**, *Kyoto University*, Japan.
Supervisor : **Kenichi Yoshikawa** (Kyoto University)
- Non-linear phenomena in OP-AMP 27 such as bifurcation

2007   **Undergraduate Research (Third year first semester)**, *Kyoto University*, Japan.
Supervisor : **Tsuyoshi Nakaya** (Kyoto University)
- Lifetime of ortho-positronium
- Ratio of 2γ and 3γ from para- and ortho-positronium respectively

Teaching

2011 - Present   **Teaching assistant for Advanced Student Laboratory**, *Department of Physics, ETH Zurich*, Zurich.

2009   **Summer School Teaching Assistant**, *High Energy Accelerator Research Organization (KEK)*, Tsukuba.

2009   **Science Camp Teaching Assistant**, *3rd Asian Science Camp*, Tsukuba.

2008 - 2009   **Undergraduate Tutor**, *Department of Science, Kyoto University*, Kyoto.

Informatics

2013 - Present   **IT Officer**, *Telejob and ETH GET HIRED job platform*, ETH Zurich.

2013 - Present   **Web master**, *Website for Malaysian Swiss Association*, Zurich.

2011 - Present   **Web master**, *Website for Precision Physics at Low Energy group*, ETH Zurich.

Languages

Chinese	Native	*Mandarin, Fujien and Cantonese*
English	Fluent	*TOEFL iBT : 101/120*
German	Beginner	*Level A2-B1 in the Common European Framework (CEF)*
Japanese	Fluent	*Japanese Language Proficiency Test N1 : 165/180*
Malay	Fluent	*National language*

Technical skills

Operating System	Microsoft Windows, Mac OSX and Linux	**Script**	Shell script
Programming languages	C/C++, Python and Fortran	**Simulation**	GEANT4, COMSOL
Document	Latex, Microsoft Office and Open Office	**Web**	HTML, PHP, CSS, Javascript and Silva CMS
Analysis and Plots	Mathematica, MATLAB, ROOT, R and Gnuplot	**Electronics**	CAMAC and NIM, DRS4 and FPGA
Technical Drawing	Autodesk Inventor		

Publications

Kim Siang Khaw, Aldo Antognini, Paolo Crivelli, Klaus Kirch, Elvezio Morenzoni, Zaher Salman, Andreas Suter, and Thomas Prokscha. Geant4 simulation of the psi lem beam line: energy loss and muonium formation in thin foils and the impact of unmoderated muons on the μsr spectrometer. *e-Print: arXiv:1506.01779*, 2015.

Yu Bao, Aldo Antognini, Wilhelm Bertl, Malte Hildebrandt, Kim Siang Khaw, Klaus Kirch, Angela Papa, Claude Petitjean, Florian M. Piegsa, Stefan Ritt, Kamil Sedlak, Alexey Stoykov, and David Taqqu. Muon cooling: Longitudinal compression. *Phys. Rev. Lett. 112, 224801*, 2014.

Kirch Klaus and Kim Siang Khaw. Testing antimatter gravity with muonium. *Int. J. Mod. Phys. Conf. Ser. 30, 1460258*, 2014.

A. Antognini, P. Crivelli, T. Prokscha, K.S. Khaw, B. Barbiellini, L. Liszkay, K. Kirch, K. Kwuida, E. Morenzoni, F.M. Piegsa, Z. Salman, and A. Suter. Muonium emission into vacuum from mesoporous thin films at cryogenic temperatures. *Phys. Rev. Lett. 108, 143401*, 2012.

Presentations

Oral

2014 **Towards next generation fundamental precision measurements with muons**, *CENPA Seminar (SKYPE), University of Washington*, Seattle, United States.

2014 **Testing Gravity with Muonium**, *Gravitational Tests of Lorentz Invariance, LVGR'14*, Indiana University, Bloomington, Indiana.

2014 **Towards next generation fundamental precision measurements with muons**, *Fermilab Research Techniques Seminar*, Fermilab, United States.

2013 **Development of a novel muon beam line for next generation precision experiments**, *Joint Zurich Particle Physics Ph.D. Seminar 2013*, ETH Zurich, Switzerland.

2012 **Muonium emission into vacuum from mesoporous thin films at cryogenic temperatures**, *Joint Zurich Particle Physics Ph.D. Seminar 2012*, University Zurich-Irchel, Switzerland.

2012 **Muonium emission into vacuum from mesoporous thin films at cryogenic temperatures**, *SPS Annual Meeting 2012*, ETHZ, Switzerland.

2012 **Muonium emission into vacuum from mesoporous thin films at cryogenic temperatures**, *QED 2012*, Cargèse, Corsica, France.

2011 **Muonium vacuum yield in SiO2 thin films of porous material**, *Joint Zurich Particle Physics Ph.D. Seminar 2011*, ETHZ, Switzerland.

2011 **Studies of the NMSSM Higgs decaying to four taus with the ATLAS detector using a new hadronic tau reconstruction algorithm**, *Invited talk by the theory group of Department of Physics, USM*, University Science of Malaysia (USM).

2010 **Search for NMSSM Higgs decaying to four taus with the ATLAS detector using new hadronic tau reconstruction**, *The Physical Society of Japan (JPS) Autumn Conference*, Kyushu, Japan.

2010 **Higgs Boson Search in the VBF Channel of NMSSM with the ATLAS detector**, *Higgs Working Group Meeting (HSG4) of ATLAS*, CERN, Switzerland.

2010 **Higgs Boson Search in the VBF Channel of NMSSM with the ATLAS detector**, *The Physical Society of Japan (JPS) Spring Conference*, Okayama, Japan.

2010 **Higgs Boson Search in the VBF Channel of NMSSM with the ATLAS detector**, *International Center for Elementary Particle Physics Symposium 2010*, Nagano, Japan.

Poster

2014 **Muonium production for fundamental physics experiments**, *Annual Meeting of Swiss Physical Society 2014*, Fribourg, Switzerland.

2013   **Development of a novel muon beam line for next generation precision experiments**, *3rd Workshop on the Physics of Fundamental Symmetries and Interactions at low energies and the precision frontier*, Paul Scherrer Institute, Villigen, Switzerland.

2013   **Development of a novel muon beam line for next generation precision experiments**, *Joint Annual Meeting of Swiss Physical Society and Austrian Physical Society 2013*, Johannes Kepler-University, Linz, Austria.

2013   **Muonium emission into vacuum from mesoporous thin films at cryogenic temperatures**, *International Poster Presentation of young researchers at KEK 2013*, KEK, Tsukuba, Japan.

2012   **Muonium emission into vacuum from mesoporous thin films at cryogenic temperatures**, *QED 2012*, Cargèse, Corsica, France.

2011   **Muonium vacuum yield in SiO2 thin films of porous material**, *European Summer Campus 2011*, Strasbourg, France.

2011   **Muonium vacuum yield in SiO2 thin films of porous material**, *Joint Annual Meeting of Swiss Physical Society and Austrian Physical Society 2011*, Lausanne, Switzerland.

2009   **External Cavity Laser Diode (ECLD) for cantilever cooling**, *Presentation of bachelor thesis by First KEK Summer Challenge students*, KEK, Japan.

Other related experiences

Summer/Winter/International Schools

2013 **Participant**, *1st thematic CERN School of Computing (tCSC) 2013*, Split, Croatia.

2013 **Participant**, *The Excellence in Detector and Instrumentation Technologies (EDIT) 2013*, KEK, Tsukuba, Japan.

2012 **Participant**, *PSI Summer School on Particle Physics*, Zuoz, Switzerland.

2012 **Participant**, *Cargèse International School on QED & Quantum Vacuum, Low Energy Frontier*, Cargèse, Corsica, France.

2011 **Participant**, *European Summer Campus 2011*, Strasbourg, France.

2010 **Participant**, *CERN School of Computing (CSC) 2010*, Brunel University, UK.

2007 **Participant**, *First KEK Summer Challenge*, High Energy Accelerator Research Organization (KEK), Tsukuba.

Social

2012 - Present **Committee Member**, *Malaysian Swiss Association*, Zurich.

2009 - 2011 **Committee Member**, *Malaysia Student Association in Tokyo University (MSATU)*, Tokyo.

2005 - 2008 **President and Committee Member**, *Kyoto International Student House*, Kyoto.

2004 - 2009 **Committee Member**, *Malaysia Student Association in Japan (MSAJ)*, Japan.

Scientific Outreach

2013 **High Speed Positron Detector with G-APD and Plastic Scintillating Fiber**, *13th Swiss Day for Physics and Teaching*, DPK & Physics Department, ETHZ.

2012 **High Speed Positron Detector with G-APD and Plastic Scintillating Fiber**, *Physics Department's Day 2012*, Physics Department, ETHZ.

2011 **A Brief Introduction to Particle Physics**, *Research colloquium at CLHS for high school students*, Chung Ling High School (CLHS), Penang.

2010 **First Step into Science by Foreign Scientists**, *Science communication event "Science Agora"*, Tokyo Academic Park, Odaiba, Tokyo.